

Multi-scale analysis of automotive lithium-ion batteries safety: thermodynamic characterization and nail penetration

Zur Erlangung des akademischen Grades einer
DOKTORIN DER INGENIEURWISSENSCHAFTEN (Dr.-Ing.)

von der KIT-Fakultät für Maschinenbau des
Karlsruher Instituts für Technologie (KIT)
angenommene

DISSERTATION

von

M.Sc. Hyojeong Kim

Tag der mündlichen Prüfung

20.November 2025

Hauptreferent/Hauptreferentin

Prof. Dr. Hans Jürgen Seifert

Korreferenten/Korreferentinnen

Prof. Dr. Johannes Wandt

*“Here, on the edge of what we know,
in contact with the ocean of the unknown,
shines the mystery and beauty of the world.
And it’s breathtaking.”*

From <Seven brief lessons on physics> by Carlo Rovelli

Abstract

Lithium-ion batteries (LIBs) have become pivotal energy storage devices, particularly for battery electric vehicles (BEVs), due to their superior energy density and long cycle life. However, their widespread adoption is accompanied by significant safety concerns, primarily associated with thermal runaway (TR) events initiated by internal short circuits (ISCs). Among LIB chemistries, nickel-rich layered oxide cathode materials, such as lithium-nickel-manganese-cobalt oxide (NMC) and lithium-nickel-cobalt-aluminum oxide (NCA), are increasingly favored to meet demands for higher energy density. Yet, their poor thermal stability introduces elevated safety risks at the cell level, making the thorough investigation of their thermal and thermodynamic behavior critical.

This dissertation systematically addresses the existing research gap by experimentally analyzing the thermal and thermodynamic stability of commercial high-nickel cathode active materials and correlating these intrinsic material properties with LIB cell-level safety performance under abuse conditions. To achieve this, a multi-faceted experimental approach was adopted, combining both material-level and cell-level investigations: **High Temperature Drop Solution Calorimetry (Setaram MHTC and Alexsys-1000)** was applied to determine the standard enthalpies of formation of NMC materials, providing quantitative measures of intrinsic thermodynamic stability across different cathode compositions; **Differential Scanning Calorimetry (DSC)** and **Thermogravimetric Analysis (TGA)** were conducted on fully charged cathodes harvested from commercial automotive LIBs to investigate decomposition onset temperatures, reaction kinetics, and corresponding mass loss behavior under thermal abuse conditions; **Accelerating Rate Calorimetry (ARC)** was employed to evaluate thermal runaway threshold and self-heating rates at the cell level under quasi-adiabatic conditions, demonstrating the uniform thermal properties between floating can and can on potential; and **Nail/Needle Penetration Test** was extensively optimized and utilized not only to induce reproducible ISCs but also to study ISC formation mechanisms, current characteristics, and temperature evolution *insitu*.

The results reveal **a strong correlation between intrinsic cathode thermodynamic stability and overall cell safety**. Specifically, DSC measurements demonstrated that increasing nickel content in NMC compositions leads to lower decomposition onset temperatures and accelerated exothermic heat release, indicating decreased thermal stability with higher Ni loading. High temperature drop solution calorimetry further confirmed that the enthalpy of formation becomes progressively less exothermic as manganese content decreases, reflecting diminished thermodynamic stability in Ni-rich NMC compositions. Furthermore, this work offers a refined understanding of NCA stability by introducing the concept of “*degree of reaction*” to quantify the reaction kinetics. While prior studies often interpreted NCA cathodes as thermally stable based primarily on relatively high onset temperatures, the present study demonstrates that, under realistic conditions in the presence of electrolyte, NCA undergoes rapid exothermic degradation once decomposition initiates. This explains why LIB cells employing NCA cathodes exhibit reduced robustness against ISC-induced thermal runaway despite their seemingly favorable onset temperatures.

Beyond establishing material-to-cell level correlations, this work also highlights how cell design features substantially influence ISC resilience. In particular, the “**floating can**” configuration in prismatic LIB cells was experimentally validated as an effective safety feature. While cells with a “**can**

on potential” design allow high ISC currents between the outermost anode and cell casing, leading to rapid heating and thermal runaway, floating can cells introduce additional electrical resistance that limits ISC current and mitigates catastrophic TR initiation.

Furthermore, the study investigates how ***electrode assembly architectures*** affect ISC severity. Comparative analysis between stacked and jelly roll assemblies revealed two distinct ISC formation mechanisms. In jelly roll cells, the continuous long electrode geometry promotes more extensive ISC regions, increasing short-circuit current and joule heating compared to stacked cells, where ISCs are spatially more localized. These findings are supported by ISC current profiles, penetration force periodicity, and internal temperature measurements obtained during penetration testing.

Collectively, this dissertation provides comprehensive experimental evidence linking cathode material stability, electrode design, and safety-critical failure modes in automotive LIBs. The findings contribute valuable insights for the development of safer, high energy density lithium-ion battery systems, offering practical guidelines for both material optimization and cell design strategies to mitigate thermal runaway risk in BEV applications.

Kurzfassung

Lithium-Ionen Batterien (LIB) haben sich insbesondere für BEVs (battery electric vehicles) als zentrale Energiespeicher etabliert, da sie eine hohe Energiedichte und eine lange Lebensdauer bieten. Ihre breite Anwendung ist jedoch mit erheblichen Sicherheitsbedenken verbunden, die vor allem durch thermisches Durchgehen (thermal runaway, TR) infolge interner Kurzschlüsse (internal short circuit, ISC) ausgelöst werden. Unter den LIB-Chemien werden nickelreiche Kathodenmaterialien wie Lithium-Nickel-Mangan-Kobalt-Oxide (NMC) und Lithium-Nickel-Kobalt-Aluminium-Oxid (NCA) zunehmend bevorzugt, um den Anforderungen an höhere Energiedichten gerecht zu werden. Allerdings führt deren geringe thermische Stabilität zu erhöhten Sicherheitsrisiken auf Zellebene, was eine detaillierte Untersuchung ihres thermischen und thermodynamischen Verhaltens erforderlich macht.

Diese Dissertation schließt systematisch bestehende Forschungslücken, indem sie experimentell die thermische und thermodynamische Stabilität kommerzieller, nickelreicher Kathodenaktivmaterialien analysiert und diese intrinsischen Materialeigenschaften mit der Sicherheitsperformance von LIB-Zellen unter Missbrauchsbedingungen korreliert. Zu diesem Zweck wurde ein multifaktorieller experimenteller Ansatz gewählt, der sowohl material- als auch zellbezogene Untersuchungen kombiniert: **Hochtemperatur Einwurf-Lösungskalorimetrie (Setaram MHTC und Alexsys-1000)** wurde eingesetzt, um die Standardbildungsenthalpien von NMC-Materialien zu bestimmen und damit quantitative Aussagen über die thermodynamische Stabilität unterschiedlicher Kathodenzusammensetzungen zu ermöglichen; **Dynamische-Differenz-Kalorimetrie (DSC)** und **Thermogravimetrische Analyse (TGA)** wurden an vollständig geladenen Kathoden aus kommerziellen automobilen LIBs durchgeführt, um die Onset-Temperaturen, Reaktionskinetik und das zugehörige Masseverlustverhalten unter thermischem Missbrauch zu untersuchen; **Accelerating Rate Calorimetry (ARC)** wurde verwendet, um unter quasi-adiabatischen Bedingungen die Schwelle zum thermischen Durchgehen sowie Selbstheizraten auf Zellebene zu bewerten, wobei gezeigt wurde, dass die thermischen Eigenschaften zwischen Floating Can und Can on Potential vergleichbar sind. Der **Nagel/Nadel Penetrationstest** wurde umfassend optimiert und eingesetzt, um nicht nur reproduzierbare ISCs auszulösen, sondern auch um die Mechanismen der ISC-Entstehung, Eigenschaft des Stroms und Temperaturentwicklung in situ zu untersuchen.

Die Ergebnisse zeigen **eine starke Korrelation zwischen der intrinsischen thermodynamischen Stabilität der Kathode und der allgemeinen Zellsicherheit**. Insbesondere zeigte sich in den DSC-Messungen, dass ein steigender Nickelanteil in NMC-Zusammensetzungen zu niedrigeren Onset-Temperaturen und beschleunigtem exothermen Wärmefreisetzungsverhalten führt, was auf eine abnehmende thermische Stabilität bei höherem Ni-Gehalt hinweist. Die Hochtemperatur Einwurf-Lösungskalorimetrie bestätigte zudem, dass die Bildungsenthalpie mit abnehmendem Mangananteil weniger exotherm wird – ein Indikator für die reduzierte thermodynamische Stabilität in Ni-reichen NMC-Zusammensetzungen. Darüber hinaus liefert diese Arbeit eine verfeinerte Betrachtung der NCA-Stabilität durch die Einführung des Begriffs *“Reaktionsgrad”*, um die Reaktionskinetik zu quantifizieren. Während frühere Studien NCA-Kathoden häufig aufgrund ihrer relativ hohen Onset-Temperaturen als thermisch stabil einstufte, zeigt die vorliegende Untersuchung, dass NCA unter realistischen Bedingungen in Anwesenheit eines Elektrolyten rasch exotherm zerfällt, sobald die Zersetzung beginnt. Dies erklärt, warum LIB-Zellen mit NCA-Kathoden – obwohl sie aufgrund ihrer

erhöhten Zersetzungstemperaturen zunächst als stabil gelten – eine geringere Robustheit gegenüber ISC-induziertem Thermal Runaway aufweisen.

Neben der Etablierung von Korrelationen zwischen Material- und Zellebene zeigt diese Arbeit, wie stark sich Zell-Design-Merkmale auf die ISC-Resilienz auswirken. Insbesondere wurde die Konfiguration von **“Floating Can”** in prismatischen LIB-Zellen experimentell als effektives Sicherheitsmerkmal validiert. Während Zellen mit **“Can on Potential”** hohe ISC-Ströme zwischen äußerster Anode und Zellgehäuse zulassen – was zu rascher Erwärmung und Thermal Runaway führt – führt die Konfiguration von Floating Can zu einem zusätzlichen elektrischen Widerstand, der den ISC-Strom begrenzt und eine katastrophale TR-Auslösung abschwächt.

Darüber hinaus untersucht die Studie, wie sich **Elektrodenarchitekturen** auf die Schwere von ISCs auswirken. Ein vergleichender Analyseansatz zwischen gestapelten und Jelly Roll-Zellen zeigte zwei unterschiedliche Mechanismen der ISC-Bildung. In Zellen mit Jelly Roll begünstigt die kontinuierlich lange Elektrodengeometrie ausgedehntere ISC-Regionen, was zu höheren Kurzschlussströmen und stärkerer Joule-Erwärmung führt, während ISCs in gestapelten Zellen räumlich stärker lokalisiert auftreten. Diese Ergebnisse werden durch Stromprofile bei ISC, Periodizität der Penetrationskraft und interne Temperaturmessungen während des Nagel-Penetrationstests gestützt.

Insgesamt liefert diese Dissertation umfassende experimentelle Nachweise für die Zusammenhänge zwischen Kathodenmaterialstabilität, Elektrodenaufbau und sicherheitskritischen Fehlermodi in automobilen LIBs. Die Erkenntnisse bieten wertvolle Impulse für die Entwicklung sicherer Lithium-Ionen-Batteriesysteme mit hoher Energiedichte und liefern praxisnahe Empfehlungen sowohl zur Materialoptimierung als auch zur Zelldesignstrategie zur Minimierung des Thermal-Runaway-Risikos im BEV-Einsatz.

Acknowledgement

First and foremost, I would like to express my heartfelt gratitude to **Prof. Dr. Hans J. Seifert** and for his in-depth academic and invaluable scientific guidance throughout every stage of my doctoral research. His deep insight, constructive feedback, and enduring patience have been instrumental in bringing this dissertation to completion. Especially without his commitment, the commissioning of the measurements with MHTC would hardly have been possible. Furthermore, my special thanks go to **Dr. Jochen Friedl** for his in-depth academic supervision, unwavering encouragement and support for countless challenge throughout the entire doctoral period. He was always available to answer detailed questions regarding technical issues, further optimizations, and the interpretation of measurements. His support extended beyond the academic sphere, contributing meaningfully to the completion of this work.

My sincere thanks go to all members of the **Institute for Applied Materials – Applied Materials Physics (IAM-AWP)** at the **Karlsruhe Institute of Technology**, for fostering such a collaborative and motivating research environment. I am sincerely grateful to **Dr. Carlos Ziebert** for his insightful comments and continued interest in my work. His thoughtful questions during presentations and feedback for conference-posters and -presentations always challenged me to think more critically and refine my ideas with greater precision. Many thanks for the detailed support with data analysis and interpretation especially for ARC measurement. Also, I would like to thank **Christoph Gebert** for his technical support in the calibration and measurement with the Alexsys-1000 system, and for generously sharing his knowledge through countless discussions. I am also deeply thankful to **Nils Uhlmann** for his guidance during the calibration of the ARC system and his help in evaluating the experimental data.

The many personal discussions in the **Battery Cell Competence Center (BCCC)** and **Technology and Materials Analytics departments at BMW Group** were extraordinarily valuable! Their support and collaboration have played a significant role throughout my research. Their countless supports and contributions have made a lasting impact. A special note of appreciation goes to **Dr. Sebastian Scharner**, who was always willing to engage in problem-solving discussions and supported me immensely in overcoming technical challenges related to MHTC. I also wish to thank **Dr. Filippo Maglia** for kindly arranging the NMC materials necessary for the study of formation enthalpy measurements.

I would like to thank my teammates from **Cell Safety and Analysis** as well as my BMW colleagues from the **production and orientation placements** for their many small but meaningful contributions and insights into their daily work. Special thanks go to **Mohamed Laifi** and **Davud Ramazanov** for their dedicated support in testing numerous prismatic cells and in optimizing the nail penetration test. I am also grateful to the **BMW PhD network**—the opportunities for exchange and collaboration within this network were immensely valuable. A particular highlight was the two-week visit to BMW China (Shenyang and Shanghai), which underscored the reach and uniqueness of this initiative.

Beyond the academic and professional realm, I am deeply grateful to my **family and partner** for their unwavering love, patience, and support throughout this long journey. Their constant belief in me, even during moments of self-doubt, gave me the strength to persevere. I am especially thankful to

my partner, who stood by my side with remarkable patience and care during the final stages of this dissertation — despite the added challenges of planning our future together. His support helped me stay grounded and focused through one of the busiest and most meaningful periods of my life. I would also like to thank my **friends**, who have shown such understanding and brought lightness, laughter, and companionship into my life — especially during the most challenging periods of this journey.

Lastly, I would like to thank **everyone who, in one way or another, contributed to this dissertation** — whether through collaboration, mentorship, technical help, or simply by standing by my side.

Munich, August 2025

Hyojeong Kim

Contents

Abstract	i
Kurzfassung.....	iii
Acknowledgement.....	v
List of Publications.....	x
List of Figures.....	xi
List of Tables.....	xvi
List of Abbreviations.....	xviii
1 Introduction.....	1
2 Fundamentals	5
2.1 Lithium-Ion Battery (LIB)	5
2.1.1 Working Principle.....	5
2.1.2 Cathode Active Materials	7
2.1.3 Anode Active Materials.....	12
2.1.4 Liquid Electrolyte and Formation of Solid Electrolyte Interphase (SEI)	15
2.1.5 Separator.....	18
2.2 Thermal and Thermodynamic Study of Cathode	20
2.2.1 Decomposition Pathways of Layered Metal Oxides with Oxygen Release	21
2.2.2 Previous Studies of Thermal and Thermodynamic Behavior of Cathode Active Materials	22
2.2.3 Previous Studies of Enthalpy of Formation of Cathode Active Materials	24
2.3 Safety of LIB Cells.....	26
2.3.1 Thermal Runaway and its Triggers	27
2.3.2 Internal Short Circuit (ISC).....	30
2.3.3 How to Reproduce ISC in Lab.....	32
2.4 LIB for battery electric vehicle (BEV)	34
2.4.1 Commercial Cell Designs	34
2.4.2 Safety Elements in an automotive prismatic LIB Cell	36
2.4.3 Lithium-Ion Batteries in BEV.....	40
3 Experimental Methods.....	43
3.1 Thermal and Thermodynamic Study of Cathode	43

3.1.1	Differential Scanning Calorimeter (DSC).....	43
3.1.2	Thermogravimetric Analysis (TGA).....	48
3.1.3	High Temperature Drop Solution Calorimeter (Alexsys-1000 and MHTC).....	50
3.2	Study of ISC and TR at LIB Cell Level	64
3.2.1	Accelerating Rate Calorimeter.....	64
3.2.2	Nail/Needle Penetration Test	67
3.3	General Chemical or Cell Analysis.....	77
3.3.1	Inductively Coupled Plasma-Optical Emission Spectroscopy (ICP-OES)	77
3.3.2	Computed Tomography.....	78
4	Determination of the Enthalpies of Formation of NMCs.....	80
4.1	Thermodynamic Cycles and Reaction Mechanisms	81
4.1.1	Reactions in the Thermodynamic Cycle	81
4.1.2	Thermodynamic Cycles for NMC Formation.....	83
4.2	Accuracy and Limitation of MHTC compared to Alexsys-1000.....	84
4.2.1	Enthalpies of Drop Solution by MHTC and Alexsys	84
4.2.2	Comparison between MHTC and Alexsys-1000	85
4.3	Enthalpies of Formation of Commercial NMCs.....	87
4.3.1	Calculation of Formation Enthalpies	87
4.3.2	Thermodynamic Stability of Commercial NMCs	88
4.4	Conclusion.....	90
5	Study of the Impact of Cell Assembly on ISC	92
5.1	Experimental Setup.....	92
5.2	Comparison of ISC-Behavior	93
5.2.1	Periodical Behavior of Penetration Force	96
5.2.2	ISC Current Behavior and Mechanisms	99
5.2.3	Internal Temperature	106
5.3	Conclusion.....	108
6	Study of the Impact of the Floating Can on Thermal Runaway.....	111
6.1	Experimental Setup.....	112
6.1.1	Needle penetration test.....	112
6.1.2	Accelerating rate calorimeter	115
6.2	Results and Discussion	116
6.2.1	Effect of Can Connection on Thermal Runaway Behavior	116
6.2.2	Quantitative Analysis of ISC Current	122
6.2.3	Validation of Thermal Equivalence via Heat-Wait-Seek Tests in the ARC	125
6.3	Conclusions	127
7	Correlation between Cathode Thermal Stability and Li-Ion Cell Safety.....	129
7.1	Experimental	130
7.1.1	Automotive prismatic LIB cell samples.....	130

7.1.2	Needle Penetration.....	133
7.1.3	Electrode Material Preparation and Thermodynamic/Thermal Analysis	133
7.2	Results and Discussion	134
7.2.1	Comparative Analysis via Needle Penetration Test	134
7.2.2	Thermal stability of NMC- and NCA-based Positive Electrodes	138
7.2.3	The Correlation between Safety on Cell Level and Thermal Stability of the Positive Electrode	146
7.3	Conclusion	147
8	Summary and Outlook	150
	Reference.....	157

List of Publications

Journal publications

- Hyojeong Kim*, Abdulbashir Sahebzadeh, Hans Jürgen Seifert, Carlos Ziebert, Jochen Friedl, *Needle penetration studies on automotive lithium-ion battery cells: Influence of resistance between can and positive terminal on thermal runaway*, Journal of Power Sources, 592, 233902, **2024**
- Hyojeong Kim*, Hans Jürgen Seifert, Carlos Ziebert, Philipp Finster, Jochen Friedl, *A comparative study of commercial automotive prismatic Li-ion cells using nail penetration test, differential scanning calorimetry and thermogravimetric analysis*, Journal of Power Sources, 623, 235416, **2024**

Conference contributions

Oral Presentations:

- "Needle penetration studies on the internal dynamics during internal short circuits in automotive lithium-ion battery cells – Measurement of internal temperature and short circuit current", 244th The Electrochemical Society (ECS), Gothenburg, Sweden, 08 to 12. October **2023**.
- "Needle penetration studies on the internal dynamics in automotive lithium-ion battery cells – Measurement of internal temperature and short circuit current", FEMS EUROMAT23, Frankfurt am Main, Germany, 03 to 07. September **2023**.
- "Needle penetration studies on automotive lithium-ion cells – Influence of resistance between can and positive terminal on thermal runaway", 40th International Battery Seminar, online (Orlando, FL, United States), 20 to 23. March **2023**.

Poster Presentations:

- "Needle penetration studies on automotive lithium-ion battery cells", 12th Battery Safety Summit, Tysons, VA, United States, 12 to 14. October **2022**.

List of Figures

Figure 1. Rocking chair principle of Li^+ ion in LIB while charging and discharging, reproduced from literature [14].....	6
Figure 2. Graphite as anode active material: (a) prismatic surface and basal plane surface with Li^+ presented as red dots, (b) charge profile with a schematic representation of the staging phenomena of the formation of graphite intercalation compounds (GICs), reproduced from literature [41] and (c) an edge of a charged anode layer with a gradation in GICs and colors. .	13
Figure 3. Closing pore processes behaviors (shutdown) of trilayer (PP/PE/PP) separators.	19
Figure 4. Schemes of possible decomposition paths for delithiated layered metal oxides with or without oxygen release, reproduced from literature [6].	22
Figure 5. Compositional Gibbs triangle for the LiNiO_2 - LiMnO_2 - LiCoO_2 (NMC) system with symbols on compositions whose enthalpies of formation are studied, reproduced from literatures [8,9,68–70].	24
Figure 6. Average onset temperatures of reactions before or by thermal runaway [1,88].	30
Figure 7. Common causes causing ISC and leading to TR.	30
Figure 8. Real automotive prismatic cell structure with average relative ratio between cell layers calculated from eight commercial LIB cells.....	34
Figure 9: Three types of formats of automotive LIB cell: (a) prismatic, (b) cylindrical and (c) pouch cell. (The presented aspect ratio does not represent the real size of LIB cells.)	35
Figure 10. Two types of the connection between can and positive terminal: (a) can on potential and (b) floating can.	37
Figure 11. Gas- and particle release and jet from vent during thermal runaway induced (a) by nail penetration and (b) by an inserted particle between can and jelly roll in an automotive prismatic LIB cell with 58 Ah and (c) by nail penetration in a LIB cell with 34 Ah.	38
Figure 12. Terminal in a prismatic LIB cell with Fuse and CID, (a) in a normal state, (b) Fuse is activated by abnormal temperature and (c) CID is precipitated by abnormal pressure. (This presented figure does not represent every automotive prismatic LIB cell but only as an example how it can be implemented.).....	39
Figure 13. Definition of cell, module and pack (a) schematic example of cell building module and pack of automotive prismatic LIBs and (b) battery pack of BMW i3 models [106].	41
Figure 14. Scheme of heat flux DSC, reproduced from literature [110].	44

Figure 15. Onset temperature, T_{onset} plotted against heat rate, β of four references (a) Indium, (b) Tin, (c) Bismuth and (d) Zinc and (e) the difference ($\Delta T_{\text{corr}} (\beta=0)$) between literature onset temperature, $T_{\text{lit, onset}}$ and the extrapolated onset temperature, $T_{\text{onset}}(\beta \rightarrow 0)$ and $\Delta T_{\text{onset}}/\Delta \beta$ as function of $T_{\text{onset}}(\beta \rightarrow 0)$	45
Figure 16. Thermogram (a) definition of interpolated baseline, reaction area, T_i , T_f , T_{onset} and T_p , (b) definition of Q_T and Q_{total} to define the degree of reaction and (c) profile of the degree of reaction, α_T	47
Figure 17. Schematic TGA trace, the setup of temperature profile with blue dashed line and the corresponding mass change with red line as a function of time.....	50
Figure 18. Schematic structure of high temperature drop solution calorimeter (Alexsys-1000 from Setaram) and drop solution calorimeter with a molten oxide solvent, reproduced from literatures [7,118,120,122].	51
Figure 19. Structure and components of the MHTC: (a) components of lid, sample & reference crucible and bar, (b) the complete assembly of components in (a), (c) schematics of the assembly in MHTC, where the position of the middle line of furnace and thermoelement are adjustable and (d) schematics of the assembly in Alexsys-1000 as a comparison.....	54
Figure 20. Optimization of the height, (a) overview of MHTC, (b) the upper part of the calorimeter with a focus on the sensor area and (c) how the height of the drop sensor can be adjusted by altering the height of the red height indicator arrow.	55
Figure 21. Investigating why the base line fluctuates: (a) base line during sapphire calibration with temperatures of sample and cooling water (input & output) and (b) measurement set-up of temperature of cooling water.	56
Figure 22. Illustration of peak integration window during a sapphire drop.....	58
Figure 23. The linear relationship between sapphire mass and measured heat flow signal with the coefficient of determination.	59
Figure 24. The step of synthesizing the solvent.	61
Figure 25. The concept of a flexible mold for the cold isostatic pressing to form a NMC pellet: (a) two different pellet sizes and (b) schematic of the cold isostatic pressing.	62
Figure 26. The order of preparation of sample pellets: (a) the molded silicon from two different mold, (b) the cold isostatic pressing and (c) pressed pellets with size 1 and 2.	63
Figure 27. Schematic set up of a prismatic LIB cell in an ARC chamber.	64
Figure 28. Typical ARC procedure with HWS method (a) example of temperature on cell surface for three Heat-Wait-Seek cycles and (b) process loop of HWS method.	65
Figure 29. Schematic of the electrons and Li^+ transport path between cathode and anode during nail penetration process and shorting resistances.....	68
Figure 30. The metallographic microsection of a LIB cell from nail penetration test without thermal runaway by optical microscopy (The diameter of the nail used in the experiment was 1 mm).....	72
Figure 31. How to improve the repeatability and define the penetration depth, d , (a) schematic of the nail/needle penetration test, post-mortem CT evaluation of a LIB cell after needle penetration test (b) with compression and (c) without compression, (d) example of the worst-	

scenario in cases of penetration test without compression and (e) example test demonstrating how to define the penetration depth using V_{NP} and V_{NN} .	73
Figure 32. Investigation of ISC behavior by measuring internal local temperature in a LIB cell (a) schematic of the nail penetration, (b) a LIB cell with a small free-can window, (c) longitudinal section and (d) horizontal section of the CT of custom-designed nail and (e) dimension of the custom-designed nail.	75
Figure 33. Investigation of ISC behavior by measuring ISC current (a) schematic of the nail penetration (b) picture of the test setup with a shunt (400 A, 75 mV) and the second victim cell with an identical capacity as the current source (c) picture of the test setup with a shunt (10 A, 75 mV) and power supply as the current source.	76
Figure 34. Comparison between measurements of drop solution enthalpies from MHTC and Alexsys-1000.	86
Figure 35. Enthalpies of formation, $\Delta_f H^{\Theta, \text{oxides}}$ from constituent oxides (Li_2O , NiO , MnO_2 and CoO) and O_2 and $\Delta_f H^{\Theta, \text{elements}}$ from elements of NMC622, NMC85 and NMC94 determined by experiments, compared to NMCs with compositions of $\text{LiNi}_x\text{Mn}_y\text{Co}_{1-2x-y}\text{O}_2$ and $\text{LiNi}_{0.8-y}\text{Mn}_y\text{Co}_{0.2}\text{O}_2$ [7] as a function of (a) Ni and (b) Mn molar composition in NMC.	89
Figure 36. Results of nail penetration test of Cell A and B, demonstrating the evolution of major parameters during penetration: current of ISC, internal temperature and temperatures on the surface, cell voltage, voltage between nail and negative terminal and force on the nail: (a) type A with stacks and (b) type B with jelly rolls.	94
Figure 37. Nail penetration force vs. depth for Cell A (top curve), Cell B (middle curve) and reference cell (bottom curve).	96
Figure 38. Post-test internal short circuit traces observed in a cell after nail penetration test.	97
Figure 39. Schematic presentation how ISCs are induced in the nail penetration test with a real automotive prismatic cell structure with average relative ratio between cell layers.	102
Figure 40. The ISC-current of Cell A with stacks and B with jelly rolls in the nail penetration test.	102
Figure 41. Hypothesis of ISC formation in the LIB with stacks: (a) schematic of the nail penetration process through a stacked cell, (b) sequence of ISC development for each step of penetration, illustrating the flow of electrons and lithium cation and (c) detail-view of the area marked with yellow box in Step 1 & 2.	103
Figure 42. Hypothesis of ISC formation in the LIB with jelly rolls: (a) schematic of the nail penetration process in a prismatic cell with a jelly roll assembly, (b) sequence of ISC development at each stage, illustrating electron and Li^+ flow and (c) detail-view of the area marked with yellow box in Step 1 & 2.	105
Figure 43. Internal temperature of Cell A with stacks and Cell B with jelly rolls.	106
Figure 44. Cell voltage and temperature profiles for Groups A and B during thermal runaway: (a) cell voltage for can on potential; (c) temperature at positive terminal for can on potential; (e) temperature at negative terminal for can on potential; (g) vent temperature for can on potential; (b) cell voltage for floating can (for an enlarged detail view, see Figure 60 in Appendix); (d) temperature at positive terminal for floating can; (f) temperature at negative terminal for floating can; and (h) vent temperature for floating can, reproduced from literature [19].	117

Figure 45. Cell voltage and temperature profiles of Group C with soft short: (a) cell voltage profile (for an enlarged detail view, see Figure 61 in Appendix), temperature profile (b) on positive terminal, (c) on negative terminal and (d) on vent, reproduced from literature [19].	118
Figure 46. Visual comparison of the cell surface and vent conditions after experiencing thermal runaway and soft short events: (a) illustrates Group A (can on potential cells after thermal runaway), (b) depicts Group B (floating can cells after thermal runaway), and (c) shows Group C (floating can cells after soft short).	119
Figure 47. Classification of thermal responses (soft short vs. thermal runaway) based on the potential configuration of the cell can (floating can vs. can on potential), reproduced from literature [19].	122
Figure 48. ISC current measurements recorded during needle penetration tests: (a) can on potential cell and (b) floating can cell over the complete testing period, (c) detailed view of can on potential cell, and (d) detailed view of floating can cell during the interval from -20 s to +10 s, as highlighted in yellow in (a)-(d).	123
Figure 49. Illustration of the distinct short circuit current scenarios arising during needle penetration tests: (1) a localized short circuit between the cell can and the outermost anode (Case 1), (2) localized layer-to-layer short circuits between internal electrode layers (Case 2), and (3) a complex short circuit scenario combining both types simultaneously (Case 3).	124
Figure 50. Self-heating rate profiles of two floating can cells and two can on potential cells: (a) overview from 0 to 400 °C, and (b) detailed view from 60 to 200 °C.	126
Figure 51. The number of penetrated layer-sets (PLS) was examined in relation to six potential influencing factors: (a) nickel molar fraction and (b) lithium molar fraction in the cathode active material, (c) the total capacity of the LIB cell, (d) separator thickness, (e) aluminum current collector thickness, and (f) the electrolyte mass fraction, excluding the can, reproduced from literature [32].	135
Figure 52. The correlation between PLS/TLS and Ni molar fraction in cathode active materials.	137
Figure 53. DSC analysis of positive electrodes extracted from LIB cells at 100% SOC: (a) cell type A, (b) cell type B, (c) cell type C, (d) cell type D, (e) cell type E, and (f) cell type F. Each cell type was tested in duplicate, with results represented by a dashed blue line and a solid red line, respectively, reproduced from literature [32].	139
Figure 54. The average extrapolated onset temperature together with the average penetrated layer-sets (PLS), reproduced from literature [32].	140
Figure 55. The average reaction enthalpy of six cell types with the average penetrated layer-sets (PLS).	141
Figure 56. Average degree of reaction as a function of temperature, reproduced from literature [32].	142
Figure 57. TGA results for harvested positive electrodes from 100% SOC LIB cells: (a) cell type A, (b) cell type B, (c) cell type C, (d) cell type D, and (e) cell type F. Each sample was analyzed in duplicate, shown as dashed and solid lines, reproduced from literature [32].	144
Figure 58. Summary of mass loss trends and electrolyte content: (a) average mass loss across three temperature intervals: 20–150 °C (green), 150–300 °C (yellow), and 300–500 °C (orange) and (b) mass percentage of electrolyte (excluding cell can weight), reproduced from literature [32].	144

Figure 59. Correlation between cell-level safety and the thermal stability of the positive electrode, reproduced from literature [32].	146
Figure 60. Enlarged detail view of Figure 44 (b).....	153
Figure 61. Enlarged detail view of Figure 45 (a).....	153
Figure 62. A detailed presentation of five characteristic temperatures (T_1 to T_5) using the HWS graphs of cell 4 with floating can as a representative example.	154

List of Tables

Table 1. Two ways of definition of cathode and anode.	6
Table 2. Relative costs of battery to BEV depending on LIB type and BEV, average relative cost of materials to battery, and average relative costs of cathode to battery and materials.	8
Table 3. Comparison of state-of-the-art cathode active materials in automotive LIB cell [17,23,24].	9
Table 4. Comparison of state-of-the-art anode active materials in automotive LIB cell [36,37].	12
Table 5. State-of-the-art components of electrolyte in automotive prismatic LIB.	17
Table 6. Studies of cathode active material harvested from LIB using DSC and TGA.	23
Table 7. Enthalpy of dissolution from high temperature oxide melt solution calorimetry, enthalpy of formation from oxides and enthalpy of formation from elements at 298 K of various cathode materials in LIB cell.	25
Table 8. EUCAR Hazard levels. [24].	26
Table 9. Categories of automotive LIB cells.	36
Table 10. Overview of four safety elements in an automotive prismatic LIB cell.	36
Table 11. Energy density and number of modules and cells [107,108] and calculated chance of failure depending on BEV.	41
Table 12. Sapphire drop data: peak area [$\mu\text{V}\cdot\text{s}$] and theoretical enthalpy increment [J] depending on the weight of sapphire [mg] for each drop during calibrations.	59
Table 13. Determination of calibration factors for each drop in both calibration runs.	60
Table 14. Several trials to optimize each parameter to minimize baseline fluctuation with optimized parameters marked in green.	61
Table 15. Examples of studies using nail penetration test.	69
Table 16. ICP Measurement of positive electrode from cell type A in chapter 7 and determination of chemical composition based on two different assumptions.	78
Table 17. Reactions in thermodynamic cycle which are used for the determination of the enthalpy of formation from oxides of $\text{LiNi}_x\text{Mn}_y\text{Co}_{1-x-y}\text{O}_2$ compounds from binary oxides and oxygen using high temperature drop solution calorimetry in $3\text{Na}_2\text{O}\cdot 4\text{MoO}_3$ solvent at 701°C .	81

Table 18. Values of enthalpy of drop solution of binary oxides in $3\text{Na}_2\text{O}\cdot 4\text{MoO}_3$ solvent at 974 K that can be possibly used in this study as reference.	82
Table 19. Thermodynamic cycles used to determine the enthalpies of formation of NMC622, NMC85 and NMC94 from oxides and O_2	83
Table 20. The values of enthalpy of drop solution of NMC622 and NMC85 samples in $3\text{Na}_2\text{O}\cdot 4\text{MoO}_3$ at 974 K determined by MHTC and Alexsys-1000.	85
Table 21. Standard enthalpies of formation ($\Delta_f H^{\Theta, \text{oxide}}$ and $\Delta_f H^{\Theta, \text{elements}}$) of NMC622 and NMC85 determined by MHTC and Alexsys-1000.	88
Table 22. Specifications of the tested automotive prismatic LIBs, Cell A and B.	93
Table 23. The penetration depth at which force drops occurred, and spacing between those consecutive drops for Cell A and B.	98
Table 24. Electrical and thermal conductivity of cell components at room temperature.	100
Table 25. Four possible ISC scenarios in a LIB and their characteristics.	100
Table 26. Effective thermal conductivities in the plane of the electrodes vs. through the thickness (cross-plane) for LIB with stack and jelly roll assemblies.	107
Table 27. Protocol for needle penetration tests consisting of three parts (I, II and III).	114
Table 28. Results of cell 1-15 depending on the type of can and the type of reaction.	120
Table 29. Characteristic thermal parameters ($T_1 - T_5$) comparing two cells each from floating can and can on potential configurations.	127
Table 30. Information of the six selected automotive prismatic LIB types.	132
Table 31. Total layer-sets (TLS) and the ratio of PLS to TLS of six lithium-ion cell types.	136
Table 32. Cathode active material composition (molar fractions of Ni, Mn or Al, Co, Li and O) for the six automotive prismatic LIB types, along with their mean penetrated layer-set (PLS) values.	137
Table 33. PLS, onset temperature and the degree of reaction at 225 °C, α_{225} depending on Ni molar fraction.	156

List of Symbols and Abbreviations

Al	aluminum
ARC	accelerating rate calorimetry
ASSB	all-solid-state battery
BCCC	battery cell competence center
BEV	battery electric vehicles
BMS	battery management system
BTMS	battery thermal management system
CID	current interrupt device
CIP	cold isostatic pressing
CMC	carboxymethyl cellulose
Co	cobalt
CT	computed tomography
Cu	copper
DEC	diethyl carbonate
DMC	dimethyl carbonate
DSC	differential scanning calorimetry
EC	ethylene carbonate
ECS	external short circuit
EMC	ethyl methyl carbonate
EUCAR	european council for automotive research and development
EV	electric vehicle
EV	extended volume
Fe	iron
GC-MS	gas chromatography–mass spectrometry
HF	heat flow
HWS	heat-wait-see method
ICP-OES	inductively coupled plasma–optical emission spectroscopy
IQR	interquartile range
ISC	Internal short circuit
LCO	lithium cobalt oxide
LFP	lithium iron phosphate
Li ⁺	lithium ion
LIB	lithium-ion battery
LTFOP	lithium tetrafluoro oxalate phosphate
LTO	lithium titanium oxide
Mn	manganese
NASA	national aeronautics and space administration
NCA	lithium nickel cobalt aluminum oxide
Ni	nickel
NMC	lithium nickel manganese cobalt oxide
NREL	national renewable energy laboratory
OEM	original equipment manufacturer
PC	propylene carbonate
PCM	phase-change material
PE	polyethylene

PIDU	Proportional integral derivate unit
PP	polypropylene
PVDF	polyvinylidene fluoride
PVDF-HFP	Poly(vinylidene fluoride-co-hexafluoropropylene)
SBR	Styrene butadiene rubber
SEI	solid electrolyte interphase
SOC	state of charge
SOH	state of health
TGA	thermogravimetric analysis
THT	thermal hazard technology
TLS	total layer-sets
TR	thermal runaway
VC	vinylene carbonate
XRD	X-ray diffraction

Physical Abbreviations and Universal Constants

σ	Ionic conductivity	S/m, mS/cm
λ	Thermal conductivity	W/m·K
ϵ	dielectric constants	
η	viscosity	Pa·s
I_{sh}	Current flowing over shunt	A
$\Delta_{ds}H^{974}$	enthalpy of drop solution	kJ/mol
$\Delta_f H^{\ominus, \text{elements}}$	formation enthalpies form the elements	kJ/mol
$\Delta_f H^{\ominus, \text{oxides}}$	formation enthalpies form the oxides	kJ/mol
ΔG^{\ominus}	Gibbs free energy change of a reaction	J
Δm	Mass change	G
C_p	heat capacity	J/g·K
d	Penetration depth determined by force applied on nail	mm
d_{anode}	penetration depth at the outermost anode	mm
d_{can}	penetration depth at the aluminum can	mm
D_{crit}	critical penetration depth	mm
E or U	cell potential or electromotive force	V
F	Faraday's constant (96.485)	C/mol
I_{CA}	the short circuit current between the cell can and the outermost anode	A
I_{LL}	short circuit current between cell layers	A
I_{sc}	current of ISC	A
n	number of moles of electrons transferred in the redox reaction	
\varnothing	diameter	mm
PLS	penetrated layer-sets	
Q_T	partial heat (Q_T) released up to temperature	J/g, J/mol
Q_{total}	total heat released during the reaction	J/g, J/mol
R_{CA}	resistance between the can and outermost anode	Ω
R_{CC}	resistance between the can and cathode	Ω
$R_{contact}$	resistance between the nail and the cell components	Ω
R_i	internal resistance of the cell	Ω
R_{ISC}	resistance of ISC	Ω
R_{LL}	resistance of ISC between layers in a LIB	Ω
R_{nail}	resistance of nail	Ω
$R_{particle}$	resistance of particle	Ω

T	temperature	K, °C
T_1	onset temperature of the initial exothermic reaction (self-heating rates > 0.02 K/min)	K, °C
T_2	temperature at which vent-induced cooling occurs	K, °C
T_3	onset temperature of a secondary exothermic reaction (self-heating rates > 0.02 K/min)	K, °C
T_4	temperature at which the catastrophic thermal runaway initiates (self-heating rate > 60 K/min)	K, °C
T_5	maximum temperature recorded during thermal runaway events.	K, °C
T_f	final peak temperature	K, °C
T_i	initial peak temperature	K, °C
T_m	melting point	K, °C
T_{onset}	onset temperature	K, °C
T_p	peak maximum temperature	K, °C
T_R	temperature of reference pan	K, °C
T_S	temperature of sample pan	K, °C
T_{true}	the corrected 'true' onset temperature	K, °C
T	thickness	μm
$T_{A-S-C-S}$	thickness of one complete electrode-separator unit, including a double-coated anode with copper current collector, separator, double-coated cathode with aluminum current collector, and an additional separator	μm
T_{can}	Thickness of cell can (long sides)	μm
V_{NN}	voltage between the nail/needle and the negative terminal	V
V_{NP}	voltage between the nail/needle and the positive terminal	V
V_{sh}	voltage drop across the shunt	V
α_T	degree of reaction	
β	heating rate	K/min
ΔH	enthalpy change	J
ΔH_r	reaction enthalpy	
ΔS	entropy change	J/K
ΔT	temperature difference	K, °C
$\Delta T_{corr}(\beta)$	temperature correction function based on heating rate	K, °C
Φ_{FR}	the heat flow rate into a reference pan	W
Φ_{FS}	the heat flow rate into a sample pan	W

1 Introduction

Lithium-ion batteries (LIBs) have served as the foundation for energy storage in diverse applications, from mobile electronics to the rapidly growing market of battery electric vehicles (BEVs). The potential of LIBs for high energy density and long cycle life has been well recognized, yet these advantages come with significant safety challenges. Numerous reviews [1–3] have documented the hazards associated with LIBs in BEVs and elucidated the mechanism that lead to thermal runaway (TR). In these studies, mechanical, electrical, and thermal abuse are consistently identified as key triggers, all of which share one critical feature: the induction of an internal short circuit (ISC). ISC, often initiated by damage or degradation of the separator through mechanical impact, melting, or dendrite growth, is widely recognized as the most common precursor to TR.

The stakes associated with LIB safety and TR in BEV applications are particularly high. As Feng [1] has noted, while fire incidents in BEVs may not occur at a higher rate than in conventional vehicles, the enormous energy stored in these LIBs creates an inherent trade-off — extended driving range comes at the expense of reduced safety margins. High-nickel cathode materials, such as lithium-nickel-manganese-cobalt-oxide (NMC) and lithium-nickel-cobalt-aluminum-oxide (NCA), are favored for their superior capacity; however, their lower thermal stability means that even modest abuse can trigger premature decomposition. When these materials decompose, oxygen is liberated and reacts exothermically with the flammable electrolyte, initiating a self-propagating TR event.

During TR, the decomposition of the positive electrode and associated exothermic reactions release heat at magnitudes that can far exceed the original electrical energy stored in the LIB cell. For example, ISC produces intense localized heating (Joule heating), and this thermal energy initiates further exothermic degradation of NMC or NCA with the specific threshold dependent on the chemical composition. Consequently, the intrinsic stability of the cathode plays a critical role in determining overall cell safety, as the decomposition of cathode active materials can be significantly accelerated in the presence of electrolyte, leading to increased heat generation [4]. As highlighted by Zhang et al. [3] and Lisbona and Snee [4], employing thermally stable components — such as LiFePO_4 — can markedly enhance LIB safety. Yet, despite substantial theoretical and laboratory investigations, a comprehensive, experimental linkage between cathode thermodynamics and cell-level failure modes remains to be established.

Thermodynamics offers an indispensable framework for addressing these challenges. Advanced analytical methods such as differential scanning calorimetry (DSC) and thermogravimetric analysis (TGA) have been widely applied to investigate the thermal behavior of cathode active material. However, high temperature drop solution calorimetry, which precisely measures the enthalpy changes during material decomposition, has not been fully exploited to quantitatively determine thermodynamic stability of high-Ni cathode active materials. Shurtz et al. [4,6] have provided theoretical insights into how thermodynamic stability of cathode active materials contributes to heat generation in LIB cells, however direct experimental evidence—particularly one linking such measurements with cell-level outcomes—is still lacking.

To bridge this gap, LIB safety must be evaluated experimentally using reproducible methods that closely mimic real-world ISCs. Field failures are often difficult to analyze due to the destruction

caused by fire; therefore, controlled laboratory abuse tests are essential. Realistic ISC testing methods that replicate the initiation and progression of failure are needed in order to quantify the relationship between cathode materials stability and LIB cell safety.

Against this backdrop, the central motivations for this work are threefold:

- 1) ***To investigate the thermal and thermodynamic stability of commercial high-nickel cathode active materials for BEV***
- 2) ***To systematically quantify the behavior of internal short circuits in automotive LIBs***
- 3) ***To establish a correlation between the intrinsic stability of cathode materials and cell-level safety.***

Despite extensive literature on the thermal abuse behavior of LIB components, many studies are limited to theoretical models or lab-synthesized materials. For instance, Masoumi et al. [7–9] demonstrate that lab-prepared Ni-rich NMC is intrinsically less stable compared to compositions with lower Ni content. However, these studies did not fully address the behavior of commercially produced cathodes under real-world conditions and does not reflect anymore the state-of-the-art NMC with higher Ni molar ratio > 0.8 . Similarly, while ISC is widely acknowledged as a key trigger for TR, its behavior in automotive cells has yet to be systematically characterized. To remedy these gaps, an optimized method is required to induce ISC under conditions closely resembling field scenarios while quantifying its severity.

Moreover, by correlating the intrinsic stability of cathode materials — assessed through calorimetric and thermal analyses — with observed cell-level responses during controlled abuse tests, this work seeks to bridge material properties with overall LIB safety. Ohneseit et al. [10] reported that 21700 cells with NMC or NCA cathodes exhibited thermal runaway onset at lower temperature compared to LFP-cells using accelerating rate calorimetry and presented the possible correlation between cathode materials and LIB safety. However, further material-level investigation has not been pursued, leaving a critical gap that this dissertation aims to fill.

To achieve these objectives, this study employs a **comprehensive and multi-level approach to LIB safety** including **both the material level behaviors** (*thermal and thermodynamic stability*) and the **cell level outcomes** (*resilience against ISC on cell level*). This research employs a suite of experimental techniques, each selected to probe a specific aspect of material intrinsic stability and LIB safety. The key methodologies include:

- **High Temperature Drop Solution Calorimetry:** this technique is used to quantify the enthalpy of formation of commercial high-Ni cathode materials for BEVs. It provides how stable a material is in a fundamental sense, but not how fast it might break down in a battery. In this work, a Setaram MHTC was utilized to measure formation enthalpies of NMCs, while a Setaram Tian-Calvet Alexsys-1000 was primarily applied to validate the apparatus and procedure of MHTC.
- **Differential Scanning Calorimetry (DSC):** it is employed to study the thermal reactions of positive electrodes out of automotive commercial LIB possibly under same conditions as those in a real LIB cell. By determining the onset temperature of exothermic peaks and the released heat energy, inherent thermal stabilities were compared between cathodes from different automotive LIBs. In this study, DSC was crucial for examining not only how Ni content in cathodes influences the temperature at which the cathode begins to energetically react with electrolyte, but also how fast heat is generated by those reactions.

- **Thermogravimetric Analysis (TGA):** it complements DSC by measuring mass changes in a material as it is heated. Any process that causes mass loss — such as evaporation of electrolyte, release of oxygen from the cathode, or decomposition of binder — will be seen as a drop in the sample mass. In this work, TGA was used alongside DSC on the same samples to correlate exothermic events with mass loss.
- **Accelerating Rate Calorimetry (ARC):** to investigate thermal characteristics at the cell level, ARC was used on commercial automotive cells. ARC tests provide a simulation of worst-case thermal runaway because no heat can escape under the adiabatic condition — mimicking a large pack in BEV where heat is trapped inside. It can determine the onset temperature of exothermal reactions and thermal runaway at a cell level.
- **Nail/Needle Penetration Test:** to reproduce internal short circuit conditions in a controlled way, this study applies nail or needle penetration tests. Nail penetration is a simple and widely adopted abuse test and included in several battery safety qualification standards. However, the simplicity of nail penetration comes usually at the cost of reproducibility and realism. In this study, we mitigated these issues of low reproducibility by optimizing the nail penetration method. It was also optimized to measure the short circuit current and internal temperature close to ISC position, enabling quantitative measurement of ISC.

By combining these methods, this work captures a holistic view of LIB safety: calorimetry techniques (DSC, TGA and high temperature drop solution calorimeter) reveal the intrinsic stability and reaction energetics of materials, while abuse tests (ARC, nail penetration) demonstrate the macroscopic cell response under simulated failure conditions. This multi-pronged experimental approach allows this work to link material-level properties to cell-level outcomes, as will be seen in the results.

This work is organized into chapters that progressively build the story from fundamental theory to applied safety testing, ultimately connecting how cathode active material stability impacts cell safety in BEV applications and how resilience of LIB cell against ISC can be differentiated by safety element in a cell or cell assembly. Below is an outline of the research structure, with a brief description of each chapter and its role in the overall thesis.

- The **Fundamentals in Chapter 2** offer a theoretical background on LIBs and their safety with a detailed literature review. This chapter covers the working principles of LIB cells and each of their components, then delves into findings on thermal and thermodynamic stability of cathode active materials, and the phenomenon of thermal runaway at the cell level. This establishes the foundation and context for the experimental work.
- The **Chapter 3 – Experimental Methods** documents the experimental techniques employed in the dissertation. It explains the calibration and operating parameter of DSC, TGA, and high temperature drop solution calorimetry and the setup for ARC and nail/needle penetration tests. Any custom experimental setups of novel measurements approaches such as the modified nail test with insitu measurements are described here.
- As the first results chapter, the **Chapter 4 – Determination of the Enthalpies of Formation of NMCs** focuses the thermodynamic stability at the materials level. It addresses the question: *How thermodynamically stable are Ni-rich cathode materials, and how does composition affect its own stability?* To find the answer to the question, it starts with the setup of MHTC with motivation to verify the possibility of measurement of enthalpies of formation using MHTC and define its limit compared to Alexsys-1000. It presents the measured enthalpies of formation for various cathode chemistries. Key findings are discussed, such as how precisely drop solution enthalpies can be measured using MHTC compared to Alexsys in terms of uncertainties, the number of drops, or distribution of measured value and how increasing Ni (or decreasing Mn) content correlates with less favorable formation enthalpies, indicating lower intrinsic stability. These fundamental data offer a guideline how to use MHTC or define its limitation and ultimately provide a thermodynamic stability of cathodes.

- The next **Chapter 5 – Study of the Impact of Cell Assembly on ISC** transit to the cell level, investigating how the internal assembly of an automotive prismatic cell influences its response to an induced ISC. Modern prismatic LIB cells can have different electrode stacking configurations or wound jelly rolls, which might affect how ISC propagates inside a cell. Using the optimized nail penetration test, a comparative study is conducted on cells built with different assembly methods (stack vs. jelly roll). The findings are not only relevant for manufacturers choosing cell design for safety but also fill a research gap in understanding mechanical aspects of ISC. The parts of this research was presented at the ECS conference in Gothenburg (2023).
- The **Chapter 6 – Study of the Impact of the Floating Can on Thermal Runaway** examines a specific safety enhancement feature in prismatic LIB cells — the so-called floating can design — and evaluates its effectiveness. In prismatic cells, the outer aluminum can (which is connected to the cathode potential) is electrically isolated from the electrode stack by insulator, to prevent it from directly contacting the outermost anode layer. Using the advanced needle penetration tests, ISC between the can and the outermost anode was induced, and the current of ISC current and temperature evolution are compared between floating can and can on potential. Additionally, both types of cells are tested in the ARC, isolating the possibility that the floating can influence the cell's inherent thermal stability. The findings demonstrate how effective the floating can can mitigate ISC between the can and anode, providing guidance for future cell safety designs. The main results of this study have been published in the journal of Power Sources in 2024.
- Having studied the material stability (Chapter 4) and various cell-level safety factors (Chapters 5 and 6), **Chapter 7 – Correlation between Cathode Thermal Stability and Li-Ion Cell Safety** brings the two scales together. It addresses the overarching question posed at the start: *does the thermal stability of the cathode material influence the safety performance of a whole cell?* In this chapter, a broad set of prismatic automotive cells with different cathode chemistries and designs but very similar anode and separator were analyzed, using the needle penetration test to quantify their tolerance to internal short circuits. From the needle penetration test, it was found that a strong dependence of the cell resilience against ISC on the cathode's Ni content was found. To probe the material further, cathode samples from these cells are tested via DSC/TGA from fully charged state to determine their thermal stability. Especially, this work introduced the concept of a 'degree of reaction' as a novel way to quantify how quickly heat is released once reaction of cathode starts. This chapter validates the hypothesis that improving cathode stability can translate to safer cells. The main finding were published in Journal of Power Sources in 2024.
- The final **chapter 8 – Summary and Conclusion** summarizes the key findings of the dissertation and reflects on their implications. It highlights how the balance between LIB energy density and safety can be achieved by informed choices in materials and cell design, based on the evidence gathered.

Overall, the dissertation progresses from fundamental to applied studies in the presented sequence. By first understanding what makes a cathode intrinsically stable or unstable (thermodynamics in Chapter 4), we set the stage to investigate how cell design features influence failure (Chapter 5 and 6), and finally why certain cells fail more readily by linking back to the cathode (Chapter 7). This structure ensures that each chapter builds up the insights of the previous ones: the knowledge of material stability informs the interpretation of cell tests, and the cell-level observations circle back to emphasize the importance of material. Through this multi-level approach, this work provides a comprehensive view of LIB safety relevant to BEVs, from the atomic scale (material bonding energetics) to the cell level (ISC-induced failure modes and thermal runaway). The findings not only contribute to scientific understanding of lithium-ion battery failures but also offer practical guidance for developing safer high-energy batteries for electric vehicles.

2 Fundamentals

2.1 Lithium-Ion Battery (LIB)

Battery is a storage device for electricity consisting of serial or parallel connected elements. In a lithium-ion battery, electrical energy is either released or stored through the intercalation of Li^+ into interstitial site in either positive or negative electrode. A typical electrochemical cell comprises two electrodes (anode and cathode) with different potential, a separator and an electrolyte. Each electrode consists of active materials, serving as both charge-transfer media and as active masses in the redox reaction, thereby making a battery a closed system, and inactive components such as current collectors, binders and conductive additives, as following:

- **Active Materials:** responsible for an ion storage for the redox reaction, contributing directly to the energy storage capacity of the battery.
- **Inactive Components:** essential for the operation of active materials but do not participate in energy storage. These include:
 - **Current Collectors:** typically made of copper (Cu) for the negative and aluminum (Al) for the positive electrode along with adhesion-enhancing reagents to improve electrical contact with electrode materials.
 - **Binders:** polymeric materials such as polyvinylidene fluoride (PVDF), carboxymethyl cellulose (CMC), styrene-butadiene rubber (SBR), which provide mechanical stability to the electrode structure.
 - **Conductive Additives:** Carbonaceous materials such as carbon black that enhance electrical conductivity. [11]

This configuration ensures that the storage of chemical energy and its subsequent electrochemical transformation into electrical energy occur entirely within the battery. For the electrode to function effectively, it must exhibit both ionic and electronic conductivity, while the electrolyte functions as a pure ionic conductor. Specially, the lithium-ion battery (LIB) system relies on the movement of lithium ions (Li^+) between cathode and anode during the charge and discharge processes.

2.1.1 Working Principle

The movement of Li^+ ions between two electrodes in a rechargeable LIB is known as the “rocking chair” principle (intercalation/deintercalation). Regarding the definition of anode and cathode, there are two ways of definition as presented in Table 1. [12]

Table 1. Two ways of definition of cathode and anode.

	Electrochemical Definition		Definition for Battery	
Nomenclature	Cathode	Anode	Cathode	Anode
Electrode	negative	positive	positive	negative
Charging	reduction	oxidation	oxidation	reduction
Discharging	oxidation	reduction	reduction	oxidation

This work follows the nomenclature of the battery convention based on the redox reaction during discharging. In this work, cathode refers the positive electrode and anode does the negative.

A typical anode in LIB is made of graphite or graphite with silicon and stores lithium ions during charging, while common materials in cathode include lithium cobalt oxide (LCO) and layered nickel-rich oxide compounds like NCM or NCA, storing lithium during discharging. In Figure 1, the charging and discharging mechanism in LIB cell is depicted using LiCoO_2 (LCO) as cathode and graphite as anode, as the first LIB cell introduced by Sony in 1991 [11,13].

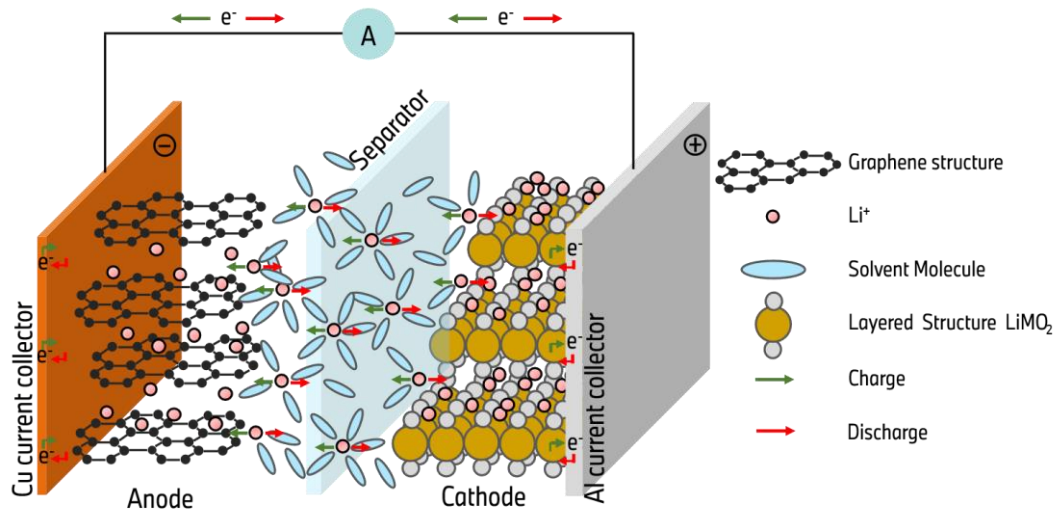
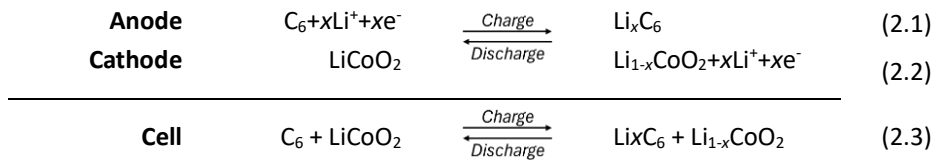


Figure 1. Rocking chair principle of Li^+ ion in LIB while charging and discharging, reproduced from literature [14].

The rocking chair principle of Li^+ ion in LIB cell during charging and discharging can be described as follows, exemplified with a LCO cathode:



Charging

To charge a LIB, it is connected to an external electrical power source that applies an external voltage exceeding the cell's equilibrium voltage (overvoltage). This overvoltage forces the electrons to flow from the positive electrode (cathode) to the negative electrode (anode) via the external circuit. Simultaneously, the lithium ions (Li^+) migrate through the electrolyte from the cathode to anode, where they enter into the porous host structure of the anode material in a process known as intercalation. During deintercalation of Li^+ in cathode, the cobalt ions are oxidized from the Co^{3+} state to the Co^{4+} state. Once the battery is fully charged and the power supply is disconnected, the electrons have no external path to flow and become stored in the anode material.

Discharging

The charged battery can then be utilized to supply power to an external circuit, resulting in the battery discharging. During discharge, the electrons migrate from the anode, through the circuit, and return to the cathode, generating an electric current. Simultaneously, the lithium ions Li^+ that were intercalated in the anode migrate back through the electrolyte and reintegrate into the cathode material. The $\text{Co}^{3+/4+}$ redox couple facilitates charge compensation, ensuring the electrochemical stability of the system, while maintaining the layered structure of the cathode material.

This reversible transport of the lithium ions and electrons between the anode and cathode (via deintercalation and intercalation) constitutes the core mechanism, enabling the rechargeability of LIBs. When designing a lithium-ion cell or selecting its components, several critical parameters must be considered to achieve an optimal balance between those. These include energy density (efficient utilization of cell volume and active materials or applying active materials with higher capacity or more extreme potentials), cycle life and safety. In the subsequent chapter, various representative electrode materials including state-of-the-art materials are discussed as active materials based on these criteria. Additionally, the roles of the electrolyte and separator are discussed in detail.

2.1.2 Cathode Active Materials

The development of cost-effective cathode active materials that simultaneously deliver high thermal stability and elevated energy density is of paramount importance for the widespread adoption and commercialization of battery electric vehicles (BEVs). This is primarily due to two key factors: the significant contribution of the cathode to the overall cost of a LIB and hence BEVs, as presented in Table 2, and the critical role of the cathode in determining the energy density and safety characteristics of LIB.

The cathode active material typically accounts for around 24 % of the relative cost of a LIB, while the battery itself makes up 14-32 % of the overall cost of a BEV [15]. This means that the development of cost-effective cathode active materials is essential for producing affordable BEVs and making them accessible to a wider consumer base. Advances in cathode materials that can reduce the manufacturing costs while maintaining or improving their performance are crucial for the commercialization of BEVs.

Furthermore, the cathode active material is the key to achieving the delicate balance between energy density and safety in LIBs. Cathodes with higher energy increase energy density of LIB, which directly translates to longer driving ranges for BEVs. However, this often comes at the expense of safety, as higher energy density materials may be prone to thermal instability and potential safety hazards. Developing cathode active materials that can maximize energy density while maintaining robust safety features is therefore a critical challenge. By addressing these two key aspects — *cost-effectiveness* and *the energy density-safety balance* — the development of advanced cathode active materials is crucial for the widespread option and commercialization of BEVs.

Table 2. Relative costs of battery to BEV depending on LIB type and BEV, average relative cost of materials to battery, and average relative costs of cathode to battery and materials.

BEV	LIB Type (Cathode & Battery Capacity)	Relative Cost of		
		Battery*	Materials**	Cathode**
2025 Cadillac Escalade IQ	Nickel Cobalt Manganese Aluminium 200 kWh			
2025 RAM 1500 REV	Nickel Cobalt Manganese 229 kWh			
2023 Tesla Model S	Nickel Cobalt Aluminum 100 kWh			
2023 Ford Mustang	Lithium Iron Phosphate 70 kWh			
2023 VW ID.4	Nickel Cobalt Manganese (NMC622) 62 kWh			
2022 Rivian Delivery Van	Lithium Iron Phosphate 135 kWh			

*from reference [16]

**presented as an average value from reference [15]

Since the commercial success of LiCoO_2 developed by Goodenough as a cathode active material (theoretical capacity 274 mAh/g [17]), extensive research has been conducted to investigate the effects of incorporating other transition metals into lithium-based metal oxides (e.g. LiMO_2 , where M= Co, Ni, Mn, or a combination of those etc.). [17] Transition metals serve to mitigate charge imbalances that arise during lithium insertion (intercalation) and extraction (deintercalation) processes occurring throughout redox reactions. Consequently, their incorporation significantly influences the overall electrochemical performance of cathode. Each transition metal element or aluminum contributes uniquely to cathode performance, cost and safety:

- **Nickel** (Ni) increases the theoretical capacity but introduces safety concerns, particularly due to its thermal instability in high-Ni cathodes.
- **Cobalt** (Co) improves rate capability but poses economic and environmental concerns due to its high cost and toxicity.
- **Manganese** (Mn) and **Aluminum** (Al) enhance structural stability but at the cost of reduced specific capacity.

Specially a LIB cell for BEV should offer high energy density with affordable cost to enable longer driving-range electric vehicles. To meet the original equipment manufacturer (OEM) targets for 2025, lithium-ion battery cells must achieve a specific energy density of 300 Wh/kg with a cathode active material energy density of at least 750 Wh/kg. [18] One strategy to achieve this target is increasing Ni content in cathode active material. For example, the energy content of nickel cobalt aluminum cathode materials used in automotive LIB has been predominantly increased through higher incorporation of nickel from NMC111 to NMC523, NMC622 and NMC811, where the

numerical values represent the decimals molar ratios of nickel, manganese and cobalt, respectively. With increasing Ni content, the charging capacity of those increases from 175 to 186, 198 and 213 mAh/g, respectively [4]. Also, NIO and CATL battery manufacturers collaboratively developed LIB utilizing NMC chemistry, specifically advancing toward nickel-rich compounds to enhance energy density. Their developments encompassed various NMC formulations, including NMC111, NMC532, NMC622 and NMC811, tailored for BEV application in 2019. [19] The increase in nickel content has been the primary driver behind the improvements in the energy density for these NMC cathode materials for automotive LIB applications. [20,21] Beyond just increasing the energy content, there is also a strong incentive to lessen the reliance on cobalt, because cobalt is a scarce and costly metal, primarily mined from Central Africa. [20]

In contemporary prismatic LIB cells for automotive application, nickel cobalt manganese (NMC) and nickel cobalt aluminum (NCA) with a high nickel content are widely implemented due to their high energy density. [22] While both NCA and NMC cathodes exhibit high energy densities, they present distinct trade-offs in cost, cycling stability and thermal safety. Therefore, in the realm of LIB cathode active materials for automotive applications, lithium iron phosphate (LFP) has also emerged, besides NMC and NCA, as a state-of-the-art solution, particularly in the Chinese market. Before delving deeper into the individual material, Table 3 provides a comprehensive overview of the three common automotive LIB cathode active materials including the well-established LCO chemistry.

Table 3. Comparison of state-of-the-art cathode active materials in automotive LIB cell [17,23,24].

Material	LCO	NMC	NCA	LFP
Average voltage [V]	3.7	3.6	3.6	3.4
Specific capacity [mAh/g]	135-150	160-220	180-200	130-170
Structure		Layered structure		Olivine
Channels for Li ⁺ diffusion		Two-dimensional		One-dimensional
Cycle number	low	moderate	moderate	excellent
Safety performance	moderate	poor	poor	excellent
Price	moderate	moderate	poor	excellent

- **NMC cathodes** are relatively more cost-effective due to their lower cobalt content and their specific capacity can be increased by adjusting the Ni molar fraction. However, their thermal stability remains lower in comparison to LCO or LFP cathodes.
- **NCA cathodes** offer improved capacity retention compared to NMC, but they pose higher safety risks due to their low thermal stability.
- **LFP cathodes** exhibit excellent safety performance with the best cycle life among the three, but they present the lowest specific capacity, mainly due to the lower potential of the LFP active material.

The selection of the optimal cathode active material for automotive LIBs involves a careful balance of factors, including cost-effectiveness, energy density, cycle life, and safety considerations, to meet the demanding requirements of the electric vehicle market.

NMC Cathode Active Material

The $\text{LiNi}_x\text{Mn}_y\text{Co}_{1-x-y}\text{O}_2$ (NMC) solid solution derives its electrochemical redox activity primarily from the $\text{Ni}^{2+/3+}$ and $\text{Ni}^{3+/4+}$ redox couple, while Mn^{4+} ions serve to stabilize the layered structure. Enhancing Ni content in NMC cathodes increases energy densities but Ni-rich NMCs are thermodynamically unstable especially in highly oxidized (charged) states. One of the primary challenges in Ni-rich NMC cathodes is cation disordering, where Ni^{4+} ions readily reduce to Ni^{2+} at elevated temperatures and Ni^{2+} ions migrate into Li^+ sites. This process impedes lithium-ion diffusion and diminishes the overall electrochemical performance. This cation disordering issue is more pronounced in high-Ni NMC compositions due to the similar ionic radii of Ni^{2+} (0.69 Å) and Li^+ (0.76 Å), which facilitates the undesirable Ni^{2+} migration into the lithium-ion sites. [25–27]

As temperature increases, the layered metal oxide structure ($R\bar{3}m$) undergoes successive phase transitions, first into a disordered spinel ($Fd\bar{3}m$) and ultimately into a rock-salt phase ($Fm\bar{3}m$). These transformations release oxygen from the crystal lattice, which can react with flammable electrolytes, posing severe safety risks, including potential thermal runaway and catastrophic failure. [28,29] Studies have demonstrated a nearly linear decrease in thermal stability with increasing Ni content in NCM cathodes. [30–32] In comparison to cathode materials with lower Ni content (e.g., NMC111), for example, layered Ni-rich oxides (e.g., NMC523, NMC622, or NMC811) exhibit increased oxygen release at lower onset temperatures, leading to significantly higher heat generation. [22] The oxidation from Ni^{2+} to Ni^{4+} in highly delithiated states further compromises thermal stability, requiring additional stabilization techniques. Although Mn enhances structural stability, it simultaneously introduces challenges, such as Mn dissolution and passive layer formation on the cathode surface, which hinder lithium-ion diffusion. Research has shown that in highly delithiated states, the dissolution of Co^{4+} and $Ni^{3+/4+}$ exacerbates passive layer formation. As Ni content rises, Co^{3+} and Mn^{4+} remain structurally stable, whereas Ni^{4+} readily reduces to Ni^{3+} , accelerating metal dissolution and contributing to capacity fade. The thermal stability aspect of NMC will be further discussed in Section 2.2. Despite its decreasing thermal stability, it is an unavoidable trend to adopt high-nickel NMC, particularly those with nickel content exceeding 80% for their high specific capacity. [15] However, optimizing Ni content remains a critical challenge in commercial automotive cathode materials, requiring a delicate balance between capacity, stability and safety.

NCA Cathode Active Material

The $LiNi_xCo_yAl_zO_2$ ($x + y + z = 1$), NCA, cathode active material achieves structural stabilization through the partial substitution of cobalt (Co) with aluminum (Al). However, several challenges persist, including:

- Formation of NiO-like inactive phases on particle surfaces, reducing electrochemical performance
- Particle cracking, leading to degradation over extended cycling
- Poor thermal stability.

Especially, the poor thermal stability at material level remains a major concern for NCA-based LIB cells, because it possibly leads to thermal runaway of a cell. This risk is further heightened in deeply delithiated states, where oxygen releases from the crystal structure induces further exothermic reactions at over 200 °C, structural phase transitions lead to a rock-salt configuration, irreversibly altering the cathode structure. A study by Besli et al. [22] demonstrated that upon heating delithiated $Li_{0.3}Ni_{0.8}Co_{0.15}Al_{0.05}O_2$ from 25 to 450 °C, progressive Ni reduction occurs, while oxygen release accelerates phase transformations, which will be further discussed in Section 2.2. This phenomenon significantly increases safety risks, potentially triggering thermal runaway in LIB cells. To enhance thermal stability and mitigate degradation, researchers have investigated the following strategies: 1) optimizing Al content while reducing Ni and Co concentrations to improve thermal resilience and 2) applying electrochemically inactive surface coatings to reinforce structural integrity. [25]

NMC and NCA: Challenges and Improvements

Capacity and power degradation in NMC and NCA materials primarily arise from structural transformations and transition metal dissolution during cycling. To address these issues, researchers have explored several mitigation strategies:

- Surface coating (e.g., metal oxides, phosphates, fluorides, oxyfluorides, hydroxides) to limit electrolyte interactions and act as HF scavengers.

- Core-shell structures, incorporating a Ni-rich core for high capacity and Mn-rich shell for enhanced thermal stability. This compositionally graded cathodes enable gradual transitions in material composition to minimize mechanical stress and improve cycling performance. [24]

Future research and development efforts must prioritize integrating these stabilization strategies to ensure that NMC and NCA cathodes remain viable for high-performance EV applications.

LiFePO₄ as an Alternative Cathode Active Material

The olivine structure of LiFePO₄ (LFP) consists of a hexagonally close-packed oxygen array. The distribution of cations in LFP is distinct from that in layered (LCO, NMC and NCA) and spinel structures (lithium manganese oxide, LMO). Since LFP does not form a continuous network of FeO₆ edge-sharing octahedra, it presents relatively poor ion and electron conductivity, so that it is commonly used with conductive carbon to enhance Li⁺ transport. [33] Besides its low electrical conductivity (10⁻⁸-10⁻¹⁰ S/cm [17]), the structure of LFP makes lithium movement possible only along one-dimensional channels, which are also easily blocked by defects or impurities. [23] However, lithium iron phosphate (LFP) has gained significant attention due to its low cost (32% cheaper than NMC in 2023), low environmental impact, and moderate theoretical specific capacity comparable or higher than LCO but lower than NMC and NCA (theoretically 130-170 mAh/g [17,23,24]). Moreover, unlike Ni-rich layered oxides such as NMC and NCA, LFP exhibits outstanding stability, because the strong P-O bond enables it to maintain the structure even if all active lithium ions are deintercalated.

The shift from nickel-based cathodes to LFP is recently driven by cost-effectiveness and growing safety concerns. According to BNEF 2024 Electric Vehicle Outlook, the market share of LFP cathodes in the passenger BEV is projected to expand significantly by 2035, while nickel-based chemistries have been dominantly applied in 2021-2025 with a transition from low-nickel NCM (NMC 111/532/662) to high-nickel NMC and NCA (NMC721/955) as the most widely used cathode active materials. [34] Worthy to mention is that LFP implementation in BEV is geographically unequally distributed mainly in China, holding 65 % of the market share worldwide as the world's largest producer and consumer of LFP. [23] Although LFP is gaining ground, nickel-based chemistries still play a crucial role in high-energy-density applications, such as premium EVs and long-range vehicles. The passenger BEV segment still retains a notable share of nickel-based cathodes, suggesting that high-performance EVs requiring greater specific energy will continue to rely on Ni-rich chemistries.

In addition to LiFePO₄, olivine phosphates of the general formula LiMPO₄ (where M=Fe, Mn, Co, Ni) have been commercialized as cathode materials for LIB cells. Advancements in composite formulations, particle morphology control, and surface modifications may enable the practical application of LFP and related phosphate-based cathodes in next-generation LIBs. [35]

Cathode Active Materials and Scope of This Study

The discussed LIB cathode active materials can be broadly categorized into two groups based on their performance characteristics. The first group consists of high energy density materials, such as NMC and NCA cathodes, which offer higher energy densities compared to other chemistries. However, these high-nickel compositions demonstrate poor thermal stability, which poses safety concerns. In contrast, the second group comprises high thermal stability materials, exemplified by LFP cathodes, which exhibit excellent thermal stability and safety performance. Nevertheless, cells with LFP cathodes have a relatively lower specific energy density compared to NMC and NCA. These two categories of cathode materials each present distinct advantages and drawbacks, leading to their adoption in different regional markets based on the specific requirements. NMC and NCA have been the commonly used as cathode materials globally, while LFP has recently gained a crucial role, especially in the Chinese market. This work focuses on the development of Ni-rich NMC and NCA cathodes, as the global BEV market has been primarily driven by the strategy of increasing the energy density of LIB cells. In the following sections, the focus will be on automotive prismatic lithium-ion cell with NMC and NCA as cathode active material.

2.1.3 Anode Active Materials

To ensure high performance, durability and safety, anode active materials in LIB cells must meet several key criteria:

- **High Energy Density:** the anode material should exhibit both high specific capacity and high volumetric capacity, maximizing the energy storage capability. Also, the operating potential should be low, ideally close to that of metallic lithium, to enhance energy density of a full LIB cell.
- **Structural and Chemical Stability:** the material must reversibly accommodate lithium-ion intercalation and deintercalation (or alloying and dealloying with Li for Si) without undergoing significant structural or phase changes.
- **Electrochemical Stability and SEI Formation:** the stability toward the electrolyte and the ability to form a robust solid electrolyte interphase (SEI) layer are crucial for maintaining long-term cycling performance and preventing side reactions.
- **Fast-Charging Capability:** high lithium-ion diffusion kinetics and high electronic conductivity are required to facilitate rapid charge and discharge process.
- **Cost and Sustainability:** the material should be cost-effective and ideally recyclable, contributing to the sustainability of LIB technology.

Given these criteria, a thorough assessment of both state-of-the-art and emerging anode materials is necessary. Prior to an in-depth analysis of individual materials, Table 4 presents a comprehensive summary of the three leading anode active materials currently in use.

Table 4. Comparison of state-of-the-art anode active materials in automotive LIB cell [36,37].

Material	Li ₄ Ti ₅ O ₁₂	Graphite	Graphite+Si 98/2 wt%	Silicon
Working voltage [V vs. Li/Li ⁺]	~1.5	~0.1	0.1-0.4	~0.2-0.4
Specific capacity [mAh/g]	175	339-372 (LiC ₆)	436	1857 (Li ₁₅ Si ₄)
Rate capability	Excellent	Good	Moderate-good	Moderate
Initial coulombic efficiency	Excellent	Moderate	Poor-moderate	Poor
Volume change (%)	Excellent (~3)	Moderate (13)	Poor-moderate	Poor (300)
Safety performance	Excellent	Moderate	Poor-moderate	Poor
Working temperature	-40-60 °C	-20-40 °C	Uncertain	Uncertain

Lithium titanium oxide Li₄Ti₅O₁₂ (LTO) Anode Active Material

The spinel-structured lithium titanium oxide exhibits relatively minimal volume change during cycling and operates over a wide temperature range, which confer substantial safety advantages. These features make it a promising anode material for lithium storage, despite its relatively low theoretical capacity of approximately 175 Ah/g. [24] While it is prone in a LIB cell with graphite to grow Li-metal dendrites when charged at high current or at low temperature, LTO with high working potential flat charge/discharge plateau can eliminate the possibility of Li plating risk. These benefits present exceptional thermal stability and an extended cycle life. The remarkable structural stability of LTO is also attributed to its “zero-strain” lithium intercalation and deintercalation mechanism with the volume change 0.3-3 %. The intercalation and deintercalation process of LTO follows a unique mechanism governed by two distinct reactions as following:



A significant advantage of this lithiation process is the formation of a metastable solid electrolyte interphase (SEI), without the consumption of Li⁺ for SEI film formation, as observed in cells utilizing graphite anodes. By preventing Li-dendrite formation and meta-stable SEI, LTO substantially

enhances the safety, performance and durability of LIB cells, enabling them to endure tens of thousands of charge-discharge cycles. [36]

However, LTO faces several challenges, including high material costs due to titanium content, inherently low electronic conductivity ($\sim 10^{-13}$ S/cm) [17], and gas evolution caused by reactions between LTO surfaces and organic electrolytes. To mitigate these drawbacks, two primary strategies have been explored. The first involves surface modifications, such as coating LTO with carbon or lithium titanate, which can enhance conductivity. However, carbon coatings may also accelerate electrolyte decomposition, leading to SEI layer deposition at elevated temperatures. The second approach focuses on engineering nanostructured LTO, which improves lithium-ion diffusion kinetics.

Graphite Anode Active Material

Graphite is the dominant anode material for automotive prismatic LIB cells, owing to its high stability and cycle life. Graphite exhibits two distinct surface types with unique characteristics as shown in Figure 2 (a).

The basal plane surface is constructed with the covalently bonded hexagonal carbons and demonstrates low chemical reactivity, resulting in minimal interactions with the electrolyte. While it may contain minor structural defects, its overall reactivity remains low, making it relatively stable during cycling. In contrast, the prismatic surface, also known as edge plane, is significantly more reactive and can accommodate various functional groups. This surface plays a crucial role in lithium intercalation, serving as the primary site for lithium-ion intercalation. However, its heightened reactivity also makes it more susceptible to degradation and the formation of the solid electrolyte interphase (SEI) over extended cycling, which can influence the long-term performance and stability of graphite-based anodes. [38,39]

Figure 2 (b) shows that lithium cations intercalate through the prismatic faces and lodge between basal planes of graphite, generating a series of graphite-lithium intercalation compounds, each with a distinct molar entropy. Reynier et al. [40] found that the entropy associated with lithium intercalation into Li_xC_6 is positive at low lithium concentrations ($x < 0.25$), but becomes negative as the lithium content increases beyond $x > 0.25$. In contrast, the intercalation enthalpy remains consistently negative across all stages of lithiation, although it becomes progressively less exothermic with increasing lithium concentration.

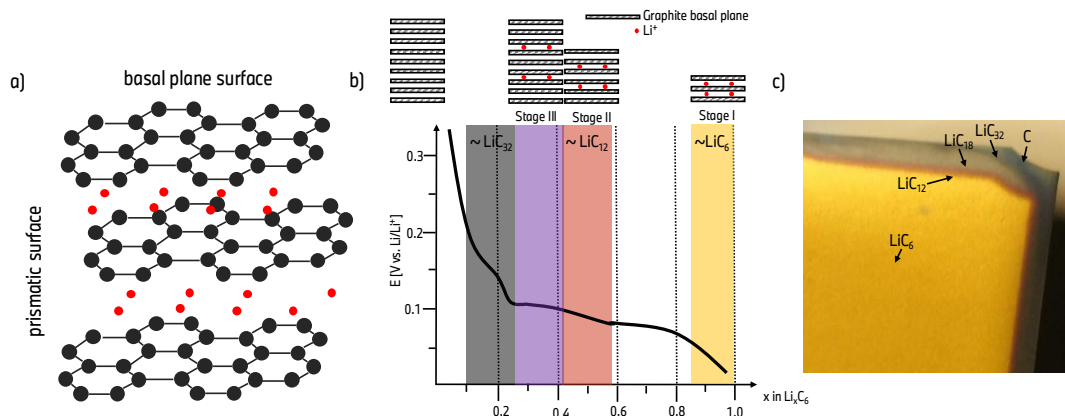


Figure 2. Graphite as anode active material: (a) prismatic surface and basal plane surface with Li^+ presented as red dots, (b) charge profile with a schematic representation of the staging phenomena of the formation of graphite intercalation compounds (GICs), reproduced from literature [41] and (c) an edge of a charged anode layer with a gradation in GICs and colors.

One of graphite's greatest advantages is its relatively low volume expansion ($\sim 13\%$) upon lithiation compared to silicon, ensuring good mechanical stability and an extended cycle life exceeding 1000 charge-discharge cycles. [36] However, its rate capability is limited compared to LTO, which affects

fast-charging performance, and its electrochemical behavior declines at low temperatures, which might result in Li-dendrite, posing challenges in extreme environments.

Silicon Anode Active Material

The state-of-the-art strategy to improve graphite's capacity involves integrating small amount of silicon.



For instance, a composite of graphite (98 wt%) and silicon (2 wt%) achieves a theoretical capacity of 436 mAh/g, approximately 117 % of that of pure graphite, 372 mAh/g. [17,42] However, such composites often exhibit higher irreversible capacity decline due to increased side reactions and SEI formation. Currently, graphite-Si composites with low silicon content (5-15 %) are being incorporated into automotive cylindrical LIBs [34], striking a balance between capacity enhancement and cycling stability. The optimum silicon fraction is governed by the electrode's fully lithiated porosity as well as the proportions of conductive additive and binder; in an idealized design, S.Chae et. al. [35] calculated an upper theoretical limit of 11.68 wt % Si to maximize volumetric capacity.

Lithium Metal Anode Active Material

Rechargeable lithium metal anodes were first introduced in 1989 by Moli Energy, but commercial adoption (1.3 million of these cells) was halted due to safety risks, including dendrite formation and thermal runaway. Despite these challenges, lithium metal remains a promising candidate due to its exceptionally high theoretical capacity (3860 mAh/g), significantly surpassing graphite (372 mAh/g). However, the high reactivity of lithium metal presents multiple challenges:

- Electrolyte instability, leading to continuous SEI formation and lithium consumption
- Non-uniform lithium deposition, resulting in the accumulation of highly reactive lithium sponge-like structures, reducing charge efficiency and long-term cycle stability
- Dendritic lithium growth, which can pierce the separator, causing internal short circuits and potential thermal runaway events. [43,44]

To address the challenges associated with lithium metal anodes, researchers are exploring several stabilization approaches. One key strategy involves electrolyte engineering, where advanced formulations are designed to suppress unwanted side reactions and promote uniform SEI formation. The development of solid-state electrolytes is another promising approach, as they can act as physical barriers against lithium dendrite growth. However, many solid-state systems require elevated operating temperatures above 60 °C to achieve sufficient ionic conductivity, which introduces additional engineering challenges. Another area of focus is optimizing electrode architectures to facilitate uniform lithium deposition. By designing nanostructured lithium metal electrodes, researchers aim to minimize dendrite formation and enhance the long-term stability of lithium plating and stripping processes. These combined efforts are crucial in making lithium metal anodes a viable solution for high-energy-density battery applications.

Anode Active Materials and Scope of This Study

Graphite continues to serve as the benchmark anode material, though graphite-silicon composites are emerging as a promising alternative to enhance capacity while retaining stability. Meanwhile, lithium metal anodes hold immense potential for next-generation high-energy-density batteries, but their practical implementation remains constrained by safety challenges. The prismatic automotive LIB cells examined in this study incorporate state-of-the-art graphite anode active materials and the scope of this work is centered on graphite.

2.1.4 Liquid Electrolyte and Formation of Solid Electrolyte Interphase (SEI)

The electrolyte in a LIB serves as a transport medium for lithium ions (Li^+) between the anode and cathode during charge and discharge cycles. The Li^+ concentration remains constant in a closed system, because electrolyte itself contains Li^+ as part of a supporting electrolyte. Electrolytes can be categorized into liquid, polymer, and solid state with liquid organic electrolytes being the state-of-the-art technology in commercial LIBs due to their balance between stability and ionic conductivity. In this work, the liquid organic electrolyte that is commercially used for automotive prismatic LIB cell is mainly discussed. An ideal electrolyte must satisfy several fundamental requirements:

- High dielectric constants, ϵ and high ionic conductivity but low viscosity, η to ensure efficient Li^+ transport
- Electrochemical stability at both the anode and cathode to prevent degradation and electrolyte decomposition. If this condition is not given, then a stable SEI must form.
- Thermal stability to withstand a wide operating temperature range without initiating thermal runaway
- Low volatility and vapor pressure to reduce flammability and enhance safety
- Good film forming ability for stable SEI formation, particularly on graphite anodes
- Non-toxic and environmentally friendly properties, though most current commercial electrolytes remain toxic.

A multi-component electrolyte system is necessary to meet these requirements, consisting of a lithium salt, solvents with good solvation properties and functional additives to enhance stability, conductivity and safety.

Lithium Hexafluorophosphate as Li-Salt

The most widely employed lithium salt in LIB electrolyte is lithium hexafluorophosphate (LiPF_6). A key advantage of LiPF_6 lies in its participation in the formation of the solid electrolyte interphase (SEI), a critical layer that stabilizes the anode surface and supports long-term cycling stability. Additionally, LiPF_6 offers relatively high ionic conductivity and large counter-anions PF_6^- reduce anion mobility, facilitating efficient lithium-ion transport within the electrolyte. Another key benefit is its role in protecting the aluminum current collector, as it helps to prevent corrosion at high voltages, making it a viable choice for high-energy LIB applications. However, LiPF_6 is far from being an ideal lithium salt. Its thermal and chemical stabilities are relatively low due to the weak P-F bond and the auto-decomposition reaction from PF_6^- to PF_5 + F^- . One major drawback is its instability in the presence of moisture, where even trace amounts of water lead to the formation of hydrofluoric acid (HF) and other highly reactive byproducts. Extremely low moisture contents (< 20-40 ppm) are therefore required. These degradation reactions not only increase the corrosivity of the electrolyte but also accelerate electrode deterioration over time. Additionally, at elevated temperatures, LiPF_6 undergoes thermal decomposition, releasing PF_5 , a strong Lewis acid that catalyzes unwanted polymerization reactions within the electrolyte, further compromising cell stability. Given these limitations, there is an urgent need for alternative or at least partial replacements for LiPF_6 in LIB electrolytes. While various alternative salts have been proposed, they often introduce new challenges, such as reduced solubility, aluminum current collector corrosion, or lower ionic conductivity. As a result, LiPF_6 remains the dominant choice for commercial LIB applications despite its inherent limitations, as no superior alternative has yet achieved widespread adoption. However, LiTFSI has been extensively studied as a potential alternative due to its superior thermal stability, with melting point at 234 °C and an initial decomposition temperature of 360 °C, compared to LiPF_6 , which has a melting point of 200 °C and an initial decomposition temperature of 125 °C. Additionally, LiTFSI exhibits an ionic conductivity of 9 mS/cm, which is comparable to that

of LiPF_6 (10.8 mS/cm). [45] Furthermore, ongoing research efforts focus on stabilizing LiPF_6 through optimized electrolyte formulations, including advanced electrolyte additives that suppress its degradation pathways while enhancing overall battery performance and safety. [46]

Liquid solvent

The transport of Li^+ ions within the liquid electrolyte occurs via a series of solvation and dissociation steps, influenced by solvent polarity and anion stability. Due to its small ionic radius, lithium ions typically form solvation sheaths consisting of two to four solvent molecules. For effective Li^+ transport, only dissociated, unpaired ions can migrate in the electric field. High-dielectric constant solvents prevent ion pair formation, ensuring that Li^+ ions remain mobile rather than neutralized by their counterion.

The solvent system in commercial LIBs is typically a mixture of cyclic and linear carbonates, chosen to optimize dielectric constant, viscosity and lithium-ion mobility. Ethylene carbonate (EC) is an essential component, as it enables SEI formation on graphite anodes and ensures stable battery operation. However, EC must be combined with low-viscosity solvents such as dimethyl carbonate (DMC), diethyl carbonate (DEC) or ethyl methyl carbonate (EMC) to improve overall electrolyte fluidity. These main solvents have following characteristics.

- **Ethylene Carbonate** (EC): high dielectric constant (89.78 at 25 °C), essential for SEI formation
- **Propylene Carbonate** (PC): high dielectric constant but not suitable for graphite anodes due to co-intercalation effects
- **Dimethyl Carbonate** (DMC), **Diethyl Carbonate** (DEC), **Ethyl Methyl Carbonate** (EMC): low viscosity to enhance lithium-ion mobility (e.g. DMC, DEC with 0.59 at 20 °C and 0.75 at 25 °C) but showing lower dielectric constant [47]

An optimal solvent mixture balances ionic conductivity, stability and interfacial compatibility while maintaining safety and durability.

Electrolyte Additives for Safety and Stability

To improve electrolyte stability, SEI quality and safety, several functional additives are introduced into the electrolyte formulation. Examples are listed as following:

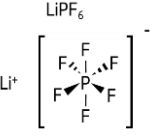
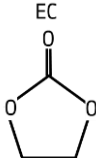
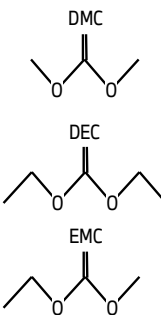
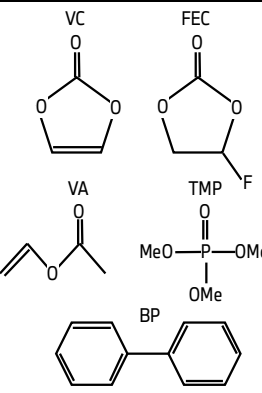
- SEI film-forming additives enhance SEI uniformity (e.g. vinylene carbonate (VC))
- Protective cathode additives prevent cathode degradation especially at high voltage (e.g. N,N-diethylamino trimethyl silane reacts with water and HF, preventing dissolution of cathode)
- Electrolyte stabilizers suppresses LiPF_6 decomposition and HF formation (e.g. LiF)
- Fire retardant additives lower the flammability of the liquid electrolytes (e.g. trimethyl phosphate)
- Overcharge protection additives polymerize to form insulating layers or trigger gas-release mechanism for current interruption (e.g. metallocenes). [46]

State-of-the-Art Electrolyte System

Table 5 summarizes the electrolytes constituents most frequently adopted in contemporary prismatic automotive cells. Commercial systems almost invariably employ LiPF_6 at 1.0 – 1.2 mol/L, dissolved in a mixed-carbonate solvent matrix composed of EC/EMC/DEC and/or DMC. Typically, ethylene carbonate (EC) is widely employed as one of the major components (around 30 wt%) in electrolyte solvents for LIB with graphite anode due to the ability to build SEI. Ethylene carbonate undergoes electrochemical decomposition at approximately 0.8 V versus Li/Li^+ , leading to the formation of a protective solid electrolyte interphase (SEI) on low-potential anode surfaces. Moreover, thanks to high dielectric constant, it facilitates the effective dissociation of lithium salts.

However, their relatively high viscosity can impede ion transport, particularly during storage. To enhance practical applicability, linear carbonates such as dimethyl carbonate (DMC), diethyl carbonate (DEC), and ethyl methyl carbonate (EMC), which exhibit lower viscosity, are blended with cyclic carbonates to form composite electrolytes and their composition varies depending on lithium-ion cells. These mixtures provide a balance of chemical and electrochemical stability while ensuring favorable interfacial properties. [24] Finally, < 5 wt % of functional additives (film-forming, overcharge inhibitors, flame retardants, etc.) are routinely incorporated to fine-tune interfacial reactions and safety characteristics. [48].

Table 5. State-of-the-art components of electrolyte in automotive prismatic LIB.

Components	Li-Salt	Solvent		Additives
Requirements	Li ⁺ with a bulky counter anion	High dielectric solvents +ability to form SEI	Low viscosity solvents	Several functional additives
State-of-the-art materials	$\text{Li}^+ \left[\text{PF}_6 \right]^-$ 			

Formation and Function of the Solid Electrolyte Interphase (SEI)

The solid electrolyte interphase (SEI) is a passivation layer formed on the anode surface during initial battery cycling. The terminology of solid electrolyte interphase was introduced first in 1979 by Pele to describe this passivation layer. Subsequently, in 1990, Dahn et al. reported the beneficial effects of incorporating EC into the electrolyte formulation for the formation of a more stable and effective SEI layer on graphite anodes, as shown in Table 5. [49] SEI is electrically insulating but ionically conductive, allowing Li⁺ transport while preventing direct electron exchange that could degrade the electrolyte.

The SEI originates from the reductive decomposition of electrolyte components on the anode's surface in formation, consuming inherently approximately 10 % of the original capacity in an irreversible process. This formation is a double-edged sword. From an energy density or cell cost perspective, the total surface area of the anode should be minimized. However, this minimization comes with a performance trade-off, as a lower anode surface area leads to reduced power density due to solid-state diffusion limitations. In contrast, a higher anode surface area is beneficial for power density, but it also results in a greater consumption of lithium inventory when passivating the surface to form the SEI layer, thereby decreasing the overall energy density. To avoid internal electrical shorts, the anode capacity is often kept about 10 % higher than the cathode capacity (N/P ratio of 1.1, where N is the negative electrode and P is the positive electrode). This additional anode material must also undergo SEI layer passivation, adding to the cell cost and further reducing the total cell energy. Optimizing the N/P ratio is crucial for minimizing the initial lithium inventory loss and decreasing the initial irreversible capacity. However, for long-term capacity retention and coulombic efficiency, optimizing only the capacity ratio would be insufficient, as the SEI continuously grows and consumes electrolyte and lithium ions when it is not well-formed. [49]

The formed SEI layer on the anode plays crucial role in the optimal functionality of the LIB:

- As a protective barrier, impermeable to solvated lithium ions, to prevent excessive electrolyte consumption and unwanted side reactions
- For a mechanical stability, as it must withstand the repeated expansion and contraction of electrode materials during charge-discharge cycles. However, this function is being challenged with high-capacity anode materials, such as graphite with silicon, because this negative anode undergoes more substantial volume changes [14]
- To impedance growth over time, with its development slowing as thickness increases. (excessive SEI growth can hinder charge transfer, reducing the rate capability of the battery.) [46]

The formed SEI layer, typically ranging from 10 to 50 nm in thickness [14], is composed of a complex mixture of organic and inorganic decomposition products from the electrolyte. The morphology and chemical composition of the SEI layer are unique to the specific graphite surface and electrolyte solution pairs, but it can generally be described as consisting of three distinct regions: an outer porous, less-compact layer formed from the organic compounds near the liquid electrolyte zone; an inner more-compact inorganic structure adjacent to the graphite surface; and an intermixed layer with intermediate properties between the inner and outer layers. [49] Also, temperature plays a significant role in SEI stability. Higher temperatures accelerate SEI growth, particularly during extended rest periods, potentially leading to increased internal resistance and reduced battery lifespan. The optimization of the SEI layer formation and composition is a critical aspect of LIB design and performance, as it directly impacts the battery's capacity, efficiency, safety and long-term stability.

Future Research and Development Trends

With increasing demands for higher energy density and improved safety, LIB electrolyte research is evolving in several key directions:

- Development of LiPF₆ alternatives with better thermal and chemical stability
- High performance electrolyte additives to enhance SEI stability
- Non-flammable liquid electrolytes for improved safety
- Solid-state electrolytes to eliminate flammability risks and lithium dendrite formation.

2.1.5 Separator

Among the components of a LIB, the separator plays a fundamental role in ensuring both operational efficiency and safety. The primary function of the separator is to provide a physical barrier between the anode and cathode, preventing direct contact while allowing lithium-ion transport between electrodes. [24,50,51] This structure is critical in preventing short circuits, particularly under extreme conditions such as overcharging, mechanical stress, or thermal fluctuations. To effectively function within a LIB, a separator must meet several crucial requirements:

- **Chemical Stability:** the separator should remain chemically inert in the presence of electrodes and electrolytes, preventing undesirable reactions that could compromise battery performance.
- **Thermal Stability:** given the high temperatures LIBs may experience during operation, separators must resist heat-induced degradation. A key feature of modern separator is their thermal shut down capability, preventing thermal runaway.
- **Wettability:** proper electrolyte absorption is necessary for efficient ionic conductivity. The separator should exhibit high wettability to ensure uniform electrolyte distribution without undergoing deformation.

- **Mechanical Strength:** sufficient puncture resistance is required to maintain the structural integrity of the separator during battery assembly and throughout its operational lifespan.
- **Porosity:** optimized porosity is essential for effective lithium-ion transport while maintain sufficient mechanical strength. [52]

Conventional Polyolefin Separators and Trilayer Separators

Commercial separators are predominantly composed of polyolefin-based microporous polymeric membranes, particularly polyethylene (PE) and polypropylene (PP), to meet the requirements. Polyolefin separators typically exhibit thicknesses ranging from 12 to 25 μm , with a porosity of approximately 40 % and an average pore size of 50-100 \AA . Additionally, they demonstrate an ionic resistivity of 1.5-2.5 Ωcm^2 . These attributes contribute to their electrochemical stability and mechanical robustness. [53,54]

However, a key limitation of polyolefin separators is their relatively low electrolyte wettability and susceptibility to thermal shrinkage, even at moderate temperatures. PE and PP separators begin to shrink at 120 $^{\circ}\text{C}$ and 150 $^{\circ}\text{C}$, respectively, which can compromise the safety and efficiency of LIBs. The meltdown of PE ($\approx 130^{\circ}\text{C}$) and PP ($\approx 160^{\circ}\text{C}$) further poses a significant risk [55,56]. Interestingly, separators fabricated by laminating layers of PE and PP can maintain their mechanical integrity up to 180 $^{\circ}\text{C}$. This phenomenon is attributed to the high viscosity, which allows it to retain its physical structure despite thermal exposure. But a complete melting results in direct electrode short-circuiting, leading to excessive heat generation and potential thermal runaway. [24,53,57]

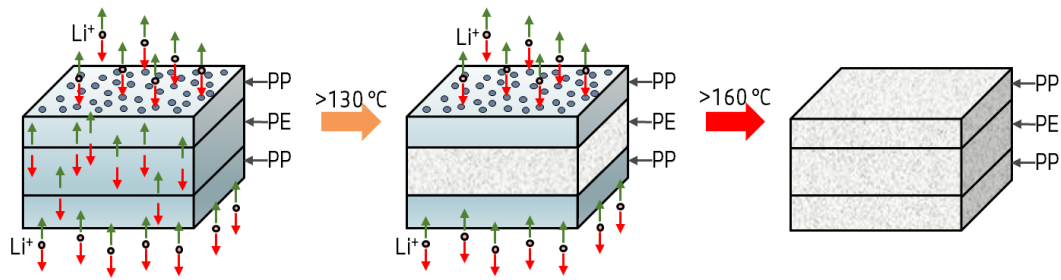


Figure 3. Closing pore processes behaviors (shutdown) of trilayer (PP/PE/PP) separators.

To mitigate these thermal risks, manufacturers have developed trilayer membranes, PP/PE/PP, which are predominantly used in a commercial automotive LIB cell as one of main safety elements, as demonstrated Figure 3. This design is typically called shutdown separators and incorporates a thermal pore-closing mechanism: the PE layer melts at elevated temperatures, ceasing ion transport, while the PP layers maintain structural integrity to prevent the shrinkage of PE layer and eventually internal short circuits. Despite these advancements, further improvements in thermal stability are required to meet the demands of high-power and high-temperature applications.

Ceramic Coating on Conventional Polyolefin Membranes

In addition to trilayer separators, an effective strategy to enhance the thermal stability of polyolefin separators is the application of ceramic coatings. These coatings, composed of thermally robust inorganic materials such as aluminum oxide (Al_2O_3), titanium dioxide (TiO_2) and silicon dioxide (SiO_2), significantly improve heat resistance while preserving electrochemical performance. Ceramic-coated separators exhibit minimal shrinkage at elevated temperatures, thereby mitigating the risk of thermal runaway. Furthermore, the hydrophilic nature of ceramic particles enhances electrolyte wettability, facilitating efficient lithium-ion transport. [57]

In commercial prismatic LIB applications, separators can be coated on a single side or on both sides. Both-side-coating is always more valuable for the safety perspective; however, one side coating can be applied in the perspective of cost. In commercial automotive prismatic LIB cells, the single-side

coating is typically oriented toward the positive electrode. This orientation would be presumably crucial due to two primary facts:

- 1) There is a side reaction that occurs between the cathode (specifically O_2 , generated from the decomposition of the cathode material) and the electrolyte during high-voltage (>4.5 V) operation [54,58] or at elevated temperatures.
- 2) Especially LFP cathode active material typically exhibit lower conductivity compared to the anode active materials. Applying a ceramic coating on the cathode-facing side can enhance overall ionic conductivity, as the ceramic-coated separator can absorb a greater amount of electrolyte due to its increased surface area and the high hydrophilicity of the ceramic coating binder, thereby facilitating improved Li^+ transport. [59]

However, excessive ceramic deposition may lead to pore blockage, impeding ion transport and negatively affecting battery performance. [57] Also, the successful integration of ceramic coatings necessitates the use of an appropriate polymeric binder to ensure adhesion under mechanical stress. Poly(vinylidene fluoride-co-hexafluoropropylene) (PVDF-HFP) has emerged as promising polymeric binder due to its excellent flexibility, chemical stability, and strong adhesion properties. By optimizing the ratio of polymeric binders to ceramic coatings, LIB separators can present superior thermal resistance while maintaining essential mechanical and electrochemical characteristics. [50,51] Therefore, selecting an optimal binder with both high adhesive strength and exceptional thermal stability is critical for ensuring dimensional stability. Additionally, excessive ceramic deposition may lead to pore blockage, impeding ion transport and negatively affecting battery performance [57].

2.2 Thermal and Thermodynamic Study of Cathode

The thermal and thermodynamic behavior of the constituents of a lithium-ion battery (LIB) must be characterized for two practical reasons. First, lithium-ion battery safety is critically influenced by the thermal behavior of its components, because the cell safety is dictated by the temperature at which exothermic reactions of cell materials begin and by the heat they release. [24] Second, the sheer number of possible cell architectures makes comprehensive, full-scale calorimetry economically prohibitive — particularly for battery-electric-vehicle (BEV) packs. Because large-format calorimetric testing is costly, slow and often infeasible in early-stage battery design, designers require robust material-level data that allow safety to be predicted before committing to pack-level prototypes. This challenge is particularly relevant for next-generation batteries, such as all-solid-state batteries (ASSBs), where new materials must be assessed for safety before large-scale production.

The thermodynamic analysis of battery components relies fundamentally on understanding the Gibbs free energy change (ΔG) associated with electrochemical reactions. Two central equations govern this relationship [60]:

$$\Delta G^\circ = -nFE \quad (2.7)$$

n : number of moles of electrons transferred in the redox reaction,

F : Faraday's constant (96.485 C/mol) – the charge of one mole of electrons,

E : cell potential or electromotive force – the voltage produced by the cell.

The negative sign signifies that a positive cell potential corresponds to a negative Gibbs free energy change, indicating a spontaneous electrochemical process.

Additionally, the Gibbs free energy change can be expressed in terms of enthalpy and entropy as:

$$\Delta G = \Delta H - T\Delta S \quad (2.8)$$

ΔH = enthalpy change (J) — heat absorbed or released at constant pressure,

T = temperature (K),

ΔS = entropy change (J/K) — measure of disorder or randomness.

Reaction spontaneity is thus influenced by both enthalpy and entropy. For example, an exothermic reaction with increasing entropy is always spontaneous ($\Delta G < 0$).

Among all components, the charged cathode is the dominant source of heat during thermal runaway, while many cell components (cathode, anode, separator, electrolyte) contribute to overall heat generation. In a charged state, cathode materials can easily release oxygen at elevated temperatures, and this oxygen readily reacts with the organic electrolyte, often leading to thermal runaway and fire. [4,61] In contrast, the lithiated anode and other components, though reactive, typically contribute less heat and do not produce oxidizing gases. The disproportionate heat release (and accompanying oxygen evolution) from the cathode underscores why it poses a higher risk in abuse conditions. Moreover, differences in cell-level safety can be traced among automotive prismatic lithium-ion cells primarily to the cathode chemistry, because commercial prismatic cells use essentially the same graphite anodes, polyolefin separators and electrolyte system. Accordingly, this study focuses on the cathode's thermal and thermodynamic behavior as a key to understanding and then improving cell safety and performance.

Material-level experimental studies (differential scanning calorimetry, thermogravimetric analysis and high temperature drop solution calorimetry) therefore serve two roles. Experimentally, they identify thermal stability of compositions at an early stage, such as onset temperature, heat capacity (C_p) and mass change (Δm). Analytically, the resulting enthalpies of formation (ΔH_f) and reaction enthalpies (ΔH_r) feed predictive models that estimate cell-level heat release without testing every configuration.

Section 2.2.1 reviews how Shurtz et al. [4,6] used such data to map decomposition pathways of layered metal oxides and calculate thermal runaway energy based on enthalpies of formation (ΔH_f) and reaction enthalpies (ΔH_r). Section 2.2.2 summarizes previous experimental studies of thermal and thermodynamic behavior including ΔH_r of cathode active materials using TGA and DSC, while Section 2.2.3 compiles prior works on the enthalpies of formation of cathode materials. These three subsections establish the cathode's governing influence on cell safety and underpin the detailed analyses presented later in Chapter 7.

2.2.1 Decomposition Pathways of Layered Metal Oxides with Oxygen Release

Shurtz [4,6] highlighted that the state of charge and cathode chemistry play a critical role in heat generation, with highly delithiated materials exhibiting the higher exothermic reaction and demonstrated that staged heat release from layered metal-oxide cathodes can be accurately predicted using fundamental thermodynamic properties.

In general, Mn-based cathodes tend to have higher thermal stability, whereas Ni-rich cathodes exhibit greater heat release during decomposition, making them more prone to thermal runaway. Another key thermodynamic aspect of LIB safety is oxygen release from the cathode at high temperatures. As Huggins [62] demonstrated, oxygen evolution from metal oxide cathodes is fundamentally linked to their electrode potential and high-voltage cathodes exhibit increasingly higher equilibrium oxygen pressures as the potential rises. This oxygen release is critical because the liberated oxygen can readily react with the highly reducing organic electrolyte, leading to highly exothermic combustion reactions. The interaction between oxygen and electrolyte not only generates additional heat but also intensifies the decomposition process, strongly amplifying thermal runaway risks. Therefore, the presence of electrolyte significantly increases the energy release of cathode decomposition reactions, emphasizing the importance of considering solvent oxidation enthalpies and oxygen evolution thermodynamics in safety assessments.

Figure 4 illustrates the decomposition pathways of layered metal oxides suggested by Shurtz and Hewson [6], showing how different phase transformations lead to varying amounts of heat release.

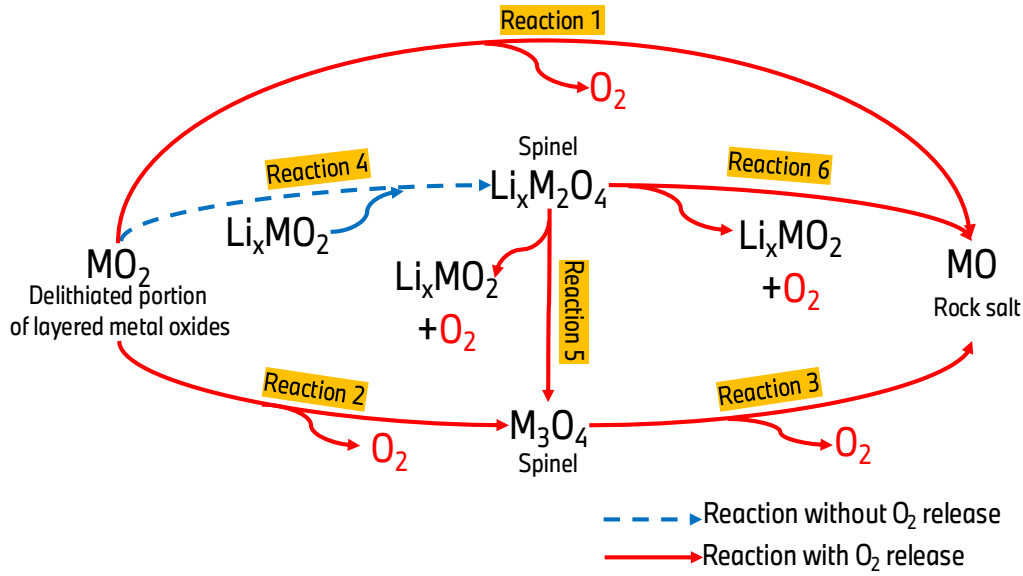
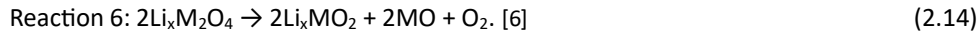
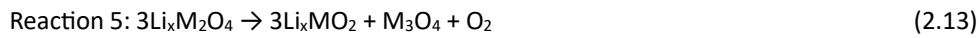
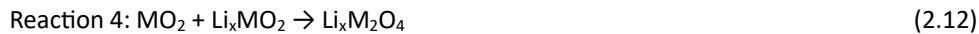


Figure 4. Schemes of possible decomposition paths for delithiated layered metal oxides with or without oxygen release, reproduced from literature [6].

The delithiated layered metal oxide part in a charged LIB cell can be decomposed either over spinel structure (Reaction 2 to 6) or directly to rock salt (Reaction 1). When it is transformed to a spinel, which is thermodynamically favored, the reaction can flow with or without oxygen release. Evolved oxygen leads most likely to reactions directly with electrolyte components, so that it is crucial to investigate cathode active materials with the presence of electrolyte in studying thermal and thermodynamic stability of LIBs components as demonstrated in Section 3.1. The quantitative reactions in Figure 4 are as follows:



Thermodynamic studies are indispensable for assessing and mitigating safety risks in LIBs. By leveraging enthalpies of formation, reaction enthalpies, and decomposition pathways, researchers can predict thermal runaway energy without relying solely on experimental testing. This predictive capability is particularly valuable for early-stage battery design, where safety considerations must be addressed before large-scale manufacturing.

2.2.2 Previous Studies of Thermal and Thermodynamic Behavior of Cathode Active Materials

Extensive investigations into the thermal stability of cathode active materials have employed differential scanning calorimetry (DSC) and thermogravimetric analysis (TGA). Most studies, however, have examined freshly synthesized powders under idealized, electrolyte-free laboratory conditions. This chapter therefore summarizes research that replicate cathode active materials in

conditions closely comparable to those found in commercial LIBs: cathodes harvested directly from lithium-ion cells, analyzed in partially delithiated states and/or in the presence of electrolyte (see Table 6).

Table 6. Studies of cathode active material harvested from LIB using DSC and TGA.

Author	Year	Topic
Zhang et al. [63]	1997	investigated the thermal stability and reactivity of delithiated Li_xNiO_2 , Li_xCoO_2 , $\text{Li}_x\text{Mn}_2\text{O}_4$ cathodes and lithiated graphite from coin cells using differential scanning calorimetry (DSC). The primary goal is to understand how differently cathodes react with electrolytes under elevated temperatures. Their results suggest that the total heat generation of delithiated cathodes is significantly higher than that of lithiated graphite and approximately 10 times of heat is produced from delithiated Li_xNiO_2 with electrolyte compared to it without electrolyte and the reactivity of the cathode materials increases nearly linearly with the charge capacity [mAh/g].
Veluchamy et al. [64]	2009	assessed the thermal stability of Li_xCoO_2 cathodes, extracted from commercial pouch LIBs with various SOC, using TGA and DSC. According to TGA, mass loss occurs in three distinct temperature regions; 1) around 100 °C, attributed to electrolyte evaporation and SEI decomposition, 2) 200-400 °C, major mass loss due to Li_xCoO_2 decomposition into LiCoO_2 , Co_3O_4 and oxygen release and 3) above 450 °C, from reduction of Co_3O_4 into CoO due to interactions with decomposed electrolyte. Also, heat release during decomposition was investigated by DSC, presenting that major exothermic reactions occur at higher temperatures (125 – 500 °C) due to decomposition of Li_xCoO_2 into LiCoO_2 and Co_3O_4 and reaction between oxygen released from the cathode and electrolyte solvent.
Lee et al. [65]	2017	systemically studied the thermal stability of delithiated cathodes in LIBs, focusing on the role of inorganic salts (LiPF_6), organic solvents (e.g. EC, DMC, DEC etc.) and additives (e.g. vinylene carbonate (VC)), to assess the thermal behavior of cathode (NCA)-electrolyte interactions. The impact of electrolyte was studied systemically by measuring pure solvents, LiPF_6 salt alone, delithiated cathode alone and combinations of cathode and salt, cathode and solvent and cathode and electrolyte with additives. Their findings showed that delithiated cathodes with salt have a lower onset temperature and higher heat release than delithiated cathodes without salt. Vinylene carbonate decreases the thermal stability of cathode, increasing thermal runaway risks in LIBs. The study suggests that material selection, especially electrolyte formulation, is critical in mitigating LIB safety risks.
Yu et al. [61]	2017	investigated the thermal stability of three cathode materials ($\text{LiNi}_{0.5}\text{Co}_{0.2}\text{Mn}_{0.3}\text{O}_2$, LiMn_2O_4 , LiFePO_4) harvested from coin cells using TGA and DSC. NCM523 has poor thermal stability, especially when mixed with electrolyte, due to oxygen release from structural breakdown and LMO still undergoes significant electrolyte-driven exothermic reactions even with better thermal stability, while LFP has the best thermal stability due to its strong P-O covalent bonds, which prevent oxygen release.
Kvasha et al. [66]	2018	investigated harvested electrodes (NCA, LFP) from cells at different states of charge (SOC) — 0, 50 and 100 % — using DSC under both dry conditions and in the presence of electrolyte (1M LiPF_6 in EC/DMC/DEC). In addition, the original cells from which cathode materials were extracted were evaluated using accelerating rate calorimeter (ARC) to assess safety at the cell level, allowing for comparison with the thermal stability of the isolated materials. This study reveals that cells incorporating materials with higher decomposition enthalpy exhibit faster self-heating rates during thermal runaway. These findings provide critical insights into the significance of material selection for enhancing battery safety.

Author	Year	Topic
Barkholtz et al. [67]	2019	examined how different cathode chemistries at various SOC contribute to thermal instability of commercial 18650 LIBs, mainly using DSC, TGA and ARC. Their findings from DSC and TGA analysis on thermal stability of component level presented that LCO and NCA cathodes start decomposing at 150-200 °C, releasing oxygen that accelerates thermal runaway, while LFP cathodes remain stable until 500-550 °C, making them significantly safer. This result from TGA and DSC can support the findings from ARC, that NCA cells show the most violent runaway reactions, with maximal temperature rates exceeding 21,000 °C/min at SOC 100 % (noting that the typical measurement limit of ARC is approximately 1,000 K/min). Collectively, this study provides a comprehensive multi-scale analysis of LIB thermal stability, demonstrating that cathode composition is the primary determinant of thermal runaway risk.

As demonstrated, DSC and TGA are valuable techniques for assessing the thermal reactivity or stability of active materials in LIBs and these studies confirm that cathode composition and state of charge govern both the onset and the magnitude of exothermic reactions, validating the thermodynamic framework introduced in Section 2.2.1. Detailed experimental procedures for DSC and TGA appear in Sections 3.1.1 and 3.1.2, respectively. Furthermore, new data obtained in this work are presented in Chapter 7.

2.2.3 Previous Studies of Enthalpy of Formation of Cathode Active Materials

Numerous studies have investigated the enthalpy of formation of cathode active materials to better understand their thermodynamic stability and optimize their electrochemical performance. Notably, Masoumi et al. [8,9] analyzed state-of-the-art NMC materials in the series $\text{LiNi}_x\text{Mn}_x\text{Co}_{1-2x}\text{O}_2$ and $\text{LiNi}_x\text{Mn}_y\text{Co}_{1-x-y}\text{O}_2$, while Manthiram et al. [68] and Idemoto et al. [69] determined the enthalpy of formation of chemically delithiated Li_xCoO_2 and $\text{Li}_x\text{Ni}_{0.333}\text{Mn}_{0.333}\text{Co}_{0.333}\text{O}_2$ calorimetrically. The investigated compositions are mapped onto the Gibbs compositional concentration triangle for the LiNiO_2 - LiMnO_2 - LiCoO_2 systems (Figure 5), with their corresponding enthalpy values listed in Table 7.

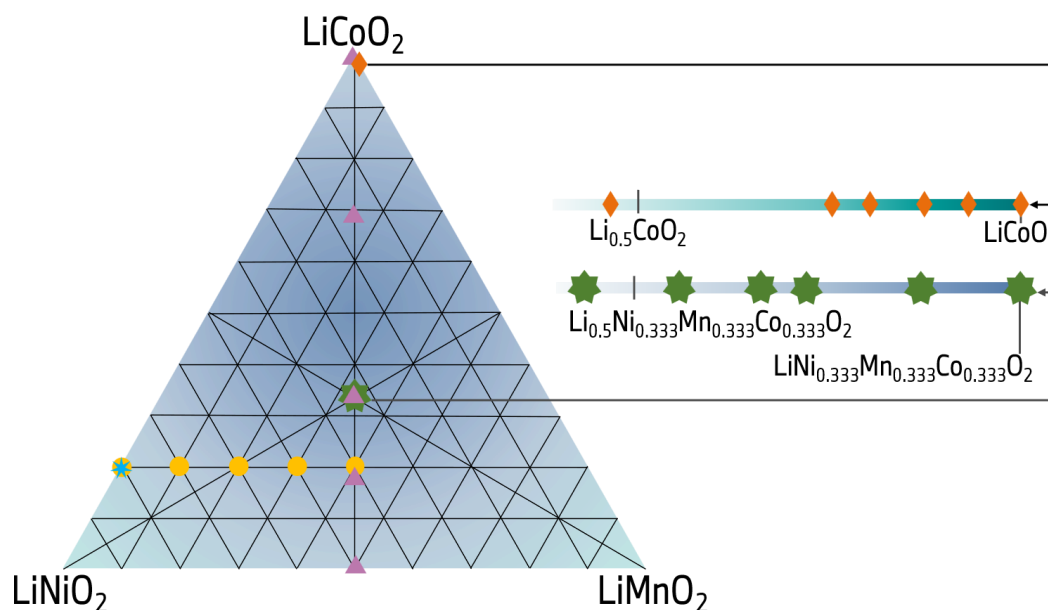


Figure 5. Compositional Gibbs triangle for the LiNiO_2 - LiMnO_2 - LiCoO_2 (NMC) system with symbols on compositions whose enthalpies of formation are studied, reproduced from literatures [8,9,68–70].

Table 7. Enthalpy of dissolution from high temperature oxide melt solution calorimetry, enthalpy of formation from oxides and enthalpy of formation from elements at 298 K of various cathode materials in LIB cell.

Composition	$\Delta_{\text{ds}}H^{974}$ [kJ/mol]	$\Delta_f H^\theta$, oxides [kJ/mol]	$\Delta_f H^\theta$, elements [kJ/mol]	Source	Mark
$\text{LiNi}_{0.167}\text{Mn}_{0.167}\text{Co}_{0.666}\text{O}_2$	112.10±1.53	-117.30±1.93	-702.41±2.12	[9]	▲
$\text{LiNi}_{0.333}\text{Mn}_{0.333}\text{Co}_{0.333}\text{O}_2$	100.70±1.08	-85.39±1.62	-717.74±1.72	[9]	▲
†	-	-	-649.74±2.05	[69]	★
††	-	-	-652.49±0.45	[69]	★
$\text{Li}_{0.877}\text{Ni}_{0.333}\text{Mn}_{0.333}\text{Co}_{0.333}\text{O}_2^\dagger$	-	-	-603.19±1.54	[69]	★
$\text{Li}_{0.725}\text{Ni}_{0.333}\text{Mn}_{0.333}\text{Co}_{0.333}\text{O}_2^{\dagger\dagger}$	-	-	-562.89±0.51	[69]	★
$\text{Li}_{0.665}\text{Ni}_{0.333}\text{Mn}_{0.333}\text{Co}_{0.333}\text{O}_2^{\dagger\dagger}$	-	-	-535.87±2.30	[69]	★
$\text{Li}_{0.556}\text{Ni}_{0.333}\text{Mn}_{0.333}\text{Co}_{0.333}\text{O}_2^\dagger$	-	-	-512.99±0.70	[69]	★
$\text{Li}_{0.420}\text{Ni}_{0.333}\text{Mn}_{0.333}\text{Co}_{0.333}\text{O}_2^{\dagger\dagger}$	-	-	-507.63±0.58	[69]	★
$\text{LiNi}_{0.4}\text{Mn}_{0.4}\text{Co}_{0.2}\text{O}_2$	98.86±1.09	-75.35±1.65	-726.59±1.72	[9]	▲
	97.97±0.65	-56.09±1.56	-725.70±1.49	[8]	●
$\text{LiNi}_{0.5}\text{Mn}_{0.3}\text{Co}_{0.2}\text{O}_2$	89.79±0.59	-74.46±1.40	-697.58±1.46	[8]	●
$\text{LiNi}_{0.6}\text{Mn}_{0.2}\text{Co}_{0.2}\text{O}_2$	80.24±0.70	-73.19±1.45	-668.08±1.53	[8]	●
$\text{LiNi}_{0.7}\text{Mn}_{0.1}\text{Co}_{0.2}\text{O}_2$	72.16±0.55	-73.34±1.42	-640.05±1.50	[8]	●
$\text{LiNi}_{0.5}\text{Mn}_{0.5}\text{O}_2$	95.89±0.62	-60.07±1.44	-739.66±1.53	[9]	▲
$\text{LiNi}_{0.8}\text{Co}_{0.2}\text{O}_2$	61.39±0.56	-70.80±1.47	-609.34±1.56	[8]	●
	62.38±2.20	-71.79±2.20	-610.33±2.64	[70]	★
LiCoO_2	118.90±0.84	-144.61±1.47	-682.49±1.94	[9]	▲
	118.27±0.66	-143.99±1.38	-	[68]	◆
$\text{Li}_{0.93}\text{CoO}_2$	116.03±0.50	-138.10±1.24	-	[68]	◆
$\text{Li}_{0.88}\text{CoO}_2$	114.57±0.67	-134.04±1.28	-	[68]	◆
$\text{Li}_{0.80}\text{CoO}_2$	113.02±0.74	-128.34±1.25	-	[68]	◆
$\text{Li}_{0.75}\text{CoO}_2$	107.78±0.79	-120.50±1.24	-	[68]	◆
$\text{Li}_{0.47}\text{CoO}_2$	93.13±1.05	-91.31±1.26	-	[68]	◆

†Solid-state synthesized sample

††Solution method-synthesized sample

Masoumi et al. [9] explored the thermodynamic properties of $\text{LiNi}_x\text{Mn}_y\text{Co}_{1-2x}\text{O}_2$ compounds, which are widely used as cathode materials in LIBs, using high temperature oxide melt drop solution calorimetry. The results revealed that increasing the Mn and Ni content leads to more exothermic enthalpies of formation, indicating improved structural stability. A subsequent study [8] further examined $\text{LiNi}_{0.8-y}\text{Mn}_y\text{Co}_{0.2}\text{O}_2$ compositions, demonstrating a near-linear correlation between Mn content in NMC composition and enthalpy of formation. This study reinforces the correlation observed in the previous study, enabling the interpolation of thermodynamic stability across a broader compositional range.

Manthiram et al.[68] studied the enthalpy of formation of chemically delithiated Li_xCoO_2 using high temperature oxide melt solution calorimetry, revealing that the enthalpy of formation increases linearly with lithium content, x decreasing. This trend indicates that Li_xCoO_2 becomes less stable as lithium content decreases. Similarly, Idemoto et al. [69] investigated the enthalpies of formation of delithiated $\text{Li}_x\text{Ni}_{0.333}\text{Mn}_{0.333}\text{Co}_{0.333}\text{O}_2$, but these values were calculated using Gibbs free energy and Hess's law, assuming $T\Delta S \approx 0$. This approach differs from other studies where enthalpies of formation were directly measured using high temperature oxide melt solution calorimeter. However, the work also presents that the thermodynamic stability decreases with lowering lithium content. This thermodynamic assessment provides critical insights into the design and optimization of NMC cathode active materials, guiding the development of stable LIB systems.

The high temperature drop solution calorimeters used for measurements of formation enthalpy are described in detail in Section 3.1.3 and the results of formation enthalpies of high-Ni NMCs will be discussed in Chapter 4.

2.3 Safety of LIB Cells

The Kelly Blue Book published in 2024 a report that presented findings from a study analyzing the relative fire risk associated with electric vehicles compared to gasoline-powered vehicles. According to data, BEVs in USA were involved in approximately 25 fire incidents per 100,000 vehicles sold, whereas gasoline-powered and hybrid vehicles exhibited significantly higher fire incident rates, at 1,530 and 3,475 per 100,000 vehicles sold, respectively. [71] Additionally, in 2020, reported fire incidents were very rare, with 17 cases among approximately 350,000 Tesla vehicles (~49 ppm) and 3 cases among about 175,000 BMW i3 vehicles (~17 ppm) [72].

Despite these statistical findings indicating that BEVs have the lowest incidence of fire among vehicle types, concerns regarding their safety persist. This is largely due to the distinct nature and circumstances of fire events in BEVs, which differ from those in gasoline-powered vehicles. In internal combustion engine vehicles, most fire incidents occur while the vehicle is in motion. This scenario typically allows passengers a critical window of time to safely evacuate, report the incident, and initiate firefighting measures. In contrast, BEV fire risks extend beyond operation, occurring not only while driving but also during parking and charging. For instance, in South Korea, 6 out of 17 recorded BEV fire incidents (2018-2021) occurred in enclosed spaces, such as underground parking garages and manufacturing facilities [73]. Similarly, in China, 21% of BEV fire incidents in 2019 occurred during charging, while 32% took place while the vehicle was parked [32,74].

The unique thermal and chemical characteristics of LIBs exacerbate these risks, making fire suppression more challenging and often requiring specialized firefighting techniques and equipment. That is because BEV battery cells undergo highly exothermic reactions, leading to thermal runaway and ultimately to propagation. A notable case illustrating these risks occurred in 2024 when an unplugged Mercedes-Benz EQE350+ caught fire and exploded in an underground parking lot, resulting in damage to over 900 neighboring vehicles, with approximately 70 vehicles completely burned out. Firefighters required over eight hours to fully extinguish the blaze. [75] Such incidents underscore the variability in BEV fire dynamics compared to conventional gasoline-powered vehicles and contribute to ongoing safety concerns. Addressing these safety challenges through improved design, safety features, and public awareness will be crucial for the widespread adoption and acceptance of BEVs.

The thermal hazards associated with commercial automotive LIB failures arise from various failure modes. When LIB in BEV fails, the associated hazards can be systemically categorized, as listed in Table 8.

Table 8. EUCAR Hazard levels. [24]

Hazard level	Description	Classification criteria and effect
0	No effect	No effect, no loss of functionality
1	Passive protection activated	No defect; no leakage; no venting, fire, or flame; no rupture; no explosion; no exothermic reaction or thermal runaway; cell reversibly damaged; repair of protection device needed
2	Defect/damage	No leakage; no venting, fire, or flame; no rupture; no explosion; no exothermic reaction or thermal runaway; cell irreversibly damaged; repair needed
3	Leakage, $\Delta m_{\text{mass}} < 50\%$	No venting, fire, or flame; no rupture; no explosion; weight loss $< 50\%$ of electrolyte weight (electrolyte = solvent + salt)
4	Venting, $\Delta m_{\text{mass}} \geq 50\%$	No fire or flame; no rupture; no explosion; weight loss $\geq 50\%$ of electrolyte weight
5	Fire or flame	No rupture; no explosion (i.e., no flying parts)
6	rupture	No explosion, but flying parts of the active mass
7	explosion	Explosion (i.e., disintegration of the cell)

This scale, known as the thermal runaway severity levels by the European Council for Automotive Research and Development (EUCAR), outlines the severity levels of thermal runaway in LIBs and

categorizes the hazard severity based on the visual observation of physical changes and battery function. This classification system provides a structured assessment of hazard severity but does not explicitly define specific temperature thresholds or voltage parameters as part of its criteria. Consequently, thermal hazards are generally considered tolerable up to level 3 on the severity scale [76], as levels beyond this threshold typically indicate critical failure modes such as fire incidents.

Ensuring the safety of LIB cells especially in automotive applications presents a significant challenge, as it requires balancing safety, performance, durability, and cost. While stringent safety standards are essential, they often come at the expense of energy density, power output, and economic feasibility. In BEVs, battery systems must provide sufficient power and energy while maintaining a compact and lightweight design, as space constraints limit the expansion of battery packs. This necessity for higher volumetric energy density has led to the adoption of highly reactive cathode materials, such as Ni-rich NCM compounds, and the integration of silicon into anodes to enhance energy capacity. A clear example of this trend is seen in the evolution of the BMW i3 battery pack, which has progressed from 60 Ah to 94 Ah and subsequently to 120 Ah, reflecting the industry's shift toward higher capacity and greater energy density. [19]

However, as energy density increases, so do safety risks. The occurrence of thermal runaway and its subsequent thermal propagation becomes more severe, particularly in automotive battery packs that contain hundreds of interconnected cells arranged in series and parallel configurations. Unlike smaller electronic devices (e.g., laptops or smartphones), where a single-cell failure has limited consequences, cell failure in an automotive battery pack can release a substantial amount of thermal energy, potentially triggering a chain reaction that propagates throughout the entire system if adequate safety mechanisms are not in place.

Moreover, cost constraints significantly impact the feasibility of safety solutions. The cost ratio of LIBs relative to BEVs remains high, ranging from 14 to 32 %, as presented in Table 5, making affordability a critical factor in commercialization. While advanced safety technologies — such as separators coated with magnesium nanoparticles, which act as heterogeneous nucleating sites to prevent lithium dendrite formation [77] — can effectively reduce the risk of failure, they substantially increase production costs, potentially driving BEV prices beyond a competitive threshold.

The challenge of balancing safety, energy density, and cost underscores the reality that, despite ongoing advancements, the complete elimination of safety risks in LIBs remains unattainable. Nevertheless, continuous research efforts focus on optimizing safety, performance, and durability, aiming to develop commercially viable and reliable energy storage solution for electric mobility.

2.3.1 Thermal Runaway and its Triggers

Thermal runaway in lithium-ion batteries (LIBs) refers to a hazardous phenomenon characterized by an uncontrollable chain reaction that results in rapid temperature escalation. This process is primarily driven by exothermic reactions occurring within the cell, which can lead to catastrophic outcomes, including non-stoppable explosions. [78] Fundamentally, the initiation of thermal runaway is dictated by the balance between heat generation and heat dissipation. If heat is produced at a rate significantly higher than the cell's capacity to dissipate it, the LIB cell temperature continues to rise, eventually reaching a critical threshold where exothermic reactions become self-sustaining. This process leads to an uncontrollable escalation, often culminating in fire, gas venting, and potential explosion. The efficiency of heat dissipation is primarily governed by the thermal properties of the cell and the effectiveness of the battery cooling system. [79,80]

At present, no universally accepted quantitative criterion exists for defining thermal runaway (TR) in lithium-ion batteries. TR is commonly associated with catastrophic events — fire, flame ejection, and explosion — and, in the EUCAR hazard rating schemes, corresponds to levels 5-7 (see Table 8). Because such classifications rely on visual or experiential judgment, an objective metric is needed.

One promising avenue is to use accelerating rate calorimetry (ARC) to identify the critical self-heating rate at which TR begins. Reported thresholds, however, span a wide range — ≥ 10 K/min [81], 60 K/min [82] or ~ 80 K/min — owing to variations in cell size, format, and electrochemistry. In addition, this definition is restricted in quasi-adiabatic condition and measurement of self-heating rate using ARC is logged at discrete time intervals; because self-heating accelerates sharply at the onset of TR, the true maximum rate may be under- or overestimated between data points. In the scope of this work, thermal runaway during nail/needle penetration testing is defined as the point at which the cell-surface temperature rises abruptly and is immediately followed by a steep voltage drop.

Moreover, understanding the heat generation in a LIB cell is complex, as it requires a detailed analysis of how electrochemical reaction varies, as well as the distribution of current, particularly in LIB with a large capacity. [12] The total energy released during TR equals the joule heating from the stored electrical energy plus the chemical energy liberated by exothermic decomposition. For example, mechanical abuse such as nail penetration produces extensive internal short-circuits, whose Joule heating triggers further exothermic reactions that in turn aggravate the short-circuits, creating a self-reinforcing loop. Consequently, the thermal energy released can far exceed the cell's initial electrical energy; Stringfellow et al. [83] reported that the total thermal output can reach approximately three times the stored electrical energy.

The primary triggers to thermal runaway are internal defects, mechanical abuse, over-discharge, over-charge, over-current, and over-temperature. Although those causes have different paths to initiate ISC, the separator failure will be caused eventually. [84] Those possible triggers are demonstrated as follows.

- **Internal Defects:** the lithium-ion cell production goes through a series of manufacturing processes, and the neglect of any element will be the source of risks. The root cause of the well-known fire incident of Samsung Galaxy Note 7 is an internal defect inside cells. [85] Internal defects are mainly categorized into structural deformation and manufacturing-induced defects occurring during the manufacturing process. Structural deformation mainly refers to the defects in the separators and electrodes, such as cracks in the separators, burrs on the electrodes, double (or folded) electrode causing Li-plating and misaligned separator between anode and cathode resulting in a contact between those. Manufacturing-induced defects mainly refer to foreign objects introduced in the manufacturing process, including non-metal particles (like dust) and metal particles (such as Fe, Ni, Cu, Al, Co, Mn).
- **Mechanical failure:** BEVs can inevitably suffer collision failures during daily usage. Applied force can cause destructive deformation and displacement upon collision. Multiple failures of battery systems will take place, amongst the most serious risk is the mechanical abusive condition, mainly including crush, squeeze or penetration. The ISC caused by crush or penetration is mainly a pin-point short circuit. Hence, at the short-circuit point, a large ISC current is generated, which results in vigorous heat generation and sharp temperature rise. Side reactions inside the cell are easily triggered, which may lead to TR ultimately.
- **Overdischarge:** means the cell voltage drops below the cut-off voltage. Overdischarge will cause irreversible chemical reactions and internal structure damage, which can cause capacity degradation and induce ISC forming. When overdischarge happens, the delithiation of the anode and the lithiation of the cathode is performed simultaneously with the continuous discharge. The cell voltage declines with overdischarge, which is attributed to the rapid anode potential increase and the gradual cathode potential decrease. The anode potential continuously increases until it can overcome the overpotential required for copper dissolution, where the anode potential reached a maximum value of around 4.8 V vs. Li/Li⁺ [86]. When the anode potential reaches the overpotential that the copper dissolution needs, the anodic corrosion of copper is triggered. Copper is oxidized to Cu⁺/Cu²⁺, which depends on the anode potential. When the LIB cell is again recharged, which leads to deposition of dissolved copper

ions, copper dendrites are formed on locations with suitable potential, often anodes. As a result, the separator can be penetrated by copper dendrites, which implies that ISC is forming.

- **Overcharge:** is defined as continues charging of the cell after it reached its nominal cut-off voltage. Overcharge is one of the most common and dangerous cell failures, which can be induced by the malfunction of the charger, failure of the BMS, and the inconsistency of cells. The overcharged-induced ISC is harsher than overdischarge. At the beginning of overcharge, the cell generates little joule heat that causes the cell temperature to rise slightly. The anode potential increases during overcharging, the cathode material destruction and decomposition will take place, and the electrolyte will decompose with gas generating. Simultaneously, the lithium from the over-delithiated cathode reacts with the solvent which thickens the SEI film and generates gas. The gas causes the cell to swell, thereby increasing the distance between the cathode and the anode. Under these conditions, lithium plating tends to initiate at sites where Li^+ travels the shortest distance — particularly at graphite edge, which are typically situated closest to the cathode. As the over-charge continues, the plated lithium makes lithium dendrites grow continuously at the anode. In this process, lithium dendrites are likely to penetrate the separator forming ISC. When the temperature reaches the melting point of the separator, the separator will shrink and even collapse, which causes a large-scale ISC. Since more electrical energy is stored by overcharge in a LIB cell, thermal runaway can be more dramatic than in other causes.
- **Over-current:** it is caused by excessive current flow. The primary reasons for over-current are external short circuit (ESC) and fast charging. ESC may be caused by battery system failure (such as line aging) and harsh operating conditions (like water immersion). With the continuous over-current flow, a large amount of heat can be accumulated which makes the cell temperature rise sharply, depending on the heat dissipation. The rising temperature may exceed the thermal decomposition thresholds of the cell components and further trigger ISC and lead to catastrophic damage to the cell ultimately.
- **Temperature abuse:** the temperature window of regular operation is narrow for LIBs. Exposing LIB to either low temperatures ($15\text{ }^{\circ}\text{C}$) or high temperatures ($40\text{--}50\text{ }^{\circ}\text{C}$) can progressively reduce their cycle life. At temperature higher than $70\text{ }^{\circ}\text{C}$, the threat of thermal runaway increases significantly, ultimately leading to cell failure and compromising the safety of LIB. [12] Overheat may be induced by high ambient temperature and poor heat dissipation of the battery thermal management system. Under elevated temperature, due to the poor heat tolerance of cell components, thermal decomposition and reaction between those components happen inside the cell. Generally, the common separators are polyolefin membranes, like polyethylene (PE) and polypropylene (PP), which start to meltdown at $130\text{--}160\text{ }^{\circ}\text{C}$. The melting of the separator results in the contact between the cathode and the anode, which enables ISC. Massive joule heat generated induces the temperature to increase dramatically. The cathode decomposition will be triggered by the elevated temperature, and further generates oxygen. Moreover, the oxygen reacting with the electrolyte further aggravates side reactions. Subsequently, the anode structure collapses, massive heat and gas are generated. This reaction flow is presented in Figure 6. [84,87] Due to the differences in cell components and temperature, the corresponding sequence of the above-mentioned reactions may be different. However, once the internal chain reactions are triggered, ISC and even TR can be caused.

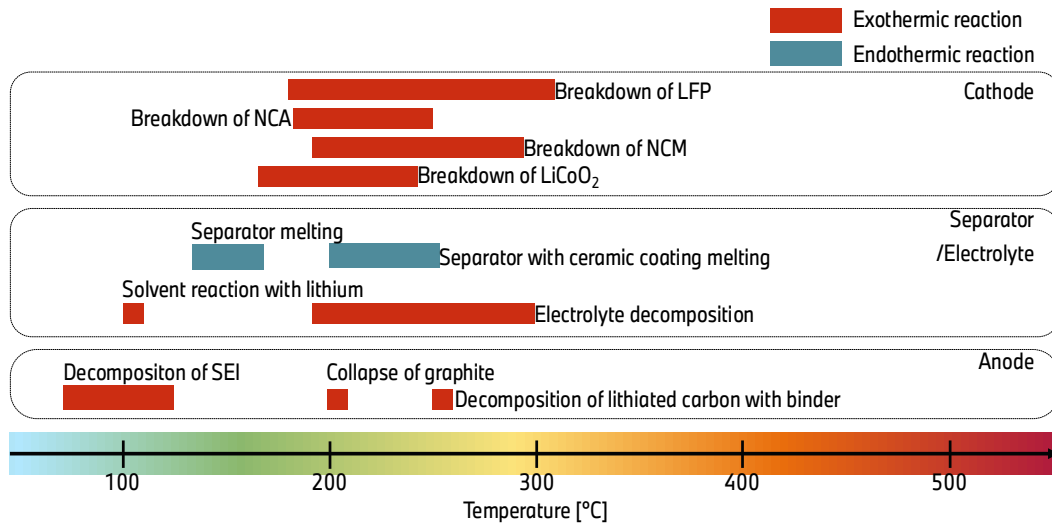


Figure 6. Average onset temperatures of reactions before or by thermal runaway [1,88].

In short, numerous factors could induce ISC as presented in Figure 7. Although the failure process may be different, the common feature is the breakdown of the separator. [89] ISC typically serves as a direct pathway to trigger TR, leading to severe hazards. In contrast, a high-ohmic ISC may not initiate TR; instead, it can result in gradual capacity fading, shortened service life, or even serious impact on the performance of the entire battery pack.

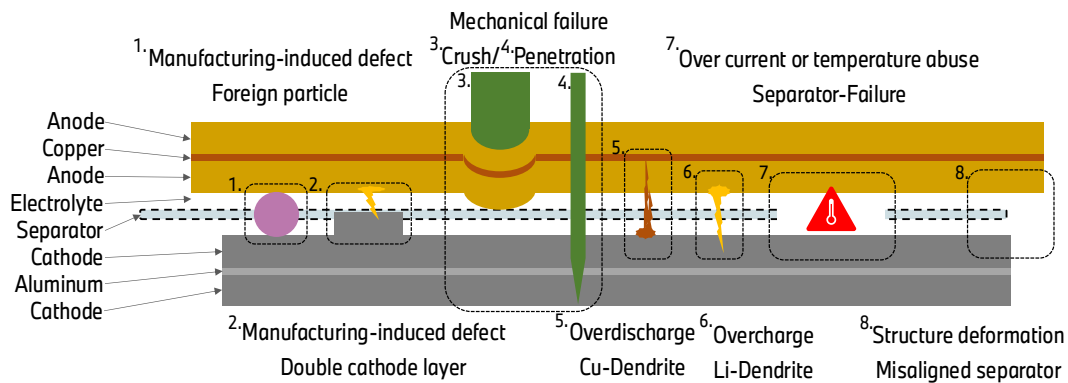


Figure 7. Common causes causing ISC and leading to TR.

2.3.2 Internal Short Circuit (ISC)

Internal short circuits (ISCs) are widely recognized as a primary trigger for thermal runaway (TR) in lithium-ion batteries (LIBs) as discussed in Section 2.3.1. While various failure mechanisms can lead to ISC formation, the common factor among them is the failure of the separator, which allows direct contact between the anode and cathode. The fundamental danger of an internal short circuit lies in its ability to create an uncontrolled, high-current discharge path within the cell. This results in intense joule heating at the ISC site, which can elevate temperatures beyond the decomposition thresholds of key battery components.

Examples of ISCs Leading to Thermal Runaway

Several real-world cases have demonstrated the catastrophic consequences of internal short circuits in lithium-ion batteries.

- The Samsung Galaxy Note 7 incident is a well-documented example of an internal short circuit (ISC) failure attributable to manufacturing defects. The incident was attributed to manufacturing anomalies within the LIB, which led to spontaneous internal short circuits. One of the most critical design flaws was the deformation of electrode layers near the cell edge, where a series of local compressions caused the layers to collapse sequentially — similar to a cascading mechanical failure — likely due to unintended mechanical stress on the negative electrode windings. Additionally, the pouch-cell design was identified as a contributing factor, as insufficient internal spacing within the battery structure led to compression-related deformations. Specifically, the corners of the battery were found to be folded over. These localized mechanical deformations can promote lithium deposition and dendritic growth. Furthermore, lithium dendrite at these defect sites increases the risk of penetration through the thin separator, thereby exacerbating the probability of an internal short circuit. [85,90,91]
- In 2013, Boeing's latest and most technologically advanced aircraft, the 787 Dreamliner, was withdrawn from commercial operation worldwide following multiple fire incidents linked to its onboard LIB system. One such event occurred on flight JA829 from Yamaguchi to Tokyo, where a battery powering the auxiliary power unit experienced thermal runaway, resulting in combustion. Investigations suggested that the underlying cause was internal short circuit within one of the battery cells. [19,85] This ISC likely triggered localized heating, leading to further thermal instability and the propagation of failure throughout the battery pack. The incident underscored the critical safety risks associated with LIB design in aviation applications and highlighted the necessity for enhanced thermal management and fault-tolerant battery architectures.
- The United States Federal Aviation Administration reported a total of 206 LIB fire and explosion incidents in air/airport environments between 1991 and 2018. Among notable LIB fire incidents, in 2011, a Chevrolet Volt ignited three weeks after undergoing a crash test, suggesting a delayed thermal runaway event. In 2013, multiple Tesla Model S vehicles caught fire after sustaining damage from road debris. While Tesla subsequently reinforced the battery shielding in both new and existing models, battery-related fire incidents persisted. In 2016, a Tesla electric vehicle caught fire in France during a promotional event. [55]
- Mechanical failure has been identified as a significant trigger for internal short circuits, ultimately leading to thermal runaway in LIB systems as presented in 2.3.1. Several high-profile incidents involving BEVs illustrate the critical role of mechanical stress in battery failures. In Seattle, a Tesla Model S caught fire after colliding with a large piece of metal debris, which penetrated and destroyed one of its battery modules, leading to an ISC and subsequent combustion (*penetration*). In another severe accident, a Tesla Model S plunged off a cliff, collided with multiple boulders, fragmented upon impact, and caught fire due to battery failure (*drop*). A similar incident occurred when a Tesla Model S, traveling at 177 km/h, crashed into a concrete barrier while navigating a roundabout, resulting in extensive battery damage and fire (*crash*). Another case involved a BYD e6, which was struck from behind at 180 km/h, subsequently crashing into a tree and suffering deep structural penetration of approximately one meter, erupting into flames (*crash*). A notable example involves several hundred newly built Maserati vehicles that caught fire after exposure to seawater during port flooding, leading to chemical reactions that triggered combustion within the battery systems and spread to adjacent vehicles. (*Immersion*). [72] In Moscow, Russia, a Tesla Model 3 crashed into a truck and caught fire. (*crash*) [92] In such mechanical abuse scenarios, LIB cells can undergo severe deformation, leading to compression or rupture of the separator. If these mechanical failures result in localized ISCs and the generated heat is not dissipated efficiently, the thermal instability can propagate, escalating into a full-scale thermal runaway event throughout the battery pack. These incidents underscore how mechanical abuse can result in ISC or even further in thermal runaway.

These incidents reveal that diverse initiating events ultimately converge on the formation of internal short circuits, underscoring the need to examine ISC as the principal driver of thermal runaway.

2.3.3 How to Reproduce ISC in Lab

As discussed in 2.3.2, there are constantly safety issues in automotive LIB cells, and it is of importance to understand triggers and behaviors of thermal runaway. Hence, there have been many discussions how to realistically induce thermal runaways in a laboratory environment. This chapter introduces several experimental techniques for inducing internal short circuits (ISC) in LIB cells with their own advantages and limitations, including two typically applied methods, namely accelerating rate calorimeter and nail penetration test.

Experimental Methods for Inducing ISC and Their Challenges

Studying internal short circuits is complex because inducing an ISC under controlled conditions is extremely difficult. Several experimental methods have been attempted, yet each presents challenges that limit their practicality:

- ***Internal Heating Method:*** Yan et al. [93] embedded a mini-heater cartridge inside commercial 1860 cells to simulate internal heating failures to induce thermal runaway. Their findings presented that internal heating resulted in a more localized, faster failure with shorter venting time before TR and with more abrupt mass loss compared to external heating. This technique induces separator failure by applying localized heating, which presents a more feasible real-world scenario, however, it does not accurately replicate actual ISC conditions. The introduction of foreign objects inside the cell may alter the short-circuit behavior. This method relies on generating localized heat to induce separator failure, but it does not accurately replicate how ISCs occur within real battery cells. Additionally, the presence of alien substances inside the cell can influence the short circuit behavior.
- ***Thermally ISC-Triggering Method:*** the thermal approach relies on phase-change materials (PCMs) or shape memory alloys to induce an ISC when a specific temperature threshold is reached. The National Renewable Energy Laboratory (NREL) and the National Aeronautics and Space Administration (NASA) developed a method where a separator is pre-damaged and mended with a phase-change material. Once the temperature reaches the melting point, the ISC is triggered. Another PCM method, developed by Sandia National Laboratories, employs low-melting metals or alloys that breach the separator insulation upon reaching their melting temperature, leading to an ISC. [87] As another thermal-triggered method, Zhang et al. [94] proposed embedding a shape memory alloy inside the LIB during manufacturing. Upon reaching around 70 °C, the alloy undergoes a temperature-induced transformation, resulting to puncture the separator and to two ISCs; i) Al-Anode ISC leading to TR and explosion and ii) Cathode-Anode ISC only causing localized overheating and burn-traces but no explosion. Also, Finegan et al. [95] integrated a self-developed ISC device into 18650 cylindrical LIB cells during manufacturing. The device was activated by heating the cell until the embedded wax layer melted (around 57 °C), allowing electrical contact between electrodes and creating a short between the negative electrode and the aluminum current collector. Those methods offer precise control over ISC location and contact modes with consistency and reliability. However, practical implementation of phase-change materials or shape-memory alloys in lithium-ion batteries is only viable at the cell-manufacturing stage, when they can be incorporated directly on the production line. Retrofitting a finished cell would require dismantling it, unavoidably introducing mechanical stresses, disturbing the internal pressure, and exposing moisture- and air-sensitive components to the environment.

- Reproducing Manufacturing Defects:** manufacturing defects can be artificially introduced to replicate ISCs observed in real-world battery failures. However, controlling key parameters such as lithium plating distribution, rate and temperature remains challenging. One approach involved inserting an additional cathode to induce lithium plating through cycling. In this case, the area of ISC may play a critical role as demonstrated in the study by Santhanagopalan et al. [96], which employed thermal-electrochemical model to assess ISC behavior in LIB cells. The findings indicate that micro-shorts (around 0.1 mm^2) generally self-extinguish without inducing severe thermal runaway. In contrast, macro-shorts ($> 1 \text{ mm}^2$) result in elevated localized heating, significantly increasing the likelihood of thermal runaway in cylindrical LIB cells with a capacity of 800 mAh. While this method can simulate a real-world defect, it is difficult to control and impractical due to the unpredictable time required for lithium plating to develop and trigger an ISC. Another approach involves introducing conductive particles into the cell. Metallic contamination is a known cause of ISCs in industrial settings. Sun et al. [97] investigated failure mechanisms related to copper particle contamination on the NCM cathode plate surface in a pouch LIB cell. Copper particles dissolve at the high-potential cathode and precipitate as Cu dendrites to anode, leading to separator penetration and ISC formation. This phenomenon, classified as a soft short, does not immediately cause TR but contributes to long-term self-discharge and battery degradation. This method enables to understand ISC behavior in real-world applications. However, placing foreign particles precisely within the cell where it is intended is challenging, as their location may shift during testing. Moreover, the inherent unpredictability of the internal short circuit introduces a potential risk during testing, as it remains uncertain whether an ISC will lead to thermal runaway and, if so, the precise conditions and timing of its occurrence is not clear. Also, Mohanty et al. [98] deliberately introduced several realistic manufacturing defects into coin-type lithium-ion cells — agglomerates on the electrode coating, pinholes devoid of coating, metallic contaminants (Al-foil fragments $< 2 \text{ mm}$ and Co powder $< 0.01 \text{ g}$), and pronounced coating non-uniformity. Defective cells showed accelerated capacity fade and poorer high-rate performance relative to defect-free controls. However, the investigation is confined to coin cells with low-nickel NMC cathodes, limiting its broader applicability.
- External Heating or Accelerating Rate Calorimeter (ARC):** ARC methods are commonly used to study TR. This method enables precise thermal characterization of LIB cells by subjecting them to controlled heat-wait-seek cycles. It allows researchers to determine the onset temperature of self-heating and thermal runaway, providing insights into the thermal stability of different chemistries or various SOC. For instance, Ohnseit et al. [10] evaluated the thermal safety of commercial 21700 LIB cells with different cathode chemistries (NCM, NCA, and LFP) using heat-wait-seek tests. The study revealed that NCM/NCA cells exhibited lower TR onset temperatures ($196\text{--}203 \text{ }^\circ\text{C}$), whereas LFP cells required significantly higher temperatures ($256 \text{ }^\circ\text{C}$) to experience a thermal runaway. The finding highlights the need for robust thermal management in high-energy-density LIBs, while LFP cells offer superior safety in applications where stability is a priority. Unlike real-world scenarios, where heat dissipates outward from the cell, laboratory setups often apply heat externally, reversing the natural heat dissipation gradient. Furthermore, the quasi-adiabatic conditions inherent in the heat-wait-seek method do not accurately represent the heat dissipation dynamics observed in real-world scenarios. A detailed discussion of the ARC and its heat-wait-seek methodology is provided in the subsequent Section 3.2.1.
- Nail (or needle) penetration:** this method remains widely adopted due to its procedural simplicity. International standard SAE J2464 requires that penetration-type mechanical tests be conducted at the cell, module, and pack levels. [76] However, its ability to accurately replicate real-world internal short-circuit (ISC) conditions remains a subject of ongoing debate. Factors such as nail size, material composition, and penetration speed influence the test outcome and must be carefully considered to establish meaningful correlations with practical failures.

Further discussion on studies employing the nail penetration technique is presented in the following Section 3.2.2.

This chapter provides a comprehensive overview of ISC initiation methods, highlighting their strengths and challenges. Ongoing discussions focus on the development of advanced diagnostic techniques and insitu monitoring tools for lithium-ion battery analysis. In the Sections 3.2.1 and 3.2.2, two widely utilized methodologies, the Accelerating Rate Calorimeter (ARC) and nail penetration testing, are examined in greater detail.

2.4 LIB for battery electric vehicle (BEV)

While LIBs are widely used in both BEVs and consumer electronics (e.g., smartphones, laptops, portable household, e-bikes and tablets), there are significant differences in design, performance requirements, safety considerations and durability. The distinctions primarily arise due to the higher energy and power demands, durability requirements and safety risks associated with large-scale battery packs in electric vehicles (EVs). Therefore, the cell design and safety elements of LIBs that are exclusively applied for BEV are studied in this chapter.

2.4.1 Commercial Cell Designs

In contrast to the previous schematic representation, Figure 1, illustrating the fundamental principle of a lithium-ion battery (LIB), the actual structure of an automotive prismatic LIB features a significantly thinner separator positioned between the cathode and anode, with both electrode layers being approximately ten times thicker than the separator. As a result, even small Li- or Cu-dendrites or microscopic metal particles can critically contribute to the formation of an internal short circuit, posing significant safety risks. Figure 8 presents the average relative thickness distribution of each cell layer, derived from an analysis of eight commercial prismatic LIB cells.

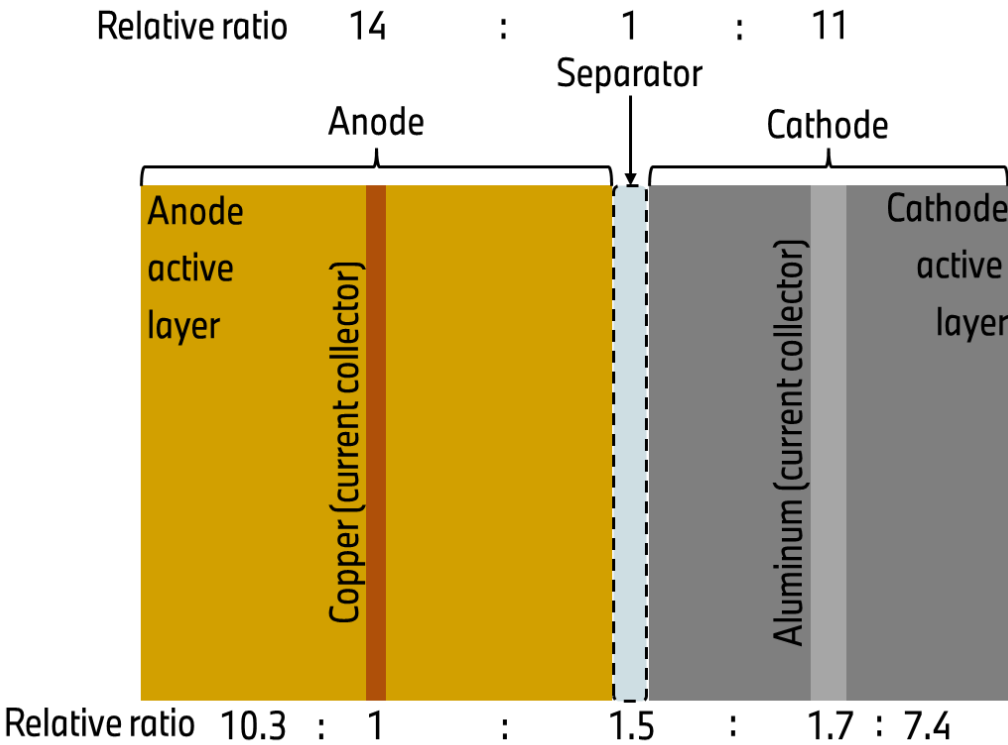


Figure 8. Real automotive prismatic cell structure with average relative ratio between cell layers calculated from eight commercial LIB cells.

The relative thickness of each layer in commercial automotive prismatic LIB cells follows a structured balance to ensure optimal performance. The anode active layer and the cathode active layer generally maintain comparable thicknesses to achieve charge balance between the electrodes. The copper current collector, typically around 10 μm thick, is thinner than the aluminum current collector, which measures averagely 17 μm . This difference arises from the higher electrical conductivity of copper, allowing for a thinner layer, whereas aluminum requires increased thickness to compensate for its lower conductivity. Also, the thickness of the separator is carefully optimized to balance safety, ionic conductivity and mechanical integrity, typically ranging from 10 to 20 μm . Its exact thickness depends on whether it is ceramic-coated and whether the coating is applied to one or both side(s).

Lithium-ion battery cells are available in different geometrical configurations, primarily categorized as prismatic, cylindrical and pouch cell as presented in Figure 9. These variations in cell design influence manufacturing processes, mechanical properties, energy density and integration efficiency within battery packs. [8] The internal structure of LIB cells, consisting of the electrode-separator assembly, varies in terms of size, stacking method and manufacturing techniques. Cylindrical and some of prismatic cells are produced using a high throughput winding mechanism, forming a jelly roll structure, whereas pouch cells and some of prismatic cells are typically manufactured through a layered stacking process. The hard cases of cylindrical cells are predominantly composed of Ni-containing stainless steel and the case of typical prismatic cells is composed of lightweight aluminum, chosen for its low cost, ease of fabrication and corrosion resistance. The rigid metal casing enhances the mechanical robustness of the cell, allowing it to withstand external shocks and vibration, making these formats preferable for applications where structural durability and long-term reliability are crucial.

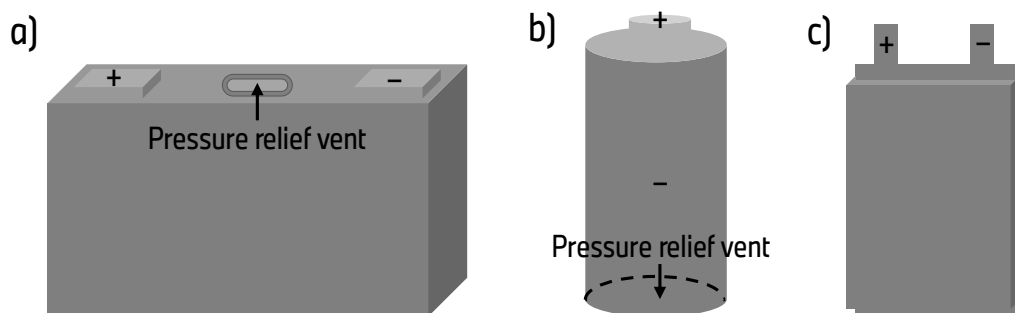






Figure 9: Three types of formats of automotive LIB cell: (a) prismatic, (b) cylindrical and (c) pouch cell. (The presented aspect ratio does not represent the real size of LIB cells.)

Among the three formats, cylindrical cells have been the most widely used (beyond BEV application) due to their established production infrastructure, high manufacturing efficiency and mechanical stability. Its long history in the market has led to continuous optimization of production equipment, ensuring cost-effectiveness and consistent quality. Prismatic cells, on the other hand, offer superior packaging efficiency, as their rectangular design allows for better space utilization within a battery module or pack. This makes them particularly advantageous for customized battery pack designs that require precise form factors. Pouch cells, in contrast, are the lightest and most space-efficient among the three formats, as they lack a rigid metal enclosure. This allows for higher packing efficiency, typically 90-95%, making them suitable for applications where energy density and weight reduction are priorities. However, the absence of a protective casing makes pouch cells more vulnerable to mechanical stress and external impact, increasing the risk of mechanical failure under harsh operating conditions. These characteristics depending on formats are listed in Table 9. [18]

Table 9. Categories of automotive LIB cells.

Shape	Prismatic		Cylindrical	Pouch
Electrode arrangement	Two Jelly rolls	Stacks	Jelly roll	Stacks
Cross-section view				
Typical housing	Metal (Aluminum)		Metal (Ni-containing stainless Steel)	Al-polymer laminated film
Potential of housing can	Positive		Negative	Neutral
Mechanical stress	High	Low	High	Very low
Battery pack in BEV	Module to Pack		Cell to Pack	Module to Pack

2.4.2 Safety Elements in an automotive prismatic LIB Cell

Ensuring the safety of LIBs is essential for alleviating the results of internal short circuits and other failure modes, mitigating thermal runaway. In commercial automotive prismatic LIB cells, safety elements must not only fit into very small spaces but also be relatively cheap. Beside tri-layer-separator, typically four critical safety design elements are found: 1) floating can, 2) safety vent, 3) fuse and 4) current interrupt device (CID). Table 10 presents an overview of those four safety elements, and each of them is discussed in detail in the following sections.

Table 10. Overview of four safety elements in an automotive prismatic LIB cell.

Safety elements	Type of function	Primary trigger/activation	Usage type
Floating can	Electrical	No activation needed	Passive/Continuous (non-triggered)
Safety Vent	Mechanical	Pressure	One-time use (non-resettable)
Fuse	Electrical	Heat from overcurrent	One-time use (non-resettable)
CID	Electrical with mechanical activation	Pressure	One-time use (non-resettable)

Floating can vs. can on potential

In prismatic lithium-ion battery cells, the metallic casing (cell can) serves as both a structural support and a potential electrical interface with the internal components. The way the cell can is electrically connected plays a significant role in determining safety performance and failure behavior. Typically, the cell can is made of aluminum (prismatic cell) or stainless steel (cylindrical cell) and surrounds the jelly roll or stacked electrodes inside the cell. For operational reasons, it is essential in prismatic LIB cells, to keep the aluminum casing at a potential above 1V versus the lithium reference (vs. Li/Li^+). This prevents any undesirable chemical reactions between the aluminum and the lithium ions in the electrolyte, which could otherwise lead to material degradation. To achieve the potential ($> 1\text{ V vs. Li/Li}^+$), manufacturers often apply a “can on potential” design, where the metal can is electrically connected to the positive terminal of the cell. While this method effectively addresses the issue of can potential, it introduces another risk. If a conductive particle happens to bridge the space between the can and the outermost anode layer, it could result in an internal short circuit (ISC). In this configuration, the low resistance of the short circuit path would allow a large ISC current to flow, increasing the likelihood of catastrophic failure.

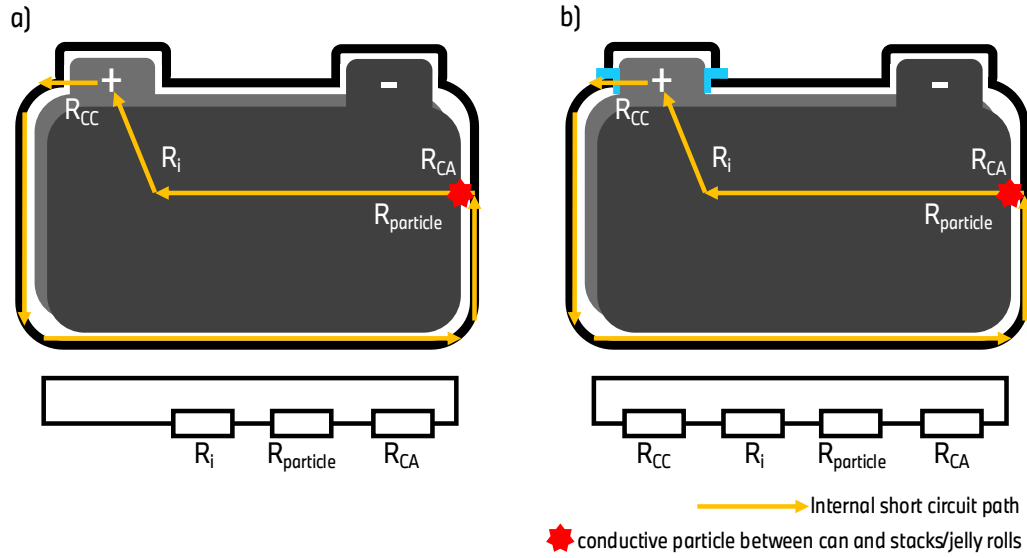


Figure 10. Two types of the connection between can and positive terminal: (a) can on potential and (b) floating can.

An alternative approach is the “floating can” design (see in Figure 10 (b)), where the metal casing is electrically isolated from the positive terminal by a high-resistance connection, typically exceeding 1 kΩ. By increasing the resistance in the short circuit path, this design significantly limits ISC currents, thereby enhancing overall cell safety and reducing the risk of severe ISCs.

Assumed ISC is induced between can and outermost anode by an electrically conductive material, the resistance in this ISC current path is defined by four key resistances.

- The inner resistance of the cell, R_i
- The resistance between can and anode, R_{CA}
- The resistance of the inserted particle, $R_{particle}$
- The resistance between can and cathode, R_{CC} .

For can on potential cells, the R_{CC} is negligible, leading to a lower overall ISC resistance and increased vulnerability to high ISC current. In contrast, the floating can design includes additionally the aforementioned R_{CC} resistance typically bigger than 1 kΩ, which mitigates short circuit severity and enhances cell safety. Mathematically, the total ISC resistance can be approximated as (see in Figure 10):

$$R_{ISC, \text{ can on potential}} \approx R_i + R_{CA} + R_{particle} \quad (2.15)$$

$$R_{ISC, \text{ floating can}} \approx R_i + R_{CA} + R_{particle} + R_{CC}. \quad (2.16)$$

This distinction highlights the greater protection of floating can against ISC between cell can and the outermost anode. [19]

Safety Vents

Safety vents are an important safety feature incorporated into prismatic LIB cells. They are designed to open and release internal cell pressure, preventing an abnormal rupture of the cell can. [55] This pressure release mechanism works as follows: the major sources of gas formation include decomposition of SEI, reactions between the electrolyte and anode, thermal decomposition of cathode active material, electrolyte degradation and binder breakdown and secondary reactions among various decomposition byproducts. [99] As internal pressure within the cell increases due to ongoing reactions, a safety mechanism is activated: in one design, a spike punctures a plastic laminate membrane integrated within the vent; in another design, the vent contains predetermined

rupture points that fracture when a critical internal pressure threshold is exceeded. This allows the accumulated gases to safely escape from the cell, preventing thermal runaway or making the heat ejection direction predictable in case of thermal runaway. [53] However, this safety vent cannot eliminate hazards fully. For example, the jet ejected through vent during TR may still lead to thermal hazards and show potential for propagation. [78,100] Especially, unlike a cylindrical LIB cell, the surface ratio of vent to its can surface in a prismatic LIB cell is very small, so that thermal reaction inside the cell can go continuously even after venting and the material emission during TR is restricted. For example, the experimental study of Hoelle et al. [79] has revealed that the total emissions during venting can account for only up to 29 % of the cell's total mass, including gas, liquid and solid particle emissions in a module-like environment as found in EV battery pack with 24 mm distance between vent and cover of whole pack.

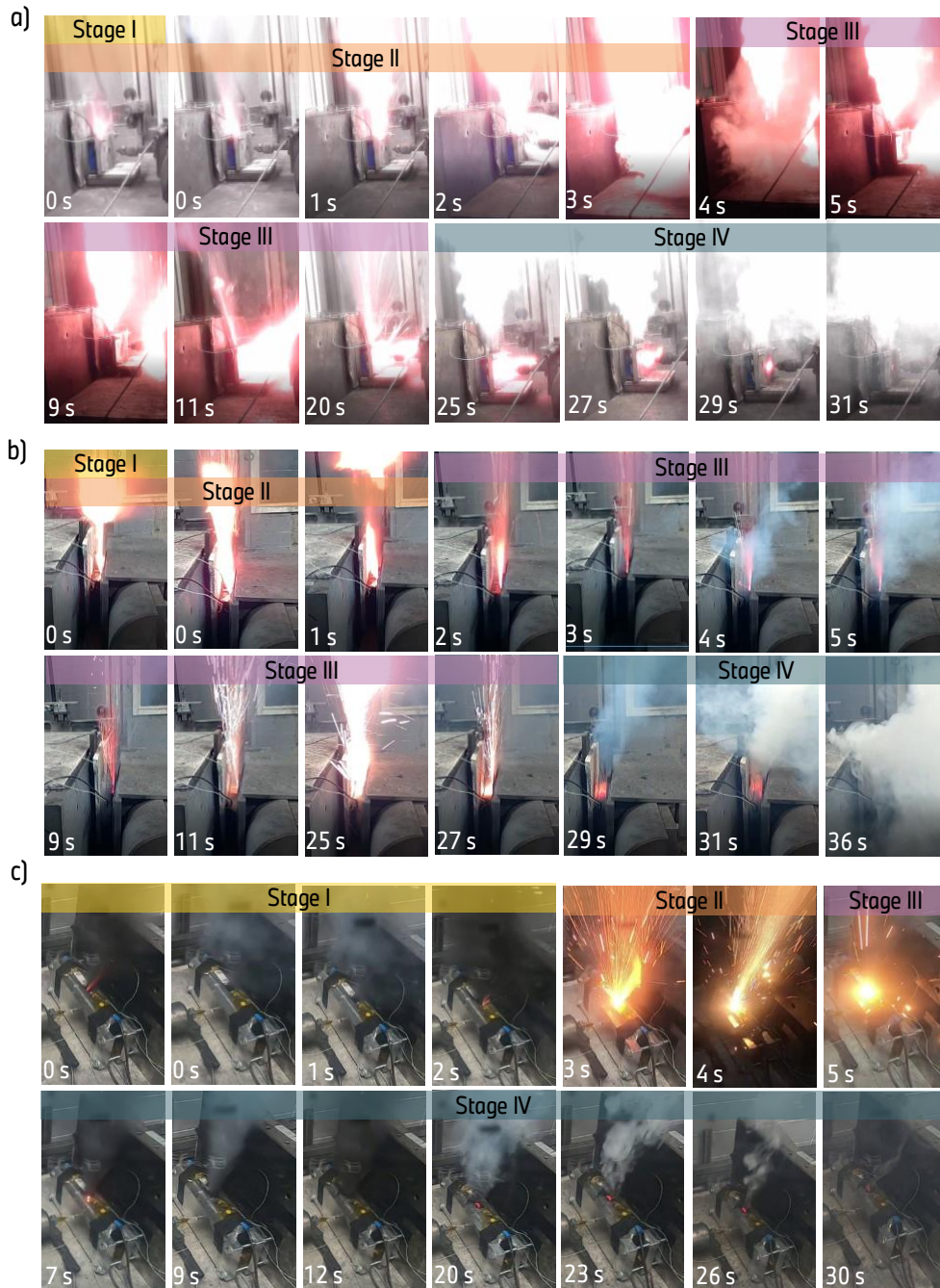


Figure 11. Gas- and particle release and jet from vent during thermal runaway induced (a) by nail penetration and (b) by an inserted particle between can and jelly roll in an automotive prismatic LIB cell with 58 Ah and (c) by nail penetration in a LIB cell with 34 Ah.

Figure 11 presents three different venting behaviors, two with same LIB cells with capacity of 58 Ah but by different trigger ((a) by nail penetration and (b) by an inserted particle) and the third one with a LIB cell with 34 Ah by nail penetration. Based on those, the process of venting can be categorized into four distinct stages [78]:

- **Stage I with Initial Vent Rupture:** when the safety vent opens, it releases a burst of gas and entrained particles. The pressure required to activate the vent depends on cell dimensions, vent geometry, and electrolyte content. Reported activation pressures exceed 10 bar for 21700 cylindrical cells [101] and are roughly 12–13 bar for 18650 cells [102].
- **Stage II with Rapid Gas Jet Formation:** the escaping gases from a concentrated high-speed jet, which often contain combustible components.
- **Stage III with Stable Jet Phase:** the venting process reaches a quasi-stable phase, during which jet can tilt, spark can burst and ignition may occur. Also, the duration varies strongly depending on the capacity of LIB cell and possibly on trigger methods.
- **Stage IV with Plume Formation:** The gas jet slows, transitioning into a diffusive plume with lower momentum, though secondary fires may still be possible if residual hot particles are present.

The duration of each stage can vary depending on multiple factors, including the LIB cell capacity, the trigger mechanism [26], but also the extent of the heat dissipation area. For instance, cell (a) and (b) exhibited significantly prolonged durations of stage II and III, for 20 and 27 seconds respectively, compared to the cell (c) with 3 seconds duration, which had a smaller capacity. Additionally, in the cell (a), which was initiated by nail penetration, heat dissipation occurred not only through the vent but also via the punctured site. In contrast, the cell (b) with same capacity, where a particle was introduced, was limited to dissipating thermal energy solely through the vent. As a result, stages II and III in cell (b) persisted longer than those in cell (a).

The behavior of venting without fire or flame, no rupture or no explosion is considered as the critical point, which is required at least by the automotive industry. Based on the EUCAR hazard levels presented in Table 8, such venting can be classified as level 3-4. [55] Therefore, the threshold of pressure to trigger venting plays a critical role and it varies depending on LIB cells.

Fuse and Current Interrupt Device (CID)

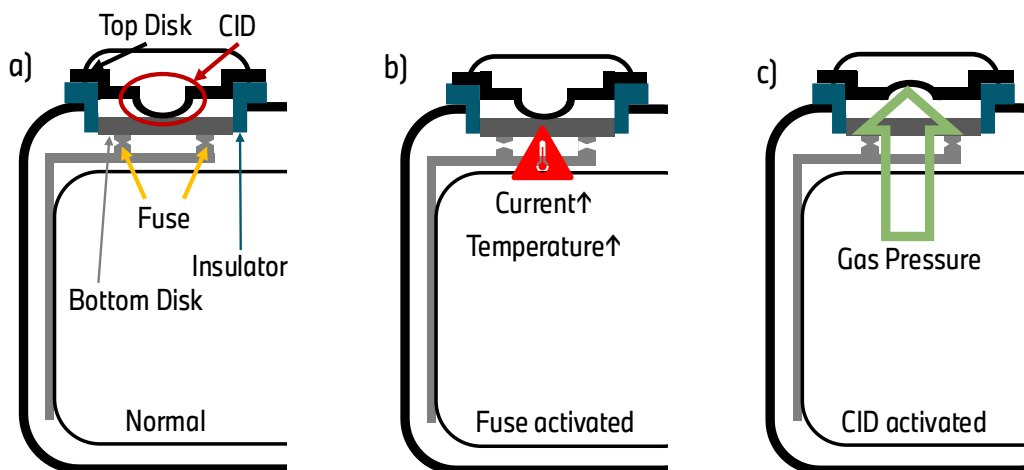


Figure 12. Terminal in a prismatic LIB cell with Fuse and CID, (a) in a normal state, (b) Fuse is activated by abnormal temperature and (c) CID is precipitated by abnormal pressure. (This presented figure does not represent every automotive prismatic LIB cell but only as an example how it can be implemented.)

Besides trilayer separator (shutdown separator), coating on separator, floating can and safety vent, automotive LIB cell are often equipped with fuse and current interruption device (CID) usually located in the cell cap terminal as safety device. [17,103] Those are one-shot (non-resettable) safety elements, that can be activated in an abnormal situation either with abnormally high current flow or with high temperature, stop the current flow in the LIB cell but the cell cannot be used again. Fuse is the most common current limiter, a thin plate or wire of fusible alloy with certain resistance and thermal properties that allow it to melt at a pre-set current or temperature within seconds and offer advantages like simple construction and low cost. The fuse for automotive LIB cell is typically set to be actuated at 30-50 °C above the maximum operating temperature. [53] Similar to fuse, CIDs shut off the battery circuit but not by temperature but by increasing pressure. When undesirable internal pressure builds up due to issues like overheating or short circuits, CID is activated and is commonly used in prismatic and cylindrical LIBs. [92,104,105]

The design and implementation of safety elements in prismatic LIBs are critical for minimizing the risk of internal short circuits and thermal runaway. While floating can be permanently used as precaution to improve the tolerance against ISC between cell can and the outermost anode, vent, fuse and CID are activated in an abnormal condition to mitigate TR or minimize hazards, and the triggered cell cannot be used anymore and should be replaced. A properly engineered LIB cell with such various safety elements is essential to control gas release and prevent catastrophic cell failure or propagation.

2.4.3 Lithium-Ion Batteries in BEV

For automotive prismatic applications, LIBs are interconnected in various configurations and integrated with control and safety circuitry to form battery modules. These modules are then assembled with additional control electronics, a battery thermal management system, and power electronic to create a complete battery pack. [12] Figure 13 presents how prismatic cells build battery module, pack and battery system in a BEV.

- **A Cell:** as the basic electrochemical unit, which is composed of at least one cathode and one anode with other necessary electrochemical and structural components [76], a lithium-ion cell provides a source of electrical energy by direct conversion of chemical energy.
- **A Module:** as a unit assembled from multiple cells connected either in parallel or series, it provides higher voltage and capacity. It is a component in the battery system, usually consisting of several cells, connectors, a battery management system (BMS), and casing.
- **A Pack:** a series of individual modules and protection systems organized in a shape that will be installed in a vehicle. A battery pack is an integral unit assembled from multiple battery modules. It is used to store and provide electrical energy. It is a higher-level component in the battery system. When the BMS monitoring state of health (SOH) and state of charge (SOC) and thermal management system detecting heat sinks, fans, or other heating and cooling mechanisms jointly control or manage several modules, this unified whole is called a battery pack. By being equipped with a BMS, the battery pack can not only improve the safety of the battery but also proactively perform thermal management to respond to battery and environmental temperature changes, improving the efficient operating range of lithium batteries.

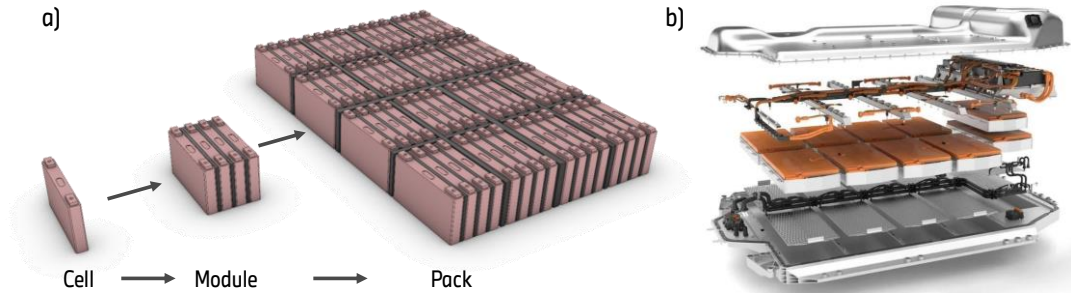


Figure 13. Definition of cell, module and pack (a) schematic example of cell building module and pack of automotive prismatic LIBs and (b) battery pack of BMW i3 models [106].

The number of LIB cells in module and pack can vary depending on BEV and few examples are listed in Table 11.

Table 11. Energy density and number of modules and cells [107,108] and calculated chance of failure depending on BEV.

Vehicle	energy density of pack [Wh/L]	Number of modules	Number of cells per pack	One failure is expected for every
BMW i3	-	8	96	104,200 vehicles
Renault Zoe	567	12	192	52,000 vehicles
Nissan Leaf	445	24	192	52,000 vehicles
Tesla Model 3	690	4	2976	3,400 vehicles
Peugeot 208	538	18	216	46,000 vehicles
BYD Han	335	Cell to Pack	178	56,000 vehicles

As discussed in Section 2.3, a catastrophic fire incident of BEV is not common and BEVs demonstrate high statistical reliability. But the expected failure rate can be estimated, as seen in Table 11, based on a LIB cell failure rate of approximately 0.1 ppm [85], primarily attributed to manufacturing defects rather than aging in the field. These failures are considered anomalies rather than indicative of a systemic reliability issue. However, given the extensive global deployment of billions of cells, failures remain an inherent possibility. For instance, one failure is theoretically expected for approximately every 3,400th Tesla Model 3.

Battery Thermal Management System (BTMS) and Cooling Method

The thermal challenges facing LIBs arise from their temperature-dependent performance. The optimal operating temperature range is between 15 °C and 35 °C. Deviating from this range will directly impact the overall performance and can result in irreversible changes to the LIB. Both low and high temperatures can have detrimental effects. Low-temperature operation leads to reduced ionic conductivity, increased charge-transfer resistance, and lithium plating on the carbon-based anode. Conversely, high temperatures accelerate thermal aging and shorten the calendar life of the LIB. Furthermore, high temperatures can also cause exothermic side reactions, generating even larger amounts of heat and resulting in thermal runaway. In the worst-case scenario, the LIB cells may undergo self-heating and thermal runaway, ultimately leading to catastrophic failure such as propagation in modules or pack. Consequently, for large-scale applications that require thousands of battery cells to constitute battery packs, such as in electric vehicles (BEV), a battery thermal management system (BTMS) becomes indispensable.

BTMS can monitor temperature, cell voltage and estimate the battery's state of health (SOH) during its lifespan. From a temperature control perspective, the BTMS must provide heating at low temperatures and cooling at high temperatures to ensure the battery operates within the optimal temperature range. The well-known techniques for the temperature regulation include:

- Air-based cooling/heating ventilation,
- Liquid-based cooling/heating,
- Phase change material (PCM)-based cooling/heating,
- Heat pipe-based cooling/heating. [109]

In the sense of safety, the cooling system can be regarded more essential. The simplest method of cooling is by air and using natural convection to dissipate heat from the battery cells into the surrounding environment. However, sudden temperature rises in the battery pack require very large volumes of air. Consequently, liquid cooling that is more efficient than air cooling should be applied in BEV battery pack. To optimize the cooling efficiency, cooling plates between batteries, cooling flow channels and tubes should be introduced. [17]

3 Experimental Methods

This chapter provides an overview on the experimental techniques used to investigate the thermal and thermodynamic characteristics of cathode and safety properties of LIB cells. The following characterization methods were employed: differential scanning calorimeter (DSC), thermogravimetric analysis (TGA), high temperature drop solution calorimeter, accelerating rate calorimeter (ARC), nail/needle penetration test, inductively coupled plasma-optical emission spectroscopy (ICP-OES) and computed Tomography (CT). Each technique was tailored to specific investigative goals. Detailed parameter settings and variations especially for nail/needle penetration are further discussed in Chapters 5-7, if there is variation.

3.1 Thermal and Thermodynamic Study of Cathode

To assess the role of cathode thermal and thermodynamic stability in the overall safety of LIB cells, cathode active materials were investigated using DSC, TGA and high temperature drop solution calorimetry.

3.1.1 Differential Scanning Calorimeter (DSC)

Differential scanning calorimetry is a sensitive thermodynamic analysis method used to study the reaction kinetics and to quantify the intrinsic thermal properties of samples such as heat capacities and enthalpies. The commonly used heat flux DSC with the construction demonstrated in Figure 14 is the heat-exchanging calorimeter, where heat flow rate, Φ is measured through a defined thermal resistance path between the sample and the environment. The primary measurement signal is the temperature difference ($\Delta T = T_S - T_R$), which is directly proportional to the heat flow rate. The difference between the heat flow rate into a sample pan (Φ_{FS}) and that into a reference pan (Φ_{FR}) is determined as a function of temperature and/or time. During such measurement, the sample and reference are subjected to the same controlled temperature program and a specified atmosphere. [110]

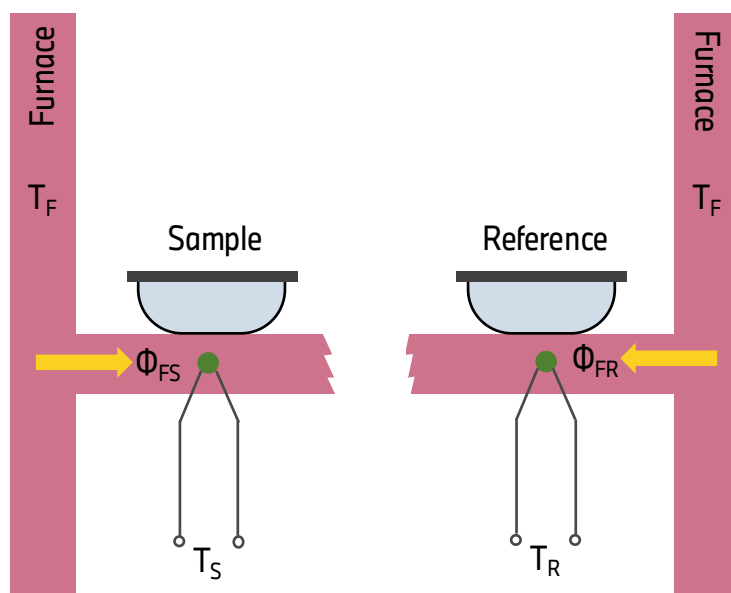


Figure 14. Scheme of heat flux DSC, reproduced from literature [110].

When the sample undergoes a phase transition or a reaction (e.g., melting, crystallization, decomposition) in a heat flux DSC, it absorbs or releases heat, leading to a temperature difference (ΔT) between the sample and reference. This temperature difference is measured using thermocouples and recorded as an exothermic (heat release) or endothermic (heat absorption) peak. The marked area in the DSC curve (see Figure 16 (a)) corresponds to enthalpy change (ΔH), which quantifies the heat effects, providing valuable insights in material stability. [111,112]

In this study, a Netzsch DSC 204 F1 Phoenix (heat-flux type) was employed. As the conventional DSC method, both the reference and sample crucible were subjected to identical heating conditions in the same furnace, allowing for precise measurement of heat flow rate or temperature difference as a function of temperature or time in a thermogram. The primary aim of the DSC experiments in this work is to evaluate the thermal stability of harvested, fully charged cathode materials (NMC and NCA), particularly in the presence of electrolyte. The following key parameters were derived in this work: the onset temperature of reaction, T_{onset} and the degree of reaction, α_r , which will be further discussed in Chapter 7. The DSC measurement and evaluation in this study are performed as following.

Measurement Procedure

- 1) **Baseline Calibration:** an empty pan run was conducted to correct for system asymmetries and thermal inertia. This zeroline was loaded as a reference for each sample measurement to calibrate the baseline.
- 2) **Temperature Calibration:** although the primary objective of DSC measurements in this work was qualitative comparison of the thermal stability across different cathode active materials, temperature calibration was still carried out. This was essential to ensure that the 'indicated' temperatures recorded by the instrument corresponded accurately to the 'true' sample temperatures. Discrepancies between indicated and actual temperatures may arise due to variations in heat transfer mechanisms (conduction, convection, radiation), which are influenced by factors such as furnace geometry and heating rate. In accordance with literature guidelines [113], calibration should be performed using at least two standard reference materials within the relevant temperature range, which lies in this study from 50 to 350 °C. In this work, four reference materials with well-defined melting points were selected: Indium ($T_m = 156.4$ °C), Tin ($T_m = 231.928$ °C) and Bismuth ($T_m = 271.4$ °C), whose reactions lie in the relevant temperature window, and Zinc ($T_m = 419.5$ °C) [114]. The calibration process proceeded as follows:

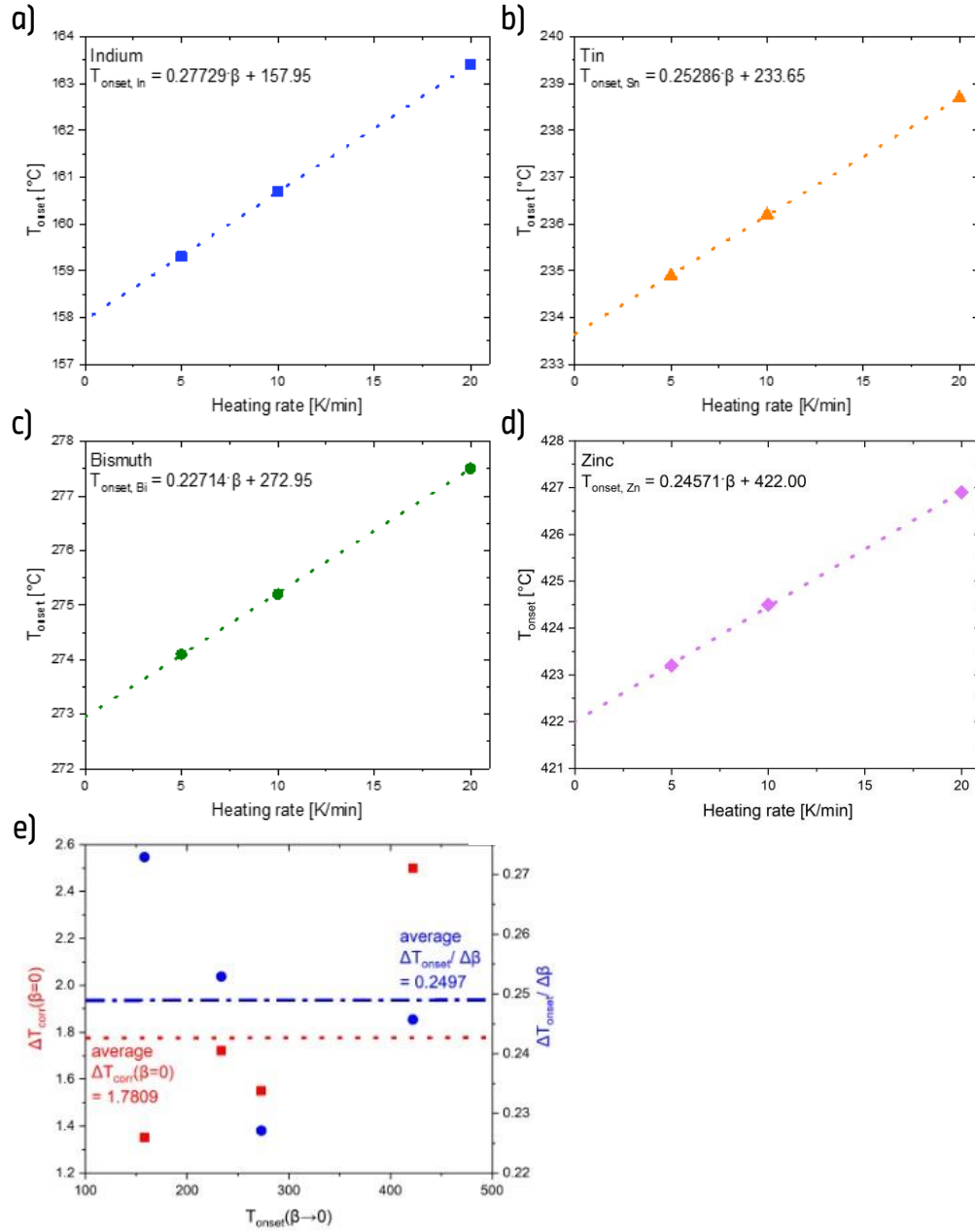


Figure 15. Onset temperature, T_{onset} plotted against heat rate, β of four references (a) Indium, (b) Tin, (c) Bismuth and (d) Zinc and (e) the difference ($\Delta T_{\text{corr}}(\beta=0)$) between literature onset temperature, $T_{\text{lit, onset}}$ and the extrapolated onset temperature, $T_{\text{onset}}(\beta \rightarrow 0)$ and $\Delta T_{\text{onset}}/\Delta\beta$ as function of $T_{\text{onset}}(\beta \rightarrow 0)$.

- The onset temperature (T_{onset}) of the four reference materials were measured at three different heating rates ($\beta = 5, 10$ and 20 K/min).
- T_{onset} was plotted as a function of the heating rate for each reference (see Figure 15 (a)–(d)), and the extrapolated value at zero heating rate, $T_{\text{onset}}(\beta \rightarrow 0)$ was determined.
- The differences $\Delta T_{\text{corr}}(\beta=0)$ between the literature onset temperature ($T_{\text{lit, onset}}$) and $T_{\text{onset}}(\beta \rightarrow 0)$ were calculated as shown in Figure 15 (e). The average difference was found to be 1.7809 °C, indicated by a red dotted line.
- The rate-dependent shift in onset temperature ($\Delta T_{\text{onset}}/\Delta\beta$) was calculated from the slope of each T_{onset} vs. β graph (see Figure 15 (a)–(d)) and averaged across the four references, yielding a value of 0.2497 , indicated by a blue dash line in Figure 15 (e).

- v. The temperature correction function based on heating rate, $\Delta T_{\text{corr}}(\beta)$ was determined as:

$$\Delta T_{\text{corr}}(\beta) = \Delta T_{\text{corr}}(\beta=0) - \beta \cdot \Delta T_{\text{onset}} / \Delta \beta = 1.78 - 0.25 \cdot \beta \quad (3.1)$$

- vi. The corrected 'true' onset temperature (T_{true}) was then calculated as:

$$T_{\text{true}} = T_{\text{onset}} + \Delta T_{\text{corr}}(\beta) = T_{\text{true}} + 1.78 - 0.25 \cdot \beta \quad (3.2)$$

- 3) **Sample Preparation:** positive electrodes were harvested from commercial automotive prismatic LIB cells at 100 % state of charge under controlled conditions in an argon-filled glove box (H_2O and $\text{O}_2 < 0.5$ ppm). The electrodes, double side coated with active material on an aluminum (Al) current collector, were punched into discs of 6 mm diameter. Aluminum was considered thermally inactive under the applied DSC conditions. The punched samples were chosen to ensure good contact with the crucible bottom surface. Each sample was sealed in a 27 μL high-pressure CrNi steel crucible equipped with a gold-plated copper seal, capable of withstanding pressures up to 100 bar. This was done to:

- reproduce the sealed, airtight conditions of an actual LIB cell
- prevent exposure of the cathode active material to ambient air.

The electrode was not rinsed, intentionally retaining the electrolyte to allow for thermal stability evaluation under realistic conditions same as in LIB cell. All samples were weighted in the crucible using a microbalance. The sample mass (positive electrode + electrolyte – Al current collector) was calculated by subtracting the tare weight of each empty crucible and the average weight of an Al current collector disc ($\varnothing = 6$ mm) from the crucible with each sample. An identical empty crucible was used as the reference pan during DSC measurements.

- 4) **Sample Loading:** before loading the sample into the furnace, the reference pan to calibrate baseline from step 2) was removed and replaced with the prepared cathode sample. Both the sample and reference pans were sealed with identical steel lid and placed in the DSC furnace chamber.
- 5) **Temperature Program:** the thermal program was configured with the temperature range and heating/cooling rate for the measurement. In this study, samples were heated from 30 °C to 350 °C at a rate of 5 K/min under an argon atmosphere (99.99 % purity) with a flow rate of 50 mL/min. This temperature window was selected based on the expected decomposition and transition events of cathode materials with electrolyte.
- 6) **Measurements:** to verify measurement repeatability, each cathode sample was tested twice. If the post-measurement mass loss exceeded 1 %, it was inferred that the crucible seal had failed, allowing electrolyte evaporation and compromising the sample environment. Only measurements exhibiting less than 1 % weight loss were accepted as valid for analysis; if either measurement exceeded the 1 % threshold, the experiment was repeated until two valid measurements were obtained.
- 7) **Data Analysis:** the heat flow difference between the sample and reference crucibles was recorded by the instrument and plotted as a thermogram. The resulting curves were analyzed using Proteus Netzsch software to identify thermal events. Endothermic and exothermic peaks were interpreted based on standard thermodynamic conventions, where heat released by the sample (exothermic) is plotted in the negative direction. The area under each peak represents the enthalpy change (ΔH) of the associated process, while the onset temperature (T_{onset}) indicates the beginning of the reaction. The analysis of each peak is described in more detail below.

Evaluation of DSC Thermograms

In theory, an ideal DSC response from a sample with negligible thermal resistance would be characterized by an infinitely sharp peak at a well-defined temperature. However, in practice, DSC thermograms are broadened due to finite heat transfer and can often be approximated by Gaussian bell-shaped curve as demonstrated in Figure 16 (a) [114].

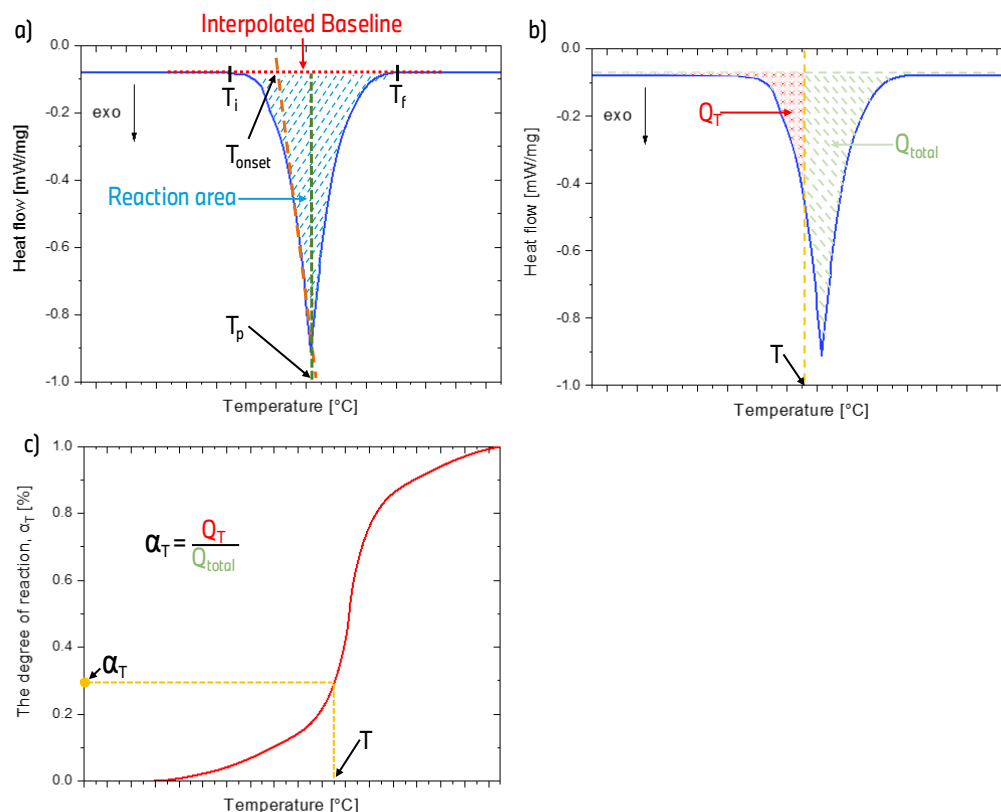


Figure 16. Thermogram (a) definition of interpolated baseline, reaction area, T_i , T_f , T_{onset} and T_p , (b) definition of Q_T and Q_{total} to define the degree of reaction and (c) profile of the degree of reaction, α_T .

As illustrated in Figure 16, the following thermal parameters were extracted in this work:

- **Initial Peak Temperature (T_i):** it is the point at which the curve deviates from the baseline, signaling the start of a thermal event.
- **Extrapolated Peak Onset Temperature (T_{onset}):** it is determined by extending a fitted tangent along the steepest slope of the peak (see the orange dashed line in Figure 16 (a) to its intersection with the baseline. The fitted-line method was adopted in the study due to its high reproducibility compared to inflectional tangents.
- **Peak Maximum Temperature (T_p):** it is designated as the temperature at which the difference between the heat flow curve and the baseline reaches its maximum. In practice, T_p is not necessarily the absolute maximum of the curve, if the baseline is increasing or decreasing.
- **Final Peak Temperature (T_f):** it is determined as the temperature at which the heat flow returns to the baseline, marking the end of the reaction.
- **Interpolated Baseline:** it is the straight linear line connecting the pre- and post-peak segments of the heat flow curve, assuming no heat exchange occurred during the transition. Although

step changes in heat capacity can distort the baseline, the linear approximation was selected for its reproducibility [115].

- **Peak Shape:** exothermic events appear as negative (downward) peaks in the thermogram, while endothermic events are demonstrated as positive (upward) by international convention. In this work, the exothermic peaks were plotted in negative direction same as international convention. Each peak begins at T_i , ascends/descends to the peak maximum/minimum, T_p and merges into the baseline again at T_f .
- **Integrated Peak Area:** it represents the total thermal energy released or absorbed during the event. Automatic integration with manual definition of T_i and T_f introduces some subjectivity, depending on the temperature range selected.
- **Degree of Reaction (α_T):** it is defined as the ratio of partial heat (Q_T) released up to temperature, T to the total heat released during the reaction (Q_{total}), as presented Figure 16 (b) and (c), respectively.

$$\alpha_T = \frac{Q_T}{Q_{total}} \quad (3.3)$$

This degree of reaction in this work was used exclusively for the comparative study, as the reactions studied were complex and not elementary. The initial and final states of the system were not precisely known. In this work, the cathode reaction is considered as a combined process involving the electrode, electrolyte, and various additives. Such a holistic perspective is essential to realistically assess the thermal behavior of commercial LIB cells. [32,115] The results of the DSC measurements are presented and discussed in Chapter 7.

3.1.2 Thermogravimetric Analysis (TGA)

Thermogravimetric Analysis (TGA) is also a widely employed analytical technique for studying the thermal decomposition of materials. One of the key advantages of TGA is to provide direct information regarding changes in sample mass as a function of temperature and time, thereby revealing insights into processes such as decomposition, volatilization, or desorption. [111] A TGA consists of a precise microbalance to measure mass loss, a furnace for heating the sample, a temperature controller for setting thermal programs (heating, cooling, isothermal) and a purge gas system to create specific atmosphere (inert, oxidizing or reducing). TGA can optionally be coupled with gas analysis techniques. [116]

However, TGA cannot detect phase transitions (like melting) without a mass change, therefore, TGA can be integrated with differential scanning calorimetry (DSC) to comprehensively study the thermal behavior of materials. In general practice, TGA is often conducted prior to DSC measurement, since DSC assumes no significant mass loss or decomposition during the analysis. TGA results can indicate whether mass loss is expected and guide the appropriate selection of crucibles if sample integrity is to be preserved. [113]

In the present study, nonetheless, the DSC analysis was intentionally performed before TGA. This decision was based on previous literature findings [1,2], which suggested that mass loss would likely occur during DSC due to electrolyte-related reactions. Furthermore, due to the samples' high sensitivity to H_2O , and the fact that sealed crucibles cannot be used for mass change measurement, TGA was performed with great caution and served primarily as a supplementary method to support and complement the DSC results.

For TGA measurements in this work, a Netzsch STA 449 F1 Jupiter instrument was used. This instrument offers high-resolution thermogravimetric capabilities, with a digital resolution in the nanogram range (0.025 μg) and a total measurement capacity up to 5 grams.

Measurement Procedure

- 1) **Baseline Correction:** prior to analyzing any sample data, a baseline correction was performed. The shape and profile of the baseline are highly dependent on the heating rate and gas flow. Therefore, it was essential to establish a baseline under the same experimental conditions intended for the actual sample runs. This procedure ensured that the subsequent thermograms could be properly interpreted without interference from baseline drift or instrumental anomalies.
- 2) **Calibration:** no calibration of temperature or mass was performed, as the primary objective of the TGA measurements in this study was qualitative rather than quantitative. The focus was placed on evaluating the total mass loss of cathode samples across three predefined temperature intervals, rather than on determining precise onset temperatures. Consequently, absolute accuracy in temperature and mass readings was not essential. Instead, the TGA was employed as a comparative tool to investigate thermal behavior trends across different commercial automotive LIB cells under identical test conditions.
- 3) **Sample Preparation:** positive electrodes were harvested from the same commercial automotive LIB cells at SOC 100 % used in DSC experiments. All procedures were conducted within an argon-filled glove box (O_2 and $H_2O < 0.5$ ppm) to prevent any reactions with ambient air. Unlike the DSC samples, which were punched into discs, the electrodes for TGA were carefully scraped off from the current collector using a ceramic scalpel. This step had to be carried out carefully to avoid damaging the aluminum (Al) current collector, as precise knowledge of the active material mass is critical for TGA analysis. Approximately 10 mg of unwashed cathode scrapings (including the electrolyte and carbon black) were collected and placed into a 27 μ L stainless steel crucible. The crucible was sealed with a gold-plated copper lid containing a small central hole, allowing gaseous species to escape during measurement. Two identical samples were prepared per cell inside the glove box.
- 4) **Sample Loading:** prior to measurement, the reference crucible from step 1) was removed and replaced with the prepared sample crucible. Both sample and reference pans were covered by identical steel lid and placed in the furnace of the DSC apparatus.
- 5) **Temperature Program:** the temperature program for TGA analysis was divided into three distinct heating segments, separated by 15-minute isothermal phases. These divisions allowed for better resolution of overlapping thermal events and aided in identifying mass loss at each reaction stage. The heating segments were as follows:
 - 35 to 150 °C at 10 K/min: in this temperature range, the evaporation of the electrolyte was expected to occur.
 - 150 to 300 °C at 5 K/min: this region corresponds to the expected onset of thermal runaway of a LIB cell, driven by exothermic decomposition reactions of the cathode material, as previously identified by DSC measurements.
 - 300 to 500 °C at 10 K/min: this range was included to capture any additional decomposition or secondary reactions that may occur at elevated temperatures.

Between each of these steps, a 15-minute isothermal hold was introduced to isolate thermal events. After the final segment, the furnace was cooled at a rate of 20 K/min. The chosen heat rate of 10 K/min was intended to mimic the rapid heat release associated with internal short circuit events in LIB cells, while maintaining consistency with the DSC heating rate (5 K/min) within the critical 150 - 350 °C window, where decomposition reaction of cathode active material was detected. This temperature profile is demonstrated with blue dashed line in Figure 17.

- 6) **Measurements:** each TGA sample was transported individually from the glove box to the instrument to minimize environmental exposure. Measurements were initiated within one hour of sample removal from the inert atmosphere to limit electrolyte evaporation and degradation.

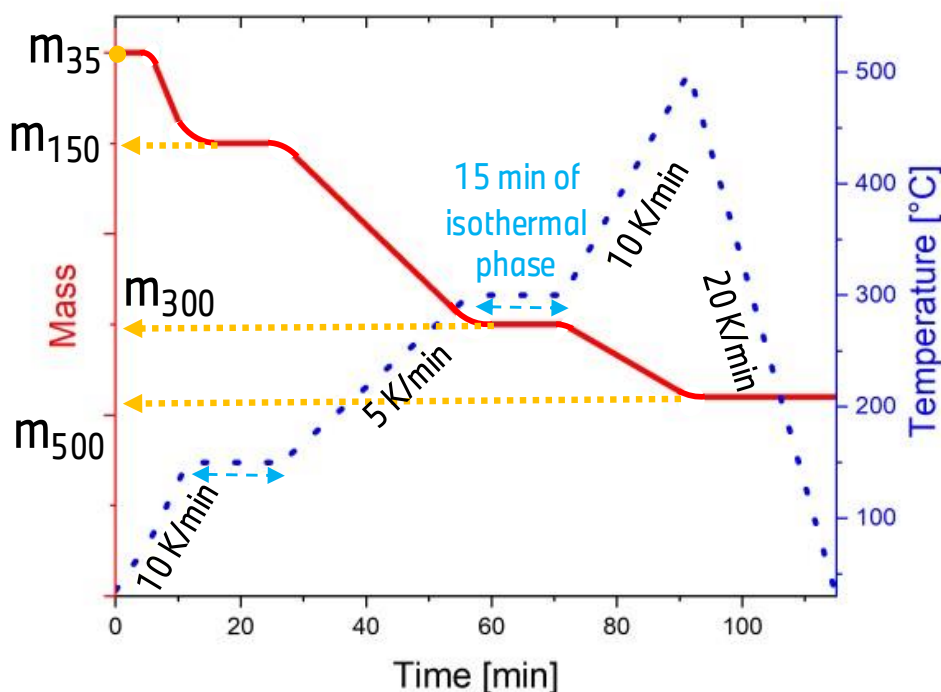


Figure 17. Schematic TGA trace, the setup of temperature profile with blue dashed line and the corresponding mass change with red line as a function of time.

- 7) **Data Analysis:** in contrast to conventional TGA analysis, which often focus on determining a single onset temperature of degradation, this study emphasized the mass loss within each of the three predefined temperature segments: $m_{35} - m_{150}$ in 35-150 °C, $m_{150} - m_{300}$ in 150-300 °C and $m_{300} - m_{500}$ in 300-500 °C. This segmentation was motivated by the complex, multi-step nature of thermal reactions in cathode materials in the presence of electrolyte. Rather than attempting to identify a single onset point for thermal runaway, it was more informative in this work to quantify mass changes in specific temperature intervals. For mass loss determination, the tangential method was applied using Proteus Netzsch software (see Figure 17). This involved measuring the vertical distance between tangents drawn to the TG curve before and after a distinct change in slope, thereby yielding accurate mass loss values across each temperature segment.

3.1.3 High Temperature Drop Solution Calorimeter (Alexsys-1000 and MHTC)

High temperature drop solution calorimetry employing molten oxide solvents has been established as a reliable method for determining the enthalpies of formation of a diverse range of compounds. The application of the high temperature oxide melt solution calorimeter dates back to 1964, originating as an adaptation of the Tian-Calvet calorimeter equipped with two identical calorimetric cells [117], and subsequently modified by Kleppa to enable high temperature operation. [7] Following modifications by Kleppa, subsequent enhancements were introduced by Navrotsky [118,119], expanding the range of materials amenable to high temperature solution calorimetry while preserving the fundamental operational principles.

As introduced in Section 2.2.3, high temperature drop solution calorimeter has been employed to investigate the enthalpy of formation and thermodynamic characters of cathode active materials. Previous studies [7–9] have predominantly utilized the Alexsys-1000 developed by Navrotsky [7,118,119] and manufactured by Setaram, due to its high precision, achieved by maintaining a highly stable baseline [120].

In this study, however, the potential for conducting thermodynamic measurements using an alternative instrument — the multi high temperature calorimeter (MHTC), also manufactured by Setaram — is explored as the primarily goal. The MHTC offers a more cost-effective and practical alternative to the Alexsys-1000. Before discussing the MHTC system, the working principles and structural design of Alexsys-1000 will be presented as the reference methodology.

Alexsys-1000 as the Reference Method

Figure 18 presents the internal architecture of the commercially available Setaram Alexsys-1000 calorimeter, which operates in an isoperibolic mode; the jacket temperature is held constant, whereas the sample temperature evolves as a function of time depending on the heat flux transmitted through a defined thermal resistance between the jacket- and sample-domains. [121]

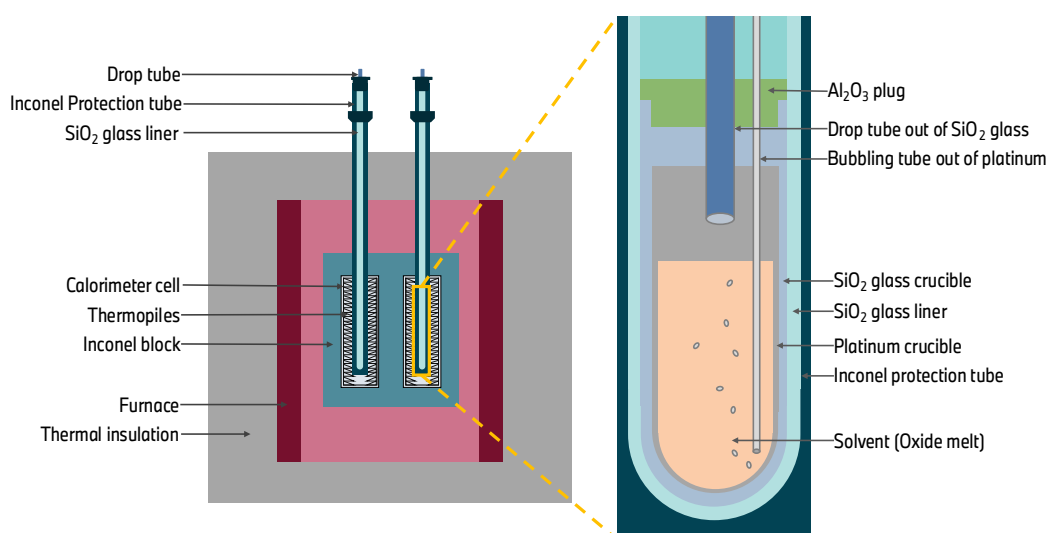


Figure 18. Schematic structure of high temperature drop solution calorimeter (Alexsys-1000 from Setaram) and drop solution calorimeter with a molten oxide solvent, reproduced from literatures [7,118,120,122].

The high temperature solution calorimeter (Alexsys-1000) consists of following four primary components:

- 1) **Insulating Casing:** the outer case and insulation regulate heat flow within the calorimeter, ensuring thermal stability
- 2) **Inconel Block:** acts as a “thermal ballast”, stabilizing the system’s temperature
- 3) **Three Furnace Elements:** the primary cylindrical electric furnace encircles the Inconel block, serving as the main heat source. Two additional “pancake” heating elements at the cylinder’s ends help maintain temperature uniformity and minimize the effect of mass movement during solution calorimetry experiments.
- 4) **Two Calorimeter Cells:** two identical calorimeter cells, each surrounded by a thermopile comprising 128 thermocouples, detect temperature changes resulting from solution experiments. These thermocouples are strategically wired to capture heat flow in all directions [122]. Each calorimeter cell encompasses the following components:

- i. **Platinum Crucible:** a Pt-crucible with 11 cm in length and 1.5 cm in diameter is nested within a silica crucible possibly with silica wool as a cushion and the Pt-crucible contains the solution. [120]
- ii. **Silica Crucible:** holds the Pt-crucible with the solution and is enclosed within a silica tubing (liner), acting as an interface between the sample crucible and the protective tube.
- iii. **Silica Liner:** can be removed from Inconel protection for each set of experiments and inserted into it.
- iv. **Inconel Protection Tube:** separates the thermopiles from the glassware and provides additional protection against solvent leaks.
- v. **Drop Tube and Bubbling Tube:** a silica glass drop tube and a platinum bubbling tube are positioned above and within the molten solvent, respectively. The bubbling tube facilitates solution stirring, promoting sample dissolution and preventing local solvent saturation.

The Alexsys-1000 employs a Tian-Calvet configuration in which the two thermopiles are connected in series opposition. Its rotating sample-drop mechanism alternates the roles of the twin calorimetric cells, so that each cell functions as the measurement vessel in turn. This intrinsic symmetry suppresses baseline drift and thereby enhances the precision of the calorimetric data.

Sodium Molybdate as Solvent for Alexsys-1000 and MHTC

One of Navrotsky's key refinements in experimental methodology [118] was the solvent choices to accommodate a wider range of sample materials. Specifically, solvents such as lead borate ($2\text{PbO} \cdot \text{B}_2\text{O}_3$) and sodium molybdate ($3\text{Na}_2\text{O} \cdot 4\text{MoO}_3$) were introduced due to their thermodynamic stability, chemical inertness, and ability to dissolve a diverse array of oxide and non-oxide compounds [120]. The selection of an appropriate solvent is critical for achieving precise dissolution of oxides and other materials. For investigations into the formation enthalpies of cathode active materials, sodium molybdate ($3\text{Na}_2\text{O} \cdot 4\text{MoO}_3$) is employed as the solvent [7,120], functioning according to these following reactions:



In this system, two charged molybdate oxyanions (MoO_4^{2-} and $\text{Mo}_2\text{O}_7^{2-}$) maintain equilibrium, effectively buffering oxygen anions and facilitating sample dissolution within the molten solvent. The behavior of the dissolved species depends on the chemical nature of the sample (basic, acidic or transition metal oxides). They might react with oxygen anions to form complex anions or may undergo redox reactions. [7]

Implementation of MHTC

While the Alexsys offers exceptional measurement precision, it demands meticulous maintenance and involves significant acquisition and operating costs. In contrast, the MHTC provides a more accessible platform with simpler setup, although it lacks certain structural features of the Alexsys, which will be discussed in detail in this section (see Figure 19). In this work, both calorimeters were used to measure the same NMC materials, enabling a direct assessment of the MHTC's limitations and performance capabilities compared to Alexsys-1000. Prior to conducting any measurements, the MHTC system first had to be implemented in battery cell competence center (BCCC), BMW, Munich in Germany. The scope of this study therefore encompasses more than the enthalpy determinations alone; it also entails the complete implementation, calibration, and optimization of the MHTC apparatus and its operating parameters.

Before any optimization or measurement could be carried out using the MHTC system, several practical setup requirements had to be fulfilled to ensure stable and safe operation of the calorimeter.

- **Water Cooling System:** the MHTC requires an external cooling system to regulate thermal stability during operation. Specifically, the water pump must provide a minimum flow rate of 3 L/min at a differential pressure of approximately 3 bars. A fully operational cooling system is indicated when all ten green LEDs on the flow meter (on the surface of MHTC device) are lit, typically at a flow rate of 3.5 to 4 L/min. Additionally, downstream pressure regulation is advised to maintain consistent flow. This can be achieved either by adjusting the upstream pressure to achieve the desired flow or by incorporating a parallel bypass line, which is regulated via a valve. By partially closing the bypass valve, more flow is redirected through the calorimeter. In this work, a rotary vane pump (E2M1.5) was used to deliver the required water flow rate of 4 L/min to the MHTC system.
- **Gas Outlet:** although the sample sizes used in high temperature drop solution calorimetry are small, the evolution of flammable or toxic gases during testing cannot be completely ruled out. This is particularly relevant in this study, since analyzing cathode coatings whose chemical formulations are protected by patents and therefore not fully disclosed. To mitigate safety risks, the gas outlet located at the rear of the MHTC unit was connected to the central gas exhaust system of the facility, thereby ensuring safe disposal of any potentially hazardous emissions.
- **Argon (Ar) Atmosphere Control:** an inert argon atmosphere is essential to prevent unwanted reactions during measurement. The system was configured with two argon flow rates: a flushing flow of 50 mL/min to continuously purge the environment inside the calorimeter, and a bubbling flow of 5 mL/min. However, since the MHTC is not equipped with a bubbling tube (unlike the Alexsys), argon was used solely for flushing. This ensures that the internal crucible environment remains free of reactive gases.

Structure of MHTC

Figure 19 demonstrates the structure of MHTC compared side-by-side with that of Alexsys to provide a clear basis for identify the strengths or limitations of the MHTC over Alexsys-1000. The MHTC system is structurally distinct from the Alexsys-1000, and these differences significantly influence both the measurement baseline and overall precision. As described, the Alexsys-1000 is equipped with two calorimeter cells and those are used in an alternating sequence, where each serve as the sample vessel while the other remains idle. The symmetric and alternating design enables a highly stable baseline and ensures high precision in enthalpy measurements. In contrast, the MHTC contains only one calorimeter cell. In this system, the sample and reference crucibles are arranged vertically — one above the other — and differ in both material composition and physical dimension. Figure 19 (a)-(c) illustrates the configuration of MHTC. This vertical alignment introduces a potential asymmetry in heat flow and sensor response, which can affect baseline stability.

In this study, the sample crucible consisted of a Pt-crucible nested inside an Al_2O_3 crucible. This configuration was selected to protect the calorimeter from potential reactions between the molten solvent, $3\text{Na}_2\text{O} \cdot 4\text{MoO}_3$ and the Al_2O_3 crucible. Although sodium molybdate is known to be relatively inert toward Al_2O_3 and SiO_2 , precautionary shielding using Platin was deemed necessary.

For the reference crucible, three sizes of Al_2O_3 crucibles are available — empty, half-filled, and fully filled. Despite attempts to balance the mass between the sample and reference crucibles by choosing the most suitable dummy, even the fully filled Al_2O_3 reference (8.4006 g) remained significantly lighter than the sample assembly (9.8901 g of Al_2O_3 + 19.9954 g of Pt + 7 g of solution \approx 37 g). Therefore, a perfect balance between sample and reference masses could not be achieved, and the unbalanced mass inevitably introduced a degree of thermal asymmetry.

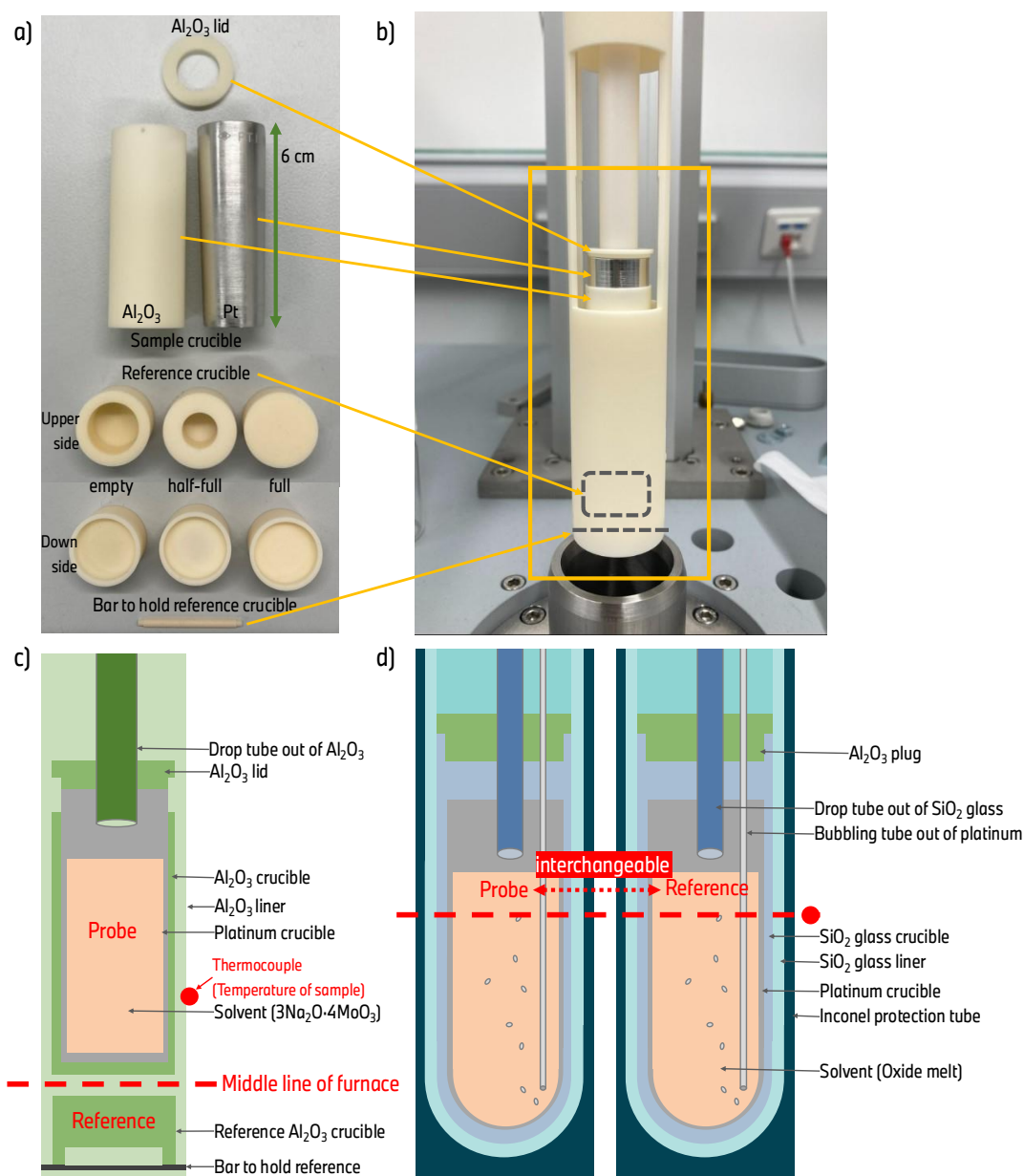


Figure 19. Structure and components of the MHTC: (a) components of lid, sample & reference crucible and bar, (b) the complete assembly of components in (a), (c) schematics of the assembly in MHTC, where the position of the middle line of furnace and thermoelement are adjustable and (d) schematics of the assembly in Alexsys-1000 as a comparison.

Another structural limitation of the MHTC is the absence of a bubbling tube. In the Alexsys-1000, argon bubbling is used to facilitate uniform and fast dissolution of samples in the molten solvent ($3\text{Na}_2\text{O} \cdot 4\text{MoO}_3$) and to prevent supersaturation or local inhomogeneity. In contrast, dissolution in the MHTC occurs solely via chemical diffusion, without the assistance of any physical stirring mechanism. Consequently, significantly longer intervals between consecutive drops were required in this work to ensure that each sample was fully dissolved before introducing the next one. This precaution was necessary to avoid any overlap or interference between successive dissolution events.

Furthermore, the number of thermocouples and the volume capacity for drops differ markedly between the two systems. The MHTC is equipped with 56 thermoelements, while Alexsys is composed of 128 thermoelements per cylindrical thermopile, which presumably results to different precision in results. Additionally, the internal volume of the Pt crucible used in the MHTC (6 cm long with diameter of 1.5 cm) is much smaller than the crucibles employed in the Alexsys system. In

practical terms, this means that only a limited quantity of solvent (7 g in this work) could be loaded into the MHTC crucible per measurement cycle to prevent supersaturation of solvent. By contrast, the Alexsys is equipped with a bigger Pt-crucible (11 cm long with diameter of 1.5 cm), allowing a larger amount of solvent (28 g) to be distributed between its two calorimeter cells. Moreover, due to its rotating-cell design, both cells in the Alexsys can be used for measurements, effectively doubling the usable solvent volume.

To systematically assess the performance limitations of the MHTC, identical NMC cathode materials had to be analyzed using both the MHTC and Alexsys-1000 systems, which will be presented in Chapter 4. This side-by-side comparison in structure prior to the measurement provide a clear basis for identifying the strengths and limitations of the MHTC in high-temperature enthalpy measurements.

Baseline-Optimization of MHTC

Due to the vertical arrangement of the sample and reference crucibles in the MHTC, unlike the symmetric dual-cell design of the Alexsys-1000, the signal obtained from the thermocouples is highly dependent on the vertical positioning — specifically, the height adjustment of the sensor assembly within the furnace. Improper height alignment can result in the thermoelements falling outside the homogeneous temperature zone of the furnace, leading to signal distortion or baseline drift. Therefore, precise adjustment of the vertical position of the crucibles and thermoelements is critical to ensure that the calorimetric signal reflects actual thermal events and not positional artifacts. Ideally, the distance between the sensor plane and the central axis of the furnace (middle line) should be minimized to ensure symmetry in heat detection (see in Figure 19 (c)). When this alignment is correctly set, the resulting heat flow (HF) signal is low, indicating minimal heat capacity difference between the sample and reference — an ideal condition for sensitive calorimetric detection. Conversely, if the height is poorly adjusted, the HF signal may exceed the amplifier's measurement range ($\pm 2000 \mu\text{V}$), rendering accurate measurements impossible.

In this work, several blank measurements were conducted during the setup phase to determine the optimal vertical positioning. By iteratively adjusting the height and reference crucible configuration, the baseline HF signal (around $-3400 \mu\text{V}$ before optimization) was successfully stabilized within the range of approximately $150\text{--}160 \mu\text{V}$.



Figure 20. Optimization of the height, (a) overview of MHTC, (b) the upper part of the calorimeter with a focus on the sensor area and (c) how the height of the drop sensor can be adjusted by altering the height of the red height indicator arrow.

The height of the sensor was adjusted to the lowest (the shortest red arrow in Figure 20 (c)) and the fully filled reference was applied through systematic adjustment. This set-up was consistently used throughout the study.

The adjusted height also impacts the positioning of the furnace's central temperature measurement zone relative to the actual sample location. It is likely that the sample is not positioned precisely at the furnace's central temperature probe. This discrepancy is evident in the measured sample

temperature, which was consistently higher (around 701 °C) than the nominal furnace temperature (around 676 °C).

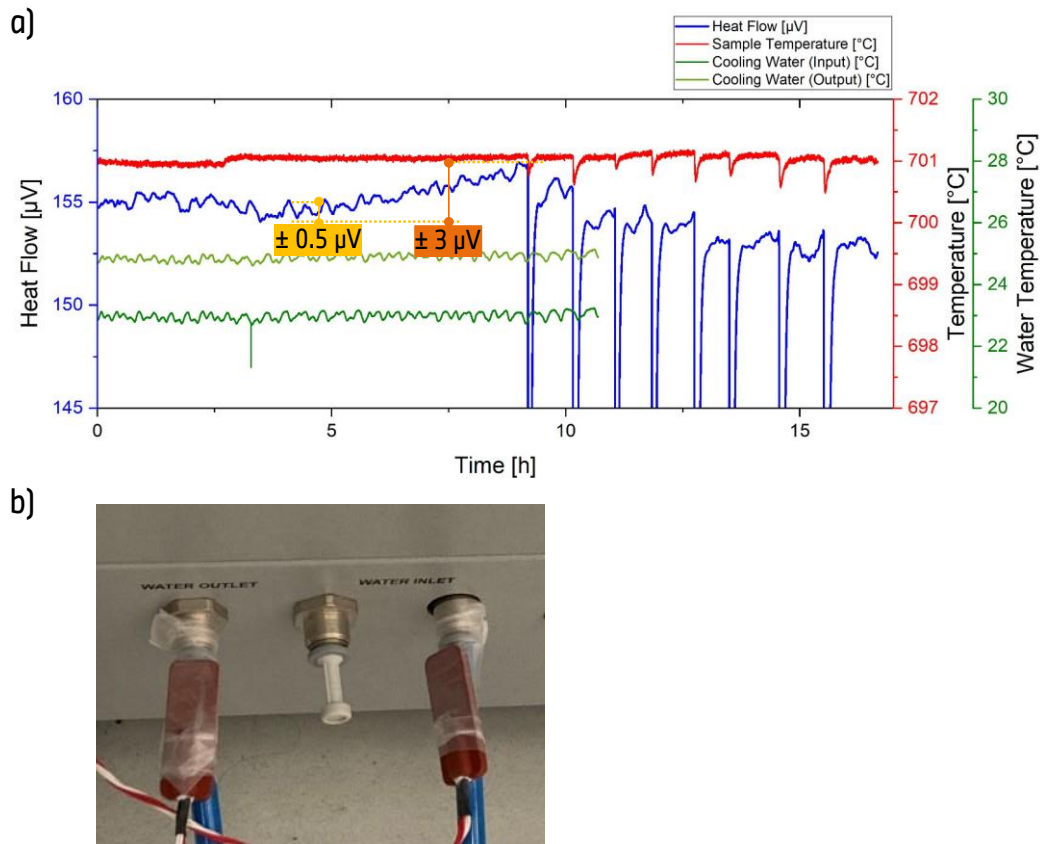


Figure 21. Investigating why the base line fluctuates: (a) base line during sapphire calibration with temperatures of sample and cooling water (input & output) and (b) measurement set-up of temperature of cooling water.

Although the baseline heat flow (HF) value was significantly improved following the optimization of sensor height and the appropriate selection of the reference crucible, a degree of fluctuation in the baseline persisted. To understand the source of residual baseline fluctuation, detailed analysis was conducted during sapphire calibration experiment. Figure 21 (a) from the second calibration set presents an enlarged view of the baseline behavior before and during sapphire drops. The baseline exhibited a repeating oscillation, which complicated the precise integration of each heat signal. This fluctuation — initially $\pm 10 \mu\text{V}$ — was gradually reduced to $\pm 0.5 \mu\text{V}$ (or up to $\pm 3 \mu\text{V}$ over the entire measurement duration) by optimizing three key parameters: 1) sensor height, 2) reference crucible selection and 3) the value of PIDU (Proportional-Integral-Derivate-Unit). While the improved baseline was suitable for most purposes, it still showed more fluctuation than the Alexsys-1000 system. To further investigate the origin of this instability, the temperature of the cooling water was monitored.

Figure 21 (b) presents measurement set-up of the inlet and outlet cooling water temperatures. As expected, the outlet temperature was around 2 $^{\circ}\text{C}$ higher than the inlet. More importantly, both showed a periodic fluctuation with a cycle of approximately 10 minutes — like the observed baseline drift in the calorimeter. This suggests that the baseline fluctuation in the MHTC was primarily influenced by slight variations in the temperature of the central cooling water supply. Since the cooling water for the MHTC originates from a centralized system, its temperature is influenced by external factors such as ambient weather and the number of devices drawing water upstream. However, the exact cause of the ca. 10-minute periodicity in water temperature remains unclear.

Energy Calibration using Sapphire

The drop sensor in the MHTC was used exclusively to determine the enthalpy of dissolution under isothermal conditions. While temperature calibration is theoretically possible, it was not performed in this work due to its limited benefit in isothermal applications. Temperature calibration would require a dynamic heating profile (ramp), which is incompatible with the isothermal drop method. Moreover, according to Setaram's guidelines, the correction of thermoelectric offsets through temperature calibration introduces its own errors and is not generally recommended for systems operating under constant temperature.

In contrast, sensitivity calibration is essential, as precise determination of enthalpy in high temperature drop solution calorimetry requires conversion of the raw heat flow signal [$\mu\text{V}\cdot\text{s}$ or $\text{V}\cdot\text{min}$] into energy units [J]. This necessitates a calibration step, wherein the sensitivity of the calorimeter is established using a standard material with a well-known heat capacity. In this work, sapphire (Al_2O_3) was selected as the calibration standard due to its stable thermal properties and widespread use in high temperature calorimetric calibration. The calibration factor [$\text{J}/\text{V}\cdot\text{min}$] was determined via a series of sapphire (Al_2O_3 rods from *Alfa Aesar* with the purity of 99.99 %) drop experiments under the same measurement conditions as used for the cathode material analysis. The calibration was carried out as below:

- 1) The Pt crucible was partially filled with silica wool, SiO_2 to approximately 50 % of its volume — comparable to the volume that would be occupied by the molten sodium molybdate ($3\text{Na}_2\text{O}\cdot 4\text{MoO}_3$) solvent during actual measurements. This served two purposes: i) to prevent the sapphire rod from rebounding upon impact with the bottom of the crucible, which could cause signal disturbances and ii) to maintain a consistent geometry and height for heat flow detection between calibration and measurement experiments.
- 2) The system was heated to 701 °C, the target isothermal temperature for both calibration and actual measurements. All other measurement parameters were kept constant during calibration, ensuring consistency with the conditions used in cathode enthalpy analysis, which will be discussed in the subsection of **Optimization of Parameters for Measurements**.
- 3) Sapphire rods with masses ranging from 30 to 100 mg were used for calibration. Although the purity of sapphire was not critical for this procedure — as long as no reactive impurities were present, samples were annealed at 900 °C for two hours at a heating rate of 5 °C/min prior to use. This annealing step ensured that any surface moisture or adsorbed species were removed, preventing interference with the heat signal. Each sapphire rod was weighed and dropped into the crucible at regular intervals of approximately one hour to ensure full equilibration of the system between drops. In the first calibration set, eight sapphires were dropped, and in the second, seven. Precise mass measurements were recorded for each drop to enable correlation with theoretical enthalpy values.
- 4) The enthalpy change for each sapphire drop, $\Delta H_{302.38 \rightarrow 975.13}$ (first set) and $\Delta H_{303.04 \rightarrow 975.13}$ (second set), was calculated using the specific heat capacity equation for Al_2O_3 (3.7), (3.8) and (3.9) [123]:

$$H_T - H_{273.15} = A \cdot T^{-2} + B \cdot T^{-1} + C \cdot \ln T + K + D \cdot T + E \cdot T^2 + F \cdot T^3 + G \cdot T^4 + H \cdot T^5 \text{ J/mol} \quad (3.7)$$

$$A = 6.6253\text{E}+07$$

$$E = -8.57516\text{E}-02$$

$$B = -4.54238\text{E}+06$$

$$F = +4.299063\text{E}-05$$

$$C = -5.475599\text{E}+04$$

$$G = -1.15192\text{E}-08$$

$$K = 2.5819702\text{E}+05$$

$$H = 1.26351\text{E}-12$$

$$D = 2.574076\text{E}+02$$

Using this, the enthalpy increment was calculated via:

$$\Delta H_{302.38 \rightarrow 975.13} = H_{975.13} - H_{273.15} - (H_{302.38} - H_{273.15}) \quad (3.8)$$

$$\Delta H_{303.04 \rightarrow 975.13} = H_{975.13} - H_{273.15} - (H_{303.04} - H_{273.15}) \quad (3.9)$$

The computed values were: $\Delta H_{302.38 \rightarrow 975.13} = 64.1696$ kJ/mol and $\Delta H_{303.04 \rightarrow 975.13} = 64.1496$ kJ/mol.

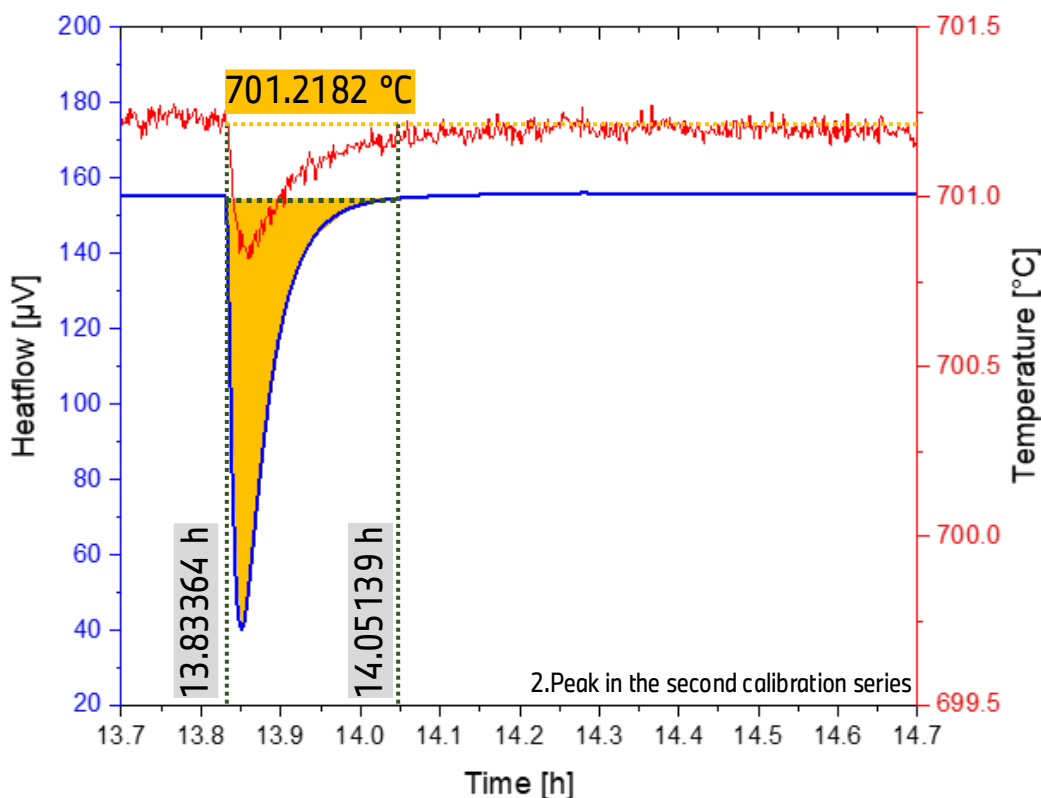


Figure 22. Illustration of peak integration window during a sapphire drop.

- 5) To determine the experimental sensitivity, each sapphire drop generated a distinct peak in the heat flow curve. The peak area was integrated to yield the signal in $\mu V \cdot s$. Figure 22 demonstrates how the starting and ending points of each peak were defined. The start point corresponds to the moment the sapphire enters the crucible at 701 °C, seen as an abrupt drop in heat flow. However, since the base line fluctuates at the degree of $\pm 0.5 - 3 \mu V$ (see Figure 21 (a)), the end point of the peak should be carefully selected. The endpoint was defined as the time at which the sample temperature returned to the initial value prior to the drop, confirming full thermal equilibration under isothermal conditions. For instance, in the example presented in Figure 22, the sample temperature was indicated as 701.2182 °C at the time of sapphire drop. The peak was integrated from the drop time (13.83364 h) until the sample temperature returned to the same temperature, 701.2182 °C (14.05139 h), yielding a peak area of 23,403 $\mu V \cdot s$. Regardless of the accuracy of the indicated temperature, this method allows for the identification of the thermal peak, potentially under near-isothermal conditions. From 13.83364 to 14.05139 h, the peak area can be determined as 23,403 $\mu V \cdot s$. From this method, all peaks are determined using Processing software and the defined peak areas are listed with corresponding weigh of sapphire and theoretical enthalpy increment in Table 12 for both calibration sets.

Table 12. Sapphire drop data: peak area [$\mu\text{V}\cdot\text{s}$] and theoretical enthalpy increment [J] depending on the weight of sapphire [mg] for each drop during calibrations.

Drop Number	Parameters	1. Calibration	2. Calibration
1	Sapphire [mg]	38.60	38.70
	Peak area [$\mu\text{V}\cdot\text{s}$]	13,894	12,389
	Theoretical enthalpy increment [J]	24.29	24.35
2	Sapphire [mg]	69.63	69.64
	Peak area [$\mu\text{V}\cdot\text{s}$]	25,462	23,403
	Theoretical enthalpy increment [J]	43.82	43.81
3	Sapphire [mg]	34.12	49.29
	Peak area [$\mu\text{V}\cdot\text{s}$]	11,523	14,551
	Theoretical enthalpy increment [J]	21.47	31.01
4	Sapphire [mg]	49.26	62.79
	Peak area [$\mu\text{V}\cdot\text{s}$]	17,942	21,027
	Theoretical enthalpy increment [J]	31.00	39.50
5	Sapphire [mg]	81.31	81.41
	Peak area [$\mu\text{V}\cdot\text{s}$]	28,413	25,183
	Theoretical enthalpy increment [J]	51.17	51.22
6	Sapphire [mg]	62.71	88.86
	Peak area [$\mu\text{V}\cdot\text{s}$]	21,002	29,521
	Theoretical enthalpy increment [J]	39.47	55.91
7	Sapphire [mg]	88.81	98.55
	Peak area [$\mu\text{V}\cdot\text{s}$]	30,055	32,030
	Theoretical enthalpy increment [J]	55.89	62.00
8	Sapphire [mg]	98.54	
	Peak area [$\mu\text{V}\cdot\text{s}$]	33,516	–
	Theoretical enthalpy increment [J]	62.02	

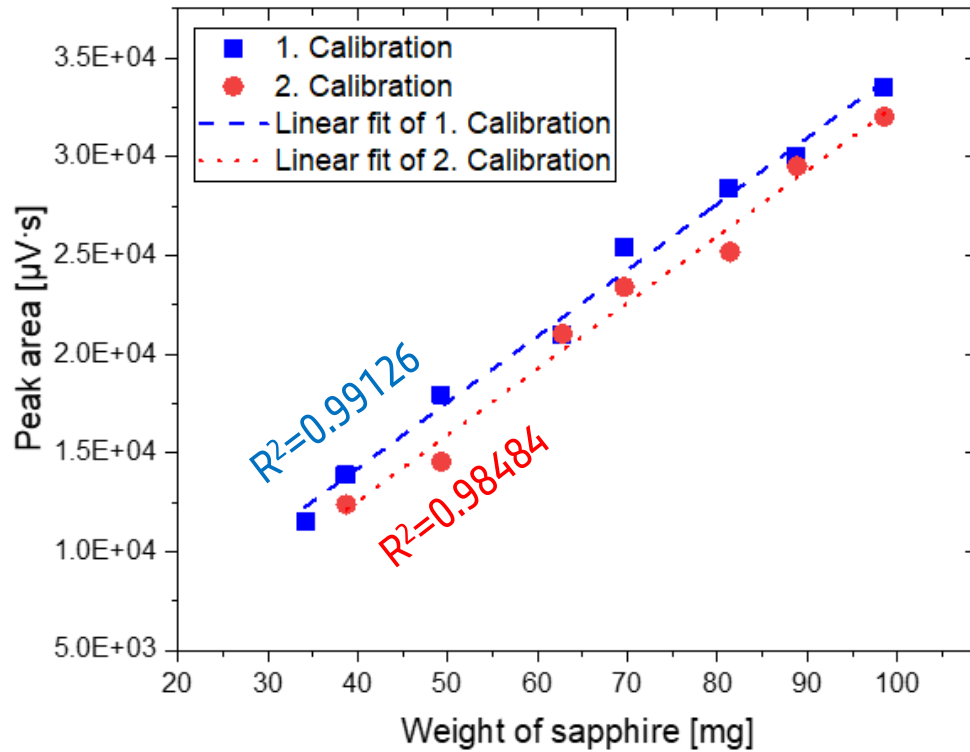


Figure 23. The linear relationship between sapphire mass and measured heat flow signal with the coefficient of determination.

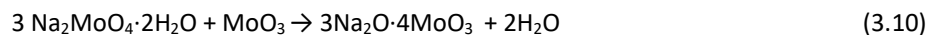
- 6) By dividing the theoretical enthalpy increment by the integrated peak area, the calibration factor (sensitivity) [J/ $\mu\text{V}\cdot\text{s}$] can be determined for each drop as presented in Table 13. For subsequent measurements of cathode materials in this study, the average sensitivity from the first calibration set — 0.00180640 J/ $\mu\text{V}\cdot\text{s}$ — was used, due to its lower error margin.

Table 13. Determination of calibration factors for each drop in both calibration runs.

	Drop Number	1. Calibration	2. Calibration
Calibration Factor [J/ $\mu\text{V}\cdot\text{s}$]	1	0.00174846	0.00196532
	2	0.00172107	0.00187217
	3	0.00186354	0.00213120
	4	0.00172790	0.00187876
	5	0.00180103	0.00203390
	6	0.00187919	0.00189380
	7	0.00185969	0.00193579
	8	0.00185035	–
Average		0.00180640	0.001958705
Standard deviation		6.14051E-05	8.78874E-05
Error [%]		1.20183	1.69593

Preparation of Sodium Molybdate as Solvent

In this study, sodium molybdate melt ($3\text{Na}_2\text{O}\cdot 4\text{MoO}_3$) was used as the solvent for high temperature drop solution calorimetry. Small batches of the solvent were prepared in the laboratory, following a controlled procedure to ensure reproducibility and suitability for high-temperature thermodynamic analysis. A 60 g batch of sodium molybdate ($3\text{Na}_2\text{O}\cdot 4\text{MoO}_3$) was synthesized from sodium molybdate dihydrate ($\text{Na}_2\text{MoO}_4\cdot 2\text{H}_2\text{O}$) and molybdenum trioxide (MoO_3) in a 3:1 molar ratio, according to the following reaction:



To prepare the mixture, 50 g of $\text{Na}_2\text{MoO}_4\cdot 2\text{H}_2\text{O}$ (*Thermo Scientific Acros*, purity > 99.5 %) and 9.915 g of MoO_3 (*Thermo Scientific Acros*, purity > 99%) were precisely weighed. The two powders were combined and thoroughly ground in a mortar to form a homogeneous mixture. A designated mortar and pestle, exclusively used for molybdate preparations, was employed to avoid contamination.

The homogeneous powder blend was transferred to a silica glass crucible and placed in a high temperature furnace. Heating was carried out at 700 °C for one hour from an ambient atmosphere to allow the mixture to fully melt and react. To facilitate rapid cooling and solidification, an additional empty silica crucible was placed adjacent to the melt crucible during heating. This prevented thermal shock and cracking of the second crucible during quenching. Following the melt, the yellow molten solvent was poured into the pre-heated second crucible for the partial quenching. The solvent was then returned to the furnace for an additional hour at 700 °C to ensure complete reaction. Finally, the crucible containing the melt was removed from the furnace and rapidly cooled in air. The resulting white solidified product was then finely ground using the same mortar and pestle.

The freshly prepared sodium molybdate ($3\text{Na}_2\text{O}\cdot 4\text{MoO}_3$) was stored in a sealed container labeled with the preparation date. No further chemical analysis was performed post-synthesis, as the starting materials were of certified purity and the process had been previously validated. For each measurement set, approximately 7.00 ± 0.05 g of $3\text{Na}_2\text{O}\cdot 4\text{MoO}_3$ was loaded into the Pt crucibles. This amount was found to be optimal for ensuring full dissolution of the sample (7 to 10 drops in this study) while maintaining a safe distance between the solvent surface and the drop tube to prevent contamination. Figure 24 illustrates this solvent preparation process, including images of the prepared solvent and stepwise schematic of the workflow.

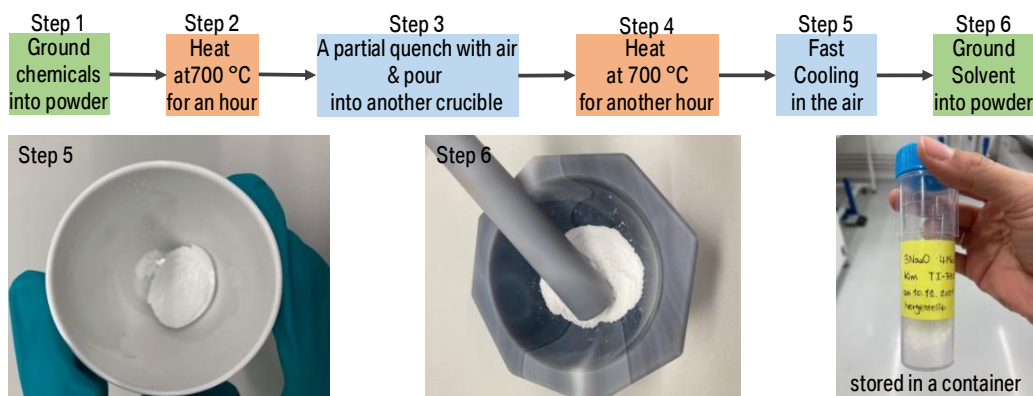


Figure 24. The step of synthesizing the solvent.

This synthesized sodium molybdate melt ($3\text{Na}_2\text{O} \cdot 4\text{MoO}_3$) serves as an effective buffer system as presented in equation (3.4)-(3.6). During sample oxidation or reduction, $\text{Mo}_2\text{O}_7^{2-}/\text{MoO}_4^{2-}$ redox pair stays in equilibrium with each other, acting as an oxygen buffer, until the sample is fully dissolved and reacts. The details of reaction with NMC compounds will be discussed in Chapter 4.

Optimization of Parameters for Measurements

The precision and reproducibility of high temperature drop solution calorimetry strongly depends on the stability of the baseline. In this study, extensive parameter testing was conducted to optimize the measurement conditions and ensure high-quality calorimetric data. The aim was to identify a set of parameters that minimized baseline fluctuation while maximizing the number of sample drops that could be performed with a single batch of solvent.

A wide range of experimental variables were systematically varied, including amount of solvent loaded in the crucible, furnace temperature, heating rate, isothermal holding phases, heat flux amplifier range, PIDU controller values. The resulting optimization matrix is presented in Table 14, where the tested conditions are summarized, and the optimal values are highlighted in green.

Table 14. Several trials to optimize each parameter to minimize baseline fluctuation with optimized parameters marked in green.

Amount of solvent [g]		6.0	6.5	7.0	7.5
Furnace temperature [°C]		676	677		
Heating rate [K/min]		5	10	15	
Isothermal phase		None		Yes (at 300 °C with 5 K/min)	
PIDU	Heat flux range	small	Large		
	5 K/min	400 7000 80 0	400 3500 80 0		
	Isothermal	400 9900 80 0	70 7500 0 0		0 9900 0 0
	10 K/min	400 7000 80 0	400 3500 80 0		

To ensure complete dissolution of each sample and prevent saturation of the solvent, the Pt crucible had to be filled with a sufficient quantity of sodium molybdate melt. However, the solvent level also needed to be kept below the drop tube to avoid contamination. In this work, the amount of solvent was optimized to 7.00 ± 0.05 g, which allowed for multiple drops per measurement cycle while maintaining a safe buffer from the drop tube.

Moreover, the furnace temperature was regulated at 677 °C, which corresponded to a measured sample temperature of 701 °C — the setpoint used for previous calorimetric measurements. The discrepancy between furnace and sample temperatures was attributed to vertical alignment of the sample within the furnace and was consistent across all measurements. The heating program was divided into three main phases: i) 30 °C to 300 °C with 5 K/min with PIDU of 400 7000 80 0, ii) isothermal hold at 300 °C for 1 hour with PIDU of 0 9900 0 0 and iii) 300 °C to 677 °C with 10 K/min

with PIDU of 400 3500 80 0 for 40 hours. This profile was selected to provide a gradual and controlled transition to the measurement temperature, minimizing thermal gradients and enabling the establishment of a stable baseline before drop experiments began. Also, the heat flow amplifier was set to the small range setting to enhance sensitivity and reduce noise. These settings produced the most stable baseline and consistent drop signals and were therefore applied across all subsequent measurements in this study.

Optimization of Method in the Sample Preparation

At the early stage of MHTC implementation, significant attention was devoted to optimizing the preparation method of NMC cathode active material samples to ensure they were compatible with high temperature drop solution calorimetry. The goal was to prepare small, mechanically stable and homogeneous pellets that could be dropped into the molten solvent without fragmentation of the baseline. Initially, the NMC powders were pressed using a conventional uniaxial press equipped with dies of 8-12 mm in diameter. To produce pellets of sufficient mechanical stability in this size range, a pressure of 4 tons/cm² was required. Once formed, these larger pellets were mechanically fractured using tweezers or a small spatula into smaller fragments with diameters of approximately 1–3 mm to fit into the drop tube of the MHTC. However, this approach proved problematic. The fractured pellets were inhomogeneous with shape and sizes, mechanically fragile and often disintegrated during handling or upon impact with the solvent, resulting in incomplete or segmented peaks in the heat flow signal. These issues introduced uncertainty in the measurement and compromised reproducibility.

To address this, alternative pressing techniques were explored. Commercially available uniaxial pressing tools capable of producing small-diameter pellets (< 3 mm) were thoroughly investigated. However, such tools were believed to lack the force capacity to produce dense, durable pellets from ceramic powders like metal oxides. As a solution, a cold isostatic pressing technique was adopted. Unlike uniaxial pressing, which applies pressure in a single direction, it applies uniform hydrostatic pressure from all directions using a flexible mold as demonstrated in Figure 25 (b). This technique results in better particle packing and improved mechanical integrity, particularly for small-sized pellets. Because of the flexible mold, isostatic pressing is not able to provide pellets with the accurate dimensions that uniaxial pressing can. That is why two casts with different sizes are considered and tested (see Figure 25).

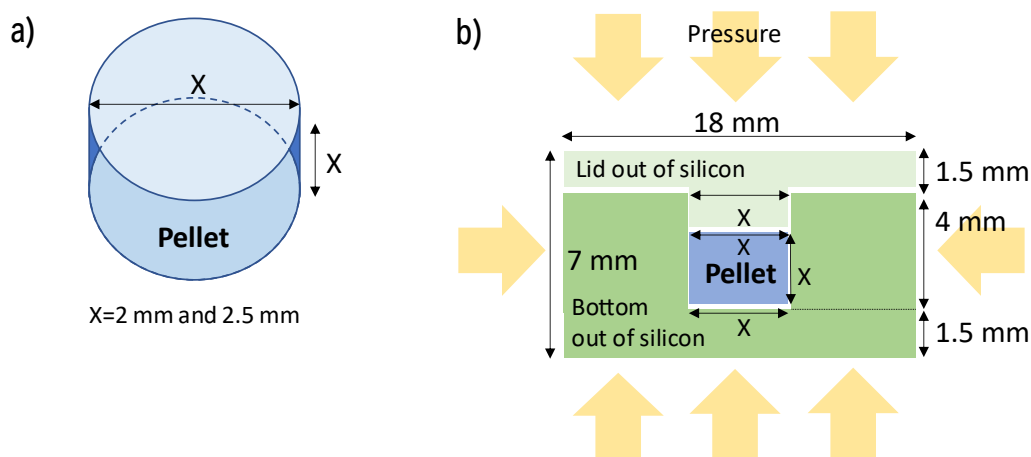


Figure 25. The concept of a flexible mold for the cold isostatic pressing to form a NMC pellet: (a) two different pellet sizes and (b) schematic of the cold isostatic pressing.

To fabricate the molds, TFC silicone rubber type 1 A and B were mixed at a 1:1 weight ratio and poured into stainless-steel molds of two different sizes. After curing, two flexible rubber molds were obtained (see Figure 26 (a)).

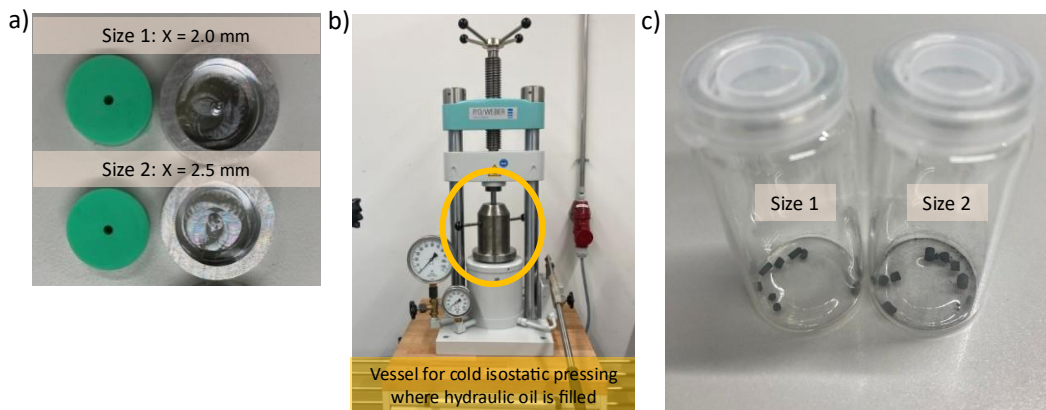


Figure 26. The order of preparation of sample pellets: (a) the molded silicon from two different mold, (b) the cold isostatic pressing and (c) pressed pellets with size 1 and 2.

The NMC powder was then carefully filled into the flexible mold under an inert atmosphere in a glove box. To prevent contamination and oxidation, the mold was sealed with paraffin sealing film before being immersed in hydraulic oil within a high-pressure CIP vessel (PW 40 from Paul Otto Weber). A pressure of 150 kN was applied to the hydraulic oil, which was uniformly transmitted through the mold to the powder (see Figure 26 (b)). This process resulted in compacted pellets, which were subsequently demolded (Figure 26 (c)). Among the two mold sizes tested, only the smallest — corresponding to pellets of $\varnothing = 2$ mm out of the size 1 — was selected for use in drop calorimetry due to its size compatibility with the MHTC. The produced pellets were stored in the glove box to avoid moisture uptake. Each pellet was removed from the glove box and dropped individually immediately prior to measurement. To avoid cross-contamination from the hydraulic oil or residual material, each silicone mold was used only once.

This optimized isostatic pressing method provided pellets with sufficient mechanical strength to withstand handling and drop impact and a proper size and geometry compatible with the drop tube of the MHTC system. These improvements were critical in enabling accurate, reproducible enthalpy measurements using the MHTC and were consistently applied in all subsequent sample preparations.

Measurement of Enthalpy of Formation using Alexsys-1000

To validate the reliability and accuracy of the enthalpy measurements obtained using the MHTC system, the same NMC cathode active materials were analyzed using the Alexsys-1000 drop solution calorimeter at the Karlsruhe Institute of Technology (KIT), Karlsruhe in Germany. The purpose of this cross-validation was to determine the extent to which the MHTC measurements aligned with those of the well-established Alexsys system and to assess the limitations of the MHTC setup.

The NMC powder samples prepared for MHTC were transported to KIT in a moisture-free environment. Each sample was transferred as double sealed in aluminum pouch bags under vacuum, placed inside an additional bag containing silica gel, and stored in a desiccator prior to measurement at KIT. Just before the drop measurements, the samples were pressed into small pellets with a diameter of 3 mm, each weighing approximately 5 to 10 mg (± 0.005 mg), using an uniaxial press. During calorimetric measurement, the pellets were dropped from ambient temperature into molten sodium molybdate maintained at 974 ± 0.1 K. Each measurement set consisted of multiple successive drops, carried out at 1 to 1.5-hour intervals to ensure full dissolution of the previous pellet and re-establishment of thermal equilibrium. This approach ensured the independence of each enthalpy value and improved measurement repeatability. To

maintain an inert and thermally homogeneous environment, argon gas was supplied in two modes, 50 mL/min for flushing and 5 mL/min for bubbling. This helps to avoid supersaturation and accelerates the dissolution process by maintaining solvent homogeneity and agitation — features that are absent in the MHTC.

The calibration of the Alexsys-1000 calorimeter was performed using sapphire spheres (7 mg, 1.5 mm diameter). The calibration factor was determined separately for both calorimeter cells: 0.00449717 J/ $\mu\text{V}\cdot\text{s}$ for the right cell and 0.00450618 J/ $\mu\text{V}\cdot\text{s}$ for the left cell. These values were then used to convert the integrated heat flow peak areas [$\mu\text{V}\cdot\text{s}$] from each NMC drop experiment into enthalpy values [J]. The calculation method was identical to that used for MHTC measurements, ensuring consistency in the data processing pipeline.

3.2 Study of ISC and TR at LIB Cell Level

To investigate the thermal runaway (TR) behavior of commercial automotive prismatic lithium-ion battery (LIB) cells and its principal trigger — internal short circuit (ISC) — a comprehensive experimental approach was employed. This involved the use of both accelerating rate calorimetry (ARC) and nail/needle penetration testing. While ARC is a well-established method for evaluating TR induced by external heating, the nail penetration test offers a direct means to provoke ISC within the cell by mechanically bridging electrodes. Unlike conventional use, where the nail test merely serves as a TR trigger, the method was refined and optimized in this study to extract in-depth, quantitative insights into ISC characteristics — particularly critical penetration depth, ISC current, and insitu temperature development. The methodological background, rationale for refinement, and specific parameter adjustments are detailed in the following subsections.

3.2.1 Accelerating Rate Calorimeter

The accelerating rate calorimeter (ARC) is a specialized instrument used in battery research to investigate the thermal properties and safety characteristics of LIBs. ARC operates by placing batteries in a sealed reaction vessel — commonly referred to as a “bomb” — and subjecting them to controlled heating or cooling cycles while simultaneously measuring heat flow, enabling researchers to analyze thermal behavior under various conditions.

Working Principle and HWS Method

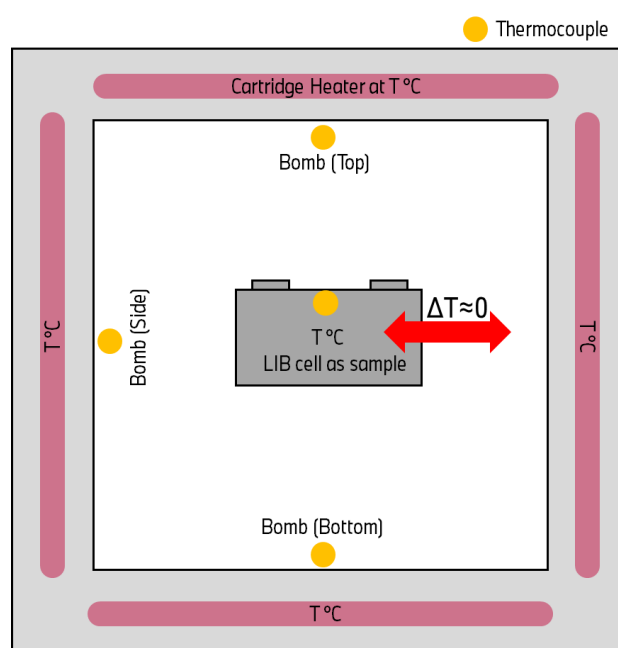


Figure 27. Schematic set up of a prismatic LIB cell in an ARC chamber.

The ARC enables precise tracking of temperature and heating rates (0.02- 15 K/min) while operating most importantly in a (quasi-)adiabatic mode. The term “*adiabatic*” refers to conditions where no heat exchange occurs, simulating worst-case scenarios. During the test, both the sample and its holder are maintained at the same temperature as the calorimeter chamber, ensuring that no heat is exchanged with the surroundings as presented in Figure 27. In an ideal adiabatic system, the measured temperature change (dT/dt) can be directly related to heat generation by multiplying it by the sample mass, m [g] and its specific heat capacity, C_p [J/g·K]. To ensure experimental precision, proper calibration is necessary to avoid two major issues; Firstly, being over adiabatic can introduce additional heat to the sample, leading to the generation of false exotherms. Secondly, being under adiabatic can mask exothermic reactions and result in underestimation of safety parameters. Both conditions should be avoided by calibration to ensure accurate and reliable experimental results. Following calibration, a drift check, which is a standard Heat-Wait-Seek test with the dummy, ensures that the self-heating and self-cooling rate of the dummy stays below 0.02 °C/K in this work.

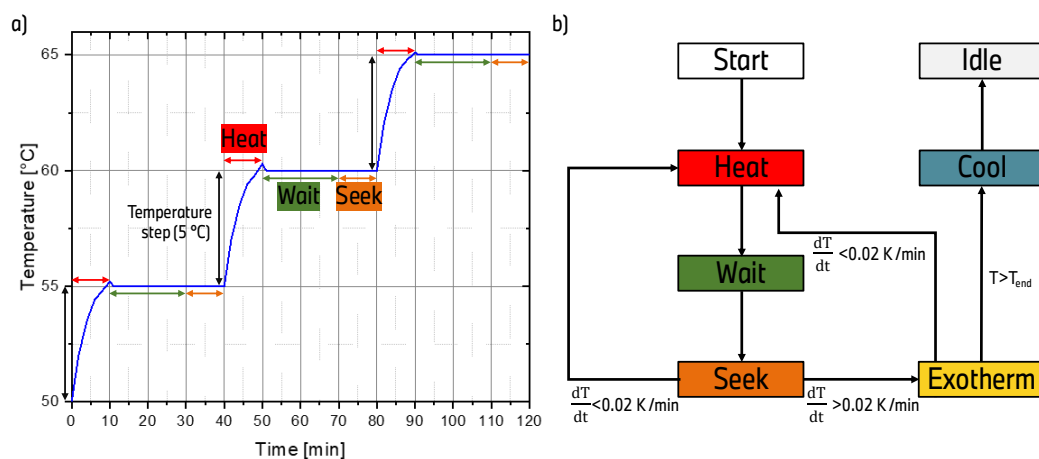


Figure 28. Typical ARC procedure with HWS method (a) example of temperature on cell surface for three Heat-Wait-Seek cycles and (b) process loop of HWS method.

The ARC test is conducted using the standard Heat-Wait-Seek method (HWS), also known as Heat-Wait-Search which typically operates within a temperature range of 50 to 350 °C. The procedure follows a systematic loop as presented in Figure 28 (b):

- **Heat Mode:** the test begins at a predefined starting temperature, increasing in small increments (typically 5 °C steps).
- **Wait Mode:** after each heating step, the system stabilizes for 20 minutes to establish thermal equilibrium.
- **Seek Mode:** once equilibrium is reached, the calorimeter detects whether the self-heating rate exceeds 0.02 K/min:
 - If heat generation remains below this threshold, the system restarts the HWS loop with an additional 5 °C increase.
 - If heat generation exceeds the threshold, the system switches to quasi-adiabatic **Exotherm Mode**.

In **Exotherm** mode, the heaters instantaneously follow the temperature change of the cell's surface, preventing heat dissipation to the chamber. Consequently, the cell continues to heat up until a thermal runaway occurs or cell components responsible for the exothermic reaction are completely consumed. Once the maximum temperature is reached, the system enters **Cooling** mode, where compressed air is used to cool the cell.

Application of ARC with Previous Studies

The HWS method in ARC provides a comprehensive approach for evaluating the thermal behavior and safety characteristics of LIB cells. By identifying the start of exothermic reactions and studying the thermal behavior of a LIB cell, its data supports development and optimization of battery technologies, ensuring greater reliability while minimizing the risk of thermal incidents. The application of ARC in the study of Li-ion battery cells includes:

- **Thermal Stability Assessment:** By applying controlled temperature ramps, ARC determines the thermal stability of LIB cells, identifying the temperature at which the battery cell may undergo exothermic reactions or thermal runaway. This is critical for safety analysis, as exothermic reactions can lead to hazardous failures. For instance, Karmakar et. al. [124] demonstrated that the onset temperature for exothermic reactions and TR decreases with increasing SOC in a NCA based Li-ion cell. Similarly, Mao et.al. [125] investigated self-heating behaviors in 18650 cells with chemistries of 98 % NMC532 and 2 % LiMn_2O_4 for cathode and graphite for anode at varying SOC levels, showing that onset temperature of self-heating increases as SOC decreases.
- **Heat Generation Analysis:** ARC offers the possibility to quantify the heat generation during different operational conditions, which is crucial for designing efficient cooling systems to prevent excessive temperature rise. For an example, Gao et al. [126] studied the effect of high-temperature aging on the heat generation of LIBs using ARC. They observed a pronounced decline in heat release after ageing, most notably at 80 °C, where the thermal-runaway (TR) heat generation was approximately 40 % lower than that of pristine cells. Moreover, exposure to 60-80 °C accelerated ageing, elevating the TR onset temperature and attenuating TR severity, effects attributed to progressive electrolyte depletion.
- **Thermal Runaway Analysis:** ARC is also a key tool for evaluating thermal runaway behavior under extreme conditions such as overcharging, nail penetration and external heating. By identifying critical thermal thresholds, ARC aids in development of safety mechanisms to mitigate catastrophic failures. Reichert et al. [127] examined thermal runaway in LIB cells at 100 % SOC using nail penetration tests under adiabatic conditions, demonstrating that LFP-based cells remained stable, reaching 115 °C with 5 % mass loss, whereas NMC-LCO cells underwent thermal runaway, peaking at 130 °C with 25 % mass loss. Likewise, Ye et al. [128] investigated overcharge-induced thermal behavior and found that higher charging rates increase the onset temperature of thermal runaway.
- **Material Characterization:** ARC can also be employed to evaluate the thermal behavior of various battery materials, including electrode and electrolyte compositions. This facilitates battery component optimization for improved performance and safety. For example, Ohneseit et al. [10] employed ARC to examine the thermal and mechanical safety properties of LIBs with different cathode compositions, including NMC, NCA and LFP, along with variations in cell design. Their finding demonstrates that the choice of cathode material significantly impacts the safety characteristics and the onset temperature to TR.

Goal and Process of ARC Measurement

In this work, Accelerating Rate Calorimetry (ARC) was employed specifically to investigate the influence of cell casing design — namely, floating can versus can on potential configurations in Chapter 6 — on the thermal characteristics of automotive prismatic lithium-ion battery (LIB) cells. The primary aim was to confirm that these two structural types, despite their different electrical grounding concepts, exhibit no significant difference in thermal behavior during runaway events.

All ARC experiments were conducted using the Extended Volume (EV) Accelerating Rate Calorimeter, manufactured by Thermal Hazard Technology (THT), located in Bletchley, United Kingdom. This calorimeter features an internal chamber volume of approximately 24,540 cm³, with a diameter of 25 cm and a depth of 50 cm. The unit is equipped with a set of thermocouples and heaters distributed across the chamber: one set at the lid, another at the bottom, and two sets along the

sidewalls, all employing Type N thermocouples. The EV ARC operates under (quasi-)adiabatic conditions, meaning that the system is designed to minimize heat exchange between the cell and its surroundings. This creates a worst-case scenario for safety evaluations, as it allows the cell to self-heat without significant thermal dissipation.

Prior to initiating measurements, the calorimeter was calibrated using the manufacturer's recommended procedure. This involved placing a dummy cell — constructed from aluminum and designed to replicate the thermal mass and geometry of the actual battery cell — into the chamber. The dummy was fitted with the same thermocouple configuration used for the real samples. In calibration mode, the ARC software optimized heater power distribution and calculated any necessary thermocouple offset corrections to ensure uniform temperature response across all sensing points. Following calibration, a drift check was performed using a standard Heat-Wait-Seek (HWS) protocol. The objective of this check was to verify that the system maintained thermal equilibrium, with both self-heating and self-cooling rates remaining below 0.02 °C/min, confirming that the system was free from unintended heat flows or gradients.

For the ARC experiments, four commercial 34 Ah prismatic LIB cells were selected — two with floating can design and two with can on potential configuration. Prior to testing, all cells were preconditioned at room temperature using a standard battery cycling protocol. Each cell underwent three full charge-discharge cycles using a C/3 constant current–constant voltage charging method. Cells were charged to 4.2 V, with a cutoff current set to C/10, and a 30-minute rest period was included after both charging and discharging steps to allow for equilibration. Following the preconditioning step, each cell was charged to 100% state of charge and then mounted inside the calorimeter chamber. Thermocouples were attached to each cell using high-temperature adhesive tape. The main thermocouple, often referred to as the bomb thermocouple (Type N), was positioned at the center of the wide front face of the cell and was used as the primary control input for the ARC's heating system (see Figure 27). An additional Type K thermocouple was affixed to the cell's vent, allowing for localized temperature monitoring during venting or gas release events. In parallel, cell voltage was continuously monitored throughout each test run.

The ARC measurements followed a Heat-Wait-Seek (HWS) protocol, starting from an initial temperature of 50 °C and proceeding up to 350 °C, the upper limit for safety evaluation. In the Heat phase, the cell was incrementally heated in 5 °C steps. Each step was followed by a 20-minute wait period, during which the system allowed the cell and chamber to reach thermal equilibrium. Once equilibrium was established, the Seek phase began, wherein the system monitored for the onset of self-heating. If the self-heating rate remained below the detection threshold of 0.02 °C/min, the cycle repeated with the next heating increment. However, if the self-heating rate exceeded this threshold, the ARC automatically switched into quasi-adiabatic Exotherm Mode. In Exotherm Mode, the ARC's heaters dynamically tracked the rate of temperature increase on the cell surface, effectively eliminating any heat loss to the environment. This ensured that the cell could self-heat without thermal interference, simulating a realistic runaway scenario. The test continued under this mode until a thermal runaway occurred or all exothermic reactions were exhausted. If no runaway was observed by 350 °C, the system initiated a controlled cooling sequence using compressed air.

In summary, ARC was used in this study not to provoke TR by overcharging or puncturing, but rather to monitor the intrinsic thermal response of fully charged LIB cells under worst-case thermal confinement, to understand the impact of floating can on thermal stability at cell-level. The result from ARC measurement will be discussed in Chapter 6.

3.2.2 Nail/Needle Penetration Test

The primary objective of this study is to achieve a deeper understanding of thermal runaway and its fundamental trigger — internal short circuit — at the LIB cell level. While ARC is a powerful tool to evaluate TR by external heating, it fails to replicate the internal heat generation mechanisms that occur during real-world ISC events. In ARC, heat originates externally and propagates inward slowly

under quasi-adiabatic conditions — at least prior to the onset temperature of exothermic reactions — whereas in ISC scenarios, heat is generated locally within the cell and spreads outward. To address this limitation, a nail or needle penetration test was employed and extensively refined in this work to enable controlled and reproducible induction of ISC under conditions that closely simulate realistic failure modes.

Working Principle and ISC Generation

The ISC process initiated during nail penetration test follows a complex electrochemical pathway. The sequence of events can be described as follows and presented in Figure 29:

- 1) The nail breaches the separator, forming an electrical contact between the anode and cathode current collectors.
- 2) Electrons generated by delithiation reactions at the anode migrate to the copper current collector and then to the cathode via the nail, facilitating the lithiation reaction at the cathode active material.
- 3) Simultaneously, lithium ions travel through the electrolyte and separator from the anode to the cathode.
- 4) Heat is generated both in the nail and the battery due to the flow of current and joule heating effects.
- 5) Over time, depletion of lithium ions at the cathode, along with resistance from the electrolyte and separator, limits the shorting current and subsequent Ohmic heating.

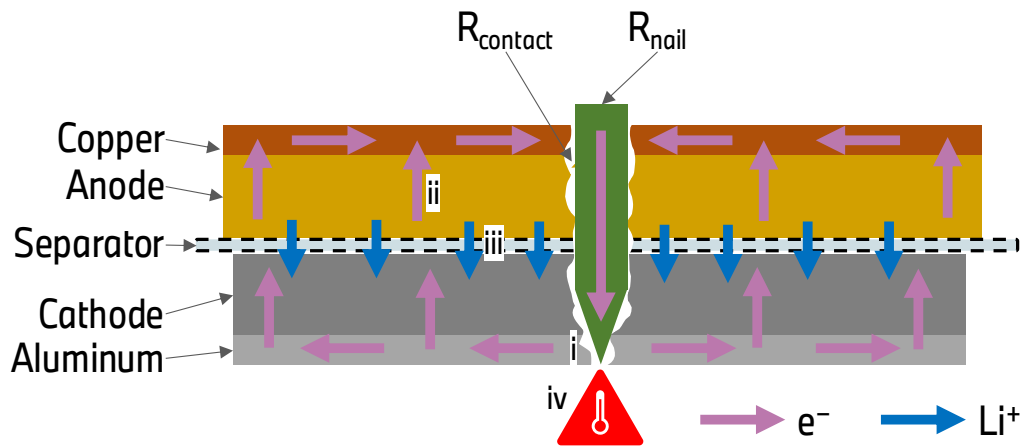


Figure 29. Schematic of the electrons and Li^+ transport path between cathode and anode during nail penetration process and shorting resistances.

The initial short-circuit current is influenced by shorting resistance, primarily determined by the contact resistance between the nail and the electrode (R_{contact}), as well as the intrinsic resistance of the nail itself (R_{nail}). The randomness in how the nail contact the electrodes leads to variations in total resistance, influencing the heating and failure dynamics of the LIB cell. This leads to the common problem of nail penetration test namely poor reproducibility. Based on this presented principle how ISC occurs during nail penetration test, the impact of cell assembly on ISC-behavior will be discussed in the Chapter 5.

Conventional Nail Penetration Tests and Their Limitations

The nail penetration test is the predominant experimental protocol for evaluating the safety response of lithium-ion batteries (LIBs) under severe mechanical abuse. ISCs during nail penetration test replicate failure modes that can arise in service, for example during vehicle collisions or from latent manufacturing defects, and the ensuing local Joule heating can trigger thermal runaway (TR).

Consequently, nail penetration testing is mandated in multiple automotive safety standards to verify a battery’s ability to withstand mechanically induced ISCs without catastrophic failure.

This test is particularly significant for automotive applications, where it is mandated by several safety standards to assess the battery’s response to internal short circuits caused by mechanical damage. For example, the international standard SAE J2464 prescribes a 3 mm-diameter rod for cell-level assessments and a 20 mm rod for module- or pack-level assessments; penetration must traverse the entire cell or, at the higher hierarchical levels, a depth of either 100 mm or the full stack of cells. In all cases the rod must remain embedded for a minimum post-test observation period of 1 h. [76,129] The FreedomCAR Abuse Test Manual similarly requires complete cell penetration by a 3 mm pointed conductive rod driven at 6 cm/s, with continuous monitoring of cell voltage, surface temperature, and any propagation effects; to pass, the battery must exhibit no fire, explosion, or molten ejecta. Large-format commercial LIBs used in electric vehicles and stationary energy-storage systems frequently fail to meet these criteria, often progressing to TR under nail penetration. [80,130]

Despite its widespread use, the conventional nail penetration test is subject to three principal criticisms. (i) The mechanical insult is not fully representative of field-relevant events (e.g. debris piercing the battery enclosure). (ii) Test-to-test reproducibility is poor. (iii) The outcome is highly sensitive to experimental variables such as rod speed, rod diameter, and material. Moreover, the method is predominantly employed merely to induce TR, yielding limited quantitative information on the ISC development itself.

The present work therefore concentrates on refining the penetration methodology so that it not only initiates TR but also furnishes critical data on ISC evolution, while addressing the reproducibility, relevance, and parameter-sensitivity issues identified above. The resulting optimized nail/needle-penetration protocol is detailed in the section of **Optimization and Refinement of Nail/Needle Penetration Tests in This Study**.

Application of Nail Penetration Test with Previous Studies

A substantial body of literature employs nail penetration experiments to elucidate the dynamics of internal short circuits (ISCs) and to quantify the influence of key variables such as state of charge (SOC), penetration speed, and penetration location. These tests have been utilized both to analyze ISC characteristics and to deliberately induce thermal runaway. Table 15 provides an overview of the application of nail penetration testing in ISC and TR investigations of lithium-ion battery (LIB) cells, highlighting areas for potential enhancement.

The works cited were selected because they offer strategies either to enhance test reproducibility or to enable quantitative measurement of ISC parameters — considerations that directly inform the methodology developed in the present study. In addition, the contribution by An et al. [131], which examines how the choice of cathode active material modulates ISC severity, is included to underscore the compositional dependence of short-circuit behavior.

Table 15. Examples of studies using nail penetration test.

Author	Year	Topic
Finegan et al. [132]	2017	adapted “ <i>smart nail</i> ” where a thermocouple is embedded to measure internal temperature, penetrating 18650-type cells at different orientations (horizontal, vertical) and positions. The study visualized thermal and structural dynamics of cell via thermal camera and high-speed synchrotron X-ray radiography.
Mao et al. [133]	2018	investigated the effects of penetration depth, position, and speed (20, 30, 40 mm/s) with various charge state on the thermal runaway of 18650 cylindrical cell. They explained the mechanism of ISC triggered by nail penetration with the aid of a “ <i>Micro Short-Circuit Cell Model</i> ”.

Author	Year	Topic
Abaza et al. [80]	2018	investigated the behavior of commercial automotive lithium-ion pouch cells under internal short circuit conditions using nail penetration test with different materials (copper, steel and plastic). Non-conducting nails did not cause a short circuit, confirming that the nail acts as the main current patch. It presents also poor reproducibility, which was attributed to variable contact resistance between the nail and electrode layers.
Wang et al. [134]	2020	investigated penetration-induced internal short circuits (ISC) and thermal runaway (TR) in lithium-ion cells with various SOC 50/75/100 % using a combination of experiments with different penetration speeds and nail diameters (3, 5 and 8 mm) and numerical simulations. Higher SOC (100%) significantly increases the risk of thermal runaway due to higher electrically stored energy leading to greater heat generation and higher short-circuit current. Smaller nail diameters (3 mm) resulted in higher temperature spikes and faster failure, while larger nails (8 mm) provided better heat dissipation and reduced TR severity. This results confront the results from An et al. [131], because the nail serves as both a conductor (causing ISC) and a heat sink (dissipating heat). Larger nails can improve heat dissipation but in thermal runaway cases larger nails cause higher short circuit currents. Heat conduction analysis revealed that over 70% of heat was transferred to the nail, reducing the likelihood of TR in non-thermal runaway cases.
Diekmann et al. [135]	2020	developed a new procedure for nail penetration of LIBs with higher reproducibility, where the tests used conductive metal nails easier to obtain reproducible results at low penetration speed like 1mm/s.
Huang et al. [136]	2020	inserted a small temperature sensor in the nail to facilitate insitu sensing in nail penetration tests. They observed multiple peaks of local temperature at ISC spot before TR, which could not be captured in conventional nail penetration tests. The findings also suggested that increasing the contact resistance between Al current collector and nail would lower ISC current, inducing temperature to drop.
Liu et al. [137]	2023	presented an insitu method for measuring dynamic internal short circuit resistance during nail penetration. The group employed nail penetration tests on various LIB cell configurations, including dry cells, wet dummy cells and working cells. A small nail and slow penetration speed were used to ensure detailed data collection, ISC resistance, current and temperature were measured simultaneously, capturing real-time changes in resistance throughout the penetration process. The study highlights that ISC resistance is highly dynamic during nail penetration and that analyzing only stable post-penetration resistance can significantly underestimate the severity of thermal runaway risks. Understanding how penetration direction, material behavior, and resistance fluctuations influence failure modes is crucial for developing safer lithium-ion cells.
An et al. [131]	2024	investigated the behaviors of lithium-ion cells with different cathode materials such as LCO, LMO, NCM and LFP subjected to nail penetration tests with various nail diameters (2, 5 and 8 mm). The order of ISC sensitivity was LCO > LMO > NMC > LFP (at 100 SOC from most to least sensitive). Larger nails of 8 mm caused lower initial temperature rise rates but led to higher maximum temperatures, while smaller one resulted in a steeper temperature rise rate, but TR temperature was less severe. The result shows LIB safety strongly depends on cathode material.

Optimization and Refinement of Nail/Needle Penetration Tests in This Study

All penetration tests were performed using a linear actuator system developed by Fritz Automation GmbH. This system was installed in a dedicated safety bunker with controlled air screen and allows the precise control of nail or needle movement with adjustable penetration speeds ranging from 0.01 to 15 mm/s. A stainless steel needle was used as the standard configuration for all penetration tests due to its low thermal conductivity and minimal mechanical disruption to the cell. In addition to this configuration, custom-fabricated nails were designed and employed specifically for experiments aimed at measuring insitu temperature. These specialized nails were equipped with embedded thermocouples, enabling real-time temperature monitoring directly at the ISC location within the cell.

The working principle of the nail/needle penetration test involves the mechanical induction of an ISC by bridging at least two internal components of the cell that are at different electrical potentials. When such a short circuit is initiated through penetration, and the subsequent reactions lead to thermal runaway, the position of the needle or nail at the moment TR begins is defined as the critical penetration depth (D_c). This parameter serves as a key indicator of how resistant or vulnerable a specific LIB cell is to ISC-induced TR. To ensure accurate measurement with the improved reproducibility of results, a range of parameters and configurations were systematically optimized. These included the mechanical setup, data acquisition strategies, and integration of electrical and thermal measurement systems. Specifically, the following aspects were refined:

- general test setup modifications to overcome the limitations of conventional methods inspired by the study of Huang et. al. [136]
 - **Nail/Needle:** The nail itself presents a source of inaccuracy. Standard nails typically have diameters between 3 and 20 mm, possess high thermal conductivity, and exhibit low electrical resistance. These properties alter both mechanical and thermal interactions within the cell during penetration and fail to reflect the highly localized nature of actual ISC events. To minimize these effects, a stainless-steel needle made of CTS20D carbide produced by Helmut Schweyer Feinmechanik in Krailing, with a diameter of 1 mm, a length of 60 mm, and a tip angle of 60°, was utilized in this study.
 - **Penetration Speed:** Conventional tests are often conducted at speeds ranging from 10–40 mm/s and can exceed 80 mm/s, which compromises the precision in determining penetration depth and understanding how ISC varies with layer-specific interactions. In this study, the penetration speed was significantly reduced to 0.01 mm/s, a value that corresponds closely with the thickness of individual layers in commercial prismatic LIB cells (e.g., Cu and Al current collectors and separators). This slower penetration rate allows for detailed investigation of ISC behavior at the layer level and facilitates precise determination of the critical penetration depth, which is discussed in more detail in the next subsection.
- The precise definition of critical penetration depth
- Insitu temperature measurement via thermocouple-embedded nail inspired by references [132,136]
- Quantification of ISC current using shunt and current source.

These methodological improvements provide a realistic, systematic, and reproducible platform for evaluating the behavior of ISC in commercial prismatic LIB cells. Last three refinements are elaborated upon in the following subsections.

The Precise Definition of Critical Penetration Depth

The penetration depth refers to the length by which the needle or nail enters the cell. A deeper penetration results in more electrode layers being short-circuited. Conventionally, a fixed

penetration depth is applied to study TR behavior, but this approach fails to provide insight into how TR initiates or how resistant a cell is to ISC-induced failure. To establish a comparative safety metric, this study defined the critical penetration depth (d_c) as the depth at which TR is triggered.

Determining this value with high precision, however, required a more advanced strategy than simply measuring the displacement of the needle. First, the mechanical response of cell components during needle penetration was carefully examined. Metallographic cross-sectional images (see Figure 30) revealed that the internal electrode layers do not rupture instantly upon contact with the needle. Instead, the layers exhibit significant mechanical deformation, bending and compressing until a critical force threshold is surpassed. Once that limit is reached, multiple layers are penetrated in rapid succession, causing a sudden, uncontrolled internal short circuit. This observation demonstrates that the onset of ISC is not gradual and reinforces the need for a reproducible and robust definition of critical penetration depth.

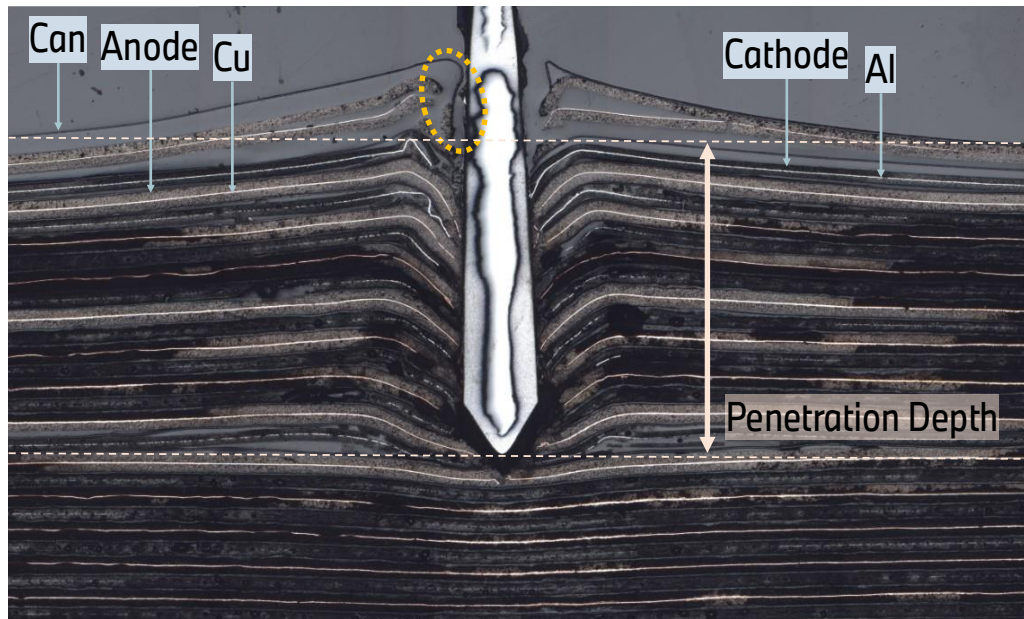


Figure 30. The metallographic microsection of a LIB cell from nail penetration test without thermal runaway by optical microscopy (The diameter of the nail used in the experiment was 1 mm).

To mitigate uncontrolled variables and ensure reproducibility, mechanical compression was applied to the test cells during all penetration experiments. The primary reason for compressing the cells was to prevent excessive deformation or gas swelling that could lead to unintended over-penetration by the needle. Without compression, the cell may swell due to gas evolution, pushing the needle further into the layers than intended, and thereby distorting the penetration depth measurement. This uncontrolled condition is illustrated in the worst-case scenario shown in Figure 31 (d). To avoid this, the cells were compressed between two stainless steel plates with a force of 5 kN, and a 15 mm diameter hole was machined at the center of the plates to allow the needle to pass through (see Figure 31 (a)).

In this setup, all LIB cells were clamped in a way that fully covered the jelly roll, replicating the mechanical boundary conditions present in real battery electric vehicle (BEV) modules. In actual BEV applications, LIB cells are compressed within modules to prevent lithium plating caused by poor contact between electrodes. The compression level of 5 kN used in this study corresponds to the range typically applied in real-world automotive battery packs. Beyond maintaining penetration control, the application of mechanical compression was also found to influence gas evolution behavior and the formation of internal venting channels during TR. As demonstrated by post-mortem CT scans in Figure 31 (b) and (c), compressed cells exhibited well-defined gas pathways that connected directly to the safety vent, forming a branching network of smaller channels. In contrast,

uncompressed cells lacked such structured venting, indicating that the presence or absence of compression significantly affects the internal dynamics of thermal runaway.

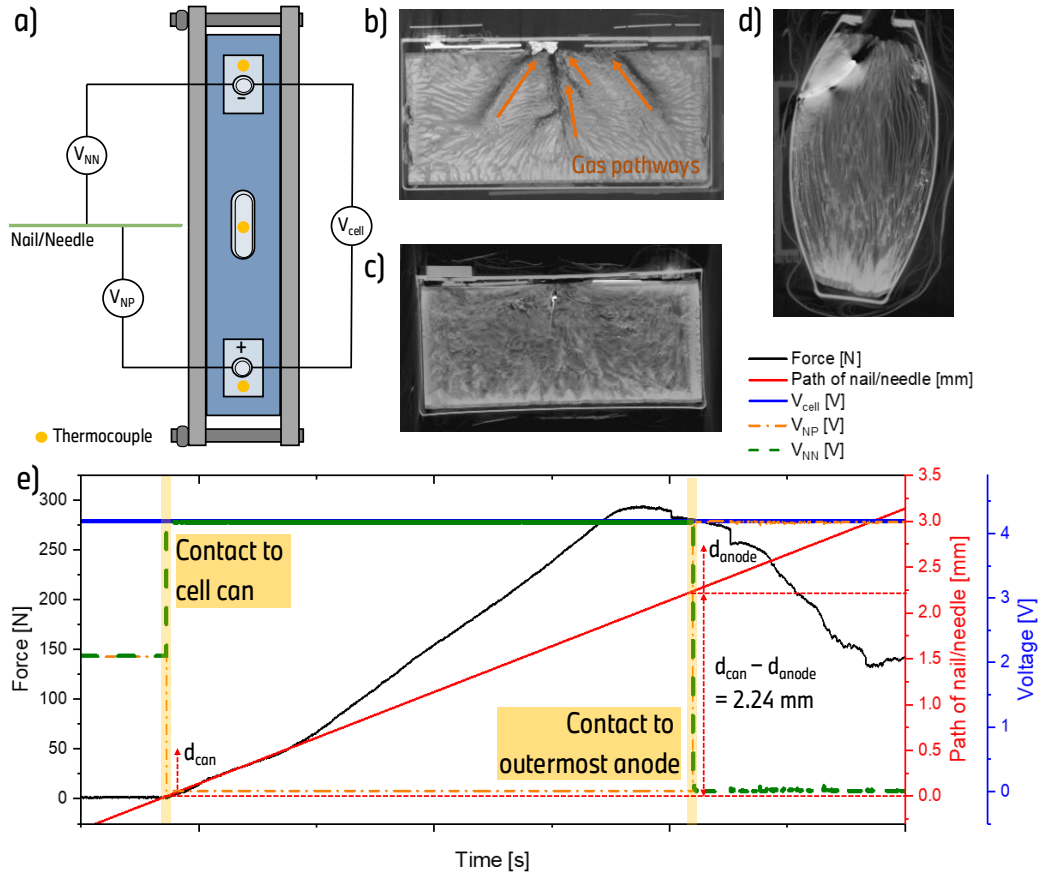


Figure 31. How to improve the repeatability and define the penetration depth, d , (a) schematic of the nail/needle penetration test, post-mortem CT evaluation of a LIB cell after needle penetration test (b) with compression and (c) without compression, (d) example of the worst-scenario in cases of penetration test without compression and (e) example test demonstrating how to define the penetration depth using V_{NP} and V_{NN} .

Second, the precise definition of critical penetration depth in this study relied not only on mechanical setup, but also on electrical signal tracking. Two voltage signals were continuously monitored during penetration:

- The voltage between the nail/needle and the positive terminal (V_{NP})
- The voltage between the nail/needle and the negative terminal (V_{NN}).

These signals were used to identify the exact points of electrical contact with both the can and the outermost anode. For example, in a prismatic LIB cell where the can is at positive potential and the cell voltage is 4.2 V, the first contact with the can is detected when $V_{NN} = 4.2 \text{ V}$ and $V_{NP} = 0 \text{ V}$. The penetration depth from this contact to the can is defined as d_{can} . Conversely, when the needle reaches the outermost anode layer, V_{NN} drops to 0 V and V_{NP} increases to 4.2 V, defining the penetration depth from the anode contact, d_{anode} . The ability to identify these two transition points allows for a more nuanced understanding of when the short circuit transitions from casing contact to internal electrode contact (see Figure 31 (e)).

Notably, the mechanical deformation of the can introduces an additional complexity: the measured difference between d_{can} and d_{anode} often exceeds the actual physical thickness of the can. In the example in Figure 31 (e), the distance between these two electrical transitions was measured as 2.24 mm, despite the actual can thickness being approximately 0.7 mm. This discrepancy is

attributed to the elastic and plastic deformation of the can material under the applied force of the needle. This bending behavior is clearly visible in Figure 30, where the can is marked with a yellow circle to highlight the region of significant deflection before rupture.

In summary, the precise definition of critical penetration depth in this work integrates both mechanical stabilization through compression and electrical diagnostics via voltage tracking. This approach allows for accurate determination of the depth at which ISC initiates and TR is triggered, forming a critical foundation for evaluating and comparing the robustness of different LIB cell designs against mechanical abuse.

Insitu Temperature Measurement via Thermocouple-Embedded Nail

To study the behavior of internal short circuits (ISCs) with greater precision, it is essential to measure the temperature rise at the exact site of the short, rather than relying on surface-mounted thermocouples, which cannot capture the highly localized and rapid heating that occurs internally. In this study, a method was developed to measure insitu internal local temperature as close as possible to the actual ISC position by employing a custom-designed nail embedded with a thermocouple. As shown in Figure 32 (c) — (e), the custom-designed nail was fabricated with specific structural and material characteristics to ensure thermal sensitivity while minimizing disturbance to the cell. The nail had a tip angle of 30°, a diameter of 1.2 mm, and a total length of 50 mm, with a central bore to accommodate a thermocouple wire. This allowed temperature data to be acquired directly from the region where the nail was initiating the short circuit. To optimize thermal conduction to the sensor, the nail was constructed from two different materials with contrasting thermal properties:

- The tip from AlMgSiPb alloy with high thermal conductivity (170–220 W/m·K [138])
- The body from 304 stainless steel with lower thermal conductivity (15–20 W/m·K [139]).

This combination ensured that thermal signals generated at the ISC location were efficiently transmitted to the thermocouple, while minimizing heat dissipation along the body of the nail. The objective was to ensure that the thermocouple captured the true thermal signature of the ISC without significant thermal lag or dilution due to heat conduction away from the shorting site.

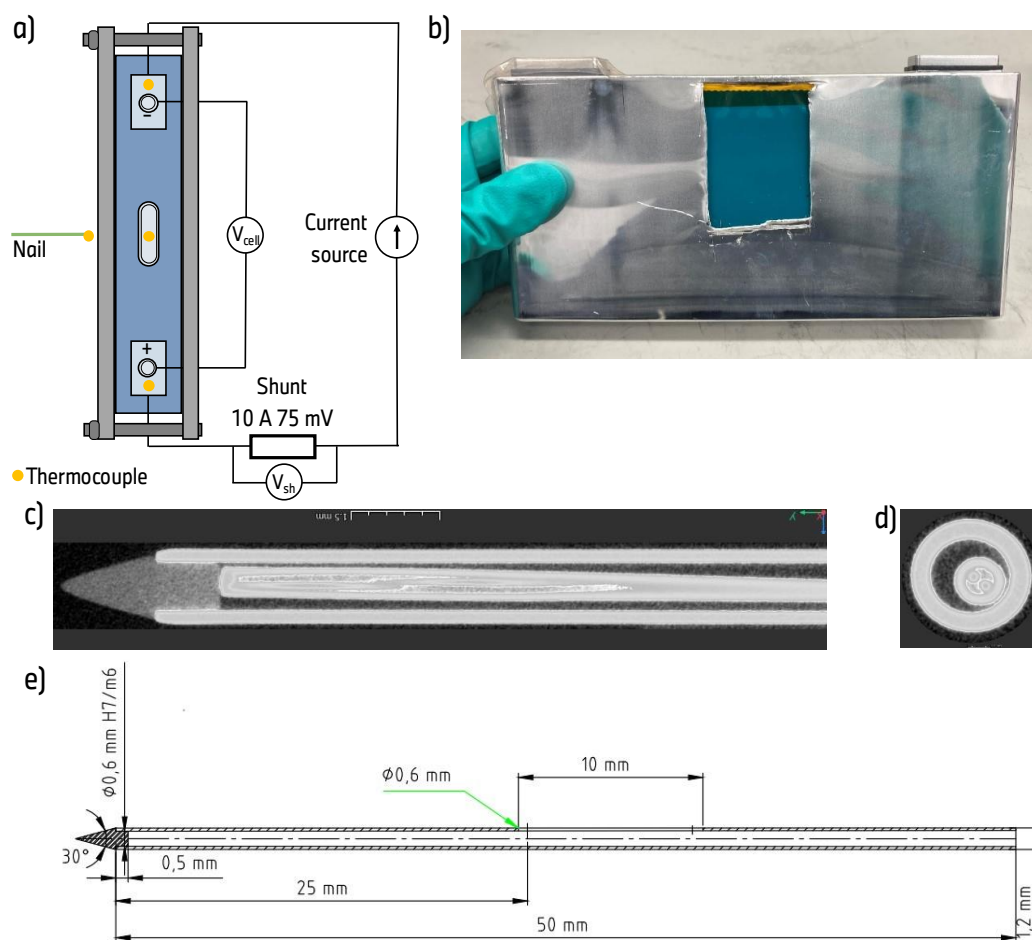


Figure 32. Investigation of ISC behavior by measuring internal local temperature in a LIB cell (a) schematic of the nail penetration, (b) a LIB cell with a small free-can window, (c) longitudinal section and (d) horizontal section of the CT of custom-designed nail and (e) dimension of the custom-designed nail.

However, the use of AlMgSiPb presented a mechanical trade-off. While its high thermal conductivity was advantageous, its hardness of 105 [140] is insufficient to pierce the cell can without being damaged. As a result, in experiments using this thermocouple-embedded nail, a portion of the cell can had to be removed in advance, as shown in Figure 32 (b). This modification created a free-can window, allowing the nail to be inserted directly into the internal layers without encountering the mechanical resistance of the outer casing. Due to the softness of the tip material and the precision of the embedded sensor, each nail could only be used once, as it would deform during penetration.

The necessity to remove part of the cell can also introduce certain limitations. Specifically, this modified setup prevented the study of critical penetration depth or thermal runaway behavior, since removing the can inhibited normal pressure buildup and prevented vent activation. Despite these limitations, the method provided unique insight into the early thermal response of a cell during different types of ISC events. It enabled the direct study of how thermal energy evolves based on the specific location, depth, and type of internal short circuit. Furthermore, this method offered an opportunity to analyze how cell architecture and electrode assembly influence localized heat generation. Because of the complexity of ISC phenomena, the insitu temperature measurement using this embedded thermocouple technique was always conducted in conjunction with ISC current measurements, as illustrated in the schematic in Figure 32 (a). The next section outlines the method developed to quantify ISC current using a shunt-resistor setup and external current supply.

Measurement of ISC Current using Shunt and Power Supply

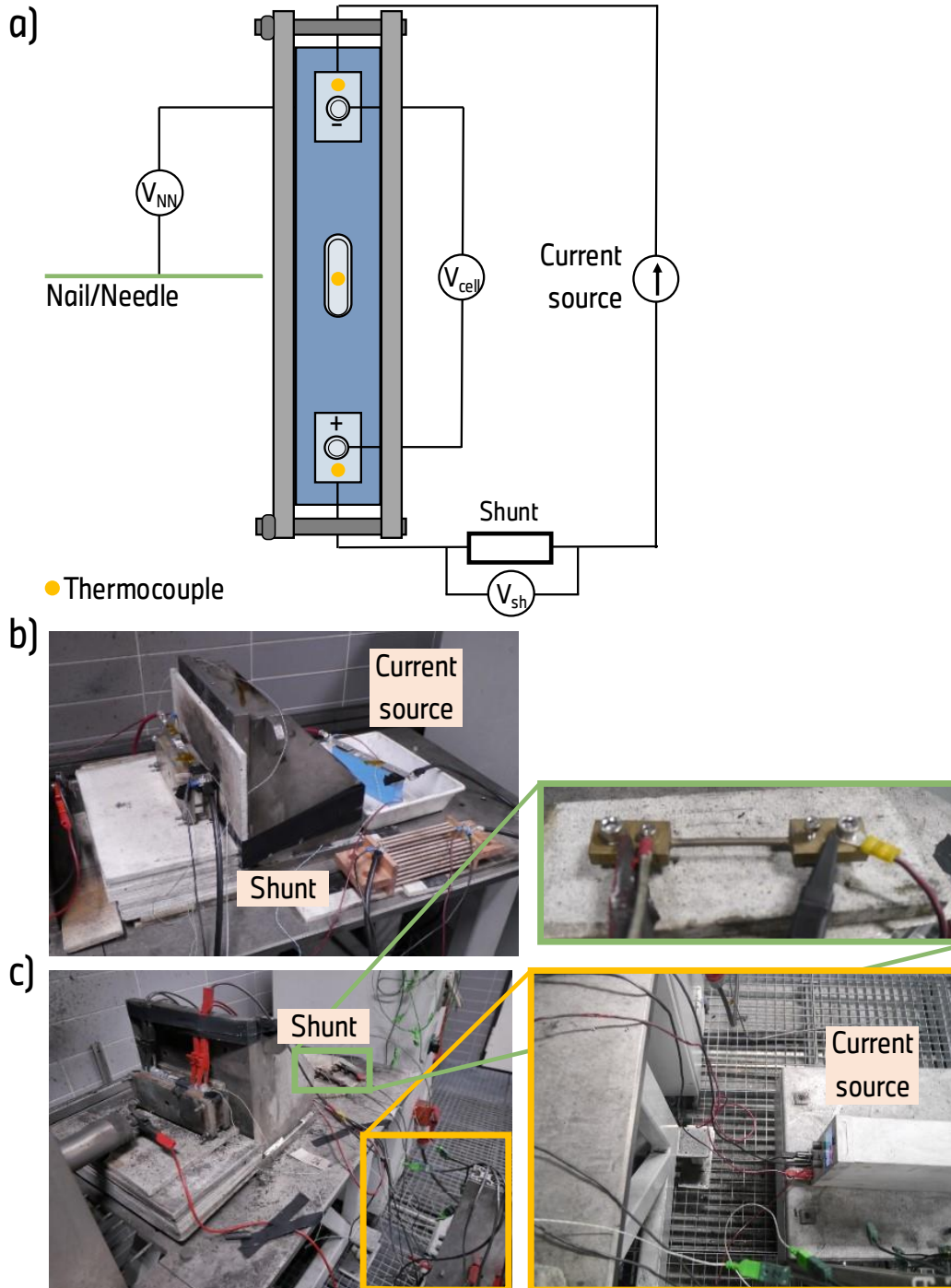


Figure 33. Investigation of ISC behavior by measuring ISC current (a) schematic of the nail penetration (b) picture of the test setup with a shunt (400 A, 75 mV) and the second victim cell with an identical capacity as the current source (c) picture of the test setup with a shunt (10 A, 75 mV) and power supply as the current source.

To quantitatively evaluate the magnitude of the internal short circuit (ISC) current, a method was established in this study based on a supplementary electrical circuit, in which the test cell was connected via a shunt resistor to an external current source. This source could either be a power supply operating in constant voltage mode or a victim cell acting as an additional energy reservoir (see Figure 33). The rationale behind this approach is that, when an ISC is triggered within the test cell, the resulting voltage drop due to internal charge depletion is immediately compensated by

current flow from the external source. In this configuration, the replenishment current serves as an indirect but practical measure of the actual ISC current.

The test cell was assumed to be at 100% state of charge, with a nominal open-circuit voltage of 4.2 V. In the case of using a power supply (see Figure 32 (c)), the voltage was held constant at 4.2 V with a defined maximum current limit of 6 A, ensuring that the compensation current did not exceed the safety limits of the experimental setup. Alternatively, when a fully charged victim cell was used as the source (see Figure 32 (b)), the compensation current could flow without such predefined limits, allowing the current to vary freely based on the demands of the ISC event. This setup replicates a parallel current-sharing configuration, where the external source dynamically maintains the cell voltage during and after the onset of the short.

To record the compensation current, a precision shunt resistor was placed in series between the external source and the test cell. The voltage drop across the shunt (V_{sh}) was continuously monitored and mathematically converted into the corresponding current (I_{sh}) using the known resistance of the shunt. Because the compensation current exactly matches the electrical energy lost due to the ISC, this current (I_{sh}) is interpreted as equivalent to the ISC current itself. The method assumes that the ISC causes a rapid drop in voltage at the shorting location, which is then restored by the current source, thus providing a direct measure of the charge flow associated with the short. While this approach does not allow spatial resolution of the ISC site or provide direct insight into the current distribution within the electrodes, it effectively quantifies the net electrical consequence of the ISC.

However, it is important to note a limitation of this method; since the external current source continuously compensates for the energy lost during the ISC, the system may artificially sustain or even amplify the extent of the short, compared to a real-world scenario where the cell discharges without external support. As a result, the measured ISC current could be higher than the actual current that would occur in a standalone cell undergoing an ISC.

This current measurement technique was applied extensively in Chapter 5 to analyze the effect of cell assembly structure on ISC dynamics. In that study, the test setup involved the use of a 40 A / 75 mV shunt resistor and a regulated power supply with an output voltage of 4.2 V and a maximum current limit of 6 A, enabling safe yet precise current quantification during the ISC events.

3.3 General Chemical or Cell Analysis

In addition to the thermal and thermodynamic characterization of cathode materials and the investigation of ISC-triggered thermal runaway at the cell level, this study also includes general analytical techniques to support the overall understanding of lithium-ion battery (LIB) cells. Two complementary methods — Inductively Coupled Plasma–Optical Emission Spectroscopy (ICP-OES) and Computed Tomography (CT) — were employed to obtain quantitative chemical compositions and to analyze internal cell structures, respectively.

3.3.1 Inductively Coupled Plasma-Optical Emission Spectroscopy (ICP-OES)

Particularly in the context of comparing various commercial automotive prismatic LIB cells, as discussed in Chapter 7, ICP-OES was carried out to determine the precise chemical composition of the cathode active materials from commercial automotive LIB cells.

The measurements were performed using the ARCOS system from SPECTRO Analytical Instruments GmbH. Cathode samples were harvested from fully charged cells at 100% state of charge (SOC100) and processed under controlled conditions. The harvested positive electrodes were first rinsed with dimethyl carbonate (DMC) to remove residual electrolyte. Following this step, the samples were dried under vacuum at 40 °C for two hours to ensure complete evaporation of the solvent. After drying, approximately 50 mg of active material was carefully scraped from the electrode surface

using a ceramic scalpel. This scraping process was conducted to avoid contamination from the aluminum current collector. The collected sample was then dissolved in aqua regia, prepared by mixing 3 mL hydrochloric acid (HCl) with 1 mL nitric acid (HNO₃). The solution was maintained at 90 °C for two hours to facilitate complete dissolution of metal oxides, after which it was allowed to cool and depressurized naturally. Subsequently, 5 mL of a 2-3 % Y(NO₃)₃ solution in nitric acid was added as an internal standard, and the mixture was diluted to a final volume of 50 mL using ultrapure water before measurement. For quantitative analysis of NMC and NCA chemistries, the following emission lines were used: Li 670.780 nm, Ni 231.604 nm, Mn 257.611 nm, Co 237.862 nm and Al 396.152 nm.

It is important to note that the scraped cathode material is not composed exclusively of the active material (e.g., NMC or NCA), but also contains conductive additives and binder components. Therefore, the measured weight percentages of elements such as Li, Ni, Mn, Co, Al, and O do not sum to 100%. To address this, two correction approaches were considered in order to estimate the true stoichiometric composition of the cathode active materials.

- 1. Correction Method: In the first method, the total weight percentage of Li, Ni, Mn, Co, Al, and O was normalized to 100%, under the assumption that all these elements originated solely from the cathode active material. This correction assumes that no additives or coatings contain any of the listed elements.
- 2. Correction Method: In the second method, the molar ratio of transition metals and Al was normalized to a total value of 1 (e.g., Ni + Mn + Co = 1 for NMC; Ni + Co + Al = 1 for NCA), and the oxygen molar ratio was fixed at 2, consistent with the expected stoichiometry of layered oxide compounds (Li_aNi_xMn_yCo_{1-x-y}O₂ or in Li_aNi_xAl_yCo_{1-x-y}O₂). This approach accommodates the fact that part of the measured oxygen may originate from non-active material components.

As an example, the ICP-OES results for the cathode from cell type A are summarized in the table below, showing both the raw data and the corrected compositions according to the two methods described above.

Table 16. ICP Measurement of positive electrode from cell type A in chapter 7 and determination of chemical composition based on two different assumptions.

Atom	Raw data [wt%]	1. Correction Method [wt%]	2. Correction Method [wt%]
Li	2.40	2.40	2.20
Ni	38.80	38.81	35.64
Mn	17.64	17.65	16.20
Co	6.29	6.29	6.00
Al	–	–	–
O	34.84	34.85	32.00
total	99.97	100.00	91.82
Determined composition		Li _{0.35} Ni _{0.66} Mn _{0.32} Co _{0.11} O _{2.18}	Li _{0.32} Ni _{0.61} Mn _{0.29} Co _{0.10} O ₂

The second correction method was found to yield more chemically consistent stoichiometries, particularly regarding the oxygen content, which better aligns with known structures of layered cathode materials. Therefore, in this work, all chemical compositions discussed in Chapter 7 were determined using the second correction method.

3.3.2 Computed Tomography

Computed Tomography (CT) was employed as a non-destructive, spatially resolved imaging technique to investigate the internal structure of LIB cells without dismantling them. In this work, CT was specifically used in support of needle penetration test optimization. It was applied to

validate penetration depth measurements and to examine internal deformation or failure mechanisms caused by penetration.

The CT imaging was conducted using Waygate v|tomex|m, operated with 270 kV and 370 μ A and a voxel size of 60 μ m. Scans were processed using Volumegraphics studio to reconstruct high-resolution images of the cell interiors. By integrating CT analysis with electrochemical, thermal, and mechanical testing, a more comprehensive picture of the cell's behavior under abuse conditions was achieved. CT thereby played a crucial supporting role in validating the nail penetration test methodology, especially for quantifying penetration depth and interpreting the failure mechanisms observed during TR events.

4 Determination of the Enthalpies of Formation of NMCs

The primary objective of this work is to validate the performance and define the limitations of the MHTC by determining the enthalpies of formation of two commercial NMC compounds, NMC622 and NMC85. These results are compared with those obtained using the well-established Alexsys-1000 at KIT, whose method has been thoroughly established — primarily through the work of Masoumi [7] — and has been widely used to determine the enthalpies of formation of various NMCs. Consequently, the results from the Alexsys-1000 serve as a reference standard to assess the accuracy and limitations of the MHTC in this study.

In addition, the second purpose of this work is to extend the investigation to state-of-the-art NMC active materials with higher Ni-molar ratio. This starts from comparing a commercial NMC622 against the same composition that was synthesized at a lab-scale and previously studied by Masoumi [7] and extends to NMC85 and NMC94 that have never been investigated before. As demonstrated in Figure 5 and Table 7, various NMC compositions have been examined by Alexsys. However, those studies were limited to a maximum Ni-molar ratio of 0.8 and were based on small-scale, laboratory-synthesized samples without coating and with insufficient Li molar ratio ($a < 1$ in $\text{Li}_a\text{Ni}_x\text{Mn}_y\text{Co}_{1-x-y}\text{O}_2$) that do not necessarily reflect the composition of NMC in commercial automotive LIB cells.

To meet those two goals, three NMC compositions were selected based on the following considerations:

- They must be commercial NMC materials currently used in automotive LIB cells.
- **NMC622 ($\text{LiNi}_{0.6}\text{Mn}_{0.2}\text{Co}_{0.2}\text{O}_2$)** has been previously investigated at a lab-produced scale but not as a commercial material. The investigated NMC622 from Umicore in this study is mass-produced for automotive LIB cell and has coating.
- **NMC85 ($\text{LiNi}_{0.85}\text{Mn}_{0.05}\text{Co}_{0.2}\text{O}_2$)** and **NMC94 ($\text{LiNi}_{0.94}\text{Mn}_{0.01}\text{Co}_{0.05}\text{O}_2$)** from Umicore represents a state-of-the-art composition with a higher Ni-molar ratio that has not been previously studied.

Although those commercial NMC samples contain a small amount of coating less than 0.5 wt% that precludes a pure composition analysis by ICP-OES, the purity of studied sample is high (> 99.5 %). Most of all, the investigation of those three commercial NMCs provides critical insights into the thermodynamic stability of NMCs as used in commercial automotive LIB cells.

The enthalpies of formation for three series of NMC samples with selected stoichiometries were determined by high temperature drop solution calorimetry (MHTC and/or Alexsys-1000) using a $3\text{Na}_2\text{O} \cdot 4\text{MoO}_3$ solvent at 701 °C under an argon atmosphere. Every step including solvent synthesis, calibration and measurements was carried out as presented in Section 3.1.3. In each experiment, a series of pellets from a given compound were sequentially dropped into the molten solvent. In this chapter, enthalpies of drop solution for each compound are presented and enthalpies of formation are calculated from the thermodynamic cycles from the average enthalpy of drop solution.

4.1 Thermodynamic Cycles and Reaction Mechanisms

When NMC samples are dropped into a high temperature solution calorimeter with $3\text{Na}_2\text{O}\cdot 4\text{MoO}_3$ solvent, several reactions happen that undergo various changes due to temperature, dissolution and oxidation/reduction et cetera. In this section, those reaction mechanisms in thermodynamic cycles are outlined, so that the enthalpy of formation can be determined from its own thermodynamic cycle.

4.1.1 Reactions in the Thermodynamic Cycle

The standard enthalpies of formation of various $\text{LiNi}_x\text{Mn}_y\text{Co}_{1-x-y}\text{O}_2$ compositions can be calculated with respect to their constituent binary oxides — Li_2O , MnO_2 , NiO and CoO — and oxygen (O_2). A thermodynamic cycle, as shown in Table 17, outlines the reactions involved in calculating the enthalpies of formation from their oxides of NMCs.

Table 17. Reactions in thermodynamic cycle which are used for the determination of the enthalpy of formation from oxides of $\text{LiNi}_x\text{Mn}_y\text{Co}_{1-x-y}\text{O}_2$ compounds from binary oxides and oxygen using high temperature drop solution calorimetry in $3\text{Na}_2\text{O}\cdot 4\text{MoO}_3$ solvent at 701 °C.

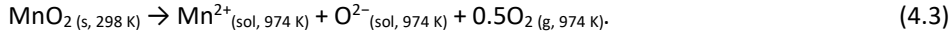
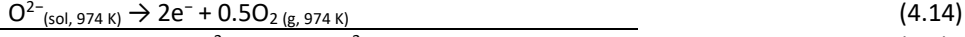
Reaction	Change in enthalpy, ΔH
$\text{Li}_2\text{O}_{(s, 298 \text{ K})} \rightarrow [2\text{Li}^+ + \text{O}^{2-}]_{(\text{sol}, 974 \text{ K})}$	$\Delta_{\text{ds}}H^{974}(\text{Li}_2\text{O})$ (4.1)
$\text{NiO}_{(s, 298 \text{ K})} \rightarrow [\text{Ni}^{2+} + \text{O}^{2-}]_{(\text{sol}, 974 \text{ K})}$	$\Delta_{\text{ds}}H^{974}(\text{NiO})$ (4.2)
$\text{MnO}_{2(s, 298 \text{ K})} \rightarrow [\text{Mn}^{2+} + \text{O}^{2-}]_{(\text{sol}, 974 \text{ K})} + 0.5\text{O}_{2(s, 974 \text{ K})}$	$\Delta_{\text{ds}}H^{974}(\text{MnO}_2)$ (4.3)
$\text{CoO}_{(s, 298 \text{ K})} \rightarrow [\text{Co}^{2+} + \text{O}^{2-}]_{(\text{sol}, 974 \text{ K})}$	$\Delta_{\text{ds}}H^{974}(\text{CoO})$ (4.4)
$\text{O}_{2(g, 298 \text{ K})} \rightarrow \text{O}_{2(g, 974 \text{ K})}$	$\Delta H^{974}(\text{O}_2)$ (4.5)
$\text{Li}(\text{Ni}_{0.4}^{3+}\text{Ni}_{0.2}^{2+}\text{Mn}_{0.2}^{4+}\text{Co}_{0.2}^{3+})\text{O}_2_{(s, 298 \text{ K})} \rightarrow$ $0.5[2\text{Li}^+ + \text{O}^{2-}]_{(\text{sol}, 974 \text{ K})} + 0.6[\text{Ni}^{2+} + \text{O}^{2-}]_{(\text{sol}, 974 \text{ K})}$ $+ 0.2[\text{Mn}^{2+} + \text{O}^{2-}]_{(\text{sol}, 974 \text{ K})} + 0.2[\text{Co}^{2+} + \text{O}^{2-}]_{(\text{sol}, 974 \text{ K})} + 0.25\text{O}_{2(g, 974 \text{ K})}$	$\Delta_{\text{ds}}H^{974}(\text{NMC622})$ (4.6)
$\text{Li}(\text{Ni}_{0.8}^{3+}\text{Ni}_{0.05}^{2+}\text{Mn}_{0.05}^{4+}\text{Co}_{0.1}^{3+})\text{O}_2_{(s, 298 \text{ K})} \rightarrow$ $0.5[2\text{Li}^+ + \text{O}^{2-}]_{(\text{sol}, 974 \text{ K})} + 0.85[\text{Ni}^{2+} + \text{O}^{2-}]_{(\text{sol}, 974 \text{ K})}$ $+ 0.05[\text{Mn}^{2+} + \text{O}^{2-}]_{(\text{sol}, 974 \text{ K})} + 0.1[\text{Co}^{2+} + \text{O}^{2-}]_{(\text{sol}, 974 \text{ K})} + 0.25\text{O}_{2(g, 974 \text{ K})}$	$\Delta_{\text{ds}}H^{974}(\text{NMC85})$ (4.7)
$\text{Li}(\text{Ni}_{0.93}^{3+}\text{Ni}_{0.01}^{2+}\text{Mn}_{0.01}^{4+}\text{Co}_{0.05}^{3+})\text{O}_2_{(s, 298 \text{ K})} \rightarrow$ $0.5[2\text{Li}^+ + \text{O}^{2-}]_{(\text{sol}, 974 \text{ K})} + 0.85[\text{Ni}^{2+} + \text{O}^{2-}]_{(\text{sol}, 974 \text{ K})}$ $+ 0.05[\text{Mn}^{2+} + \text{O}^{2-}]_{(\text{sol}, 974 \text{ K})} + 0.1[\text{Co}^{2+} + \text{O}^{2-}]_{(\text{sol}, 974 \text{ K})} + 0.25\text{O}_{2(g, 974 \text{ K})}$	$\Delta_{\text{ds}}H^{974}(\text{NMC94})$ (4.8)
$0.5\text{Li}_2\text{O}_{(s, 298 \text{ K})} + 0.6\text{NiO}_{(s, 298 \text{ K})} + 0.2\text{MnO}_{2(s, 298 \text{ K})} + 0.2\text{CoO}_{(s, 298 \text{ K})}$ $+ 0.15\text{O}_{2(g, 298 \text{ K})} \rightarrow \text{Li}(\text{Ni}_{0.4}^{3+}\text{Ni}_{0.2}^{2+}\text{Mn}_{0.2}^{4+}\text{Co}_{0.2}^{3+})\text{O}_2_{(s, 298 \text{ K})}$	$\Delta_{\text{f}}H^{\Theta, \text{oxides}}(\text{NMC622})$ (4.9)
$0.5\text{Li}_2\text{O}_{(s, 298 \text{ K})} + 0.85\text{NiO}_{(s, 298 \text{ K})} + 0.05\text{MnO}_{2(s, 298 \text{ K})} + 0.1\text{CoO}_{(s, 298 \text{ K})}$ $+ 0.225 \text{O}_{2(g, 298 \text{ K})} \rightarrow \text{Li}(\text{Ni}_{0.8}^{3+}\text{Ni}_{0.05}^{2+}\text{Mn}_{0.05}^{4+}\text{Co}_{0.1}^{3+})\text{O}_2_{(s, 298 \text{ K})}$	$\Delta_{\text{f}}H^{\Theta, \text{oxides}}(\text{NMC85})$ (4.10)
$0.5\text{Li}_2\text{O}_{(s, 298 \text{ K})} + 0.94\text{NiO}_{(s, 298 \text{ K})} + 0.01\text{MnO}_{2(s, 298 \text{ K})} + 0.05\text{CoO}_{(s, 298 \text{ K})}$ $+ 0.245 \text{O}_{2(g, 298 \text{ K})} \rightarrow \text{Li}(\text{Ni}_{0.93}^{3+}\text{Ni}_{0.01}^{2+}\text{Mn}_{0.01}^{4+}\text{Co}_{0.05}^{3+})\text{O}_2_{(s, 298 \text{ K})}$	$\Delta_{\text{f}}H^{\Theta, \text{oxides}}(\text{NMC94})$ (4.11)

Reactions (4.1) to (4.4) represent reactions in a drop solution calorimetry of the binary oxides in $3\text{Na}_2\text{O}\cdot 4\text{MoO}_3$ solvent at 701 °C (974 K) under argon atmosphere, while reactions (4.6) to (4.8) show the drop solution calorimetry of the NMC622, NMC85 and NMC94 compounds, respectively, at the same solvent and temperature.

Within the molten $3\text{Na}_2\text{O}\cdot 4\text{MoO}_3$ solvent, the decomposition of Na_2O at the temperature of calorimetry establishes an equilibrium between charged molybdate species (MoO_4^{2-} and $\text{Mo}_2\text{O}_7^{2-}$), which acts as a buffer for oxygen anions (O^{2-}) evolving from reactions of (4.1) to (4.4), (4.6) and (4.8), according to the reaction as demonstrated in reaction (3.6) ($\text{O}^{2-} + \text{Mo}_2\text{O}_7^{2-} \leftrightarrow 2\text{MoO}_4^{2-}$). For example, when NMC samples are introduced into the molten solvent $3\text{Na}_2\text{O}\cdot 4\text{MoO}_3$, the additional oxide shifts the buffer equilibrium to the right, consuming excess oxygen anions while maintaining the specific equilibrium constant.

However, upon dissolution, transition metal oxides in NMC may undergo changes in oxidation state. For instance, Mn, initially in a tetravalent state (Mn^{4+}) in MnO_2 , is reduced to a divalent state (Mn^{2+}) upon dissolution in the molten sodium molybdate (4.12)-(4.13), where the produced oxygen anions

shift the position of the buffer reaction to the right, namely $O^{2-} + Mo_2O_7^{2-} \rightarrow 2MoO_4^{2-}$, to consume the additional oxygen anions in the reaction of (3.6). The oxidation state of transition metal Mn changes by reducing from Mn^{4+} to Mn^{2+} as presented at (4.13). The electrons required for the reduction are provided through oxidation of oxygen anions present in the buffer solution (4.14). The complete reaction would be (4.3). This dissolution process can be described in these several steps:



Since such reactions release oxygen gas, it is essential to perform the drop solution experiments under an argon atmosphere to reduce the partial pressure of O_2 , thereby shifting the reaction equilibrium toward complete dissolution. The oxygen anions consumed in reaction (4.14) are compensated by the buffer reaction of (3.6), $2MoO_4^{2-} \rightarrow O^{2-} + Mo_2O_7^{2-}$ [7,120].

The enthalpy values for reactions (4.1) to (4.4) for the binary oxides have not been determined experimentally in this work because they have been reported in multiple studies (see Table 18). Table 18 compiles the literature values for the enthalpies of drop solution ($\Delta_{ds}H^{974}$) and the formation enthalpies from the elements ($\Delta_f H^{\Theta, elements}$) for Li_2O , NiO , MnO_2 and CoO . The values used in this study for NMC622, NMC85 and NMC94 are marked in green in Table 18. For comparison with the enthalpy of formation data of NMC622 reported by Masoumi [7], the same reference values for $\Delta_{ds}H^{974}$ and $\Delta_f H^{\Theta, elements}$ have been selected.

Table 18. Values of enthalpy of drop solution of binary oxides in $3Na_2O \cdot 4MoO_3$ solvent at 974 K that can be possibly used in this study as reference.

Sample	$\Delta_{ds}H^{974}$ [kJ/mol]	The number of drops	Source	$\Delta_f H^{\Theta, elements}$ [kJ/mol]	Source
Li_2O	-93.02 ± 2.24	unknown	[70]	-597.935 ± 0.334	[141]
	-90.3 ± 2.5	unknown	[142]		
NiO	35.73 ± 0.95	8	[70]	-239.743 ± 0.543	[141]
				-239.3 ± 0.4	[143]
MnO_2	128.92 ± 0.91	11	[144]	-521.493 ± 0.836	[141]
	124.92 ± 1.03	unknown	[145]		
CoO	15.35 ± 0.46	7	[70]	-238.906 ± 1.255	[141]
	16.45 ± 0.69	14	[146]	-237.9 ± 1.3	[143]
	15.66 ± 0.59	8	[147]		

The reaction (4.5) in the thermodynamic cycle in Table 17 corresponds to heating up the gaseous oxygen from room temperature (25 °C) to the temperature of calorimetry (701 °C). Its enthalpy changes equals the heat content of gaseous oxygen from room temperature to the temperature of calorimetry, because the heat of dissolution of heated gaseous oxygen (701 °C) in the solvent is neglected due to unfeasibility of such a measurement. The set-up of the high temperature drop solution calorimeter has an open system for gaseous components. Therefore, the reaction of (4.5) can be expressed as $\int_{298}^{974} C_p(O_2)dT$ and this value is determined as 5.37 J/mol using the following equation [143].

$$\int_{298}^{974} C_p(O_2)dT = [56.58 - 5.255 \cdot 10^{-3} \cdot T + 6.856 \cdot 10^5 \cdot T^{-2} - 5.780 \cdot 10^2 \cdot T^{-0.5} + 1.113 \cdot 10^{-6} \cdot T^2]_{T=974} - [56.58 - 5.255 \cdot 10^{-3} \cdot T + 6.856 \cdot 10^5 \cdot T^{-2} - 5.780 \cdot 10^2 \cdot T^{-0.5} + 1.113 \cdot 10^{-6} \cdot T^2]_{T=298} \quad (4.15)$$

4.1.2 Thermodynamic Cycles for NMC Formation

Concerning the reactants of the reactions (4.6) to (4.8) in Table 17, the main oxidation state of transition metals in NMC compound can vary. While the oxidation states of Ni, Mn, and Co in NMC with low Ni molar ratio are mainly +2, +4, and +3, respectively, the oxidation states of Ni in NMC with higher Ni molar ratio can be partially +3 and Mn and Co are still mainly tetravalent and trivalent [7]. It is presumed that the oxidation state of Ni changes gradually from Ni^{2+} to Ni^{3+} with increasing Ni molar ratio. The Ni^{2+} content in NMC622, NMC85 and NMC94 can be mathematically determined to be $\text{Li}(\text{Ni}_{0.4}^{3+}\text{Ni}_{0.2}^{2+}\text{Mn}_{0.2}^{4+}\text{Co}_{0.2}^{3+})\text{O}_2$, $\text{Li}(\text{Ni}_{0.8}^{3+}\text{Ni}_{0.05}^{2+}\text{Mn}_{0.05}^{4+}\text{Co}_{0.1}^{3+})\text{O}_2$ and $\text{Li}(\text{Ni}_{0.93}^{3+}\text{Ni}_{0.01}^{2+}\text{Mn}_{0.01}^{4+}\text{Co}_{0.05}^{3+})\text{O}_2$ respectively, to maintain electroneutrality in the theoretical formula.

Also, concerning the products of the reactions (4.6) to (4.8), the oxidation state of Ni, Mn and Co in NMC samples change in the sodium molybdate solvent. The main oxidation states of those in $3\text{Na}_2\text{O} \cdot 4\text{MoO}_3$ at 701 °C has been determined by Navrotsky's group and are found to be mainly in the forms of Co^{2+} [147], Mn^{2+} [144] and Ni^{2+} [70]. Therefore, the product of the dissolution reactions of NMC622, NMC85 and NMC94 are demonstrated with $\text{Ni}^{2+}\text{O}^{2-}$, $\text{Mn}^{2+}\text{O}^{2-}$ and $\text{Co}^{2+}\text{O}^{2-}$ and the dissolution of NMC samples with $\text{Ni}^{3+}/\text{Ni}^{2+}$, Mn^{4+} and Co^{3+} valence states involves the reduction of Mn, Co and part of Ni cation.

The standard enthalpies of formation from oxides, $\Delta_f H^{\ominus, \text{oxides}}(\text{LiNi}_{0.6}\text{Mn}_{0.2}\text{Co}_{0.2}\text{O}_2)$, $\Delta_f H^{\ominus, \text{oxides}}(\text{LiNi}_{0.85}\text{Mn}_{0.05}\text{Co}_{0.1}\text{O}_2)$ and $\Delta_f H^{\ominus, \text{oxides}}(\text{LiNi}_{0.94}\text{Mn}_{0.01}\text{Co}_{0.05}\text{O}_2)$ are equal to the enthalpy changes in the reaction (4.9) to (4.11) in Table 17. Those binary oxides in those reactions are chosen as reactants that are stable at room temperature and pressure with available data of their enthalpies of drop solution as seen in Table 18. To calculate enthalpies of formation from oxides, thermodynamic cycles for each NMC are generated based on the dissolution enthalpies of those binary oxides that are stable at given conditions and NMCs as above in Table 19.

Table 19. Thermodynamic cycles used to determine the enthalpies of formation of NMC622, NMC85 and NMC94 from oxides and O_2 .

Thermodynamic Cycle of $\Delta_f H^{\ominus, \text{oxides}}(\text{LiNi}_{0.6}\text{Mn}_{0.2}\text{Co}_{0.2}\text{O}_2)$ from reaction (4.9)		
$0.5\Delta_{\text{ds}}H(\text{Li}_2\text{O})$	$0.5\text{Li}_2\text{O}_{(\text{s}, 298 \text{ K})}$	$0.5[2\text{Li}^+ + \text{O}^{2-}]_{(\text{sol}, 974 \text{ K})}$
$0.6\Delta_{\text{ds}}H(\text{NiO})$	$0.6\text{NiO}_{(\text{s}, 298 \text{ K})}$	$0.6[\text{Ni}^{2+} + \text{O}^{2-}]_{(\text{sol}, 974 \text{ K})}$
$0.2\Delta_{\text{ds}}H(\text{MnO}_2)$	$0.2\text{MnO}_{2(\text{s}, 298 \text{ K})}$	$0.2[\text{Mn}^{2+} + \text{O}^{2-}]_{(\text{sol}, 974 \text{ K})} + 0.1\text{O}_{2(\text{g}, 974 \text{ K})}$
$0.2\Delta_{\text{ds}}H(\text{CoO})$	$0.2\text{CoO}_{(\text{s}, 298 \text{ K})}$	$0.2[\text{Co}^{2+} + \text{O}^{2-}]_{(\text{sol}, 974 \text{ K})}$
$0.15\int_{298}^{974} C_p(\text{O}_2)dT$	$0.15\text{O}_{2(\text{g}, 298 \text{ K})}$	$\rightarrow 0.15\text{O}_{2(\text{g}, 974 \text{ K})}$
$-\Delta_{\text{ds}}H(\text{LiNi}_{0.6}\text{Mn}_{0.2}\text{Co}_{0.2}\text{O}_2)$	$0.5[2\text{Li}^+ + \text{O}^{2-}]_{(\text{sol}, 974 \text{ K})} +$ $0.6[\text{Ni}^{2+} + \text{O}^{2-}]_{(\text{sol}, 974 \text{ K})} +$ $0.2[\text{Mn}^{2+} + \text{O}^{2-}]_{(\text{sol}, 974 \text{ K})} +$ $0.2[\text{Co}^{2+} + \text{O}^{2-}]_{(\text{sol}, 974 \text{ K})} +$ $0.25\text{O}_{2(\text{g}, 974 \text{ K})}$ $\text{Li}(\text{Ni}_{0.4}^{3+}\text{Ni}_{0.2}^{2+}\text{Mn}_{0.2}^{4+}\text{Co}_{0.2}^{3+})\text{O}_2 (\text{s}, 298 \text{ K})$	
$\Delta_f H^{\ominus, \text{oxides}}(\text{LiNi}_{0.6}\text{Mn}_{0.2}\text{Co}_{0.2}\text{O}_2) =$ $0.5\Delta_{\text{ds}}H(\text{Li}_2\text{O}) + 0.6\Delta_{\text{ds}}H(\text{NiO}) + 0.2\Delta_{\text{ds}}H(\text{MnO}_2) + 0.2\Delta_{\text{ds}}H(\text{CoO}) + 0.15\int_{298}^{974} C_p(\text{O}_2) - \Delta_{\text{ds}}H(\text{LiNi}_{0.6}\text{Mn}_{0.2}\text{Co}_{0.2}\text{O}_2)$		
Thermodynamic Cycle of $\Delta_f H^{\ominus, \text{oxides}}(\text{LiNi}_{0.85}\text{Mn}_{0.05}\text{Co}_{0.1}\text{O}_2)$ from reaction (4.10)		
$0.5\Delta_{\text{ds}}H(\text{Li}_2\text{O})$	$0.5\text{Li}_2\text{O}_{(\text{s}, 298 \text{ K})}$	$0.5[2\text{Li}^+ + \text{O}^{2-}]_{(\text{sol}, 974 \text{ K})}$
$0.85\Delta_{\text{ds}}H(\text{NiO})$	$0.85\text{NiO}_{(\text{s}, 298 \text{ K})}$	$0.85[\text{Ni}^{2+} + \text{O}^{2-}]_{(\text{sol}, 974 \text{ K})}$
$0.05\Delta_{\text{ds}}H(\text{MnO}_2)$	$0.05\text{MnO}_{2(\text{s}, 298 \text{ K})}$	$0.05[\text{Mn}^{2+} + \text{O}^{2-}]_{(\text{sol}, 974 \text{ K})} + 0.025\text{O}_{2(\text{g}, 974 \text{ K})}$
$0.1\Delta_{\text{ds}}H(\text{CoO})$	$0.1\text{CoO}_{(\text{s}, 298 \text{ K})}$	$0.1[\text{Co}^{2+} + \text{O}^{2-}]_{(\text{sol}, 974 \text{ K})}$
$0.225\int_{298}^{974} C_p(\text{O}_2)dT$	$0.225\text{O}_{2(\text{g}, 298 \text{ K})}$	$\rightarrow 0.225\text{O}_{2(\text{g}, 974 \text{ K})}$
$-\Delta_{\text{ds}}H(\text{LiNi}_{0.85}\text{Mn}_{0.05}\text{Co}_{0.1}\text{O}_2)$	$0.5[2\text{Li}^+ + \text{O}^{2-}]_{(\text{sol}, 974 \text{ K})} +$ $0.85[\text{Ni}^{2+} + \text{O}^{2-}]_{(\text{sol}, 974 \text{ K})} +$ $0.05[\text{Mn}^{2+} + \text{O}^{2-}]_{(\text{sol}, 974 \text{ K})} +$ $0.1[\text{Co}^{2+} + \text{O}^{2-}]_{(\text{sol}, 974 \text{ K})} +$ $0.25\text{O}_{2(\text{g}, 974 \text{ K})}$ $\text{Li}(\text{Ni}_{0.8}^{3+}\text{Ni}_{0.05}^{2+}\text{Mn}_{0.05}^{4+}\text{Co}_{0.1}^{3+})\text{O}_2 (\text{s}, 298 \text{ K})$	
$\Delta_f H^{\ominus, \text{oxides}}(\text{LiNi}_{0.85}\text{Mn}_{0.05}\text{Co}_{0.1}\text{O}_2) =$ $0.5\Delta_{\text{ds}}H(\text{Li}_2\text{O}) + 0.85\Delta_{\text{ds}}H(\text{NiO}) + 0.05\Delta_{\text{ds}}H(\text{MnO}_2) + 0.1\Delta_{\text{ds}}H(\text{CoO}) + 0.225\int_{298}^{974} C_p(\text{O}_2) - \Delta_{\text{ds}}H(\text{LiNi}_{0.85}\text{Mn}_{0.05}\text{Co}_{0.1}\text{O}_2)$		

Thermodynamic Cycle of $\Delta_f H^{\Theta, \text{oxides}}(\text{LiNi}_{0.94}\text{Mn}_{0.01}\text{Co}_{0.05}\text{O}_2)$ from reaction (4.11)		
$0.5\Delta_{\text{ds}}H(\text{Li}_2\text{O})$	$0.5\text{Li}_2\text{O}_{(\text{s}, 298 \text{ K})}$	$0.5[2\text{Li}^+ + \text{O}^{2-}]_{(\text{sol}, 974 \text{ K})}$
$0.94\Delta_{\text{ds}}H(\text{NiO})$	$0.94\text{NiO}_{(\text{s}, 298 \text{ K})}$	$0.94[\text{Ni}^{2+} + \text{O}^{2-}]_{(\text{sol}, 974 \text{ K})}$
$0.01\Delta_{\text{ds}}H(\text{MnO}_2)$	$0.01\text{MnO}_{2(\text{s}, 298 \text{ K})}$	$0.01[\text{Mn}^{2+} + \text{O}^{2-}]_{(\text{sol}, 974 \text{ K})} + 0.005\text{O}_{2(\text{g}, 974 \text{ K})}$
$0.05\Delta_{\text{ds}}H(\text{CoO})$	$0.05\text{CoO}_{(\text{s}, 298 \text{ K})}$	$0.05[\text{Co}^{2+} + \text{O}^{2-}]_{(\text{sol}, 974 \text{ K})}$
$0.245 \int_{298}^{974} C_p(\text{O}_2)dT$	$0.245\text{O}_{2(\text{g}, 298 \text{ K})}$	$\rightarrow 0.245\text{O}_{2(\text{g}, 974 \text{ K})}$
$-\Delta_{\text{ds}}H(\text{LiNi}_{0.94}\text{Mn}_{0.01}\text{Co}_{0.05}\text{O}_2)$	$0.5[2\text{Li}^+ + \text{O}^{2-}]_{(\text{sol}, 974 \text{ K})} +$ $0.94[\text{Ni}^{2+} + \text{O}^{2-}]_{(\text{sol}, 974 \text{ K})} +$ $0.01[\text{Mn}^{2+} + \text{O}^{2-}]_{(\text{sol}, 974 \text{ K})} +$ $0.05[\text{Co}^{2+} + \text{O}^{2-}]_{(\text{sol}, 974 \text{ K})}$ $+ 0.25\text{O}_{2(\text{g}, 974 \text{ K})}$	$\text{Li}(\text{Ni}_{0.93}^{3+}\text{Ni}_{0.01}^{2+}\text{Mn}_{0.01}^{4+}\text{Co}_{0.05}^{3+})\text{O}_2_{(\text{s}, 298 \text{ K})}$
$\Delta_f H^{\Theta, \text{oxides}}(\text{LiNi}_{0.94}\text{Mn}_{0.01}\text{Co}_{0.05}\text{O}_2) =$		
$0.5\Delta_{\text{ds}}H(\text{Li}_2\text{O}) + 0.94\Delta_{\text{ds}}H(\text{NiO}) + 0.01\Delta_{\text{ds}}H(\text{MnO}_2) + 0.05\Delta_{\text{ds}}H(\text{CoO}) + 0.245 \int_{298}^{974} C_p(\text{O}_2)dT - \Delta_{\text{ds}}H(\text{LiNi}_{0.94}\text{Mn}_{0.01}\text{Co}_{0.05}\text{O}_2)$		

Using these cycles, the standard enthalpies of formation from the binary oxides for NMC622, NMC85 and NMC94 are determined (see Table 19):

$$\Delta_f H^{\Theta, \text{oxides}}(\text{LiNi}_{0.6}\text{Mn}_{0.2}\text{Co}_{0.2}\text{O}_2) = 0.5\Delta_{\text{ds}}H(\text{Li}_2\text{O}) + 0.6\Delta_{\text{ds}}H(\text{NiO}) + 0.2\Delta_{\text{ds}}H(\text{MnO}_2) + 0.2\Delta_{\text{ds}}H(\text{CoO}) + 0.15 \int_{298}^{974} C_p(\text{O}_2)dT - \Delta_{\text{ds}}H(\text{LiNi}_{0.6}\text{Mn}_{0.2}\text{Co}_{0.2}\text{O}_2) \quad (4.16)$$

$$\Delta_f H^{\Theta, \text{oxides}}(\text{LiNi}_{0.85}\text{Mn}_{0.05}\text{Co}_{0.1}\text{O}_2) = 0.5\Delta_{\text{ds}}H(\text{Li}_2\text{O}) + 0.85\Delta_{\text{ds}}H(\text{NiO}) + 0.05\Delta_{\text{ds}}H(\text{MnO}_2) + 0.1\Delta_{\text{ds}}H(\text{CoO}) + 0.225 \int_{298}^{974} C_p(\text{O}_2)dT - \Delta_{\text{ds}}H(\text{LiNi}_{0.85}\text{Mn}_{0.05}\text{Co}_{0.1}\text{O}_2) \quad (4.17)$$

$$\Delta_f H^{\Theta, \text{oxides}}(\text{LiNi}_{0.94}\text{Mn}_{0.01}\text{Co}_{0.05}\text{O}_2) = 0.5\Delta_{\text{ds}}H(\text{Li}_2\text{O}) + 0.94\Delta_{\text{ds}}H(\text{NiO}) + 0.01\Delta_{\text{ds}}H(\text{MnO}_2) + 0.05\Delta_{\text{ds}}H(\text{CoO}) + 0.245 \int_{298}^{974} C_p(\text{O}_2)dT - \Delta_{\text{ds}}H(\text{LiNi}_{0.94}\text{Mn}_{0.01}\text{Co}_{0.05}\text{O}_2) \quad (4.18)$$

Subsequently, the standard enthalpy of formation from their elements can be calculated as follows. In these calculations, the standard enthalpy of formation of oxygen, $\Delta_f H^{\Theta, \text{elements}}(\text{O}_2)$ is omitted, since no net energy change occurs between the standard state of $\text{O}_{2(\text{g})}$ and $\text{O}_{2(\text{g})}$ under the conditions considered.

$$\Delta_f H^{\Theta, \text{elements}}(\text{LiNi}_{0.6}\text{Mn}_{0.2}\text{Co}_{0.2}\text{O}_2) = \Delta_f H^{\Theta, \text{oxides}}(\text{LiNi}_{0.6}\text{Mn}_{0.2}\text{Co}_{0.2}\text{O}_2) + 0.5\Delta_f H^{\Theta, \text{elements}}(\text{Li}_2\text{O}) + 0.6\Delta_f H^{\Theta, \text{elements}}(\text{NiO}) + 0.2\Delta_f H^{\Theta, \text{elements}}(\text{MnO}_2) + 0.2\Delta_f H^{\Theta, \text{elements}}(\text{CoO}) \quad (4.19)$$

$$\Delta_f H^{\Theta, \text{elements}}(\text{LiNi}_{0.85}\text{Mn}_{0.05}\text{Co}_{0.1}\text{O}_2) = \Delta_f H^{\Theta, \text{oxides}}(\text{LiNi}_{0.85}\text{Mn}_{0.05}\text{Co}_{0.1}\text{O}_2) + 0.5\Delta_f H^{\Theta, \text{elements}}(\text{Li}_2\text{O}) + 0.85\Delta_f H^{\Theta, \text{elements}}(\text{NiO}) + 0.05\Delta_f H^{\Theta, \text{elements}}(\text{MnO}_2) + 0.1\Delta_f H^{\Theta, \text{elements}}(\text{CoO}) \quad (4.20)$$

$$\Delta_f H^{\Theta, \text{elements}}(\text{LiNi}_{0.94}\text{Mn}_{0.01}\text{Co}_{0.05}\text{O}_2) = \Delta_f H^{\Theta, \text{oxides}}(\text{LiNi}_{0.94}\text{Mn}_{0.01}\text{Co}_{0.05}\text{O}_2) + 0.5\Delta_f H^{\Theta, \text{elements}}(\text{Li}_2\text{O}) + 0.94\Delta_f H^{\Theta, \text{elements}}(\text{NiO}) + 0.01\Delta_f H^{\Theta, \text{elements}}(\text{MnO}_2) + 0.05\Delta_f H^{\Theta, \text{elements}}(\text{CoO}) \quad (4.21)$$

4.2 Accuracy and Limitation of MHTC compared to Alexsys-1000

To understand the scope of measurement possibility of MHTC with its own limitation, enthalpies of drop solution of NMC622 and NMC85 are determined using MHTC and Alexsys-1000. As described in Section 3.1.3, the different number of pellets from each compound are dropped depending on the type of calorimeter into the sodium molybdate solvent at 701 °C and the average value of enthalpy of drop solution of respective compound is calculated and compared between values from MHTC and from Alexsys-1000.

4.2.1 Enthalpies of Drop Solution by MHTC and Alexsys

The values of the enthalpy of drop solution for the NMC622 and NMC85 compounds were measured using both the MHTC at BCCC and the Alexsys-1000 at KIT. For experiments using the MHTC, the accuracy of $\Delta_{\text{ds}}H$ was enhanced by increasing the number of drops and a fresh batch of solvent had to be introduced for each set of measurement. In contrast, each NMC sample measured with the Alexsys-1000 was analyzed as a single continuous set. The number of individual drops in

each set and the associated uncertainties are provided in Table 20. In each set, the highest and lowest measured values were excluded, and the remaining data were used to estimate the average value. In the listed number of drops, two drops that present the minimum and maximum values are not encompassed.

Table 20. The values of enthalpy of drop solution of NMC622 and NMC85 samples in $3\text{Na}_2\text{O}\cdot 4\text{MoO}_3$ at 974 K determined by MHTC and Alexsys-1000.

Samples	Set of measurement	MHTC		Alexsys-1000	
		Nr. of drops	$\Delta_{\text{ds}}\text{H}$ [kJ/mol]	Nr. of drops	$\Delta_{\text{ds}}\text{H}$ [kJ/mol]
NMC622	1	5	57.03 ± 3.54	13	56.90 ± 0.54
	2	8	54.62 ± 3.27		
	3	8	59.27 ± 3.63		
	4	7	50.74 ± 4.56		
	5	7	45.96 ± 2.87		
	Total	35	53.52 ± 1.74	13	56.90 ± 0.54
NMC85	1	7	56.31 ± 4.04	13	57.38 ± 0.41
	2	8	49.97 ± 9.78		
	3	8	58.81 ± 4.68		
	4	6	54.50 ± 3.81		
	5	6	69.07 ± 5.51		
	6	8	49.39 ± 3.00		
	7	5	54.25 ± 3.69		
	Total	48	55.67 ± 2.22	13	57.38 ± 0.41

While only a single set of measurements is performed with Alexsys-1000, 5 sets of measurements with total 35 drops and 7 sets with 48 drops are carried out with MHTC, respectively for NMC622 and NMC85. The drop solution enthalpies of NMC622 are determined as 53.52 kJ/mol by MHTC and 56.90 kJ/mol by Alexsys and those of NMC85 amount to 55.67 kJ/mol and 57.38 kJ/mol respectively by MHTC and Alexsys.

4.2.2 Comparison between MHTC and Alexsys-1000

To understand the capabilities and limitations of MHTC, the values of $\Delta_{\text{ds}}\text{H}$ from MHTC are compared with those from the well-established Alexsys-1000 as reference. Figure 34 provides a detailed comparison of the drop solution enthalpy ($\Delta_{\text{ds}}\text{H}$) measurements for NMC622 (left) and NMC85 (right), as obtained using two different calorimetric systems, MHTC and Alexsys-1000. Each panel illustrates three main data groupings: (1) the **Total MHTC**, which merges multiple measurements series while excluding the single highest and lowest values for every set, (2) **One set of MHTC**, representing an individual measurement series with the highest uncertainties including its maximum and minimum, and (3) the **Total Alexsys-1000** set, which is analogous to the merged MHTC data but collected using Alexsys-1000. The colored markers correspond to individual $\Delta_{\text{ds}}\text{H}$ measurements, while the box plots summarize the statistical distribution within each group.

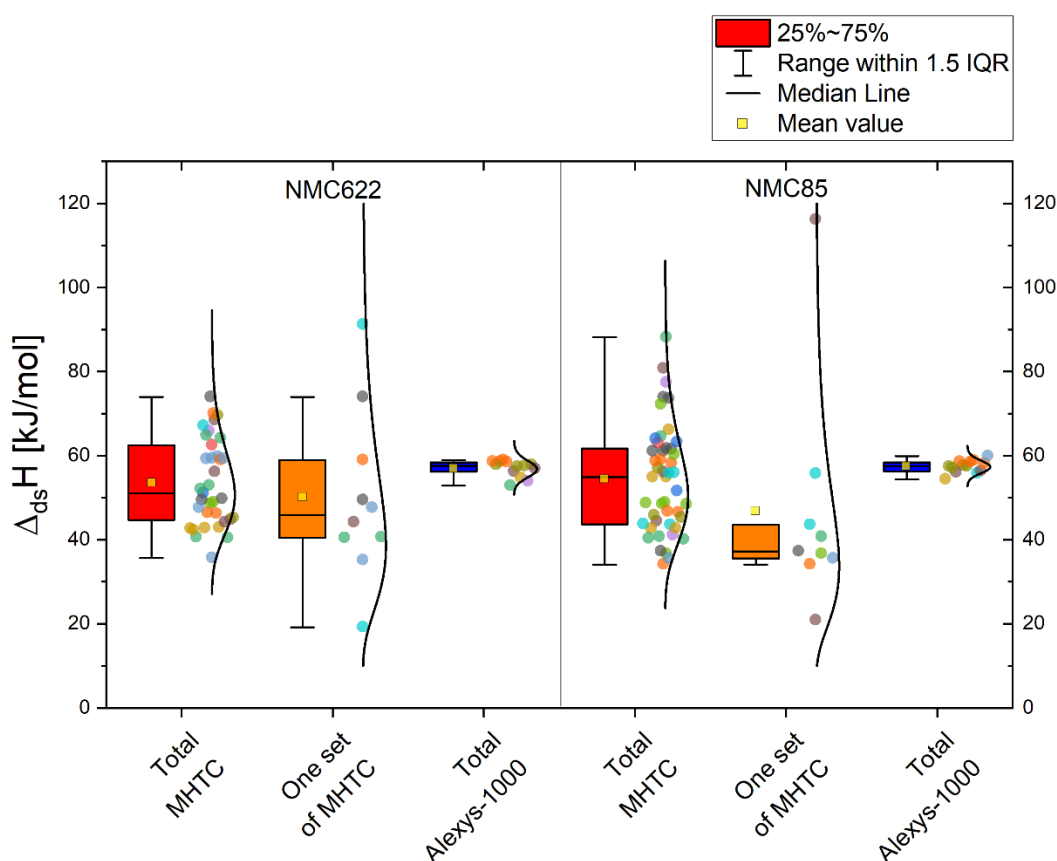


Figure 34. Comparison between measurements of drop solution enthalpies from MHTC and Alexsys-1000.

These are the main conclusions drawn by the results given in Figure 34.

- To exclude maximum and minimum values in the evaluation is intuitive but effective to exclude outliers. Although removing outliers can be a contentious practice in some fields, it can be intuitively justified here because extremely high or low $\Delta_{ds}H$ values often reflect momentary measurement anomalies. Notably, all included data in **Total MHTC** and **Total Alexsys-1000** fall well within the whisker boundaries of 1.5 times the interquartile range (IQR), highlighting that no extreme outliers remain in the final analyses.
- The vertical height of each box is significantly larger for MHTC, indicating that measurements from MHTC exhibit a broader range (or variance) than those from the Alexsys-1000. This broader distribution is also seen in a more gradual, wide-spanning lognormal shape when plotted as a frequency distribution. By contrast, the Alexsys-1000 data are tightly clustered around the mean value, forming a noticeably narrower distribution and thus suggesting greater precision.
- **One set of MHTC** represents a single batch of drops — about 10 measurements — that can yield results significantly different from the final **Total MHTC** average. For example, in the panel for NMC622, one set of MHTC produced a mean $\Delta_{ds}H$ of approximately 50.74 kJ/mol, which deviates by more than 10% from the Alexsys reference. Moreover, its uncertainty (± 4.56 kJ/mol) exceeds eight times the Alexsys-1000 uncertainty. This underscores how relying on few MHTC measurements may lead to an inflated margin of error and potentially misleading conclusions about the sample's thermodynamic stability.

Despite the broader variance in MHTC data, the final average values (i.e., **Total MHTC** after combining multiple measurement sets) do converge to a point that is within a few percent of the Alexsys-1000 result — on the order of 3-6 % deviation, as presented in Table 20. This shows that,

with sufficient repetitions (roughly 3–4 times more than typically needed for Alexsys), MHTC can approach the accuracy of Alexsys-1000 for the determination of $\Delta_{\text{ds}}H$.

The key limitation of MHTC is the larger spread (3–6 times more than the Alexsys uncertainty in this study), coupled with a significantly higher number of required measurements. Moreover, preparing and measuring samples under MHTC conditions is more labor-intensive. For instance, pressing the tiny pellets (2 mm diameter) via cold isostatic pressing can take 4–5 hours for 10–15 pellets, and the small crucible volume means the solvent must be refreshed more frequently (practically for every set). These extra steps escalate the operational complexity and duration of each series, while Alexsys-1000, with its larger capacity and more stable baseline, achieves narrower dispersion in fewer drops and less preparation time.

Overall, the box plots illustrate that MHTC can produce enthalpy of drop solution values ($\Delta_{\text{ds}}H$) that closely match those of the Alexsys-1000 when averaged over many runs, confirming its fundamental capability. However, MHTC suffers from larger scatter, higher uncertainty, and longer preparation and measurement times. Researchers aiming for high-throughput or ultra-precise calorimetric data may thus favor Alexsys-1000, whereas MHTC remains a viable (albeit more labor-intensive) alternative for laboratories that cannot access an Alexsys system. By carefully excluding outliers and substantially increasing the number of drops, MHTC's final averaged measurements can reach an accuracy that, while still inferior to Alexsys, is adequate for many comparative or exploratory studies in thermochemical research.

4.3 Enthalpies of Formation of Commercial NMCs

A secondary objective of this work is to assess the thermodynamic stability of commercial NMC cathode materials, specifically focusing on NMC622($\text{LiNi}_{0.6}\text{Mn}_{0.2}\text{Co}_{0.2}\text{O}_2$), NMC85($\text{LiNi}_{0.85}\text{Mn}_{0.05}\text{Co}_{0.1}\text{O}_2$) and NMC94($\text{LiNi}_{0.94}\text{Mn}_{0.01}\text{Co}_{0.05}\text{O}_2$). Although laboratory-scale versions of NMC622 have been previously studied, commercial samples with a small amount of protective coating has not yet been investigated. Since the exact composition of the coating are proprietary, the determination of an “absolute” enthalpy of formation is partially restricted. Nevertheless, investigating real-world commercial NMC materials remains invaluable for bridging the gap between purely academic studies and industrial applications in automotive lithium-ion batteries.

4.3.1 Calculation of Formation Enthalpies

Using the averaged drop solution enthalpies from MHTC and Alexsys-1000 (see Table 20), the standard enthalpies of formation from oxides ($\Delta_f H^{\ominus, \text{oxide}}$) were calculated via Equations (4.16) and (4.17) for NMC622 and NMC85, respectively. The formation enthalpy of $\Delta_f H^{\ominus, \text{oxide}}$ (NMC94) was determined from $\Delta_{\text{ds}}H$ (NMC94) measured only by Alexsys using Equation (4.18). Subsequently, the standard enthalpies of formation from the elements ($\Delta_f H^{\ominus, \text{elements}}$) were obtained using Equations (4.19) to (4.21), along with the necessary formation enthalpies of the constituent binary oxides (see Table 18). The final values are summarized in Table 21, while Figure 35 compares these results to those of previously investigated NMC compositions — $\text{LiNi}_x\text{Mn}_x\text{Co}_{1-2x}\text{O}_2$ and $\text{LiNi}_{0.8-y}\text{Mn}_y\text{Co}_{0.2}\text{O}_2$ — as reported by Masoumi [7].

Table 21. Standard enthalpies of formation ($\Delta_f H^{\ominus, \text{oxide}}$ and $\Delta_f H^{\ominus, \text{elements}}$) of NMC622 and NMC85 determined by MHTC and Alexsys-1000.

Samples	Enthalpy of	MHTC	Alexsys-1000
NMC622	$\Delta_{\text{ds}} H$ [kJ/mol]	53.52 ± 1.74	56.90 ± 0.54
	$\Delta_f H^{\ominus, \text{oxides}}$ [kJ/mol]	-48.93 ± 2.16	-52.31 ± 1.38
	$\Delta_f H^{\ominus, \text{elements}}$ [kJ/mol]	-643.82 ± 2.21	-647.21 ± 1.46
NMC85	$\Delta_{\text{ds}} H$ [kJ/mol]	55.67 ± 2.22	57.38 ± 0.41
	$\Delta_f H^{\ominus, \text{oxides}}$ [kJ/mol]	-62.62 ± 2.62	-64.33 ± 1.44
	$\Delta_f H^{\ominus, \text{elements}}$ [kJ/mol]	-615.33 ± 2.66	-617.04 ± 1.53
NMC94	$\Delta_{\text{ds}} H$ [kJ/mol]		49.99 ± 0.39
	$\Delta_f H^{\ominus, \text{oxides}}$ [kJ/mol]		-66.93 ± 1.48
	$\Delta_f H^{\ominus, \text{elements}}$ [kJ/mol]		-608.42 ± 1.58

4.3.2 Thermodynamic Stability of Commercial NMCs

Figure 35 compares results presented in Table 21 to those of previously investigated NMC compositions — $\text{LiNi}_x\text{Mn}_x\text{Co}_{1-2x}\text{O}_2$ and $\text{LiNi}_{0.8-y}\text{Mn}_y\text{Co}_{0.2}\text{O}_2$ — as reported by Masoumi [7]. It illustrates two separate plots of formation enthalpies versus Ni molar ratio (a) and Mn molar ratio (b) for various NMCs.

These are the main conclusions drawn by the results given in Figure 35:

(1) Comparing Formation Enthalpies from Oxides and Elements

As emphasized by Masoumi [7], since the oxidation states of the transition metals differ between reactants and products, the formation enthalpy derived from oxides can be misleading. Instead, the formation enthalpy from the elements provides a more reliable indicator of thermodynamic stability. In line with this principle, the present data show that $\Delta_f H^{\ominus, \text{elements}}$ for NMC622, NMC85 and NMC94 aligns more cohesively with the previously reported linear trends. Therefore, the formation enthalpy from elements is considered, also in this study, as a more reliable criterion for assessing thermodynamic stability.

(2) Stronger Dependence of $\Delta_f H^{\ominus, \text{elements}}$ on Mn Ratio

Figure 35 (b) reveals a notably stronger linear correlation between $\Delta_f H^{\ominus, \text{elements}}$ and the Mn molar ratio than between $\Delta_f H^{\ominus, \text{elements}}$ and the Ni molar ratio (Figure 35 (a)). This suggests that increasing Mn content exerts a greater stabilizing influence on the layered structure — an observation consistent with the higher exothermic contribution of MnO_2 ($\Delta_f H^{\ominus, \text{elements}}(\text{MnO}_2) = -521.493$ kJ/mol [141]), which exceeds that of both NiO and CoO. Consequently, NMCs with lower Mn tend to exhibit less exothermic formation enthalpies and may degrade faster due to an increased likelihood of surface reconstruction [148,149].

(3) Comparison with Previous Lab-Scale Data

NMC622: the measured formation enthalpy ($\Delta_f H^{\ominus, \text{elements}}$) value (-643.82 kJ/mol by MHTC and -647.21 kJ/mol by Alexsys) differ by about 21–25 kJ/mol (3–4 %) from the lab-scale NMC622 (-668.08 kJ/mol) reported by Masoumi [7]. This difference is not negligible, considering that the reference values of $\Delta_f H^{\ominus, \text{elements}}(\text{NiO})$ and $\Delta_f H^{\ominus, \text{elements}}(\text{CoO})$ having the discrepancy less than 1%, respectively (see Table 18). This discrepancy can be attributed to (i) the presence of a protective coating even with its small mass fraction, (ii) different stoichiometry or purity between lab-scale and mass production and (iii) possible Li-excess commonly introduced in industrial processes to counteract Li losses during formation in NMC622 in this work. (iv) Moreover, it must be also considered the lab-scale synthesized NMC622 in the work of Masoumi [3] has less not only lithium but also oxygen molar ratio than a theoretical value of

$\text{LiNi}_{0.6}\text{Mn}_{0.2}\text{Co}_{0.2}\text{O}_2$ with a chemical composition $\text{Li}_{0.94}\text{Ni}_{0.6}\text{Mn}_{0.2}\text{Co}_{0.2}\text{O}_{1.80}$, which might induce the difference.

NMC85 and NMC94: with $\Delta_f H^{\Theta, \text{elements}}$ of -615.33 kJ/mol by MHTC and -617.04 kJ/mol by Alexsys (NMC85) and -608.42 kJ/mol (NMC94) by Alexsys, commercial NMC85 and NMC94 lie between $\text{LiNi}_{0.7}\text{Mn}_{0.1}\text{Co}_{0.2}\text{O}_2$ (-640.05 kJ/mol) and $\text{LiNi}_{0.8}\text{Co}_{0.2}\text{O}_2$ (-609.34 kJ/mol) on the Mn ratio scale — thus fitting well within the broader trend predicted by Masoumi [3].

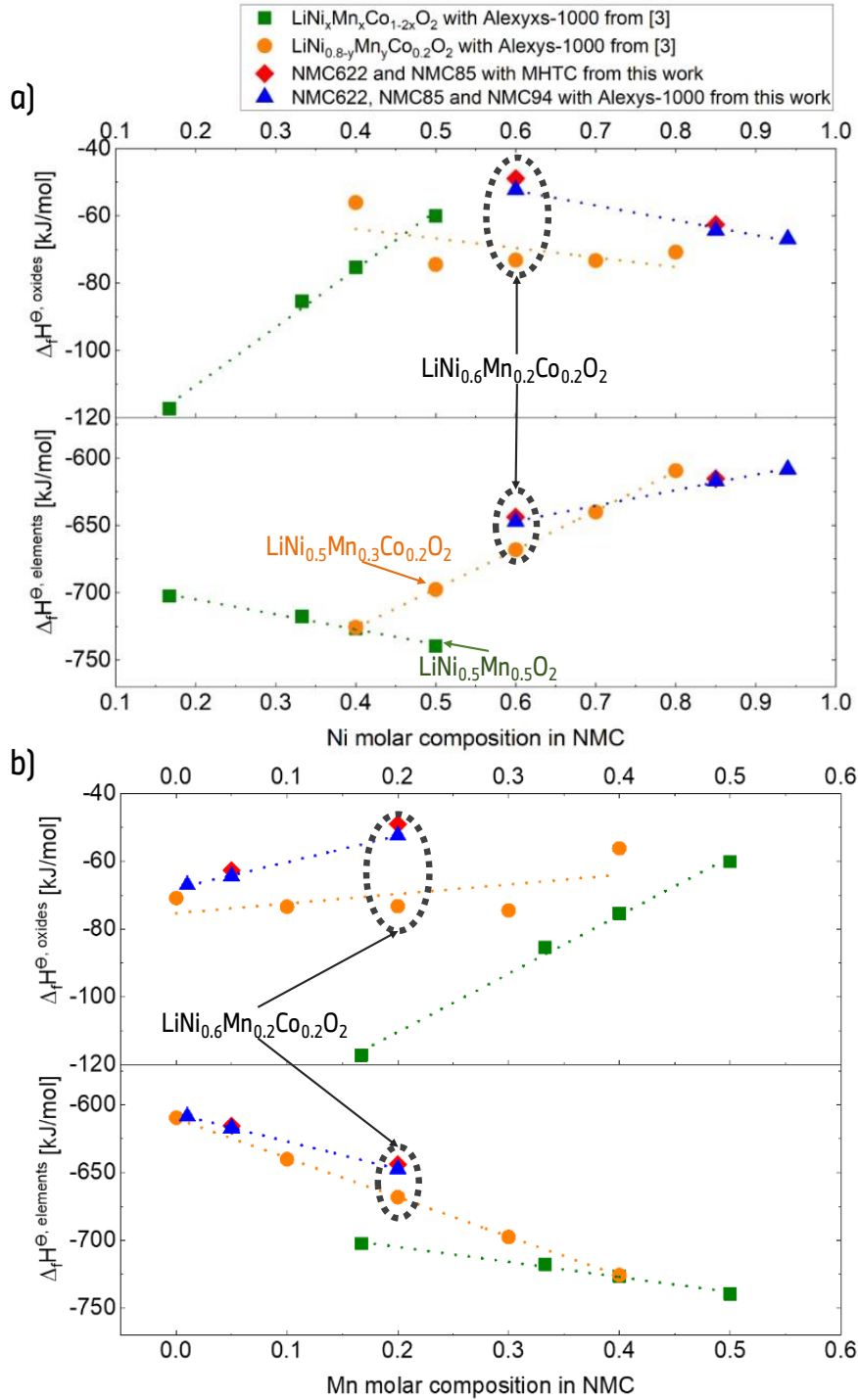


Figure 35. Enthalpies of formation, $\Delta_f H^{\Theta, \text{oxides}}$ from constituent oxides (Li_2O , NiO , MnO_2 and CoO) and O_2 and $\Delta_f H^{\Theta, \text{elements}}$ from elements of NMC622, NMC85 and NMC94 determined by experiments, compared to NMCs with compositions of $\text{LiNi}_x\text{Mn}_x\text{Co}_{1-2x}\text{O}_2$ and $\text{LiNi}_{0.8-y}\text{Mn}_y\text{Co}_{0.2}\text{O}_2$ [7] as a function of (a) Ni and (b) Mn molar composition in NMC.

In summary, the experimentally derived $\Delta_f H^{\Theta, \text{elements}}$ values for commercial NMC622, NMC85 and NMC94 fit well with the broader thermodynamic trends established for NMC systems, particularly when correlated with the Mn molar ratio. While these commercial samples exhibit slight deviations from lab-scale NMC references — likely stemming possibly from surface coatings, Li-excess in commercial NMCs or lower purity, Li-deficiency in lab-scale NMCs — the overall findings confirm that increasing Mn content leads to more exothermic enthalpies of formation and thus generally improved thermodynamic stability.

4.4 Conclusion

The primary goal of this study is to validate the MHTC for determining the enthalpies of formation of NMC materials and to delineate its operational limitations by comparing its performance against the well-established Alexsys-1000 system. This study compares the experimentally determined drop solution enthalpy ($\Delta_{\text{ds}} H$) values between two calorimeters. For example, in the case of NMC622, the drop solution enthalpy obtained from multiple measurement sets using the MHTC converged to an average value of 53.52 ± 1.74 kJ/mol. In contrast, the Alexsys-1000 system yielded a more narrowly distributed average value of 56.90 ± 0.54 kJ/mol. These comparisons provide a tangible metric to assess the precision and limitation of MHTC compared to Alexsys (see Figure 34).

Notably, while the final averaged $\Delta_{\text{ds}} H$ values for MHTC and Alexsys-1000 are in close agreement, the experimental data from the MHTC exhibit a noticeably wider spread and a higher degree of uncertainty. This larger statistical dispersion in the drop solution enthalpy measurements reflects presumably inherent limitations of the MHTC system, such as its structure with only one calorimeter cell, the absence of bubbling-tube, the asymmetry in heat flow from the vertically arranged reference crucible and the instable temperature of cooling water. In particular, the limited internal volume of Pt-crucible, combined with the absence of bubbling-tube, severely constrains the sample size and this small sample results ultimately in greater experimental uncertainty. Despite these challenges, however, the MHTC proves capable of delivering reproducible $\Delta_{\text{ds}} H$ values.

This study also highlights several practical challenges associated with the MHTC method, such as the time-consuming sample preparation process — particularly the cold isostatic pressing required to form small, homogeneous pellets — and the necessity to replenish the molten solvent frequently due to its limited volume. Most of all, nearly 3 to 4 times more drops are required to reach a similar result of Alexsys. However, even with a higher number of measurements, the precision does not reach the level achieved by the Alexsys system.

The secondary objective of this work lies to assess the thermodynamic stability of a commercial state-of-the-art NMC with a higher Ni molar ratio (NMC622, NMC85 and NMC94). The experimental data shows that as the manganese content decreases or the nickel molar ratio increases, the enthalpy of formation becomes less exothermic. This observation suggests that lower Mn content or higher Ni content, with its larger exothermic contribution as indicated by the high formation enthalpy of MnO_2 , may promote faster degradation. Overall, the obtained formation enthalpy values for NMC622, NMC85 and NMC94 fit well within the established trends and correlate strongly with Mn and Ni molar ratio.

Despite the partial confidentiality surrounding the commercial coating composition, measuring real-world NMC materials remains highly valuable for bridging fundamental studies and industrially relevant cathodes. Further investigations could focus on systematically varying the coating materials and thicknesses — or controlling Li-excess — to quantify the precise effect of each modification on thermodynamic stability. Nonetheless, the present results affirm that the enthalpies of formation for NMC622, NMC85 and NMC94 closely follow the trends predicted by prior lab-scale research and further demonstrate the feasibility of applying high temperature drop solution calorimetry to understand complex, coated cathodes in commercial lithium-ion batteries.

As a result, this study in this Chapter 4 not only validate the MHTC as a viable tool for determining enthalpies of formation in commercial NMC materials but also can potentially provide important insights into the thermodynamic underpinnings of LIB cell safety. As demonstrated in the study of Shurtz and Hewson [6], the thermodynamic stability of NMC cathodes, as reflected in their formation enthalpies, plays an integral role in determining the amount of emerging heat energy in LIB cells. The enthalpy of formation determined through high temperature drop solution calorimetry in this study can provide a crucial link between the intrinsic thermodynamical properties of NMC materials and the potential heat release during thermal decomposition. This study contribute to compile the comprehensive database of formation enthalpies for NMC, which enables prediction of heat release from various decomposition reactions before and during thermal runaway.

In the following chapters, particularly in Chapter 7, the resilience of LIB cells to internal short circuits (ISCs) will be evaluated using the advanced nail/needle penetration test and the safety of LIB cell will be linked with the stability of NMC materials in LIB cells. Thus, this work lays the essential groundwork for correlating cathode thermodynamics with cell-level safety performance, ultimately contributing to the development of more predictive thermal runaway models and the improved design of safer lithium-ion batteries.

5 Study of the Impact of Cell Assembly on ISC

Internal short circuits (ISCs) in lithium-ion batteries (LIBs) are hazardous events that can lead to rapid energy release and potentially to thermal runaway. The severity of an ISC is not only a function of the cell's chemistry and state-of-charge, but also its internal design and construction. This chapter investigates how the cell assembly architecture — in particular, the difference between stacked versus wound (jelly roll) electrode configurations in automotive prismatic cells (demonstrated in Table 9) — influences the ISC behavior. It is hypothesized that the internal electrode assembly method will impact the ISC characteristics by changing the mechanical strength, internal resistance, and shorting progression within the cell.

In this chapter, controlled internal short circuits were induced in two automotive prismatic LIB cells: one built with a stacked electrode assembly and another with two jelly rolls electrode assembly. A mechanical nail penetration test was used to induce ISC(s) in each cell under identical conditions. The resulting mechanical penetration force, ISC current and temperature evolution were recorded and analyzed in detail. By comparing these two cell designs, it is aimed to discern how the physical configuration of electrodes influences the ISC current generation, the speed and magnitude of joule heating. The findings presented in this chapter provide insight into the safety performance of different cell assembly methods.

5.1 Experimental Setup

Two automotive prismatic lithium-ion cells were selected for this study, differing significantly in internal electrode assembly technique. Cell A features a stacked electrode assembly, wherein individual sheets of anode, separator, and cathode are layered on top of each other in a flat stack (often termed a Z-fold or stack-fold design). Cell B, in contrast, uses a jelly roll assembly; long strips of anode and cathode with separators in between are rolled together into a spiral and then compressed into a prismatic can. Both cells are enclosed in hard aluminum alloy casing and have comparable nominal capacities, high-nickel cathode active materials and a graphite anode. The key specifications and design attributes of the two cells are summarized in Table 22.

An internal short circuit was initiated in each cell using a controlled nail penetration test. The experimental setup employed in this chapter integrates the internal temperature measurement method, schematically illustrated schematically in Figure 32, with the ISC current measurement approach demonstrated in Figure 33 (a) and (c) in Section 3.2.2. The cells were also connected to an external power supply capable of providing up to 10 A to compensate for any charge lost during the shorting event. This setup kept the cell voltage effectively constant at 4.2 V (100% state of charge) throughout the test, as the power supply replenished the charge drained by the ISC. The short-circuit current was measured through a shunt resistor (40 A, 75 mV) in series, allowing accurate capture of the current profile. Since the cell can was partially removed, the contact of nail to the outermost anode was detected by voltage between nail and positive electrode (V_{NP}).

Table 22. Specifications of the tested automotive prismatic LIBs, Cell A and B.

Cell		A	B
Cell design (Width x Depth x Height mm ³)		Prismatic EV32 73 x 32 x 180 mm ³	
Capacity [Ah]		72	66
Cell assembly		Stacks	Two jelly rolls
Material	Anode Active Material	Graphite	Graphite
	Separator	PE with double-side coating	PE with one-side coating
	Cathode Active Material	NCA	NMC811
Thickness [μm]	Anode	220	165
	Cu	8	6
	Separator	14	8
	Cathode	140	120
	Al	11	12
	Al to Al	374	293

For each test, the casing of the cell was partially opened, and the cell was firmly clamped in an upright position. A 3 mm diameter nail (with an embedded thermocouple near its tip) was driven into the center of the cell, perpendicular to the electrode layers. The penetration was performed at a constant speed of approximately 0.01 mm/s. This relatively slow drive speed was intentionally selected to induce ISCs gradually, effectively shorting the cell layer-by-layer; 1 mm of penetration corresponds roughly to the thickness of the thinnest layers (on the order of 6-12 μm) being breached in sequence.

It should be noted that the specific nail and test method used here can influence the absolute ISC behavior. For instance, the specially designed nail (with a thermocouple and particular materials) may not produce identical results to a standard steel nail, because the tip of the crafted nail has higher electrical and thermal conductivity — AlMgSiPb alloy with 24-32 MS/m 170-220 W/m·K [138]. Therefore, the penetration depths and current magnitudes observed in this chapter should not be compared quantitatively on a one-to-one basis with results from other chapters or studies that use different penetration techniques. However, Cell A and Cell B were tested under identical conditions, and any differences in their response can be directly attributed to their cell assembly architecture in this topic.

5.2 Comparison of ISC-Behavior

Figure 36 presents an overview of the nail penetration test results for the two cells, including the key electrical, thermal and mechanical parameters recorded. Plotted as a function of penetration (depth or time), the graphs in Figure 36 show the ISC current, the internal temperature (thermocouple reading at the nail tip), the cell voltage, the voltage between the nail and the negative terminal (V_{NN}), the force on the nail, and the temperatures measured on the cell surface for both Cell A and Cell B. The complex signals occurring simultaneously in the figure will be discussed in detail in the following sections: the comparison of forces in Section 5.2.1, the ISC current in Section 5.2.2, and the internal temperature in Section 5.2.3.

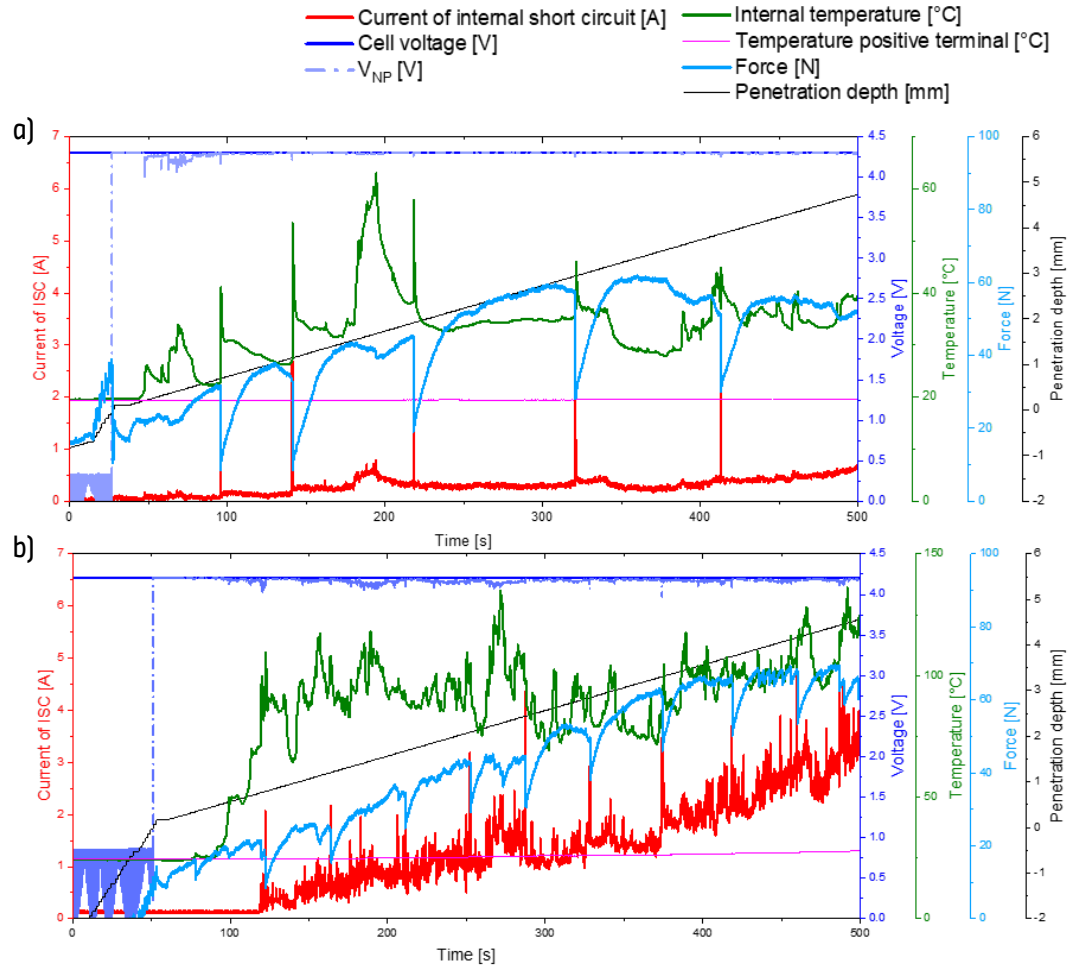


Figure 36. Results of nail penetration test of Cell A and B, demonstrating the evolution of major parameters during penetration: current of ISC, internal temperature and temperatures on the surface, cell voltage, voltage between nail and negative terminal and force on the nail: (a) type A with stacks and (b) type B with jelly rolls.

From the data in Figure 36, several observations about each measured parameter can be made.

- ISC Current and Internal Temperature:** as discussed in Section 2.3.2, it is understood that Joule heating is the main source of heat during an ISC. Consequently, the internal thermocouple temperature rises in tandem with the short-circuit current. As demonstrated in Figure 36, these two parameters are tightly coupled: whenever the ISC current increases, the temperature at the nail tip (near the short) increases as well. When the short current subsides, the internal temperature also falls. This confirms that spikes in ISC current directly lead to localized heating inside the cell. The similar behavior of internal temperature exhibiting periodic sharp peaks was also observed in the work of Huang et al. [136]. While their study was limited to a small 3 Ah Li-ion cell and focused solely on temperature measurements, the present work, through the coupled measurement of ISC current, enables a more comprehensive understanding of the evolution of ISC and the formation and local dissipation of thermal energy within an automotive prismatic cell.
- Cell Voltage:** throughout the penetration, the cell voltage of both Cell A and Cell B remains at 4.2 V (SOC 100 %). This is because the test setup actively compensates for the cell's capacity loss using an external power supply.

- **Voltage between Nail and Positive Terminal (V_{NP}):** in these prismatic cells, the outermost electrode is anode. When the nail first contacts the outermost anode and makes electrical contact between the internal negative electrode and positive terminal, the voltage between the nail and the positive terminal abruptly jumps to the full cell voltage. This indicates the moment the nail tip breaches the first anode. As discussed in 3.2.2, the signal of V_{NP} is very useful for precisely determining the penetration depth.
- **Penetration Force:** the force on the nail begins to register as soon as the nail contacts the isolation foil on top of electrodes and starts pushing into it. Initially, the electrode (either stacks or jelly rolls) resists the nail, so the force rises. The moment the nail finally pierces through electrodes (as evidenced by V_{NP} jumping to 4.2 V), the force on the nail drops sharply due to the sudden relief. The force signal then generally increases again as deeper layers offer resistance, but it exhibits a saw-tooth pattern with multiple sudden drops (this periodic behavior will be examined in detail later in Section 5.2.1). It is worth noting that using the force signal alone to determine exactly which layer is being penetrated is difficult – the force required can vary depending on the layer material, the casing strength, and how the cell deforms. In this study, however, the force signal plays a crucial role in understanding the periodic nature of the ISC events when interpreted alongside the electrical signals.
- **Surface Temperature:** external thermocouple on the cell surface (at the positive terminal) shows almost no notable temperature rise throughout the nail penetration for either cell. In both Cell A and Cell B, despite significant heating at the internal short location, the heat did not conduct quickly to the outer surface during the short duration of the test. The internal nail-tip temperature, in contrast, fluctuates significantly with each ISC event. This result highlights that conventional external temperature measurements during a nail penetration test may fail to detect internal ISC heating; a thermocouple at the short location is essential for capturing the thermal response of the ISC.
- **Penetration Depth:** as mentioned above, the penetration depth to be zero (0 mm) is defined at the point where the nail first makes electrical contact with the internal cell layers. Based on these initial observations, we can directly compare the overall ISC behavior of Cell A (stacked) and Cell B (jelly roll). Both cells demonstrate a qualitatively similar pattern in Figure 36: upward peaks in the ISC current and internal temperature, occurring simultaneously with downward force spikes (drops in the penetration force), and these events repeat periodically during the penetration. However, there are notable differences in the details of these responses between the two cell designs, as outlined below:
- **Cell A with Stacks:** in the stacked cell, the short circuit current tends to be highly intermittent. The ISC current essentially drops to nearly zero between successive shorting events, exhibiting an on-off pulsating pattern that correlates with the force drops. However, the baseline shows a slight upward trend, increasing by approximately 0.5 A over 500 seconds. Correspondingly, the internal temperature in Cell A spikes sharply each time an ISC occurs, then drops back down once the current subsides. Another key difference is the magnitude of heating: the peak internal temperature in Cell A remains relatively low (under 65 °C) during these tests. This suggests that each short in the stacked cell involves only a small portion of the cell's total energy, which will be quantified in Section 5.2.2.
- **Cell B with Jelly Rolls:** in the jelly roll cell, the ISC current also shows periodic peak structures tied to the moments when the penetration force drops, comparable to Cell A. However, unlike Cell A, the short-circuit current in Cell B does not return to zero between these events. Instead, the baseline of the current gradually rises – each successive ISC peak builds on a higher background level, indicating a more continuous or accumulating short-circuit conduction. Additionally, the internal temperature behavior in Cell B is more complex: instead of isolated sharp spikes, the temperature exhibits a more continuous rise with numerous smaller superimposed peaks. The maximum internal temperature reached in Cell B (around 150 °C) is significantly higher than in Cell A, reflecting the larger energy release during shorts in the jelly roll cell.

Both cells thus exhibit a periodic behavior during penetration, which clearly results from the repeating layered structure of the cells and the sequence of short-circuits occurring as each layer or component is breached. In the following sections, we delve deeper into the origins of this periodic behavior and analyze why Cell A and Cell B respond differently. We will first examine the mechanical response (the periodic force drops) to identify which layer is shorting at each event and then investigate the electrical response (voltage and current behavior) considering the cell architectures.

5.2.1 Periodical Behavior of Penetration Force

Before analyzing the ISC currents in detail, it is useful to understand the periodic behavior observed in the penetration force signal. Figure 37 presents only the force signal on the nail as a function of penetration depth for Cell A and Cell B (from Figure 36), along with a reference test conducted on a separate Cell B that was electrically discharged to 0 V. In the reference cell, which had no charge (thus no possibility of generating internal joule heating), the nail was driven under the same conditions to provide a purely mechanical baseline.

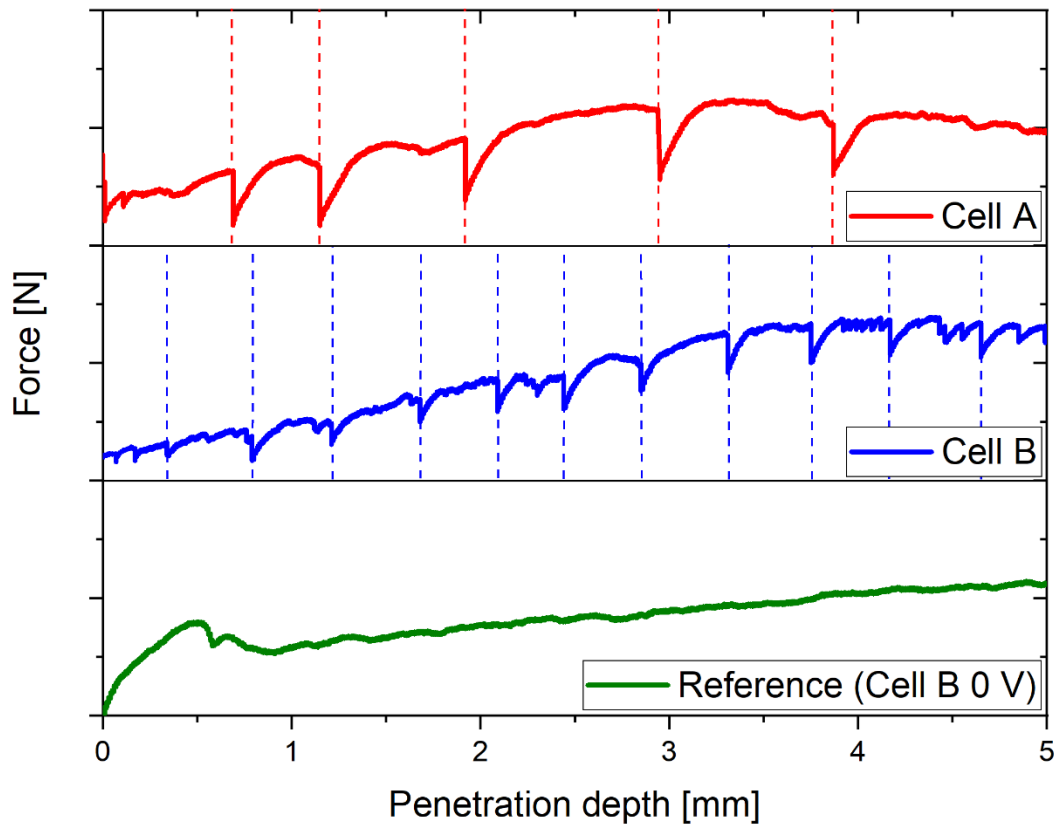


Figure 37. Nail penetration force vs. depth for Cell A (top curve), Cell B (middle curve) and reference cell (bottom curve).

As shown in Figure 37, both charged cells (Cell A and Cell B at 100% SOC) exhibit a series of abrupt drops in force at regular penetration intervals, whereas the 0 V reference cell displays a monotonically increasing force with no sudden drops. This difference confirms that the periodic force-drop phenomenon is intrinsically linked to the cell being charged and experiencing internal short-circuit events. In other words, the force does not drop simply from the nail piercing layers; if that were the case, similar drops in the overdischarged reference cell would have been observed. Instead, the force drops are a signature of something that happens only when the cell is charged — namely, internal shorting and the consequent rapid heating and material failure.

Each sudden drop in force corresponds to the nail encountering and breaching a specific internal layer or component that causes an ISC. The regular spacing of these drops suggests a repeating structural element is involved. Some possibilities can be ruled out; It is unlikely that the thick electrode layers (anode or cathode) are responsible for the rapid, small drops, considering the penetration speed of 0.01 mm/s, because punching through a thick layer would produce a larger, more gradual change in force rather than a sharp dip and recovery.

Likewise, if the separator (a very thin layer) were causing the drops, we would expect a much higher frequency of force drops (since separators are present between every electrode layer). Instead, the periodicity of 0.4 mm to 0.8 mm between drops (as can be estimated from Figure 37) points to the metallic current collectors (which occur at regular intervals in the cell stack) as the most likely culprits.

To verify the source of the force drops, Cell B was opened after the test and its internal layers were inspected for evidence of short circuits. Figure 38 shows an example of the internal short-circuit trace observed in a cell after the nail penetration test. Each short-circuit event typically leaves a charred or melted spot on the electrode layers. In Cell B, a total of 12 distinct burned “bundles” of layers (separator – anode – Cu – anode – separator – cathode – Al - cathode) were identified, corresponding closely to the 11 force drop events recorded for that cell in Figure 37. Therefore, the periodical drops in force would have originated from either copper or aluminum current collector.



Figure 38. Post-test internal short circuit traces observed in a cell after nail penetration test.

The question then arises: Why does the force drop so sharply? Two scenarios were considered:

Force drops when nail penetrates current collector because of

- 1) **Mechanical Rupture of Current Collector:** the nail physically breaks a foil (Cu or Al); the tearing of the metal could momentarily reduce the force needed to push the nail

or

- 2) **Thermal Melting of Current Collector:** the short-circuit current flowing through the foil causes rapid Joule heating, melting the metal around the nail. The molten metal would offer much less resistance to the nail, causing the force to drop until the nail advances beyond that layer.

The results of the reference cell experiment (0 V cell) help distinguish between these two hypotheses (see Figure 37). In the reference cell, the nail still mechanically pierced all the same layers (including current collectors) but, critically, no force drops were observed. If mechanical rupture alone were responsible for the drops, force drops in the reference cell would have been observed, when its Cu or Al foils were torn. The fact that the reference penetration force increased smoothly indicates that mechanical layer rupture without current does not produce a drop in the force signal. Therefore, it is assumed that the thermal effect — the melting of the current collector due to the ISC current — causes the characteristic force drop in the charged cells. Figure 38 provides,

as an example, clear evidence that the electrodes were burned or melted due to Joule heating, and that several electrode stacks have fused together. However, it remains difficult to determine whether the Al foils have also melted, either by visual inspection or under optical microscopy. In each event, the nail shorts a metallic layer, a large current flows and heats that metal, the metal rapidly softens or melts, and the nail suddenly encounters less resistance (hence a dip in force) until it presses into the next intact layer.

Between the two current collectors, aluminum is more likely to melt first because its melting point (660 °C) is much lower than that of copper (1084 °C) [150]. Thus, it is suspected that each force drop corresponds specifically to the melting of an aluminum foil as it shorts to either the anode or copper. Copper foils may also eventually get involved in some shorts, but the primary recurring event (periodic drops) points to aluminum layers being sequentially melted.

From the rate at which the force signal rises and falls, it can be inferred how efficiently the aluminum current collector absorbs thermal energy generated by the ISC and how rapidly it melts to shut down the ISC. This inference is further supported by post-test observations: the specially crafted nail tip, made of AlMgSiPb alloy with a lower melting point (585–650 °C [138]) compared to pure aluminum, was not completely melted but only partially deformed, becoming blunt. This suggests that the generated heat was rapidly and primarily conducted into the aluminum components and remained localized near the nail tip. Consequently, the measured internal temperature did not reach the melting point of pure aluminum (660 °C). It is assumed that the rapid heat absorption by the aluminum current collector, combined with its endothermic phase transition during melting, contributed to both the suppression of ISC and the observed drop in temperature.

To quantify the periodicity, Table 23 lists the penetration depths at which force drop events occurred and the distances between successive drops for both cells. The data were obtained from force–depth curves like those in Figure 37.

Cell A exhibited five force-drop events over the full penetration depth (~4 mm of nail travel through the cell layers), whereas Cell B had eleven such events (covering ~4.65 mm of penetration). The average spacing between drops in Cell A is about 795 μm , which is substantially larger than the thickness of a single cycle in that cell (~374 μm of separator-anode-cu-anode-separator-cathode-al-cathode). In Cell B, by contrast, the average spacing between drops is ~435 μm , relatively close to the actual thickness of one layer cycle in the jelly roll (~293 μm). Moreover, the drop spacing in Cell A is less uniform (ranging from ~460 μm up to ~1020 μm), whereas Cell B's spacing is relatively consistent around 410–490 μm with a single instance falling outside this range.

Table 23. The penetration depth at which force drops occurred, and spacing between those consecutive drops for Cell A and B.

Cell A		Cell B	
Penetration depth with force dropping [mm]	Spacing between drops [μm]	Penetration depth with force dropping [mm]	Spacing between drops [μm]
0.69		0.34	
1.15	460	0.79	450
1.92	770	1.21	420
2.94	1020	1.68	470
3.87	930	2.09	410
		2.44	350
		2.85	450
		3.31	460
		3.75	440
		4.16	410
		4.65	490
Average spacing	795	Average spacing	435

The difference between the observed drop spacing ($\sim 435\ \mu\text{m}$) and the physical layer pitch ($\sim 293\ \mu\text{m}$) of Cell B could be due to push-back effect of the electrode formed (see Figure 30). During quasi-static nail penetration, the layered electrodes undergo deflection before puncture: the electrode is compressed and displaced in the nail's direction until the local tensile stress exceeds the nail strength, after which true puncture occurs. Consequently, the measured penetration depth of the nail can overestimate the effective depth of layer breach.

In Cell A (stacked), however, the difference between average spacing from experiment and thickness of the cycle is way bigger than Cell B. The larger, irregular spacing (e.g., $1020\ \mu\text{m}$, which is roughly three times a single-layer thickness) suggests that this push-back effect is way stronger in the stack-assembly because cell is built with numerous individual layers. Also, it could be assumed that the nail passed through multiple layers in the stack with a small ISC without melting Al-foil. This could happen if, for example, the aluminum foil pierced did not immediately create a full short (perhaps the contact was partial or the short current in one stack unit was limited).

In summary, the periodic oscillations in the penetration force are caused by the nail sequentially shorting the layered structure of the cell, specifically melting through each aluminum current collector layer one after another. Cell A's stacked design, with layers connected in parallel stacks, resulted in less frequent shorting events (some aluminum layers did not independently cause a short until the nail reached deeper), whereas Cell B's jelly roll design produced more frequent, regular shorting events (almost every aluminum layer led to a short). This understanding of the force response provides a foundation for interpreting the electrical measurements, as each force drop corresponds to a particular short-circuit event in the cell.

5.2.2 ISC Current Behavior and Mechanisms

Based on earlier findings, the periodic drops in penetration force were attributed to melting of the aluminum current collector. This melting phenomenon provides insight into the internal short circuit (ISC) behavior: an ISC current will surge abruptly when the short involves aluminum, then fall off sharply once the aluminum melts and the circuit path is interrupted. Before examining the specific results for different cell designs, it is necessary to discuss the possible ISC scenarios that can occur during a nail penetration and how the material properties of cell components influence the severity of an ISC.

Three key material factors determine the extent and severity of an ISC. First is the electrical conductivity of the components forming the short path. A higher electrical conductivity of the short-circuit path directly allows a larger ISC current to flow. Second is the thermal conductivity of those components. Thermal conductivity indirectly influences ISC behavior: when a short-circuited component possesses low thermal conductivity, the heat generated at the short cannot be dissipated efficiently. This localized heat accumulation can lead to an increase in local electrical resistance or cause the separator to melt, thereby forming additional ISCs and generating further heat. Ultimately, this process may trigger additional chemical reactions or even thermal runaway within the affected region. The third factor is the thermal stability (onset temperature) of the materials involved — for example, the melting point of metallic current collectors or the decomposition temperature of electrode materials. A lower onset temperature (such as the $660\ ^\circ\text{C}$ melting point of aluminum) means the material will fail or melt at a relatively lower temperature, which can either mitigate the short by physically disconnecting it or contribute to heating if the material undergoes an exothermic reaction upon decomposition. In summary, an ideal scenario for a benign ISC would involve a high-resistance path (low electrical conductivity) and components that can quickly disperse heat or fail safely at lower temperatures, whereas a dangerous ISC scenario typically combines a highly conductive path with poor heat dissipation and no early fail-safe interruption.

The actual electrical and thermal properties of the cell components are crucial to understanding these factors. These properties can vary widely: the conductivity of anodes and cathodes depends

on their active material composition, binder content, particle size, and the compression from calendaring. Moreover, the state of charge (SOC) can affect the specific heat capacity of the electrode coatings due to lithium intercalation in the materials.

Table 24 presents typical ranges of electrical conductivity, thermal conductivity, and specific heat capacity for the major cell components. Generally, electrical and thermal conductivities are proportional — metallic materials that are good electrical conductors tend to be good thermal conductors. It is evident that the metal current collectors have much higher conductivities compared to the porous electrode materials. Notably, copper and aluminum exhibit high electrical conductivities on the order of $10^5 - 10^7$ S/m, many orders of magnitude greater than those of the anode (on the order of 10^2 S/m) and especially the cathode (only a few S/m). A similar trend is seen in thermal conductivities: copper and aluminum foils conduct heat two to three orders of magnitude more effectively than the battery electrodes. The anode's thermal conductivity is moderately higher than that of the cathode coating, reflecting graphite's relatively higher thermal conductance.

Table 24. Electrical and thermal conductivity of cell components at room temperature.

	Anode	Copper	Cathode	Aluminum	AlMgSiPb
Electrical conductivity [S/m]	100 [96]	6.0×10^7 [96]	3.8 [96]	3.6×10^7 [96]	$2.4-3.2 \times 10^7$ [138]
Thermal conductivity [W/m·K]	139 [151]	380-400 [96,151,152]	3.5-4.2 [140]	200-237 [96,151,152]	170-220 [138]

Several studies [87,96,136] have identified four ISC configurations that can occur inside a lithium-ion cell, based on which combinations of electrodes or current collectors are brought into contact during a short. Table 25 summarizes these four possible ISC scenarios along with the relative ISC current level, the effectiveness of heat dissipation in each scenario, and the qualitative degree of danger associated with each case. Scenarios 1 and 2 involve the positive aluminum current collector being shorted to a negative-side component (either the anode or the copper foil), whereas Scenarios 3 and 4 involve the cathode active material being shorted to a negative-side component.

Table 25. Four possible ISC scenarios in a LIB and their characteristics.

Scenario	1	2	3	4
ISC between	Aluminum	Aluminum	Cathode	Cathode
	Anode	Copper	Anode	Copper
ISC current	High	High	Low	Low
Heat distribution	Poor	Very good	Poor	Good
Degree of danger	High	Moderate	Low	Least

Each scenario can be understood as follows.

- 1) **ISC between Aluminum–Anode:** a short between the aluminum positive foil and the anode material creates a very low-resistance path, because the anode (lithiated graphite) has relatively low electrical resistivity and aluminum has highest electrical conductivity among cell components. This leads to an extremely high short-circuit current, comparable to the second scenario. What makes this configuration the most dangerous is the inadequate heat transfer on the anode side of the short – the porous anode cannot conduct heat away quickly. Consequently, a large current flows and heat builds up locally, potentially causing rapid temperature-rise and thermal runaway. The internal short between aluminum and anode is therefore considered the worst-case ISC scenario within a cell, which explains why the aluminum current collector may melt when shorted, as demonstrated in Section 5.2.1.

- 2) **ISC between Aluminum–Copper:** this scenario is effectively similar to a direct short across the cell terminals. This also yields a very high current. However, both copper and aluminum are excellent thermal conductors, so the joule heat generated at the short is dispersed through the metal foils efficiently. The localized heat accumulation around the short is minimal in this case, and thus the risk of triggering a thermal runaway is much lower than in scenario 1.
- 3) **ISC between Cathode–Anode:** this case is an internal short between the two electrode coatings without directly involving metallic current collectors. Here the available short-circuit current is much lower, because both the cathode and anode materials have high internal resistance compared to metal foils. However, the heat dissipation is still poor on the anode and cathode. As a result, the temperature rise in the vicinity of the shorted layers can be higher than in scenario 4 for the same amount of energy release. While the total energy released in a cathode–anode short tends to be limited, the localized heating could initiate decomposition of materials if the heat cannot spread.
- 4) **ISC between Cathode–Copper:** this scenario shorts the cathode coating to the copper negative collector. Similarly to scenario 3, the ISC current is limited by the cathode’s high resistivity. In this case, however, the copper foil on the negative side provides a good heat sink. The heat generated at the short is dissipated through the copper, meaning the local temperature rise is much smaller. Any energy released is dissipated more rapidly than in scenario 3, and no low-melting component on the cathode side intervenes. Thus, cathode–Cu shorts are the least severe internal shorts, typically posing a low danger level.

In the context of a nail penetration, these four ISC types do not happen in a neat one-by-one sequence. Instead, multiple short-circuit types can occur simultaneously as the nail bridges different components at the same time. The actual short-circuit in a multilayer cell is a complex superposition of these scenarios.

Figure 39 illustrates how internal shorts are combined as the nail penetrates into the cell’s layered structure. The schematic in Figure 39 uses a representative prismatic cell geometry with average relative ratio between cell layers (discussed in Figure 8). Since the outermost layer of an automotive prismatic cell is typically the anode, the first short-circuit occurs, when the nail makes contact with a cathode layer beneath that anode. At that initial moment (Figure 39 (a)), two types of ISC happen simultaneously: a cathode–anode short (scenario 3) and a cathode–Cu short (scenario 4) – effectively, the nail connects the cathode to both the anode next to it and the adjacent copper foil. This corresponds to the situation just as the nail pierces through the separator and touches the cathode while still in contact with the anode or its current collector.

As the nail drives further in, it eventually contacts an aluminum current collector. Once the aluminum is in play, scenarios 1 and 2 can occur. In fact, all four ISC types (1–4) may be present in parallel. In this state, essentially the nail has created a network of low-resistance bridges between what are normally isolated components, and a large composite short-circuit current flows. Figure 39 (b) conceptually shows this combined short. This complex internal short circuit condition will persist as long as the nail maintains contact between those layers, or until some of those connections are broken.

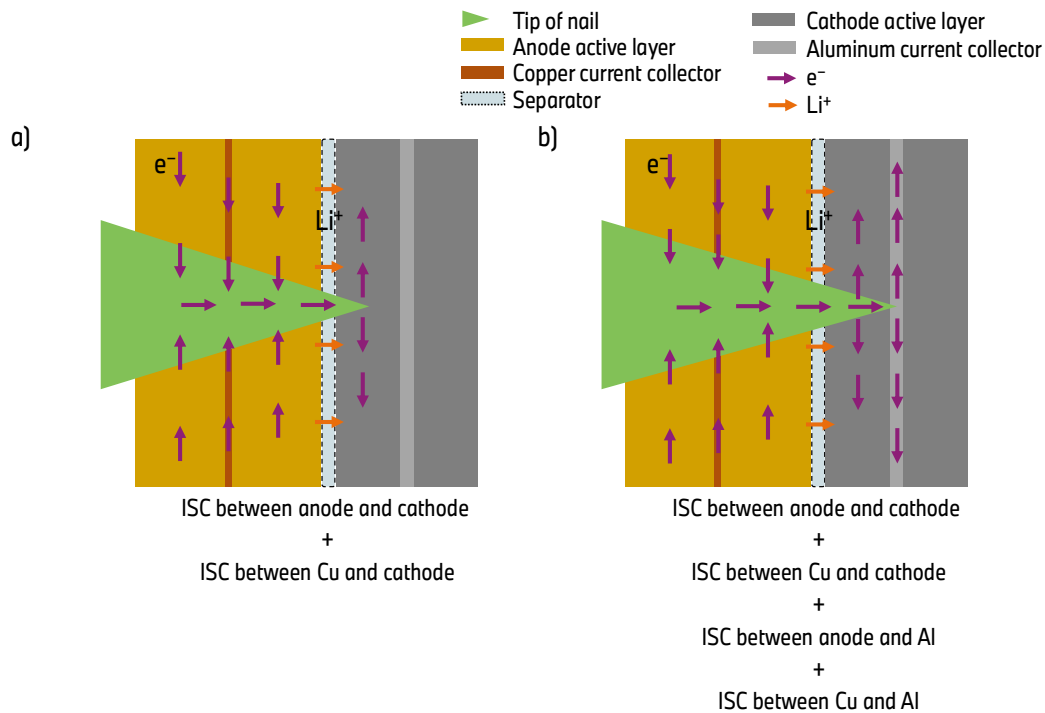


Figure 39. Schematic presentation how ISCs are induced in the nail penetration test with a real automotive prismatic cell structure with average relative ratio between cell layers.

Based on this understanding of concurrent ISC pathways, the measured ISC current profiles from the nail tests can be discussed. Figure 40 plots only the short circuit current versus penetration depth for Cell A and Cell B from the overview in Figure 36. The current is characterized by a series of peaks (spikes) for both cells, but the pattern and magnitude differ between Cell A and Cell B.

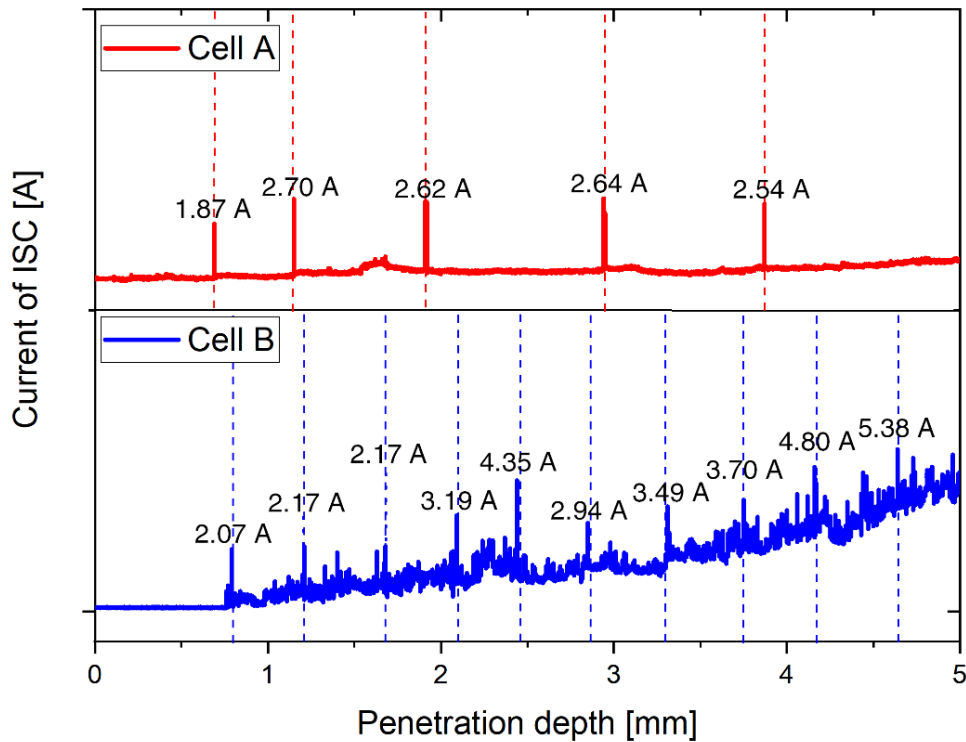


Figure 40. The ISC-current of Cell A with stacks and B with jelly rolls in the nail penetration test.

- Both Cell A and Cell B exhibit ISC current spikes periodically during penetration. Each current spike is associated with the nail contacting an aluminum current collector layer, causing a surge of ISC current, followed by an abrupt drop in current when that aluminum layer melts, and the contact is momentarily lost. This explains the “on-off” nature of the current trace.
- The ISC current of Cell A is relatively intermittent and low in magnitude, whereas the ISC current of Cell B is higher and increases more steadily with penetration. After each drop-out, the current in Cell A nearly drops to zero, with a slight baseline increase of up to 0.5 A over 500 seconds. In contrast, Cell B’s current does not drop to zero; a baseline ISC current continues to flow and grows by ISCs stacking.

To further clarify the short-circuit behavior in each design, step-by-step hypotheses for the progression of the ISC are developed each for a cell with stacks (Cell A) and jelly rolls (Cell B), illustrated in Figure 41 and Figure 42, respectively.

Hypothesis of ISC Development in Cell A with Stacks

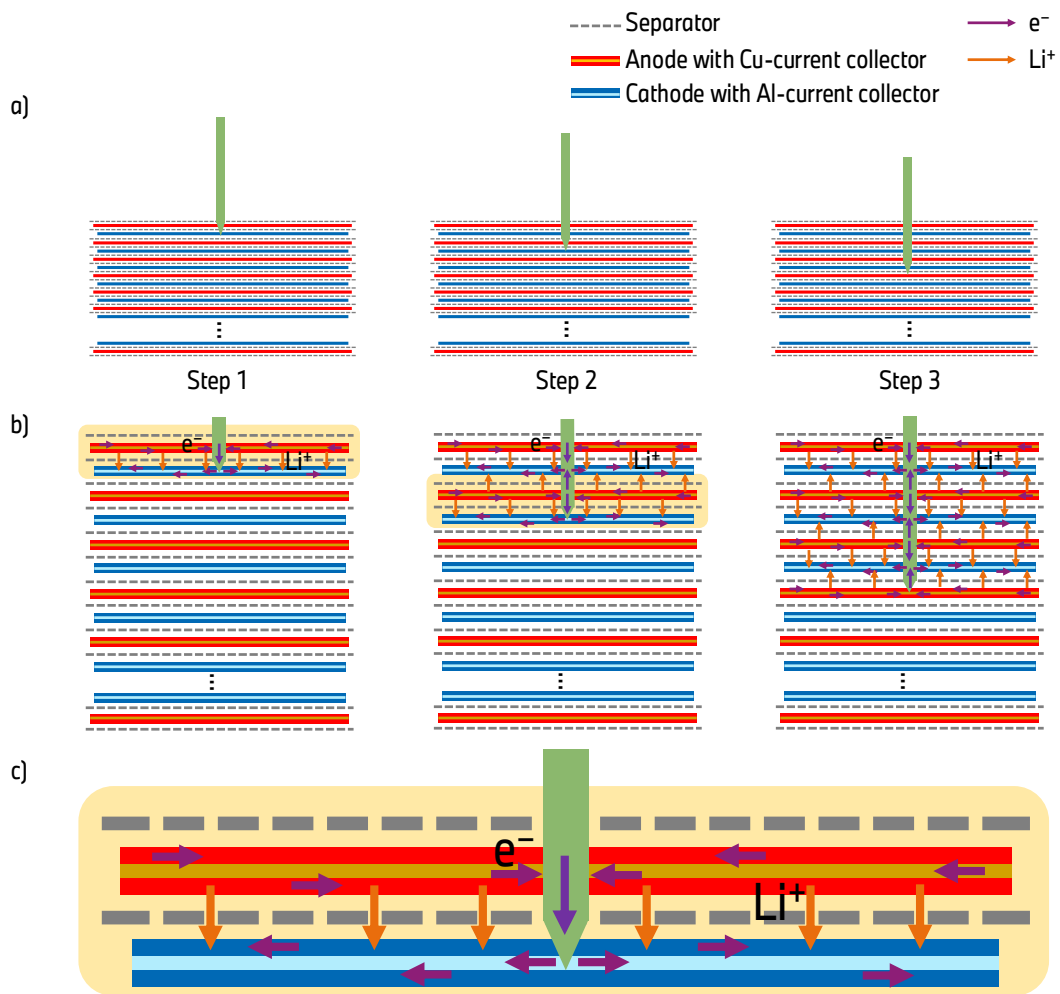


Figure 41. Hypothesis of ISC formation in the LIB with stacks: (a) schematic of the nail penetration process through a stacked cell, (b) sequence of ISC development for each step of penetration, illustrating the flow of electrons and lithium cation and (c) detail-view of the area marked with yellow box in Step 1 & 2.

Cell A can be thought of as having N individual electrode stack units connected in parallel, where N corresponds to the number of cathode layers, $N+1$ of anode layers, and $2N+2$ of separators in the stack. Each stack unit (bundle) – consisting of separator – anode – Cu – anode – separator – cathode – Al – cathode – represents a small “unit-cell” that, when isolated, would have a fraction of the total

cell's capacity. Therefore, if an ISC is confined to one unit, it effectively involves only the energy of that unit (one can roughly approximate it as 4.2/N V worth). Therefore, an internal short in Cell A that spans only one stack unit will be limited in current and energy compared to a short that spans many units.

In the initial stage of penetration (Step 1 in Figure 41), the nail has just breached the outermost stack unit. At this point, only that single unit is involved in the ISC. The result is a sharp but relatively small current spike. For instance, in Cell A the first ISC current peak reached about 1.87 A (see Figure 40). This current is limited because it is drawing energy from essentially one stack unit (one cathode–anode pair). As soon as the aluminum foil of that cathode loses electrical contact, the short in that unit is interrupted and the ISC current drops almost to 0 A. This corresponds to the first force drop and current drop observed.

As the nail penetrates deeper into the cell (Step 2), it begins to involve a second stack unit. Now the nail is simultaneously shorting two cathode–anode units in parallel. In this configuration, Li^+ ions and electrons from two units can flow into the short circuit. Consequently, the second ISC current peak (2.70 A) is higher than the first peak, since more total energy (from two units) is driving the short. However, these two units are still only a fraction of the entire cell.

By Step 3, the nail has penetrated three stack units and cathode from the fourth unit. Now multiple layers and units are involved, and the situation becomes more complex. The local temperature around the nail increases due to the joule heating from all combined shorted units. This elevated temperature can cause some ISC paths to break. Because of such effects, the ISC current in Cell A does not continue to simply add with each new unit after a certain point. In practice, after the second or third unit, the current peaks reach a plateau or fluctuate rather than increasing indefinitely. For example, in the experimental data, after the second peak (2.7 A), subsequent peaks in Cell A stayed in the 2.5–3 A range. This is attributed to the dynamic balance in the stacked cell: as more units short, the likelihood of losing one of the earlier short connections (due to melting) grows, so the effective number of units contributing at any one time is limited.

In summary, the stacked architecture of Cell A leads to a scenario where the nail triggers a series of isolated ISC events, each initially confined to a single stack or a small group of stacks. The ISC current is limited by the parallel-unit effect — each unit only provides a portion of the total current, and shorts do not all combine simultaneously across the whole cell. The result is an on-off pulsed current behavior with relatively modest peak currents in the few-ampere range for this cell, and a large portion of the cell's energy remains un-accessed at any given moment of the short.

Hypothesis of ISC Development in Cell B with Jelly Rolls

Cell B's jelly roll assembly presents a different scenario. In Cell B, the electrodes are part of continuous sheets wound in parallel, and the cell tested here contained two such jelly roll spirals connected in parallel. However, only one of the rolls was directly penetrated by the nail, so effectively about half of the cell (one jelly roll with approximately 33 Ah) was involved in the shorting process. For simplicity, one roll that was shorted is focused as it dominated the behavior.

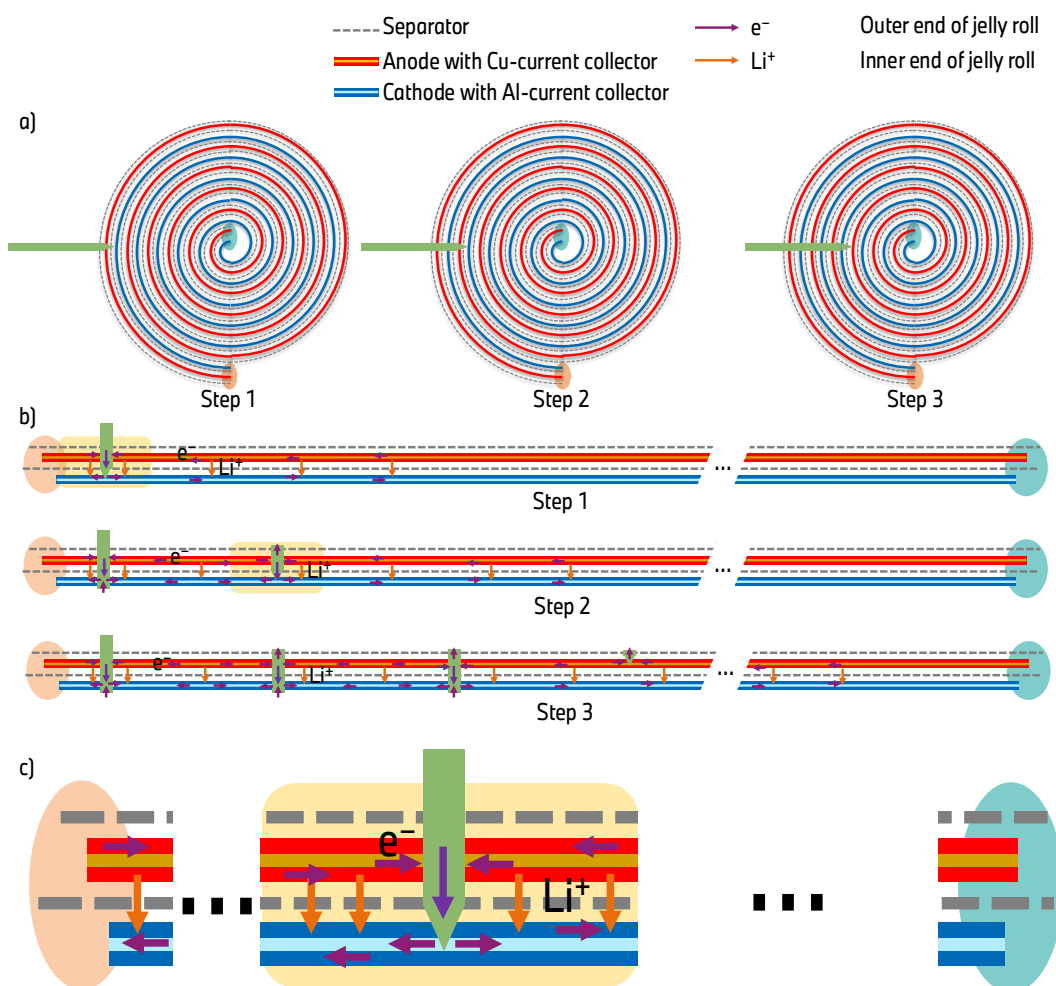


Figure 42. Hypothesis of ISC formation in the LIB with jelly rolls: (a) schematic of the nail penetration process in a prismatic cell with a jelly roll assembly, (b) sequence of ISC development at each stage, illustrating electron and Li^+ flow and (c) detail-view of the area marked with yellow box in Step 1 & 2.

At Step 1 (Figure 42), when the nail just begins to penetrate the jelly roll with 33 Ah, it is likely to short relatively wide range of layers at once. The jelly roll can be visualized with many concentric layers (Figure 42 (a)) or with one unwound long unit (Figure 42 (b)). Unlike Cell A, which consists of multiple individual electrode stacks allowing only a single stack to be involved during the initial ISC, the nail in this case immediately engages a broader area of the electrode, as there is effectively only one long negative and positive electrode arranged on a plane. By the magnitude of the first current peak (2.07 A for Cell B), which is comparable to the ISC current of Cell A, however, it is assumed that not the whole area of jelly roll is involved in ISC, but ISC remains locally. Initially only a limited area of the jelly roll is affected.

By Step 2, the nail has penetrated deeper into the jelly roll. Now, two short-circuit spots fall on the same layer unit of the roll. In this configuration, the dissipation of heat is not uniform outward, unlike in a stack, where each unit can radiate heat on its own faces; instead, heat can build up along the continuous foil between the two short points. This localized heating has two effects: it can cause local material to degrade further, potentially enlarging or restricting the shorted area, and it can also increase the resistance of that layer. The net result is that the second current peak in Cell B (about 2.17 A) is slightly higher than the first. This indicates that the short is growing in extent – more of the jelly roll's area is participating in the conduction at Step 2.

The nail has created at Step 3 a situation with four short spots all on the same continuous. Lithium ions and electrons can flow from all along that jelly roll layer toward the nail. This means the ISC

current is no longer limited to a small segment; it can draw theoretically on the entire half-cell (the whole jelly roll). Consequently, the ISC current in Cell B starts to increase more substantially and continuously as the nail goes deeper. Each new layer it contacts adds another parallel pathway, and because the jelly roll layers are long and contiguous, those pathways overlap and reinforce each other rather than remaining separate. By the time several layers are shorted together, Cell B produces a much higher current than Cell A. For example, the fifth current spike in Cell B reached 4.35 A, whereas in Cell A the fifth spike was only 2.54 A.

Overall, the jelly roll architecture of Cell B allowed ISC to propagate over a broader area of the cell and to involve multiple layers in a cooperative manner. Rather than isolated, unit-by-unit shorts, the jelly roll experienced overlapping short circuits that merged into a larger conductive network spanning much of the electrode. This resulted in the steadily rising baseline current and higher peak currents observed for Cell B, while Cell A's design inherently compartmentalized the short-circuit, preventing it from ever accessing the full cell at once.

5.2.3 Internal Temperature

Having examined the short-circuit current characteristics in Section 5.2.2, the focus now shifts to the internal temperature evolution during the nail-induced ISC and how it differs between the two cell architectures. Figure 43 illustrates the internal thermocouple measurement in Cell A (stacked) and Cell B (jelly rolls) alongside penetration depth (extracted from Figure 36). Notably, both cells exhibited sharp internal temperature spikes during the short, while no significant temperature rise was detected on any external surface at the positive terminal (see Figure 36). This clear contrast underscores the highly localized nature of the heating: conventional surface temperature monitoring cannot capture the rapid internal temperature excursions caused by an ISC.

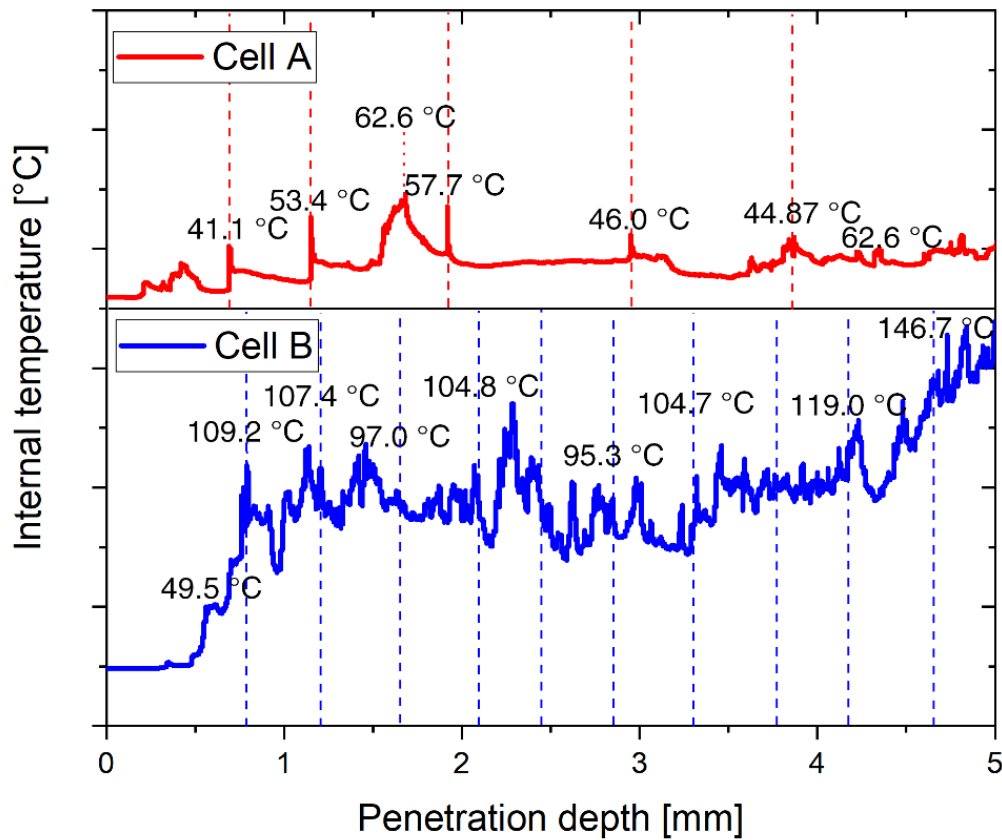


Figure 43. Internal temperature of Cell A with stacks and Cell B with jelly rolls.

- **Internal Temperature Response in Cell A with Stacks:** the embedded thermocouple near the nail recorded abrupt temperature rises coinciding with each ISC event. These spikes were short-lived – the temperature climbed quickly when an ISC occurred and just as quickly dropped back down once the local ISC current ceased. As a result, the peak internal temperature in the stacked cell remained relatively lower, not exceeding 65 °C under the tested conditions. The intermittent nature of the short (current switching on-and-off) allowed brief cooling periods between events, limiting heat accumulation.
- **Internal Temperature Response in Cell B with Jelly Rolls:** in contrast, the jelly roll cell experienced a much more pronounced and complex thermal response. The internal temperature rose significantly higher – reaching approximately 150 °C near the short location – which is over twice the maximum observed in Cell A. Moreover, the temperature – penetration depth profile in Cell B does not show a one-to-one correspondence with the distinct force drops or current peaks. Instead of isolated sharp pulses, the jelly roll's temperature trace was a complex sequence of many overlapping temperature peaks. Some thermal spikes occurs without a clearly matching single current peak or force drop. In essence, the heat generation in Cell B is more continuous and cumulative, leading to a higher thermal inertia at the short site.
- **Limitation of Measurement:** although force drops suggest melting of the aluminum current collector, the measured internal temperature does not reach aluminum's melting point (660 °C), implying a discrepancy. This discrepancy is attributed to limitations of the internal temperature measurement method. As discussed in Section 5.2.1 and demonstrated in Table 24 in Section 5.2.2, the thermal conductivity of the crafted nail tip is lower than the thermal conductivity of current collectors. As a result, heat generated at the short-circuit site is preferentially conducted within the electrode layers rather than perpendicularly through the nail to the thermocouple. Consequently, it is assumed that the recorded temperature remains below the actual localized temperature at the short-circuit location.

The key factor is the anisotropic thermal conductivity of the cell layers and how the assembly geometry affects heat dissipation. Lithium-ion cells have a highly layered structure, leading to orders-of-magnitude differences between in-plane and cross-plane thermal conductivities. Heat conducts very effectively along the planes of the electrodes (dominated by the high thermal conductivity of the copper and aluminum current collectors), but it conducts poorly through the perpendicular direction (across separators). Table 26 compares typical in-plane vs. cross-plane thermal conductivities for the two cell designs.

Table 26. Effective thermal conductivities in the plane of the electrodes vs. through the thickness (cross-plane) for LIB with stack and jelly roll assemblies.

Assembly	Thermal conductivity [W/m·K]		Reference
	In-plane	Cross-plane	
Stack	20-28	0.48-3.40	[152,153]
Jelly Roll	24	0.35-1.40	[154,155]

Those values presented in Table 26 are strongly influenced by the specific electrode chemistries; however, in the context of this study, they are considered as representative ranges to illustrate the dependence of thermal conductivity on both cell assembly type and conduction direction. [151,152]. Notably, both assemblies exhibit strong in-plane conduction but much lower cross-plane values.

Because of this thermal anisotropy, the geometry of the electrode stack vs. jelly roll plays a significant role in temperature distribution during the ISC. In the stacked cell, each electrode sheet spans the full planar dimensions of the cell, and the stack of layers can act like a spreader; a portion of the generated heat travels laterally along the metal foils toward the cell edges and casing. By contrast, in the jelly roll cell, the wound electrodes confine the heat within the same layer, and

lateral heat flow is largely limited. As a result, heat is more trapped in Cell B, because the jelly-roll architecture's geometry and the poor cross-plane heat conduction create a thermal bottleneck.

In summary, both cells showed a qualitatively similar periodic pattern in their ISC response – as the nail pierced each successive layer, concurrent spikes in current and internal temperature and a drop in penetration force were recorded. However, the finer details of the periodic heating differ between the cells. In Cell A, the temperature spikes were closely tied to individual penetration events (each likely corresponding to a specific layer shorting and then burning out), yielding a clean on-off temperature profile. In Cell B, the overlapping temperature peaks suggest that once the short progressed into the jelly roll, the thermal events from adjacent layers merged. The internal temperature in Cell B sometimes climbed even in the absence of a distinct new force drop, hinting that heat from prior layers continued to accumulate or that minor shorts persisted between major penetration events. These internal temperature results highlight how cell design can drastically influence the thermal consequences of an internal short.

5.3 Conclusion

Results and discussion in Section 5.2 can be summarized as below.

Mechanical and Geometrical Considerations

The distinct mechanical responses of the two assemblies illuminate their safety behavior. Both cells showed periodic drops in the penetration force as the nail pierced conductive layers (indicative of current collector failure/melting events). However, Cell B's force–penetration profile was more regular, with drop intervals closely matching the known layer spacing (average 0.435 mm vs. 0.293 mm actual layer cycle). This implies that the nail in the jelly roll punctured each layer in a near-uniform, consecutive manner. Cell A's force drops were less uniform and spaced further apart (average 0.795 mm vs. 0.374 mm layer cycle), suggesting that not every single layer caused a distinct force drop – some layers may have been bypassed or multiple layers failed together. This difference is likely due to the stacked structure: the individual stacks, being discrete, can shift or buckle slightly under load, so the nail sometimes pushes a stack aside rather than immediately puncturing it. The jelly roll, on the other hand, is a continuous wound structure that offers more uniform resistance, so layer penetration is more consistent. From a safety perspective, the more uniform penetration in Cell B meant that once the short started, each subsequent layer was rapidly involved, feeding the short-circuit and compounding the heating. In Cell A, the irregular mechanical response might have introduced brief delays or partial contacts that limited how many layers shorted at once, again mitigating the instantaneous severity of the short.

Influence of Assembly Architecture on ISC Severity

The comparative findings for the stacked vs. jelly-roll cells reveal that internal design plays a pivotal role in governing ISC behavior and its potential hazard. Under identical nail penetration tests, Cell A (stacked layers) and Cell B (jelly roll) both experienced repeating ISC events as the nail sequentially breached layer after layer. However, the magnitude and distribution of these events differed markedly. As demonstrated in Figure 36 and Figure 40, Cell A exhibited small, discrete current spikes (on the order of a few amperes) that were rapidly self-limited, whereas Cell B showed a higher and more sustained short-circuit current that tended to increase as the penetration continued. This difference is attributable to the architectures: in the stacked cell, each ISC was largely confined to an isolated stack unit (with only a fraction of the cell's total stored energy involved in each short), effectively acting like a series of tiny fuses blowing one after another. In the jelly-roll cell, the active short involved a continuous portion of the wound electrodes, tapping into a larger available energy reservoir at once. Consequently, the jelly-roll design delivered higher cumulative electrical energy into the fault, as evidenced by its rising ISC current profile.

These electrical differences directly translated into the thermal outcomes observed. The stacked Cell A, with its on-and-off current behavior, only ever heated locally and briefly; its peak internal

temperature ($\approx 65^\circ\text{C}$) remained relatively low. In contrast, the jelly roll Cell B underwent intense localized heating, soaring to $\sim 150^\circ\text{C}$ internally. Importantly, neither cell showed any significant temperature increase on its external surfaces during the short, meaning that in both designs the heat was largely contained inside. In Cell B, the internal short pushed the local temperature well beyond (or close to) the shutdown point of separator. Although a melting separator can in principle stop the short, it can also lead to loss of mechanical integrity and additional areas of contact, potentially exacerbating the short. Moreover, at around 150°C a fully charged cell's electrodes and electrolyte may start to decompose exothermically, as SEI layers break down and reaction between lithiated anode and electrolyte can initiate — this may lead to thermal runaway in extreme cases. Cell A, by virtue of its design, never approached these critical temperatures in the test, whereas Cell B came much closer, indicating a higher inherent risk of triggering thermal runaway.

It is notable that despite the significant difference in peak internal temperature, neither cell went into full thermal runaway during the controlled tests. After the test, the nail was drawn out from the LIB, preventing further ISC current to flow. Thus, the cells were brought to a safe state before a cascading failure could occur from stacking ISCs. Nonetheless, the results strongly suggest that if the cell were unable to dissipate the heat, the cell with jelly roll would be far more likely to enter an uncontrollable thermal runaway than the stacked cell. In a real-world scenario (e.g. an internal short from an accident or manufacturing defect), a stacked architecture may localize the short to one stack module which ejects its energy and then ceases, giving the battery management system or safety mechanisms a window to respond. By contrast, a jelly roll could sustain a high-current short across a larger area, rapidly heating the core of the cell to dangerous levels before any external intervention is effective.

Implications for Thermal Runaway Risk

The overall comparison between the stacked and jelly-roll prismatic cells demonstrates that the stacked design tends to isolate and distribute the short-circuit energy, whereas the jelly-roll design concentrates it. Cell A's multiple smaller ISC events resulted in localized damage but did not elevate the cell's bulk temperature significantly. In essence, the stacked configuration exhibited a form of inherent "current limiting" — each stack acted as a fuse, blowing before the full cell shorted, which inherently curbed the thermal buildup. This behavior can be seen as a safety advantage: even though an internal short is always dangerous, it is assumed that the stacked cell's architecture lessened the likelihood of that event escalating into a thermal runaway. In contrast, Cell B's jelly roll allowed a more extensive internal short-circuit that delivered a larger fraction of the cell's stored energy into heat in one region. The very high internal temperature (150°C) recorded in Cell B is alarming because it indicates that even though the cell survived this test, it was pushed near the brink of thermal runaway.

It must be emphasized that neither cell design is immune to thermal runaway. If enough layers short-circuit simultaneously or if the heat cannot be released, any Li-ion cell will eventually reach a critical temperature. However, this study's results clearly indicate that the stacked electrode assembly provides a greater tolerance for internal shorts in that it delays and fragments the energy release. The jelly roll assembly, in contrast, tends to produce a more contiguous short and hotspot, which is a less favorable outcome from a safety standpoint. From a battery safety engineering perspective, this suggests that large-format cells with stacked sheets could offer improved intrinsic safety against limited ISC under nail penetration-type abuse, as they might better localize the damage and avoid immediate runaway. Jelly roll cells, which are more common in cylindrical formats and some prismatic designs, may need additional mitigation to handle internal short events without catastrophe.

Limitation of This Study

This internal short-circuit (ISC) study clearly demonstrated that the assembly architecture of lithium-ion battery (LIB) cells has a pronounced influence on both the electrical and thermal responses during ISC events. These findings underscore the critical importance of considering cell

structural design — not solely electrode chemistry or capacity — when evaluating safety characteristics and failure behavior under abuse conditions.

Nevertheless, several limitations inherent to the experimental design must be acknowledged:

First, the quantification of ISC current in this study required the implementation of an external current source. While this approach ensured that the cells were maintained at a constant voltage corresponding to a 100% state of charge (SOC) — by continuously compensating for capacity loss during the ISC — it also introduced an artificial test condition. The influence of the external circuit configuration was not systematically analyzed or quantified. In practical scenarios, such external compensation does not exist at a cell level (although it may be present at the battery pack level). Therefore, the insights obtained under this controlled condition should be interpreted with caution when applied to real-world scenarios. Also, the presence of an external current source in operational cells may significantly affect the system's resilience to internal shorts, for example by altering the critical penetration depth required to trigger thermal runaway, or the magnitude and duration of the ISC current.

Second, the proposed hypotheses for ISC development presented in Section 5.2.2 do not fully consider the integrated electrical behavior of cell units within the stacked architecture. While the analysis treated ISC formation within individual cell units (separator – anode – Cu – anode – separator – cathode – Al – cathode), in practice, all stack units are electrically connected in parallel within a single cell. It is likely that a short circuit occurring in one unit may not remain completely isolated from neighboring units, although it is assumed that the inter-unit resistance is higher than the intra-unit resistance. This limitation implies that the actual ISC current pathways and their interactions may be more complex than represented in the simplified model. Further investigation — particularly through detailed electrothermal simulations — is required to better understand the electrical coupling between stacked units during ISC propagation.

Next, the internal temperature measurement approach also has limitations. Although the thermocouple was embedded in the nail, the method is constrained by the relatively low thermal conductivity of the nail material compared to the in-plane conductivity of the cell electrodes. Additionally, a spatial offset of approximately 2.5 mm between the thermocouple and the actual ISC site further limits the accuracy of the temperature readings. As a result, the measured temperatures do not reflect the true peak temperature at the ISC location. Nevertheless, this technique remains valuable for comparative analysis; it enables qualitative evaluation of internal temperature evolution across cells with different assembly types, even if the absolute insitu temperature at the short site cannot be directly measured.

Finally, a structural limitation arises from the test setup itself. The prismatic LIBs used in this study were partially disassembled, and the penetration was carried out directly through the exposed electrode layers — without the enclosing cell can. In practical cells, the metallic cell can is typically held at a positive potential and contact between the outermost anode and the can may initiate one of the most critical ISC pathways. Since the cell cans of both Cell A and Cell B were removed for the purpose of this study, such a can-to-anode short circuit scenario could not be included in the current analysis. However, this specific ISC configuration will be investigated and discussed in the following Chapter 6.

6 Study of the Impact of the Floating Can on Thermal Runaway

The parts of this chapter have been published in: Hyojeong Kim*, Abdulbashir Sahebzadeh, Hans Jürgen Seifert, Carlos Ziebert, Jochen Friedl, *Needle penetration studies on automotive lithium-ion battery cells: Influence of resistance between can and positive terminal on thermal runaway*, Journal of Power Sources, 592, 233902, 2024 [19]. The figures and results presented here are reformulated and newly prepared for the purpose of this dissertation, ensuring original presentation and contextual adaptation in line with academic integrity standards.

In automotive prismatic lithium-ion cells, a crucial type of ISC is located between the positively charged aluminum cell can and the outermost anode layer, because the potential of the aluminum can should be greater than $> 1 \text{ V vs. Li/Li}^+$ so that an alloying reaction between lithium cations from the electrolyte and the aluminum from the cell can is mitigated. [156] Typically, this is ensured by connecting the cell can directly to the cathode potential. Consequently, if an electrically conductive particle bridges the outermost anode layer and the aluminum can, potentially due to manufacturing defects, an ISC occurs.

To mitigate the risk and severity of such ISCs, the **"floating can"** concept introduces a high-resistance synthetic insulation between the cell can and the rivet, which connects the positive terminal to the cathode. In contrast, conventional automotive prismatic cells employ a direct connection between the can and the positive terminal (**"can on potential"** configuration), as detailed in Section 2.4.2.

The objective of this study is to systematically evaluate the impact of the can configuration — floating can versus can on potential — on thermal runaway characteristics using needle penetration tests. The cells tested differ solely in the connection type between the can and positive terminal, maintaining identical design parameters such as capacity (34 Ah), chemical composition, and mechanical construction. This ensures that observed variations in thermal behavior are exclusively attributable to the difference in the can-terminal connection.

Initially, cell voltage and three surface temperatures were recorded during needle penetration tests to assess the thermal stability of LIB cells based on the resistance between the cathode and cell can. The results demonstrated that the floating can significantly enhanced the cells' resistance against ISC-induced thermal runaway. Cells with a floating can exhibited greatly diminished severity of thermal events compared to cells with a direct can on potential connection, which experienced rapid and violent thermal runaway with hazard levels exceeding category 4 (see Table 8). In the subsequent part of the investigation, a specialized method for quantitatively measuring ISC current was developed. ISC currents were quantified for different ISC types, including shorts between the cell can and outermost anode, as well as layer-to-layer internal shorts within the cell. Lastly, accelerating rate calorimeter (ARC) tests validated the intrinsic thermal equivalence of the two cell

configurations, demonstrating that the difference in thermal runaway behavior arises solely from the introduced electrical resistance. This study provides critical guidance for safer prismatic cell designs and highlights how optimized needle penetration tests enhance understanding of internal LIB behavior under mechanical abuse conditions.

6.1 Experimental Setup

6.1.1 Needle penetration test

A series of needle penetration experiments were carried out to evaluate how the method of connecting the cell's metal can to its positive terminal affects safety.

Cell Preparation

A total of 17 prismatic LIB cells with a capacity of 34 Ah, composed of dual jelly rolls featuring mixed cathodes (NMC111, NMC622, and NCA) and graphite anodes, were investigated. Cells were mechanically compressed between stainless steel plates ($210 \times 79 \times 15 \text{ mm}^3$ with a central aperture of 15 mm) under a compressive load of 5 kN, replicating realistic automotive module conditions. The cells were charged to full capacity (100% SOC, 4.2 V, 34 Ah) at room temperature using a C/3 CC (constant current) - CV (constant voltage) charging protocol terminated when current decreased below 1 A.

Test protocol

Needle penetration experiments utilized carbide KW40 needles (1 mm diameter, 60 mm length, 60° tip angle) and were structured into three parts:

1. In **Part I** (Tests 01–12), cells were penetrated at predefined speeds (0.01, 0.02, or 0.03 mm/s) until thermal runaway initiation. Each test condition was repeated to confirm reproducibility.
2. **Part II** (Tests 13–15) involved penetration of floating can cells intentionally limited to depths sufficient for "soft shorts," thus avoiding thermal runaway. These soft-short tests probed the cells' behavior when an internal short occurs without ignition.
3. **Part III** (Tests 16–17) measured ISC currents quantitatively, incorporating a supplemental electrical circuit that maintained cell voltage at 4.2 V and recorded ISC current via a shunt resistor.

Throughout the needle penetration tests, several parameters were continuously recorded at a sampling frequency of 100 Hz using a Gantner measurement system (Module A101 and A104). These parameters included the cell voltage, the voltage between the needle and the positive terminal (V_{NP}), the voltage between the needle and the negative terminal (V_{NN}), the force exerted on the needle during penetration, and surface temperatures at critical locations, namely the vent, positive terminal, and negative terminal, measured with K-type thermocouples.

As detailed previously in Section 3.2.2, the precise measurement of V_{NP} and V_{NN} voltages is crucial, as it allows the accurate determination of the needle's penetration depth at two critical interfaces. Specifically, the penetration depth from the aluminum can (d_{can}) is identified at the moment when the voltage V_{NP} approaches 0 V and simultaneously V_{NN} approaches approximately 4.2 V. Conversely, the penetration depth from the outermost anode (d_{anode}) is determined when V_{NN} reaches 0 V while V_{NP} is approximately 4.2 V. In addition to these electrically measured depths (d_{can} and d_{anode}), the penetration depth derived directly from the applied mechanical force on the needle (denoted as d) was also recorded. All these penetration depths were subsequently compared to verify consistency and accuracy.

For the quantitative measurement of internal short circuit (ISC) currents, an additional electrical measurement circuit was employed specifically during Tests 16 and 17, as illustrated in Figure 33,

differed from the arrangement used for the qualitative assessments (Parts I and II) as in Figure 31. Each test cell was electrically connected in parallel to a regulated power supply set to maintain a constant voltage of 4.2 V, with a maximum current limit of 6 A. The connection included a shunt resistor rated at 40 A and 75 mV. During needle penetration, any current flowing through the shunt resistor, necessary to maintain the fixed cell voltage, represented the magnitude of the ISC current. Detailed parameters for each conducted test are summarized comprehensively in Table 27.

Table 27. Protocol for needle penetration tests consisting of three parts (I, II and III), reproduced from literature [19].

Part	Test	Group	Type of cell can	Speed of penetration [mm/s]	Measurement of V				Note
					V_{cell}	V_{NN}	V_{NP}	V_{sh}	
I	01	A	Can on potential	0.01	Y	Y	Y	N	Penetration until TR (d_{can} and d_{anode} were not determined for tests 02 and 06.)
	02			0.01	Y	N	N	N	
	03			0.02	Y	Y	Y	N	
	04			0.02	Y	Y	Y	N	
	05			0.03	Y	Y	Y	N	
	06			0.03	Y	N	N	N	
	07	B	Floating can	0.01	Y	Y	Y	N	Penetration until TR
	08			0.01	Y	Y	Y	N	
	09			0.02	Y	Y	Y	N	
	10			0.02	Y	Y	Y	N	
	11			0.03	Y	Y	Y	N	
	12			0.03	Y	Y	Y	N	
II	13	C	Floating can	0.01	Y	Y	Y	N	Penetration without TR (Soft short)
	14			0.02	Y	Y	Y	N	
	15			0.03	Y	Y	Y	N	
III	16	D	Can on potential	0.01	Y	N	Y	Y	Measurement of ISC-current
	17		Floating can	0.01	Y	N	Y	Y	

6.1.2 Accelerating rate calorimeter

Accelerating rate calorimetry tests were conducted to comparatively assess the intrinsic thermal stability of lithium-ion battery cells configured with a floating can versus those configured with a direct can on potential connection. The ARC chamber utilized for these experiments was equipped with multiple type-N thermocouples and heating elements positioned on the chamber lid, bottom, and sidewalls, creating a near-adiabatic environment characterized by minimal heat exchange with the surroundings. This arrangement ensured that the thermal conditions closely approximated worst-case thermal runaway scenarios.

Calibration and Drift-Check of EV-ARC

Prior to conducting the cell experiments, the ARC was calibrated following the manufacturer's recommended procedure. For this calibration, an aluminum dummy cell matching the dimensions, mass, and estimated heat capacity of the actual test cells was instrumented with identical thermocouples and subjected to a calibration cycle. During calibration mode, heater power outputs were adjusted as 10 % to ensure uniform heating by determining calibration offsets among the thermocouples. After completing this calibration step, a standard drift-check test — essentially a typical Heat-Wait-Seek (HWS) protocol performed on the aluminum dummy — was conducted. This test verified that the dummy cell's self-heating and self-cooling rates remained consistently below the threshold of 0.02 °C/min, confirming stable and accurate thermal measurement conditions.

Cell Preparation

For the ARC evaluations, a total of four lithium-ion cells — two with a floating can configuration and two with a direct can on potential configuration — were selected. Prior to testing, each cell underwent three charge/discharge conditioning cycles at a C/3 rate, with a 30-minute rest period between cycles. These cycles were performed to confirm the stability and reproducibility of the cell capacities and to identify any potential capacity loss or hidden defects. Following this conditioning step, each cell was fully charged to 100% state of charge (SOC). A type-N thermocouple, commonly termed a "bomb" thermocouple, was affixed centrally on the large face of each test cell to precisely control and monitor the cell temperature within the ARC chamber. Additionally, a type-K thermocouple was attached to the cell's vent to record vent temperature behavior throughout the tests. Cell voltage measurements were continuously monitored during the experiments.

Heat-Wait-Seek Test

Each ARC experiment adhered to a standardized Heat-Wait-Seek (HWS) test procedure, covering a temperature range from 50 °C to 350 °C, as illustrated in Figure 28. Within this protocol, the ARC chamber incrementally heated the test cells in defined steps of 5 °C (*Heat Mode*). Following each incremental temperature increase, the cells were maintained at that temperature for 20 minutes (*Wait Mode*) to ensure the achievement of thermal equilibrium. During the subsequent *Seek Mode*, the ARC continuously monitored the self-heating rate. If the self-heating rate of the test cell surpassed the critical threshold of 0.02 °C/min at any temperature step, the ARC chamber immediately transitioned to *Exotherm Mode*. In *Exotherm Mode*, the chamber heaters dynamically tracked and matched the cell's rising temperature, preserving near-perfect adiabatic conditions and capturing the full thermal runaway progression. If no thermal runaway was initiated by the time the cell temperature reached 350 °C, active cooling was implemented by blowing out the chamber with compressed air (*Cooling Mode*). This comprehensive testing sequence enabled the precise identification and measurement of the onset temperatures associated with various exothermic reactions and thermal runaway phenomena under controlled, quasi-adiabatic conditions.

6.2 Results and Discussion

6.2.1 Effect of Can Connection on Thermal Runaway Behavior

Figure 44 illustrates the cell voltage and the temperatures recorded at three critical surface locations during needle penetration tests (tests 01-12). Group A comprises cells configured with the can on potential design (Figures 44 (a), (c), (e), and (g)), whereas Group B includes cells with the floating can configuration (Figures 44 (b), (d), (f), and (h)). Both groups were subjected to penetration until thermal runaway occurred. In contrast, cells from Group C, depicted in Figure 45, were penetrated only to a depth sufficient to induce internal short circuits without triggering thermal runaway. For consistency and clarity, time zero across all figures denotes the onset of thermal runaway, identified by the initial decline in cell voltage.

The detailed behaviors of cell voltage and temperature for each group can be summarized as follows:

- **Group A:** for cells with the can on potential configuration, needle penetration reaching a critical depth induced a rapid and severe thermal runaway event. Upon initiation, the cell voltage collapsed instantaneously within less than one second, accompanied by sharp, simultaneous temperature spikes at all monitored locations. Within approximately two seconds, the temperatures at both terminals and the vent increased dramatically: the positive terminal reached around 259 °C, the negative terminal approximately 314 °C, and the vent temperature peaked at over 1280 °C, as displayed in Figure 44 (c), (e) and (g). This rapid temperature increase coincided with a vigorous flame jet erupting from the vent. Following this rapid venting event, the vent temperature quickly dropped due to the rapid expulsion of heated gases, whereas terminal temperatures exhibited a comparatively slower decay.
- **Group B:** cells employing the floating can configuration that experienced thermal runaway displayed broadly similar behaviors, albeit with critical distinctions. While these cells also exhibited an initial abrupt voltage drop indicative of thermal runaway, the voltage briefly recovered to approximately 4.2 V before gradually decreasing to 0 V over approximately ten seconds, as illustrated in Figure 44 (b). This behavior suggests a significantly lower ISC current compared to cells from Group A. Notably, temperatures at the terminals reached higher peak values compared to Group A (Figure 44 (d) and (f)), while vent temperatures were relatively lower (Figure 44 (h)). This observation implies that the internal heat had a longer interval for distribution throughout the cell, likely due to the delayed voltage collapse — a phenomenon termed the “*spring-back*” effect — which resulted in more uniform internal heating and avoided an immediate explosive venting event.
- **Group C:** cells from Group C, featuring the floating can configuration and penetrated to depths insufficient to trigger thermal runaway, demonstrated distinctly different behavior. These cells underwent a gentle, slow discharge over extended periods without any rapid voltage collapse or flame occurrence. Cell 14, exhibiting the deepest penetration ($d = 3.10$ mm and $d_{\text{can}} = 3.18$ mm) within this group, displayed several voltage fluctuations, reaching a minimum voltage of 3.28 V, indicative of significant resilience against ISC conditions. Correspondingly, surface temperature measurements at the vent and terminals showed no abrupt increases, as depicted in Figure 45. The most notable temperature rise occurred in Cell 15 with the biggest penetration depth from anode ($d_{\text{anode}} = 0.51$), reflecting its somewhat more pronounced yet still mild voltage decline ($\Delta V \approx 0.09$ V over three hours) compared to Cell 13 ($d_{\text{anode}} = 0.20$) and Cell 14 ($d_{\text{anode}} = 0.22$). This modest heating was uniformly distributed within the cell, as no measurement point (vent or terminal) recorded significantly higher temperatures compared to others.

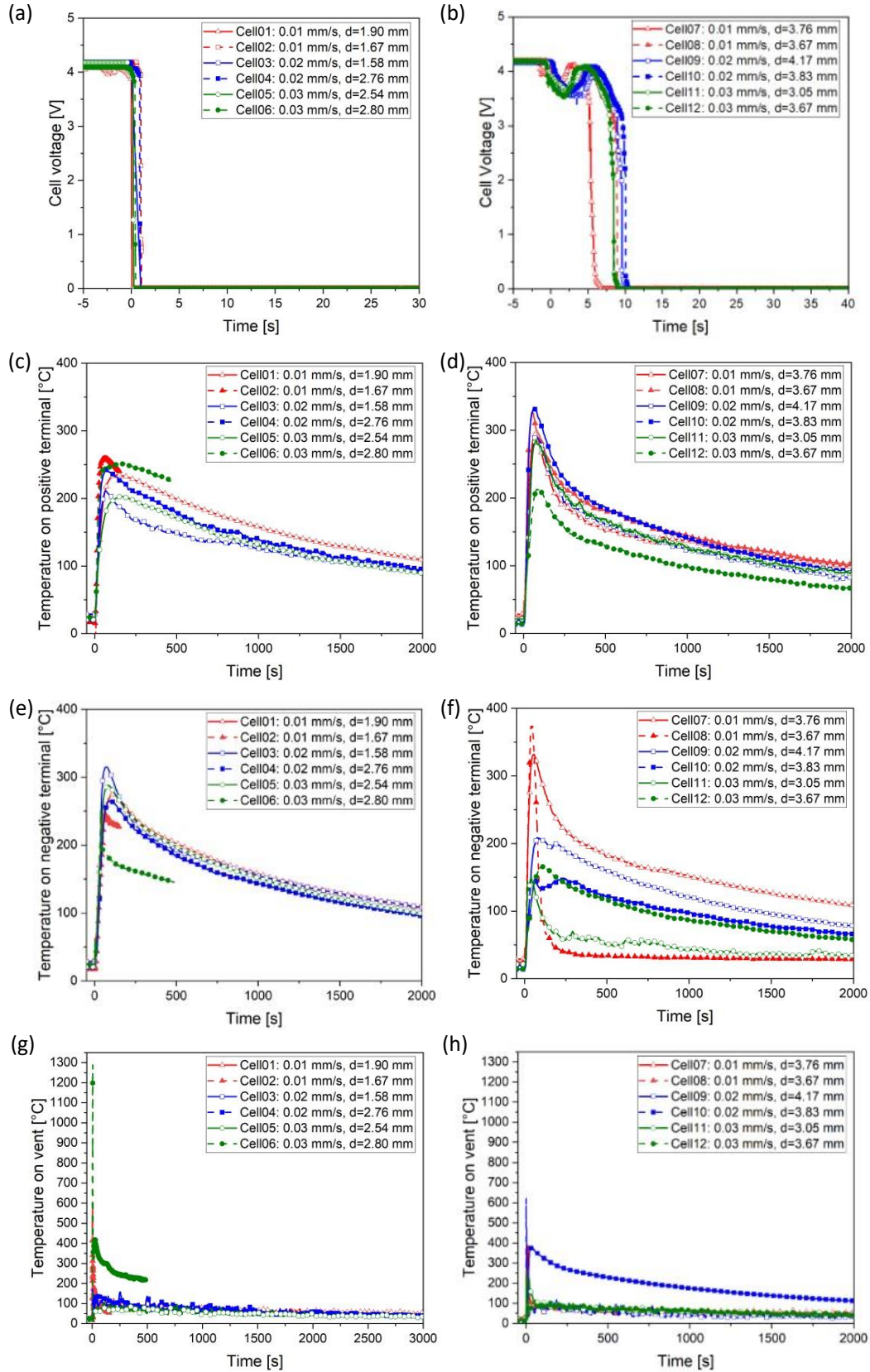


Figure 44. Cell voltage and temperature profiles for Groups A and B during thermal runaway: (a) cell voltage for can on potential; (c) temperature at positive terminal for can on potential; (e) temperature at negative terminal for can on potential; (g) vent temperature for can on potential; (b) cell voltage for floating can (for an enlarged detail view, see Figure 60 in Appendix); (d) temperature at positive terminal for floating can; (f) temperature at negative terminal for floating can; and (h) vent temperature for floating can, reproduced from literature [19].

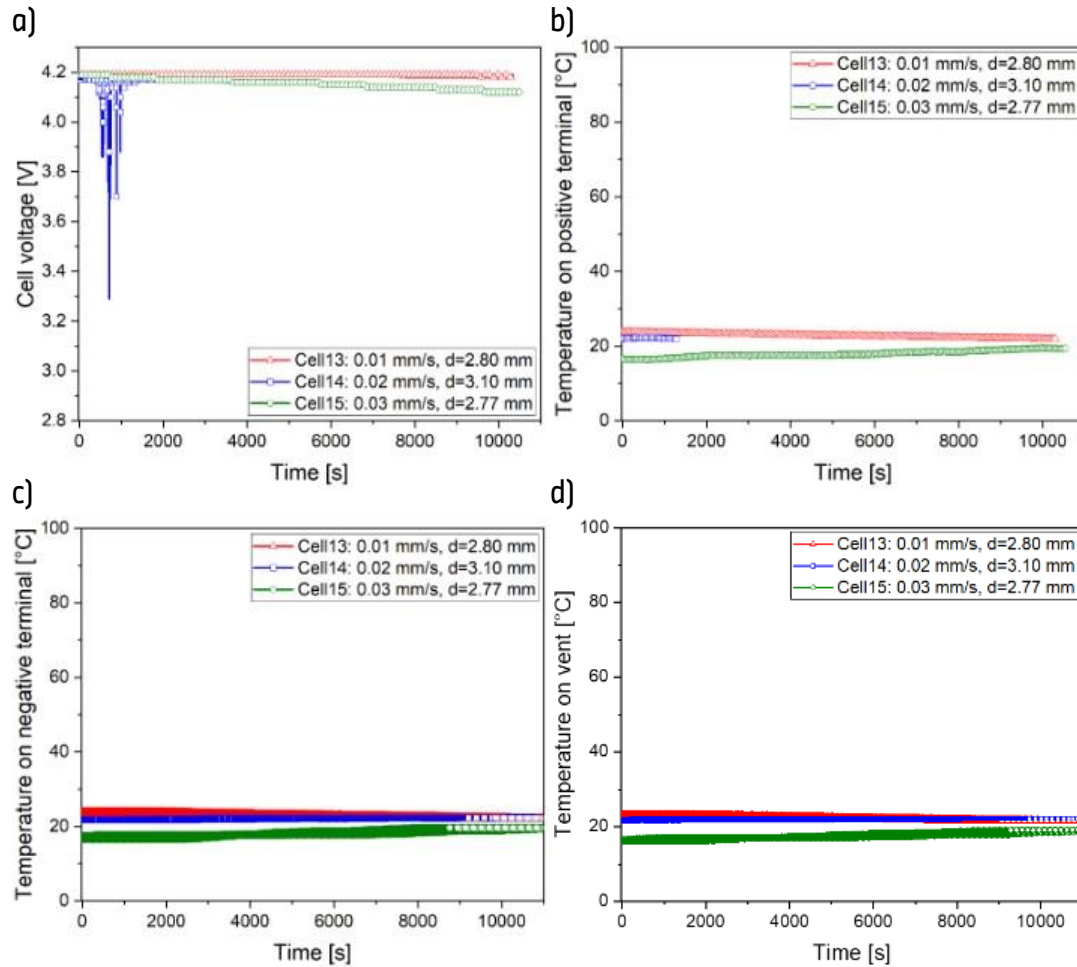


Figure 45. Cell voltage and temperature profiles of Group C with soft short: (a) cell voltage profile (for an enlarged detail view, see Figure 61 in Appendix), temperature profile (b) on positive terminal, (c) on negative terminal and (d) on vent, reproduced from literature [19].

The behaviors observed in each group can be summarized concisely as follows:

- **Group A (Can on Potential with Thermal Runaway):** the penetration test resulted in an immediate and severe voltage collapse, accompanied by extreme temperature elevations, reaching approximately 1000 °C at the vent. This rapid temperature spike coincided with an intense flame emission through the vent, categorizing the event as a catastrophic thermal runaway with an EUCAR hazard level greater than 5.
- **Group B (Floating Can with Thermal Runaway):** cells in this configuration similarly exhibited a swift voltage collapse, but crucially demonstrated a transient voltage recovery or “spring-back” phenomenon. The terminal temperatures in these cells peaked at values higher than those recorded for Group A, while vent temperatures were comparatively lower. Despite these differences, flame ejection was still observed, and thermal runaway occurred with rupture around vent marked with the red narrow in Figure 46, also corresponding to an EUCAR hazard level greater than 5.
- **Group C (Floating Can with Soft Short):** cells penetrated only to induce internal short circuits without triggering thermal runaway displayed a gradual, slow voltage decrease over several days. No flames were observed, and surface temperatures rose only marginally. Notably, the vent remained intact and closed throughout testing, resulting in no runaway event, thus corresponding to a lower EUCAR hazard level of approximately 3.

Post-test examination revealed that cells from Groups A and B were significantly charred and exhibited open vents. In contrast, cells from Group C sustained minimal damage, with vents remaining sealed and the cells themselves largely undamaged, indicative of a non-critical soft short scenario as visually represented in Figure 46.

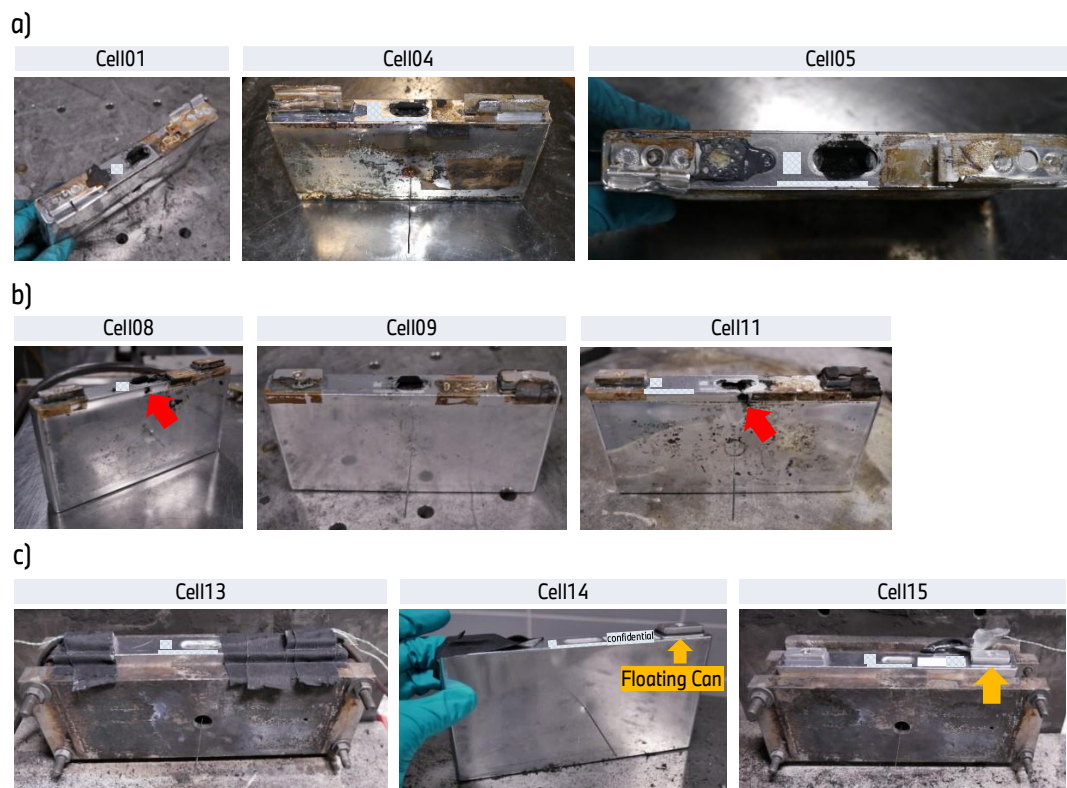


Figure 46. Visual comparison of the cell surface and vent conditions after experiencing thermal runaway and soft short events: (a) illustrates Group A (can on potential cells after thermal runaway), (b) depicts Group B (floating can cells after thermal runaway), and (c) shows Group C (floating can cells after soft short).

To systematically assess the relationships between thermal runaway or soft short behavior and the critical penetration depths, key parameters derived from Figure 44 and Figure 45 — including maximum recorded temperatures and corresponding critical penetration depths — are comprehensively summarized along with relevant test conditions in Table 28. Furthermore, to quantitatively analyze voltage behavior during testing, the time duration required for the cell voltage to decline to 2.8 V — defined by the cell manufacturer as the minimum operating voltage — was also determined and is presented in the same table.

Table 28. Results of cell 1-15 depending on the type of can and the type of reaction, reproduced from literature [19].

Parameters and Results		Cell in Group A								
		01	02	03	04	05	06			
Type of can		Can on potential								
Speed of penetration (mm s ⁻¹)		0.01	0.01	0.02	0.02	0.03	0.03			
Penetration depth (mm)	<i>d</i>	1.90	1.67	1.58	2.76	2.54	2.80			
	<i>d</i> _{can}	1.90	-	1.80	2.66	2.66	-			
	<i>d</i> _{anode}	0.02	-	0.00	0.01	0.01	-			
Max. Temp. (°C)	+ Terminal	234.8	259.1	210.1*	242	202.5	251,7			
	- Terminal	275.0	246.7	314.9	265.2	288.3	251.0			
	Vent	600.7	452.8	137.9	173.1	108.1	1288.7			
Time to V < 2.8 V		0.02 s	0.97 s	0.00 s	0.91 s	0.20 s	0.40 s			
Categorized as		Thermal runaway								
Parameters and Results		Cell in Group B						Cell in Group C		
		07	08	09	10	11	12	13	14	15
Type of can		Floating can						Floating can		
Speed of penetration (mm s ⁻¹)		0.01	0.01	0.02	0.02	0.03	0.03	0.01	0.02	0.03
Penetration depth (mm)	<i>d</i>	3.76	3.67	4.17	3.83	3.05	3.67	2.80	3.10	2.77
	<i>d</i> _{can}	3.76	3.88	4.73	4.05	3.53	3.93	2.81	3.18	3.00
	<i>d</i> _{anode}	1.48	0.88	1.35	1.15	0.77	1.24	0.20	0.22	0.51
Max. Temp. (°C)	Vent	293.8	324.2	289.4	333.7	285.8	212.7	No Change	No change	19.4
	+ Terminal	331.7	373.5	207.5	149.7*	149.4*	165.3*			19.6
	- Terminal	386.1	345.4	116.1	620.8	257.1	123.5			19.1
Time to V < 2.8 V (Group B) / Voltage [V] after time [h] (Group C)		5.35 s	8.79 s	5.08 s	9.02 s	8.05 s	8.07 s	4.16, 24	4.12, 18	4.11, 3
Categorized as		Thermal runaway						Soft short		

*The considerable difference from the max. temperature on opposite terminal is assumed to result from a defect in thermocouple-adhesive.

The primary conclusions derived from the data summarized in Table 28 can be outlined as follows:

Firstly, it is noteworthy that the needle frequently displaced the cell can by several tenths of a millimeter before actual penetration occurred. This behavior is clearly indicated by the difference between the penetration depths measured at the can (d_{can}) and at the anode (d_{anode}), which significantly exceeded the nominal thickness of the cell can (approximately 0.61 mm). Consequently, it is inferred that the needle initially pushed the cell can inward without puncturing it, as illustrated in Figure 30. Additionally, discrepancies were observed between the penetration depths measured mechanically through the applied needle force (d) and those determined electrically via voltage measurements between the needle-positive terminal (V_{NP}) or needle-negative terminal (V_{NN}). These deviations underline the critical necessity of utilizing the voltage-based measurement approach (V_{NP} and V_{NN}), as discussed comprehensively in Section 3.2.2, for accurately identifying the precise moment when the needle contacts the can surface and subsequently the outermost anode.

A crucial finding pertains to the significant disparity in critical penetration depths required to initiate thermal runaway (d_{anode}) between different cell configurations. Cells with the can on potential configuration exhibited thermal runaway at extremely shallow penetration depths (approximately $d_{\text{anode}} \approx 0.00\text{--}0.02$ mm). This rapid thermal event is likely initiated almost immediately following the short circuit connection between the cell can and the outermost anode, attributed to the inherently low short circuit resistance ($R_{\text{ISC, can on potential}}$) and high applied voltage equivalent to the cell voltage (approximately 4.2 V). The delay between the needle penetration and the subsequent voltage collapse was less than one second, emphasizing rapid heat generation due to the high ISC current facilitated by this direct connection.

In contrast, cells configured with the floating can required significantly deeper penetration depths (d_{anode}), ranging from 0.77 mm to 1.48 mm, to initiate thermal runaway. Considering the individual thicknesses of the anode, cathode, and separator layers within the tested cells (approximately 104 μm , 107 μm , and 18 μm , respectively), these critical depths correspond to the penetration of approximately 3–7 electrode layers. This indicates that the heat produced by the initial short circuit between the cell can and outermost anode alone was insufficient to trigger thermal runaway, necessitating additional internal shorts between the anode and cathode layers. Moreover, the time required for the cell voltage to drop below the critical value of 2.8 V was somewhat longer (approximately 5.08–9.02 seconds) for floating can cells compared to the can on potential cells previously described.

In Group C, penetration depths were arbitrarily selected, yet sufficiently deep to establish electrical contact between the needle and the electrode ($d_{\text{anode}} > 0$). In each of these cases, the induced short circuit between the cell can and outermost anode resulted in only minimal voltage drops without triggering thermal runaway. Notably, the arbitrarily chosen penetration depth directly influenced the rate of voltage decay. For instance, Cell 13 with the smallest penetration depth ($d_{\text{anode}} = 0.20$ mm) exhibited only a minor voltage drop of 0.04 V over a 24-hour period, whereas Cell 15, having the largest penetration depth ($d_{\text{anode}} = 0.51$ mm), experienced a much more pronounced voltage drop to 4.11 V within just three hours.

Figure 47 distinctly illustrates the pronounced influence of the cell-can configuration — specifically whether the can is maintained directly at positive potential or connected via an electrical resistance — on critical penetration depth (d_{anode}), the duration required for the voltage to decline below 2.8 V, and the resulting type of reaction (thermal runaway or soft short). Here, the time until voltage dropped below 2.8 V is plotted against the penetration depth, with each data point color-coded according to the maximum temperature recorded at the positive terminal. The smallest critical penetration depth (d_{anode}) measured for floating can cells was 0.77 mm (Cell 11), in contrast to 0 mm (Cell 3) for can on potential cells, clearly indicating that thermal runaway in the latter configuration was exclusively initiated by the short circuit between the cell can and the outermost anode.

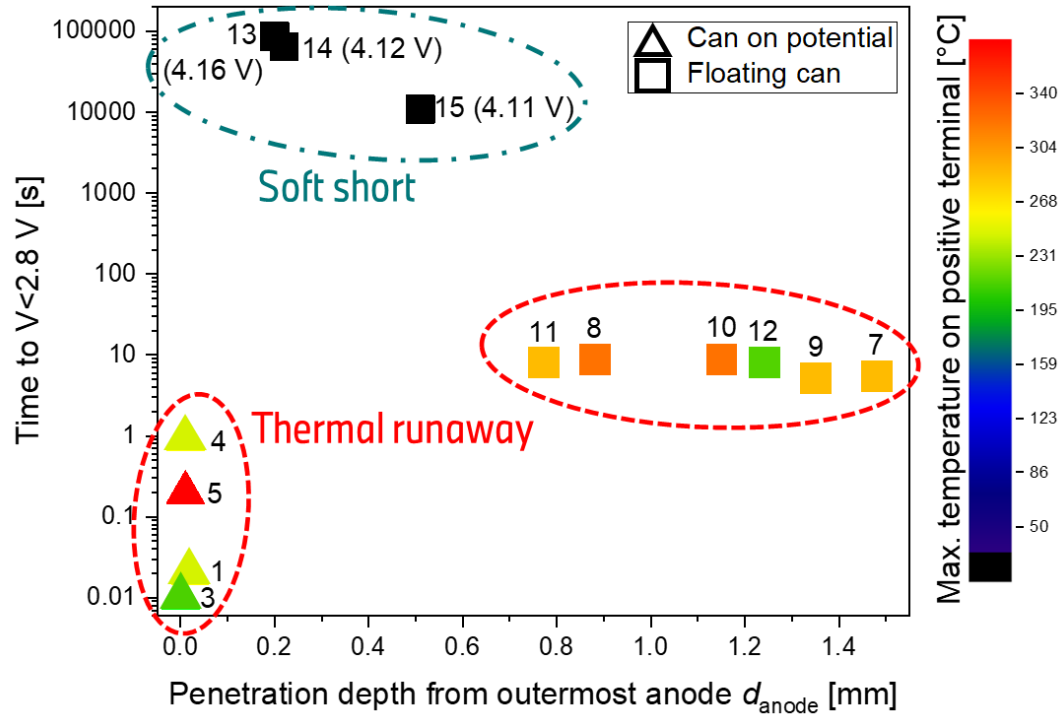


Figure 47. Classification of thermal responses (soft short vs. thermal runaway) based on the potential configuration of the cell can (floating can vs. can on potential), reproduced from literature [19].

6.2.2 Quantitative Analysis of ISC Current

Segmented current measurements provide further quantitative insight into how the type of can connection affects ISC behavior. Figure 48 presents ISC current traces during needle penetration tests for two representative cells, one configured with a can on potential and the other with a floating can design. When considering the needle penetration pathway within an automotive prismatic LIB cell, multiple ISC events occur sequentially. (1) Initially, the first ISC is established between the cell can and the outermost anode layer. Subsequently, as the needle penetrates deeper into the cell structure, additional ISCs emerge in the following order: (2) ISC between anode and cathode electrodes and ISC between the anode current collector (Cu) and cathode electrode; and (3) ISC between the anode electrode and the cathode current collector (Al), and ISC between the anode current collector (Cu) and the cathode current collector (Al). These ISC events may overlap or occur simultaneously, provided that electrical contact between the needle and internal layers remains stable and is not disrupted by melting or mechanical rupture, as discussed previously in Chapter 5.

In cells configured with the can on potential, the initial contact of the needle with the outermost anode (as indicated by the voltage V_{NN} dropping from approximately 4.2 V to 0 V) resulted in an immediate and significant surge in ISC current even higher than 6 A, even though it was limited only by the external power supply capacity of 6 A, as shown in Figure 48 (a) and (c). This observation implies that, in the absence of external current limitation, the actual ISC current could have reached even higher magnitudes.

Conversely, cells featuring the floating can configuration exhibited negligible ISC currents upon initial needle contact with the outer anode, as illustrated in Figure 48 (b) and (d). Remarkably, despite physical contact occurring at around $t = -88$ s, measurable current remained practically absent until much later, remaining negligible until approximately $t = -9$ s. This distinctly demonstrates that the high resistance introduced by the floating can configuration effectively reduces the immediate ISC current flowing between the cell can and the outermost anode to an insignificant level. Only as the needle progressed deeper, establishing multiple layer-to-layer shorts within the cell, did the ISC current gradually increase. The current profiles for floating can cells also exhibited characteristic

fluctuations and transient spikes, indicative of intermittent melting or mechanical rupture of internal cell layers, each incident briefly intensifying current flow.

These quantitative measurements conclusively illustrate the effectiveness of the floating can configuration in mitigating ISC currents. Whereas cells with the can directly connected to the positive terminal (can on potential) exhibit immediate, intense ISC currents, resembling a near-direct electrical short (> 6 A), cells employing the floating can design maintain initially negligible ISC currents. In these cells, ISC currents gradually rise only as successive internal shorts between electrode layers accumulate.

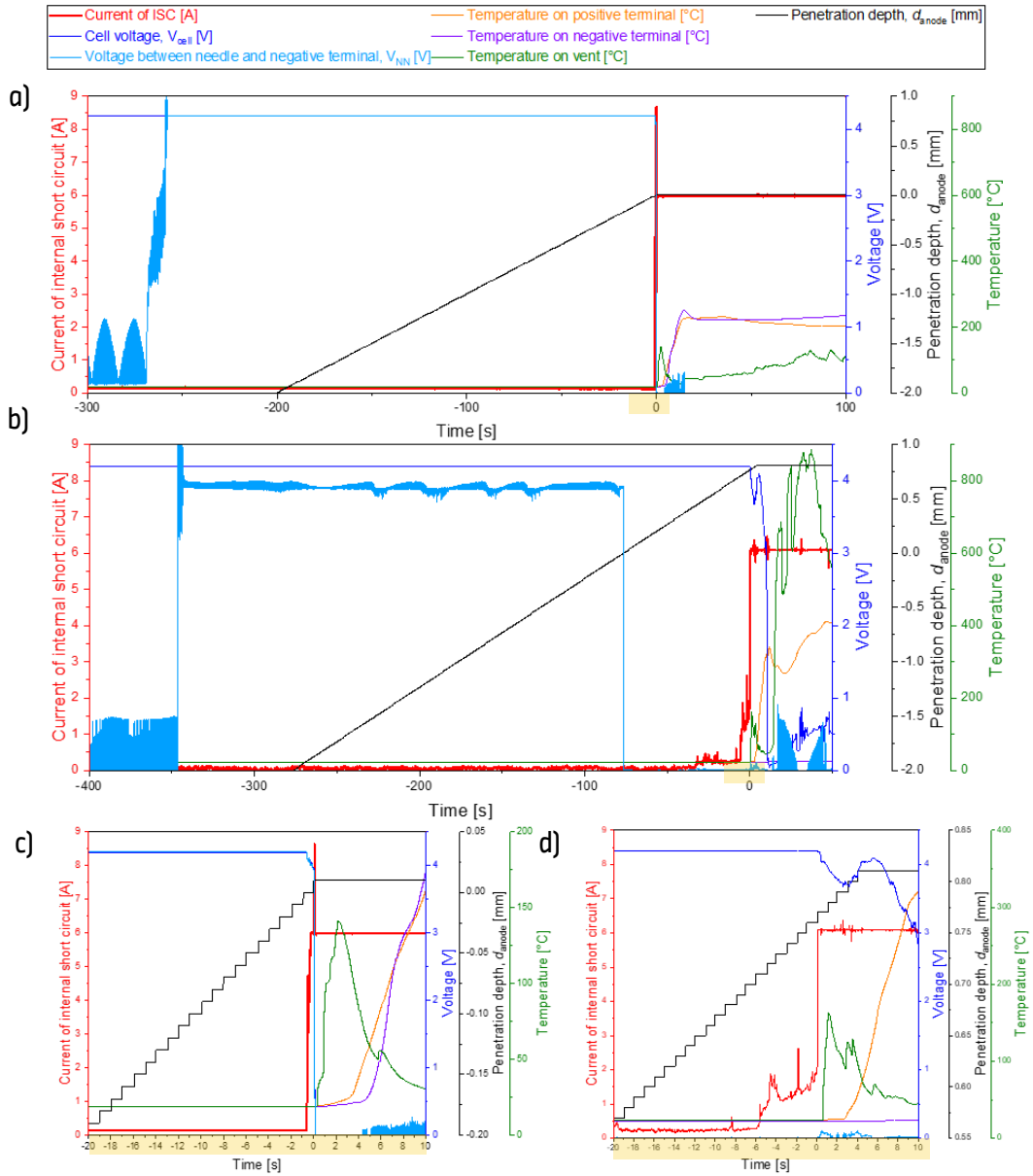


Figure 48. ISC current measurements recorded during needle penetration tests: (a) can on potential cell and (b) floating can cell over the complete testing period, (c) detailed view of can on potential cell, and (d) detailed view of floating can cell during the interval from -20 s to +10 s, as highlighted in yellow in (a)-(d).

Figure 49 further demonstrates three distinct ISC scenarios arising during needle penetration tests. Each ISC type is characterized by a short-circuit current (I_{sc}) determined by the cell voltage (U) and four fundamental resistances: the internal resistance of the cell (R_i), the resistance between the can and outermost anode (R_{CA}), the resistance between the can and cathode (R_{CC}), and the resistance

associated with the penetrating needle (R_{needle}), modified from the particle resistance (R_{particle}) described previously in Reactions (2.15) and (2.16).

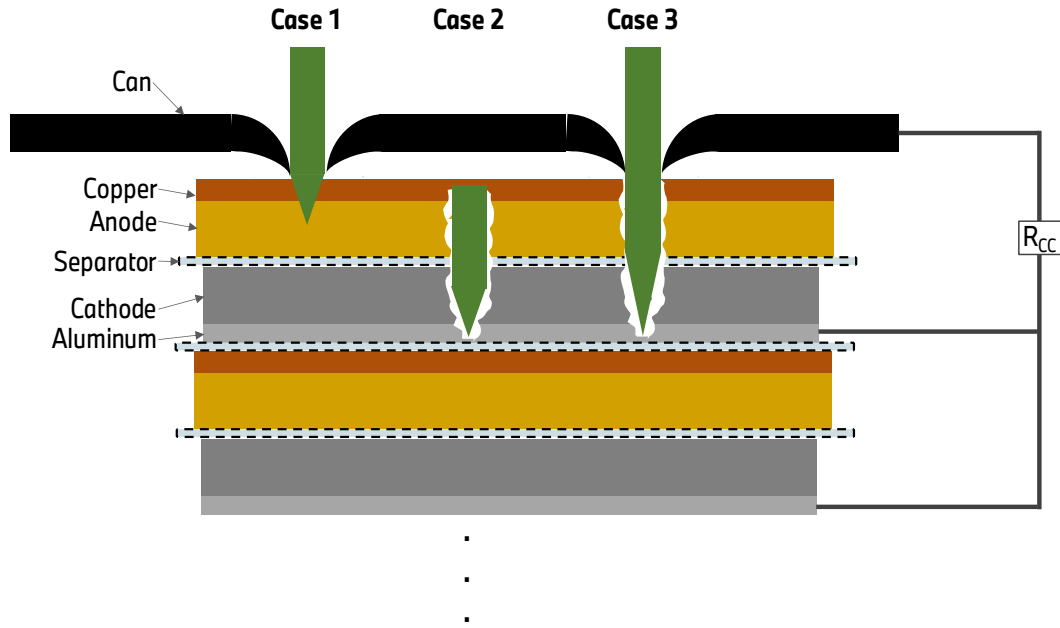


Figure 49. Illustration of the distinct short circuit current scenarios arising during needle penetration tests: (1) a localized short circuit between the cell can and the outermost anode (Case 1), (2) localized layer-to-layer short circuits between internal electrode layers (Case 2), and (3) a complex short circuit scenario combining both types simultaneously (Case 3).

- **Case 1:** the short circuit current between the cell can and the outermost anode (I_{CA}) is determined by the resistance between the can and cathode (R_{CC}), between the can and outermost anode (R_{CA}), the cell's internal resistance (R_i), and the needle resistance (R_{needle}). Given that R_{needle} and R_i are typically very small (less than 1 m Ω), their contributions can be considered negligible for practical calculations:

$$I_{CA, \text{ can on potential}} \approx \frac{U}{R_i + R_{CA} + R_{\text{needle}}} \approx \frac{U}{R_{CA}} \quad (6.1)$$

$$I_{CA, \text{ floating can}} \approx \frac{U}{R_i + R_{CA} + R_{\text{needle}} + R_{CC}} \approx \frac{U}{R_{CA} + R_{CC}} \quad (6.2)$$

- **Case 2:** the layer-to-layer short circuit current (I_{LL}) depends primarily on the layer-to-layer short circuit resistance (R_{LL}). Each additional penetrated pair of anode and cathode electrodes incrementally contributes to an increase in I_{LL} . However, the resistance of the needle, R_{needle} can vary depending on the quality of its electrical contact with the cell materials, introducing an additional variable into the current pathway:

$$I_{LL, \text{ floating can}} \approx \frac{U}{R_{LL} + R_i + R_{\text{needle}}} \approx \frac{U}{R_{LL} (+R_{\text{needle}})} \quad (6.3)$$

- **Case 3:** the total short circuit current (I_{SC}) represents a combination of the currents resulting from the can-to-anode short circuit (I_{CA}) and the cumulative layer-to-layer short circuits (I_{LL}):

$$I_{SC, \text{ can on potential}} \approx \frac{U}{R_{CA}} + \left(\sum \frac{U}{R_{LL} (+R_{\text{needle}})} \right) \quad (6.4)$$

$$I_{SC, \text{ floating can}} \approx \frac{U}{R_{CA} + R_{CC}} + \sum \frac{U}{R_{LL} (+R_{\text{needle}})} \quad (6.5)$$

In cells configured with the can on potential design, the resistance R_{CC} approaches zero, resulting in a significantly large I_{CA} , as experimentally confirmed by the data in Figure 48 (a) and (c). Conversely, in cells featuring the floating can configuration, the substantial resistance R_{CC} greatly reduces the

initial short circuit current between the can and the outermost anode. Consequently, short circuits between electrode layers (I_{LL}) dominate the ISC current profile. This explains why, as shown in Figure 48 (b), no significant current is observed immediately after the needle contacts the outermost anode; current only increases notably after multiple internal electrode-layer shorts occur. The experimental results presented in Figure 48 clearly indicate that, without the resistance R_{CC} , I_{CA} is significantly greater than I_{LL} , and thus cells with a can on potential configuration experience rapid thermal runaway solely due to I_{CA} , requiring no penetration of additional internal layers. However, for cells with a floating can, multiple internal layer shorts (I_{LL}) are necessary to induce cell discharge and ultimately thermal runaway.

6.2.3 Validation of Thermal Equivalence via Heat-Wait-Seek Tests in the ARC

Accelerating rate calorimetry (ARC) tests employing the Heat-Wait-Seek (HWS) method were conducted to confirm the intrinsic thermal equivalence of cells with floating can and can on potential configurations. Figure 50 illustrates the average self-heating rates of each cell type (two cells per configuration) plotted against temperature throughout the exothermic reaction phases. The data reveal nearly identical thermal behaviors for all four tested cells, as evidenced by overlapping temperature trajectories.

Specifically, each cell exhibited a consistent sequence of thermal events. Initially, a mild exothermic reaction, likely attributed to the decomposition of the Solid-Electrolyte Interface (SEI) layer, commenced around 80–85 °C. This was followed by an inflection in the self-heating rate, likely attributable to cooling effects induced by venting. This event occurred within the temperature range of approximately 103 to 113 °C (see Figure 62 (e) and (f) in Appendix) and was characterized by a deviation from the linear increase in the self-heating rate, suggesting that heat generation had either ceased or was minimal — below 0.02 K/min. Ultimately, a catastrophic thermal runaway event occurred at temperatures exceeding roughly 168 °C, corresponding to a rapid escalation in self-heating rate beyond 60 K/min.

The critical characteristic temperatures, labeled T1 through T5 and summarized in Table 29, were virtually identical across both the floating can and can on potential cell configurations. The close correlation of these characteristic temperature points and self-heating rates (clearly depicted in Figure 50 and quantified in Table 29) substantiates that the two cell types exhibit indistinguishable intrinsic thermal properties.

This high degree of similarity conclusively indicates that no fundamental differences exist in the thermal chemistry or intrinsic reactivity between cells configured with floating can and can on potential designs under controlled heating conditions. Consequently, the enhanced mechanical abuse tolerance of floating can cells observed in needle penetration tests can be solely attributed to the increased series resistance provided by the floating can configuration, rather than any alterations in the cell materials or intrinsic thermal characteristics.

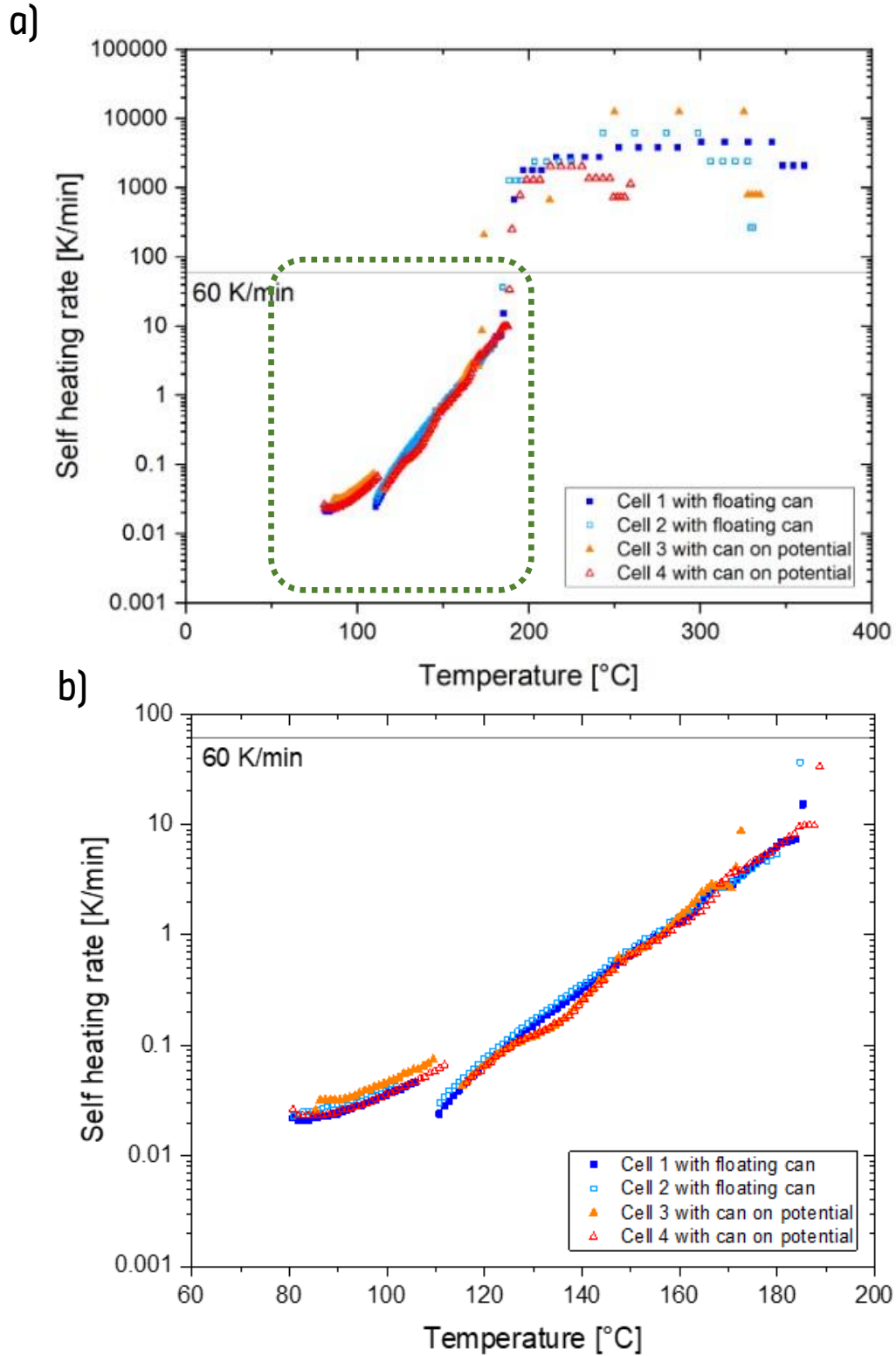


Figure 50. Self-heating rate profiles of two floating can cells and two can on potential cells: (a) overview from 0 to 400 °C, and (b) detailed view from 60 to 200 °C.

In Table 29, characteristic temperatures T_1 through T_5 are defined as follows:

- T_1 : onset temperature of the initial exothermic reaction (SEI decomposition), identified at self-heating rates exceeding 0.02 K/min.
- T_2 : temperature at which self-heating is no longer significant, attributed to cooling effects induced by venting.
- T_3 : onset temperature of a secondary exothermic reaction, again marked by a self-heating rate exceeding 0.02 K/min.
- T_4 : temperature at which the catastrophic thermal runaway initiates, defined as the self-heating rate surpassing 60 K/min.
- T_5 : maximum temperature recorded during thermal runaway events.

A detailed presentation of these characteristic temperatures is provided in Figure 62 in Appendix, using the HWS graph of Cell 4 as a representative example.

Table 29. Characteristic thermal parameters ($T_1 - T_5$) comparing two cells each from floating can and can on potential configurations.

Temperature	Floating can		Can on potential	
	Cell 1	Cell 2	Cell 3	Cell 4
T_1 [°C]	80.8	80.8	85.4	80.8
T_2 [°C]	106.6	103.4	108.9	113.2
T_3 [°C]	110.5	112.4	115.2	117.1
T_4 [°C]	168.6	188.6	173.9	190.2
T_5 [°C]	552.1	557.3	326.8	521.7

6.3 Conclusions

This investigation used advanced mechanical abuse testing to elucidate how the connection between the cell can and positive terminal affects prismatic lithium-ion battery safety. The key findings are:

- **Reproduction of Internal Short-Circuit Scenarios:** a fine stainless-steel needle driven slowly into a fully charged cell effectively simulated various internal short circuits. By recording the needle's contact voltages, it was able to distinguish shorts between the can and the first anode and between electrode layers. The "*critical penetration depth*" emerged as the measure of cell resilience: the deeper the needle had to go to initiate a short or runaway, the more robust the cell was.
- **Effect of Can Connection on Critical Penetration Depth:** cells with the metal can directly at positive potential underwent thermal runaway at minimal anode penetration (essentially zero beyond the can layer). By contrast, adding even a small resistance (floating can) dramatically increased the depth required to trigger runaway ($d_{\text{anode}} \approx 0.8\text{-}1.5$ mm). Cells with a floating can penetrated less than ~ 0.5 mm only experienced a mild, gradual self-discharge (soft short). Thus, the floating can configuration greatly enhances mechanical safety by demanding a much more severe penetration to ignite the cell.
- **Measurement of Internal Short Circuit Current:** in cells with can on potential, any short between the can and the outermost anode resulted in an almost instantaneous, large ISC (up to the test limit). In floating can cells, the high resistance (R_{CC}) — exceeding 1 kOhm — prevented any immediate current surge during initial ISC in prismatic LIBs; current only climbed slowly as more layers failed from ISC_{LL} . This confirms that the increased resistance in the floating can design is the mechanism suppressing one of the most dangerous ISC current.

- **Possibility of Improvement of ISC Current Measurement:** to improve the precision of ISC current measurements, future tests could incorporate an identical cell connected in parallel with the test cell via a shunt resistor. This setup would more closely replicate the conditions of an automotive battery module and help overcome the current limitations imposed by laboratory equipment, allowing for a more representative assessment of ISC behavior under realistic conditions.
- **Thermal Properties Unchanged:** accelerating rate calorimetry (ARC) confirmed that both floating can and can on potential cells exhibit virtually identical thermal behavior, including comparable onset temperatures, venting responses, and runaway thresholds. These findings indicate that the observed improvements in safety performance for floating can cells are not a result of any changes in cell chemistry or heat generation characteristics. Instead, the enhanced resistance to thermal runaway can be attributed solely to the electrical isolation of the can. It should be noted, however, that ARC induces thermal runaway through external heating, which differs from real-world scenarios where internal short circuits (ISCs) often initiate runaway via localized internal heating.

Taken together, the results from both needle penetration and ARC experiments demonstrate that implementing a floating can configuration can significantly enhance mechanical abuse tolerance without compromising the cell's intrinsic performance. This modification in cell architecture — achieved simply by introducing series resistance — offers a promising and practical design strategy for improving the safety of automotive lithium-ion battery cells.

The promising results of this study underscore the need for continued research into internal short circuit behavior and thermal safety across a broader range of lithium-ion battery designs. Future investigations should systematically examine cells with varying electrode chemistries, geometric formats, and capacities, as these parameters may significantly influence the cell's response to internal short circuits and thermal events. A deeper understanding of which specific factors — among materials, structure, or configuration — most strongly govern thermal behavior is essential for advancing cell safety.

Furthermore, optimized needle penetration methodologies can serve not only as a tool for probing the interplay between internal architecture and safety performance but also as a means to support the refinement of cell chemistries and mechanical designs. In this context, Chapter 7 will explore directions for further work aimed at identifying critical parameters and enhancing the predictive and diagnostic capabilities of mechanical abuse testing in lithium-ion batteries.

7 Correlation between Cathode Thermal Stability and Li-Ion Cell Safety

The findings presented here were partially published in: Hyojeong Kim*, Hans Jürgen Seifert, Carlos Ziebert, Philipp Finster, Jochen Friedl, *A comparative study of commercial automotive prismatic Li-ion cells using nail penetration test, differential scanning calorimetry and thermogravimetric analysis*, Journal of Power Sources, 623, 235416, 2024 [32]. The figures and results included in this Chapter 7 have been reworked and individually adapted to suit the context of this study.

As discussed in Section 3.2.2, the nail or needle penetration test has been widely employed in lithium-ion battery research, primarily as a standardized method to initiate thermal runaway. Although numerous studies, as listed in Table 15, demonstrate the potential of this technique to probe internal short circuits in greater detail, the majority have treated it merely as a TR-triggering mechanism rather than as a diagnostic tool for ISC-related phenomena. Moreover, comprehensive investigations that systematically apply this method to automotive prismatic LIB cells remain scarce. Also, even fewer studies attempt to correlate safety outcomes derived from penetration tests with material-level thermal stability parameters assessed through differential scanning calorimetry (DSC) and thermogravimetric analysis (TGA). The study by An et al. [131] offers valuable insight into the possible relationship between ISC susceptibility and cathode active materials. However, their work focuses exclusively on pouch cells and lacks complementary thermal analysis to substantiate the observed trends (see Table 15).

Building upon previous chapters that examined the effects of cell assembly (Chapter 5) and floating can configurations (Chapter 6) on ISC behavior, this Chapter 7 shifts focus to identifying key material- or structure-based factors that govern overall cell safety. Specifically, this chapter compares the ISC resilience of six commercially available automotive prismatic LIB cells under carefully controlled needle penetration conditions and investigates the underlying material properties that govern the observed differences in safety performance at cell level. Despite differences among the cells in geometry, internal architecture, component thicknesses, the analysis reveals that thermal behavior of the cathode is the most consistently influential factor affecting cell safety.

In the first part of this study, six prismatic lithium-ion cells designed for automotive use were subjected to the needle penetration procedure described in Section 3.2.2 (see Figure 31), in order to evaluate their tolerance to internal short circuits. A key metric derived from these tests is the critical penetration depth (D_{crit}), which reflects the depth at which thermal runaway is initiated, serving as a valuable metric for evaluating the resilience of lithium-ion cells against internal short circuits and subsequent thermal runaway (TR). To enable meaningful comparison across cell types with differing internal geometries and layer structures, the concept of penetrated layer-sets (PLS) was introduced. This metric normalizes the critical penetration depth (D_{crit}) by accounting for variations in component thicknesses, thereby offering a more consistent basis for evaluating ISC resilience.

The central motivation of this analysis lies to systematically identify which intrinsic or structural parameters predominantly govern a cell's resistance to ISC-induced failure. Therefore, defined PLSs were compared against a range of candidate parameters that have been previously proposed as potential determinants of safety performance — such as chemistries, cell capacity, electrolyte content, dimension and separator thickness. Through this comparative analysis, a strong correlation emerged between PLS and the Ni (or Li) molar ratio in cathode material — specifically in NMC and NCA chemistries. These data suggest that cathode thermal stability can be a dominant factor in governing a cell's resilience to ISC-induced thermal runaway.

This hypothesis was further explored in the second phase of the study, which involved material-level thermal analysis of the positive electrodes extracted from each cell type at 100% state of charge (SOC). DSC and TGA were employed to assess both the intrinsic thermal stability of the cathode materials and their reactivity in the presence of electrolyte as demonstrated in Section 3.1.1 and 3.1.2. In addition to determining the onset temperature of decomposition reactions, this study introduced a new metric — reaction rate (α_T) presented in Reaction (3.3) in Section 3.1.1 — to quantify the “aggressiveness” of thermal reactions and thereby provide a more comprehensive assessment of cathode stability.

In the final part of this study, the findings from the needle penetration abuse test are integrated with the thermal and thermodynamic analyses of the positive electrode in the presence of electrolyte. The results from the second part of this work reinforce the conclusion that the thermal behavior of the cathode-electrolyte system plays a decisive role in overall cell safety. Impact of other physical or design-related factors — such as cell capacity or separator thickness — on ISC resilience was found to be comparatively minor. Ultimately, this work enhances our understanding of how cathode thermal stability governs safety outcomes in lithium-ion cells and offers practical guidance for the design of future, safer battery architectures.

7.1 Experimental

7.1.1 Automotive prismatic LIB cell samples

The selection of the six automotive prismatic lithium-ion battery (LIB) cells in this study was guided by the following criteria:

- The cells must be commercially manufactured for battery electric vehicles (BEVs), ensuring a high level of production quality and adherence to automotive safety standards.
- The selected cell types should be comparable in a meaningful way — either manufactured by the same producer under similar conditions or designed with closely related specifications, importantly differing in specific parameters of interest to enable focused comparative analysis.

This selection strategy ensures that all chosen cell types are representative of real-world, high-quality automotive LIBs while enabling a systematic evaluation of how particular design or material parameters influence the cell's resilience to internal short circuits.

Despite differences in physical dimensions, internal construction, and electrode chemistry, all six cell types incorporate comparable safety features, including a vent, an integrated fuse, and a floating can design. Cell types A and B share the same external dimensions (height x depth x width as 91 × 27 × 302 mm³), while cell type F maintains the same height and depth, but has approximately half the width (148 mm) compared to A and B. The remaining cell types — C, D, and E — are uniform in size, each measuring 73 × 32 × 180 mm³.

All cells are equipped with separators coated in Boehmite-based ceramic material. The coating configuration varies between cells, with some having single-sided coatings (facing the cathode) and others featuring double-sided coatings. While no significant differences were detected in the anode active materials or main electrolyte compositions across the cells — as confirmed by X-ray diffraction

(XRD) and gas chromatography–mass spectrometry (GC-MS) — notable variations exist in the cathode active materials.

To investigate the influence of capacity on thermal runaway, some cells with identical electrode chemistries but different form factors and capacities were included. For instance, cell types B and C as well as E and F use the same cathode, anode, and separator materials but differ in cell size, and consequently in energy capacity.

Electrode thicknesses were determined through metallographic cross-section analysis. In all six cell types, both anode and cathode are double-sided coated. The anode thickness ranges from 165 μm to 220 μm , making it consistently thicker than the cathode, which ranges from 120 μm to 137 μm . The aluminum current collector (11-15 μm) is also thicker than the copper current collector (6-8 μm). A comprehensive overview of the characteristics and configurations of all six cell types included in this study is provided in Table 30.

Table 30. Information of the six selected automotive prismatic LIB types, reproduced from literature [32].

		Cell type A	Cell type B	Cell type C	Cell type D	Cell type E	Cell type F
Cell dimension Height x Depth x Width mm³		91x27x302		73x32 x180			91x27x148
Capacity [Ah]		114	116	66	72	70	61
Cell assembly		Stack	Jelly roll	Jelly rolls	Stack	Stack	Stack
Cathode active material		NMC	NMC	NMC	NMC	NCA	NCA
Anode active material		Graphite					
Separator material		PE (Boehmite coated)					
Electrolyte solvents		EC, DEC, EMC, DMC	EC, DEC, EMC, DMC	EC, DEC, EMC, DMC	EC, EMC, DMC	EC, DEC, EMC, DMC	EC, DEC, EMC, DMC
Thickness (τ) [μm]	Cell can (long sides)	630	507	500	500	554	553
	Anode (A)	180	166	165	178	220	219
	Cu current collector	7	6	6	6	8	8
	Separator (S)	11	11	10	11	14	15
	Cathode (C)	137	120	120	125	134	135
	Al current collector	11	14	15	13	12	12
	$T_{A-S-C-S}$	339	308	305	325	382	384

7.1.2 Needle Penetration

To evaluate the resistance of each cell type to internal short circuits (ISCs), nail penetration tests were conducted on six different types of commercially available prismatic lithium-ion battery (LIB) cells as demonstrated in Figure 31. Two samples from each cell type (A through F) were tested, and the average critical penetration depth (D_{crit}) — defined as the depth (d_{can}) at which thermal runaway (TR) is initiated — was determined.

Cell Preparation

All 12 cell samples were charged to 100% state of charge (SOC) at room temperature using a constant current (C/3)–constant voltage protocol, with the voltage hold phase terminated once the current dropped below 1 A, same as in Chapter 6. Before charging, each cell was clamped between two stainless-steel compression plates, applying a force of 5 kN. One of the plates included a 15 mm diameter hole aligned with the center of the largest surface of each cell to allow unobstructed nail access. The plate dimensions were selected to fully compress the internal electrode stacks or jelly rolls of each tested cell.

Test Protocol

The same needle employed in Chapter 6 was driven horizontally at a speed of 0.01 mm/s through the center of the cell's largest surface until a visual spark or fire confirmed the onset of thermal runaway. During testing, several parameters were continuously monitored: cell voltage, insertion force applied to needle, and surface temperatures at the vent, positive terminal, and negative terminal — each recorded using K-type thermocouples. For each cell, the depth at which a sudden rise in vent temperature occurred was recorded as D_{crit} .

7.1.3 Electrode Material Preparation and Thermodynamic/Thermal Analysis

To validate the hypothesis that the thermal stability of cathode material is the main parameter to determine the cell safety, positive electrode samples were prepared and studied with DSC and TGA.

Material Harvesting

For subsequent thermal analysis, all six cell types were charged to 100% SOC using the procedure described in Section 7.1.2. Cells were then disassembled inside of an inert atmosphere glove box (O_2 and H_2O levels maintained below 5 ppm). Positive electrode samples were harvested from each cell for DSC and TGA measurements as discussed in Section 3.1.1 and 3.1.2.

Differential Scanning Calorimetry (DSC)

The sample preparation method and measurement protocol are detailed in Section 3.1.1. The total mass loss remained under 1% for all samples and each cathode material was tested in duplicate to confirm reproducibility. Onset temperatures of exothermic reactions were determined using the Proteus software. Also, heat release values were normalized to the active cathode mass, excluding the aluminum collector, which is thermally inactive in the studied temperature range.

Thermogravimetric Analysis (TGA)

The method of sample preparation and measurement protocol is demonstrated in Section 3.1.2. The temperature program was divided into three segments with two 15-minute isothermal holds. In each temperature interval, mass loss was quantified using the Proteus software to support comparative analysis of thermal stability across cathode materials with presence of electrolyte.

7.2 Results and Discussion

7.2.1 Comparative Analysis via Needle Penetration Test

Due to variations in electrode stack (or separator) thicknesses among different lithium-ion cells, a normalized metric — penetrated layer-sets (PLS) — is introduced to allow for a fair comparison of ISC resilience across cell types. PLS is defined by the following expression:

$$PLS = \frac{D_{crit} - T_{can}}{T_{A-S-C-S}} \quad (7.1)$$

Where:

D_{crit} is the measured critical penetration depth from can (d_{can} at onset of TR),

T_{can} is the thickness of the cell can, and

$T_{A-S-C-S}$ represents the thickness of one complete electrode-separator unit, including a double-coated anode with copper current collector, separator, double-coated cathode with aluminum current collector, and an additional separator.

To assess which design or material parameters influence ISC resilience, the calculated PLS values are plotted against several potentially relevant factors (see Figure 51), including the molar fraction of (a) nickel and (b) lithium in the cathode active material, (c) the capacity of lithium-ion cells, (d) separator thickness, (e) aluminum current collector thickness, and (f) electrolyte mass fraction.

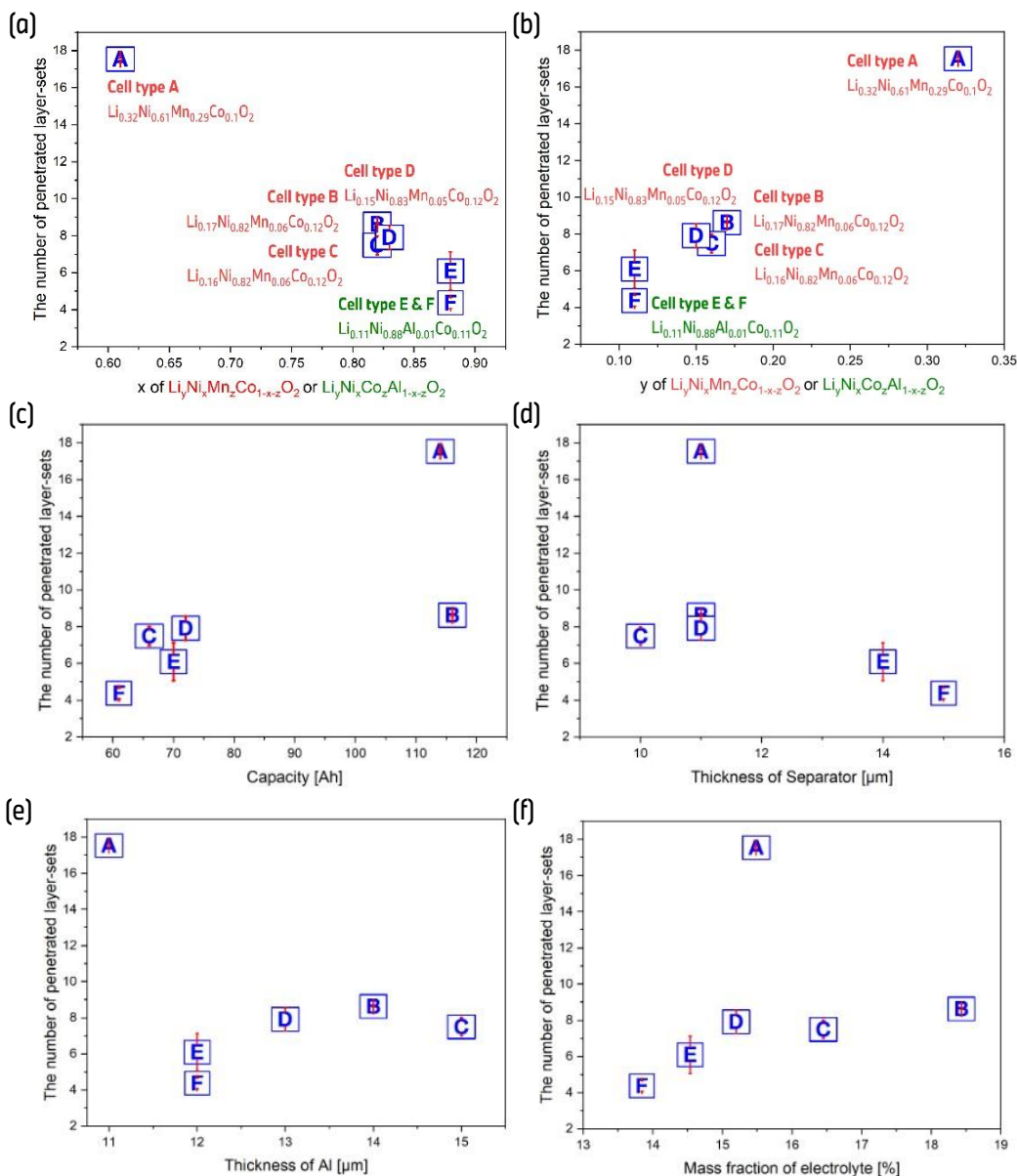


Figure 51. The number of penetrated layer-sets (PLS) was examined in relation to six potential influencing factors: (a) nickel molar fraction and (b) lithium molar fraction in the cathode active material, (c) the total capacity of the LIB cell, (d) separator thickness, (e) aluminum current collector thickness, and (f) the electrolyte mass fraction, excluding the can, reproduced from literature [32].

In Figure 51 (a) and (b), PLS correlates strongly with both the Ni and Li molar fractions in NMC/NCA cathodes, while no systematic relationship is evident for the other variables. For instance, despite having similar capacities (114 Ah vs. 116 Ah), cell type A exhibits a PLS of 17.54, whereas a PLS of only 8.62 triggers thermal runaway of cell type B (see Figure 51 (c)). This supports the notion — also noted by Feng et al. [1] — that cell capacity primarily influences total heat released during runaway, rather than the energy threshold required to initiate it.

Figure 51 (d) and (e) demonstrate that increasing the thickness of individual components — such as the separator or current collector — does not necessarily enhance ISC resilience at cell level. The six tested separators vary in thickness from 10 μm to 15 μm , yet the thickest separator (15 μm) in cell type F yields the lowest PLS (4.37), contradicting the commonly held assumption that a thicker separator improves a cell's resistance to mechanical abuse. Moreover, three cells equipped with

identical 11 μm separators (A, B and D) exhibit widely varying PLS values of 17.54, 8.62 and 7.91, respectively.

A similarly inconclusive trend is observed for the aluminum current collector thickness: cell types A, E, and F have comparable Al thicknesses (11–12 μm), yet their PLS values differ substantially. As discussed in Chapter 5, the aluminum current collector is expected to melt due to Joule heating during ISC events. Based on this understanding, it could be hypothesized that a thinner Al current collector, which melts more readily, may interrupt the short circuit earlier and thereby result in a higher PLS. However, the present results suggest that Al thickness is not a dominant factor in determining ISC resilience. Notably, the variations in Al thickness across the tested LIB types are too minor to account for the observed differences in PLS values.

Finally, electrolyte mass fraction does not exhibit a decisive effect on ISC resilience (Figure 51 (f)). Cell type A, which has the highest PLS, contains 15.5 wt.% electrolyte — midrange among the cells (13.8–18.4 wt.%). Nevertheless, a secondary influence from specific electrolyte *additives* is observed and will be discussed in Section 7.2.2.

Beyond the six primary parameters from Figure 51, additional factors are considered — including electrolyte solvent composition, cell dimension, the number of electrode layers and cell assembly — as outlined below:

- **Electrolyte Solvent Composition:** Lamb et al. [157] demonstrated that diethyl carbonate (DEC) and ethyl methyl carbonate (EMC) exhibit similar decomposition onset temperatures and gas evolution behavior, despite differences in gas quantity. Consistent with this, cell type D — formulated without DEC — shows an average PLS of 7.91, essentially matching the PLS values of cell types B and C, which possess analogous cathode chemistries (NMC). Therefore, electrolyte solvent composition is unlikely to be the primary cause of PLS variation.
- **Cell Dimension:** the three tested cell formats, which vary in dimensional footprint, do not exhibit a definitive influence on PLS. For example, cell types A and B, despite having identical form factors, display notably different PLS values. Cell dimensions do not appear to exert a decisive influence on ISC resilience.
- **Total Layer-Sets (TLS):** variations in cell assembly result in differing total layer-set counts, as detailed in Table 31. For jelly roll designs (e.g., cell types B and C), TLS is estimated by counting the number of layers along the perpendicular axis, assuming the electrodes were stacked. These jelly roll cells contain relatively fewer TLS (40–48) compared to the prismatic stacked designs (cell types A, D, E, and F), which range from 64 to 96 TLS. Although no direct correlation is observed between TLS and PLS, the ratio of PLS to TLS appears to be primarily governed by the Ni and Li molar fractions, as illustrated in Figure 52. While Chapter 5 demonstrates that the mode of cell assembly (jelly roll vs. stacked) influences ISC behavior, it is not the primary determinant of overall ISC resilience. The effect of assembly becomes secondary and only evident when the Ni/Li molar fraction is comparable across cells. For example, cell types B and C with jelly roll design require a higher proportion of PLS relative to TLS (a higher PLS/TLS ratio) than cell type D with stack architecture (see Figure 52). Nevertheless, irrespective of architectural differences, the Ni molar fraction in the cathode active material emerges as the dominant parameter governing a cell's robustness against internal short circuits.

Table 31. Total layer-sets (TLS) and the ratio of PLS to TLS of six lithium-ion cell types.

Type	A	B	C	D	E	F
PLS	17.54	8.62	7.49	7.91	6.09	4.37
TLS	72	48	40	96	77	64
PLS/TLS	0.24	0.18	0.19	0.08	0.08	0.07

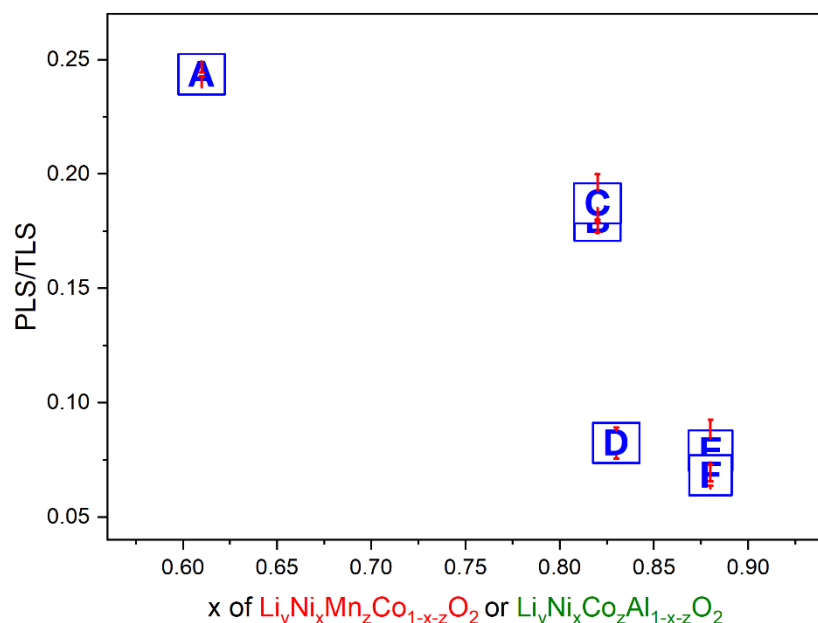


Figure 52. The correlation between PLS/TLS and Ni molar fraction in cathode active materials.

To elucidate the compositional basis of this correlation found in Figure 51 (a) and (b), ICP-OES analysis was performed on the cathode active materials of all six cell types as demonstrated in Section 3.3.1 and the result is presented in Table 32. Molar fractions of Ni, Mn (or Al) and Co were normalized to a sum of unity as 1, oxygen molar fraction was fixed at 2, and Li content was quantified accordingly. As shown in Figure 51 (a) and (b), cells with higher Ni content of lower Li content consistently exhibit reduced PLS values, indicating an increased propensity for ISC-triggered thermal runaway.

Table 32. Cathode active material composition (molar fractions of Ni, Mn or Al, Co, Li and O) for the six automotive prismatic LIB types, along with their mean penetrated layer-set (PLS) values.

Cell	ICP [wt.%]					Cathode active material	PLS		
	Li	Ni	Mn/Al	Co	O		1	2	Mean
A	2.40 ±0.017	38.8 ±0.83	17.64 ±0.017	6.29 ±0.033	34.84 ±0.074	$\text{Li}_{0.32}\text{Ni}_{0.61}\text{Mn}_{0.29}\text{Co}_{0.1}\text{O}_2$	17.58	17.49	17.54
B	1.31 ±0.013	52.55 ±0.95	3.59 ±0.035	7.68 ±0.043	34.73 ±0.079	$\text{Li}_{0.17}\text{Ni}_{0.82}\text{Mn}_{0.06}\text{Co}_{0.12}\text{O}_2$	8.64	8.60	8.62
C	1.20 ±0.018	52.04 ±0.91	3.62 ±0.023	7.58 ±0.049	34.59 ±0.065	$\text{Li}_{0.16}\text{Ni}_{0.82}\text{Mn}_{0.06}\text{Co}_{0.12}\text{O}_2$	7.12	7.85	7.49
D	1.07 ±0.011	51.61 ±1.12	2.67 ±0.041	7.57 ±0.021	33.80 ±0.081	$\text{Li}_{0.15}\text{Ni}_{0.83}\text{Mn}_{0.05}\text{Co}_{0.12}\text{O}_2$	8.37	7.45	7.91
E	0.94 ±0.012	62.45 ±0.88	0.41 ±0.039	7.76 ±0.051	38.74 ±0.065	$\text{Li}_{0.11}\text{Ni}_{0.88}\text{Al}_{0.01}\text{Co}_{0.11}\text{O}_2$	6.82	5.36	6.09
F	0.93 ±0.012	62.40 ±0.92	0.43 ±0.043	7.77 ±0.048	38.75 ±0.074	$\text{Li}_{0.11}\text{Ni}_{0.88}\text{Al}_{0.01}\text{Co}_{0.11}\text{O}_2$	4.58	4.16	4.37

Automotive prismatic lithium-ion cells are composed of four fundamental components: a cathode, an anode, a liquid electrolyte, and a porous separator, as illustrated in Figure 1. In this comparative study, the anode formulation, separator design, and electrolyte composition remain (quasi) consistent across all six cell types. As a result, variations in heat release are attributed primarily to differences in cathode chemistry. This emphasis is supported by studies from Shurtz et al. [6,158], who demonstrated that heat generation from anode–electrolyte reactions is constrained by the limited decomposition rate of the solid-electrolyte interphase (SEI), making it insufficient to initiate thermal runaway. In contrast, cathode–electrolyte reactions proceed more rapidly and are thus the dominant contributors to thermal runaway onset [159].

Accordingly, cells with cathodes containing higher nickel content and correspondingly lower lithium content exhibit thermal runaway after fewer penetrated layer-sets, indicating that fewer individual ISC events are required to reach critical thermal thresholds (see Table 32). High-nickel cathodes tend to undergo deeper delithiation at equivalent states of charge, which increases lattice strain and accelerates heat release upon internal short-circuiting [159]. This trend is consistently observed in both NMC and NCA cathodes, underscoring that the decisive factor in ISC-induced runaway is the intrinsic thermal stability of the delithiated cathode–electrolyte system — regardless of the specific cathode chemistry.

7.2.2 Thermal stability of NMC- and NCA-based Positive Electrodes

As established in Section 7.2.1, there exists a clear relationship between the resistance of lithium-ion cells to internal short circuits and the molar content of nickel or lithium in the cathode active materials, specifically NMC and NCA compositions. To explore the intrinsic thermal behavior of these materials, the positive electrodes were extracted from fully charged cells (100 % SOC) and analyzed through differential scanning calorimetry and thermogravimetric analysis.

DSC Analysis

The DSC measurements, conducted according to the protocol outlined in Section 3.1.1 and 7.1.3, are illustrated in Figure 53. The corresponding extrapolated onset temperatures and reaction enthalpies are summarized in Figure 54 and Figure 55, respectively. As previously discussed in Section 3.1.1, DSC is a widely utilized method for characterizing the thermal reactivity of cathode materials. However, many studies lack real-world relevance due to the use of laboratory-synthesized materials instead of electrodes harvested from actual lithium-ion battery (LIB) cells, or due to the omission of electrolyte during testing. Additionally, cathodes are often chemically delithiated rather than subjected to electrochemical cycling, further limiting the applicability of such data.

Theoretical work by Shurtz et al. [16] indicates that the presence of electrolyte significantly amplifies the exothermic reactivity of delithiated cathodes, potentially increasing heat output by approximately 10% per mole of metal oxide. This theoretical prediction is supported by experimental findings from Zhang et al. [63] (see Table 6), which show that delithiated LiNiO_2 (LNO) releases nearly ten times more heat in the presence of electrolyte compared to electrolyte-free conditions.

Given that electrolyte is an integral component in functioning LIB cells, it is essential that DSC experiments account for its influence on thermal behavior. To best replicate the in-cell environment during DSC analysis, the entire positive electrode assembly — including the aluminum current collector, carbon black, and residual electrolyte — was sealed in an airtight crucible immediately upon extraction. This encapsulation was performed rapidly, within one hour, to preserve the electrode's original chemical and thermal state prior to testing.

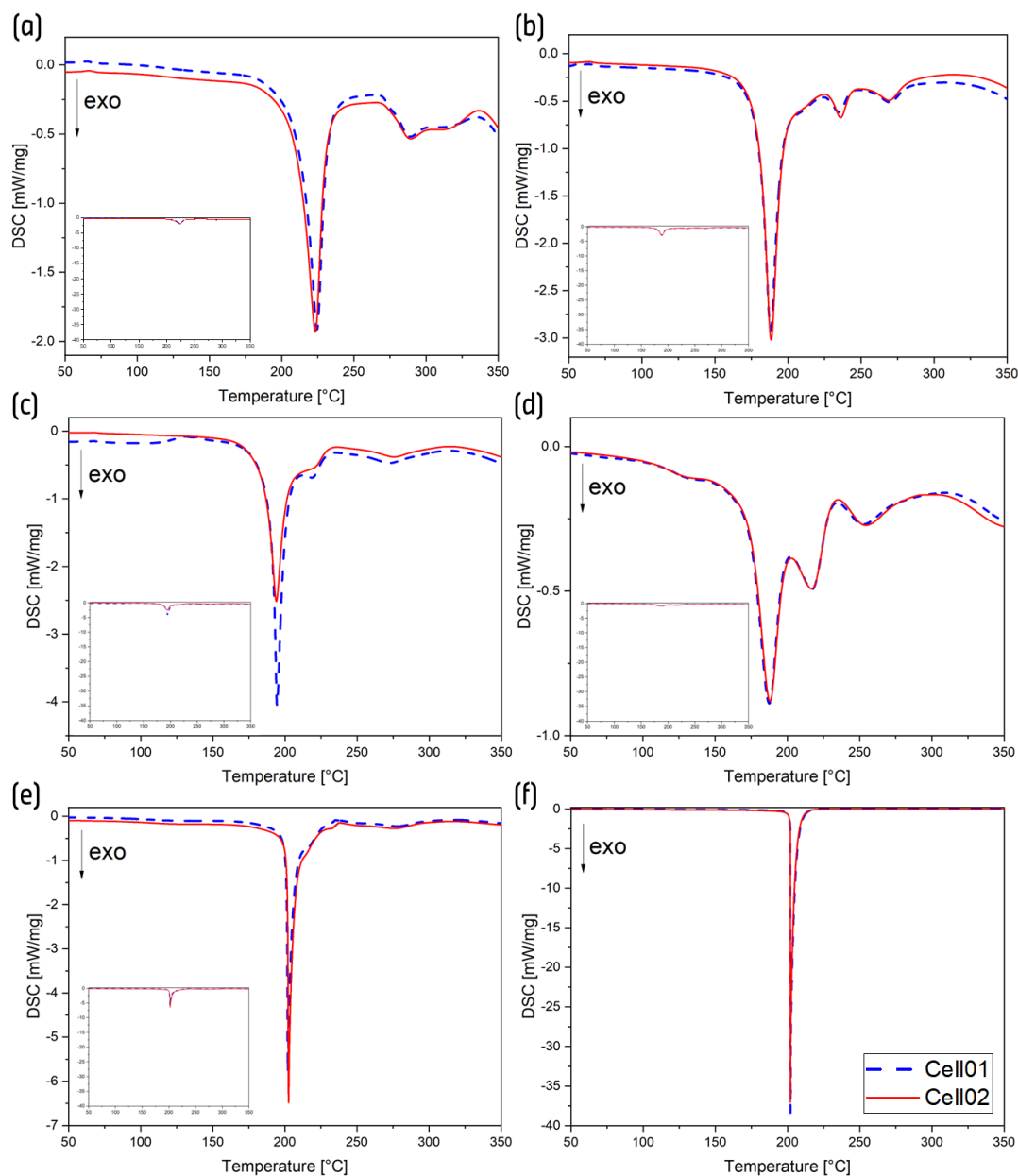


Figure 53. DSC analysis of positive electrodes extracted from LIB cells at 100% SOC: (a) cell type A, (b) cell type B, (c) cell type C, (d) cell type D, (e) cell type E, and (f) cell type F. Each cell type was tested in duplicate, with results represented by a dashed blue line and a solid red line, respectively, reproduced from literature [32].

As seen in Figure 53 and Figure 54, all samples exhibited clear exothermic behavior within the temperature range of approximately 170 °C to 250 °C. These heat-generating reactions are likely attributed to the thermal decomposition of the NMC or NCA cathode materials and the oxidative decomposition of the electrolyte. The extrapolated onset temperatures used for comparative assessment were displayed in Figure 54 with average PLS.

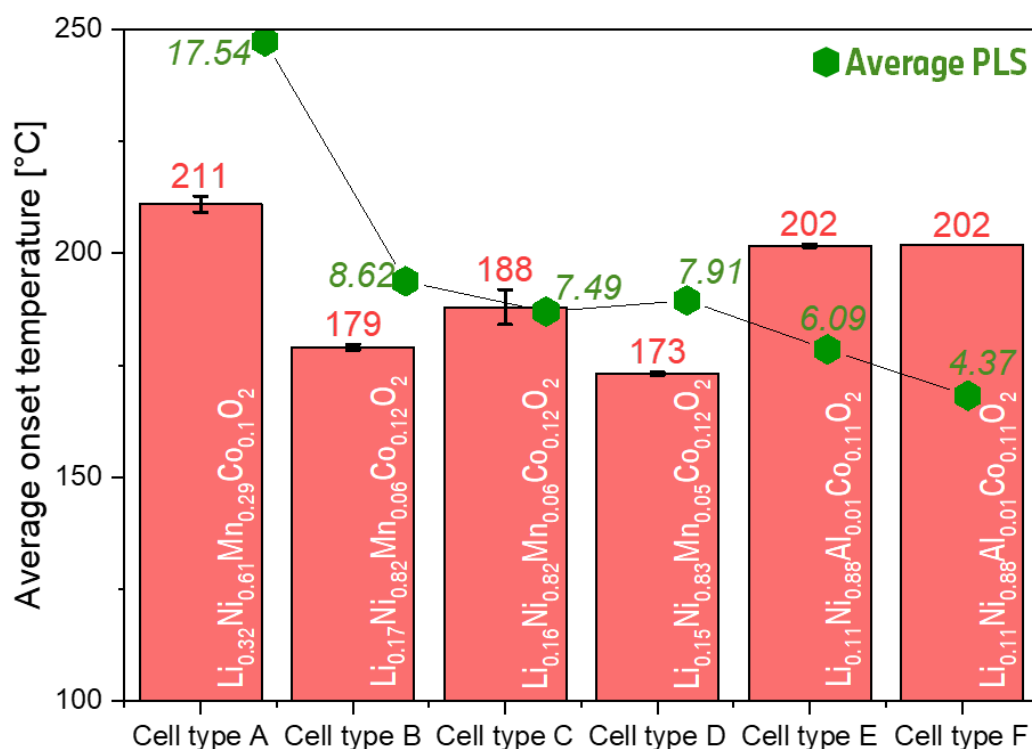


Figure 54. The average extrapolated onset temperature together with the average penetrated layer-sets (PLS), reproduced from literature [32].

The following observations and interpretations are drawn from Figure 53 and Figure 54:

- The duplicate DSC measurements for each LIB cell type with less than 1 wt.% loss from measurement demonstrate high repeatability, as evidenced by the close agreement between the two recorded curves in Figure 53.
- Among all samples, cell type A exhibits the highest extrapolated onset temperature at 211 °C, indicating superior thermal stability of its NMC cathode. This correlates with the highest observed penetrated layer-set (PLS) value of 17.54, suggesting enhanced resilience to thermal runaway compared to cell type B, C and D, which display lower onset temperatures ranging from 173 °C to 188 °C. The implications of this trend among NMC-based cathodes are further examined in Section 7.2.3.
- The thermal reactivity of NMC is strongly influenced by its lithium and nickel content. Lower lithium levels and higher nickel concentrations promote the earlier onset of reduction reactions involving Ni and Co species. In particular, highly delithiated NMC phases display pronounced structural and chemical instability due to oxygen release, which facilitates the reduction of Ni^{4+} to Ni^{2+} . This redox transition is accompanied by a structural transformation from the original layered oxide to a NiO-like rocksalt phase, proceeding through a M_3O_4 -type spinel intermediate (see Figure 4 in Section 2.2.1). Simultaneously, oxidation of the electrolyte further contributes to the exothermic heat release observed.
- In contrast, the NCA-based cathodes from cell types E and F deviate from the aforementioned trend. Despite demonstrating relatively high onset temperatures — second only to cell type A — these cells exhibit the lowest tolerance to internal short circuits. This anomaly can be partially explained by the sharper and more intense reaction peaks observed in their DSC curves, which are confined to a narrower temperature window (see Figure 53 (e) and (f)), suggesting a kinetically faster and more exothermic thermal response. This behavior is presented as the average reaction enthalpy in Figure 55 and explored further as the degree of reaction in Figure 56.

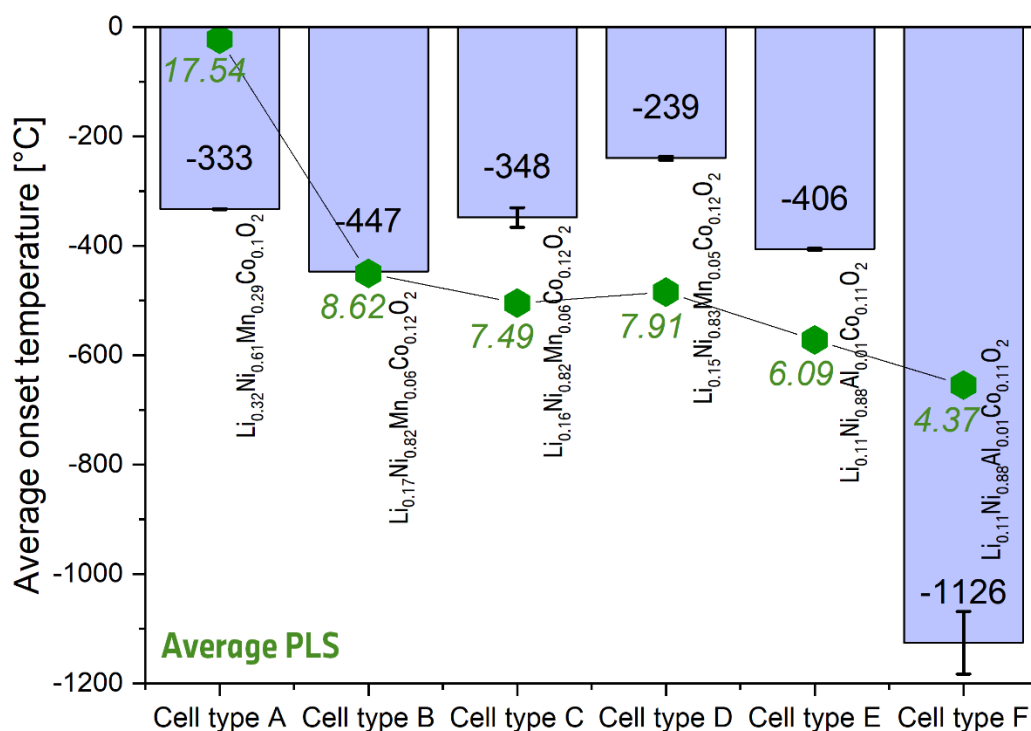


Figure 55. The average reaction enthalpy of six cell types with the average penetrated layer-sets (PLS).

- Notably, cell types E and F, sharing the same chemistry, display nearly identical onset temperatures and nearly overlapping reaction profiles, confirming consistency between replicates. Generally, NCA materials are more exothermic than NMC due to their lower lithium content, resulting in a greater proportion of reactive species per unit mass, as observed for cell type F [4]. However, a significant difference in total reaction enthalpy — approximately -406 J/g for cell type E versus -1100 J/g for Cell Type F — is evident, as demonstrated in Figure 55. This discrepancy is likely due to differing electrolyte content on the electrode surface, with cell type E samples assumed to contain substantially less embedded electrolyte than those of cell type F.
- Unlike the consistency observed between cell types E and F, cell types B and C, despite having nearly identical cathode chemistries, show differing onset temperatures and reaction profiles. This divergence is hypothesized to arise from an electrolyte additive present in cell type C: lithium tetrafluoro oxalate phosphate (LTFOP). Gas chromatography analysis confirmed the presence of LTFOP in cell type C but not in cell type B. Previous studies by Qin et al. [160] and Wang et al. [161] have shown that LTFOP enhances safety by facilitating the formation of a robust solid electrolyte interphase (SEI) and stabilizing the cathode–electrolyte interface. As a result, the inclusion of LTFOP in cell type C is associated with a higher onset temperature ($187.95 \pm 3.89 \text{ }^\circ\text{C}$) compared to cell type B ($179.05 \pm 0.64 \text{ }^\circ\text{C}$) despite similar cathode compositions.

In summary, the thermal stability of the cathode material in the presence of electrolyte is a key factor determining a LIB cell's resistance to internal short circuits, particularly with respect to the onset temperature for thermal runaway (TR). During a nail penetration test, TR is triggered when sufficient heat is generated at the ISC site. This localized heat generation differs fundamentally from the uniform heating in DSC, which gradually raises the temperature of the entire electrode sample with 5 K/min . Consequently, the internal TR onset temperature at cell level from ISC may differ significantly from the onset temperature of positive electrode with electrolyte determined by DSC.

Nevertheless, a cathode material with higher thermal stability — i.e., requiring a higher temperature to initiate decomposition and electrolyte oxidation — can delay or prevent TR even in the presence of ISC. For instance, NMC materials with a lower Ni and higher Li molar fraction demonstrate enhanced thermal stability and elevated onset temperatures. This stability is attributed in part to the

increased Mn^{4+} content, which mitigates charge-transfer resistance [31,161], whereas Ni-rich compositions contain more thermally unstable Ni^{4+} , which is more prone to reduction to Ni^{3+} or Ni^{2+} [28,162]. Furthermore, the onset temperature for oxygen release is critically influenced by the Ni content, since the reduction of Co and Mn ions typically occurs at higher temperatures. Structural integrity is also dependent on the fraction of extracted Li^+ ions, with excessive delithiation compromising the material's stability [28,159].

The presence of aluminum in the NCA composition $\text{Li}_{0.11}\text{Ni}_{0.88}\text{Al}_{0.01}\text{Co}_{0.11}\text{O}_2$, used in cell types E and F, plays a structural role similar to that of manganese in NMC materials. Specifically, aluminum helps to suppress phase transitions and mitigates volumetric changes during thermal or electrochemical stress. [163] As previously noted, the NCA-based cathodes from cell types E and F exhibit relatively high onset temperatures during DSC analysis. Nevertheless, these same cell types are among the least stable in the nail penetration test at the full-cell level.

To better understand this seemingly contradictory behavior — namely, high onset temperature but low mechanical abuse tolerance — the extent of the reaction progression in the presence of electrolyte was quantitatively assessed. This was achieved by calculating the degree of reaction (α_T) for the positive electrodes from cell types A through F, as discussed with Reaction (3.3) in Section 3.1.1. The degree of reaction at a given temperature T , denoted α_T , is defined as the ratio of the integrated exothermic energy released up to that temperature (Q_T) to the total energy released over the entire reaction window from 50 °C to 350 °C (Q_{50-350}) as $\alpha_T = Q_T / Q_{50-350}$.

The average α_T values, based on duplicate DSC runs for each sample, are presented in Figure 56. It should be noted that this calculation is used solely for comparative analysis within the context of this study, as discussed in Section 3.1.1. The reaction pathway is not elementary, and the precise initial and final states of the involved processes are unknown. [110] Instead, the exothermic behavior of the positive electrode — including all reactions involving the active material, electrolyte, and any additives — is treated as a composite, inseparable reaction system. This approach reflects the complexity of commercial LIB cells, where individual reactions cannot be isolated but must be evaluated collectively to understand the overall thermal response.

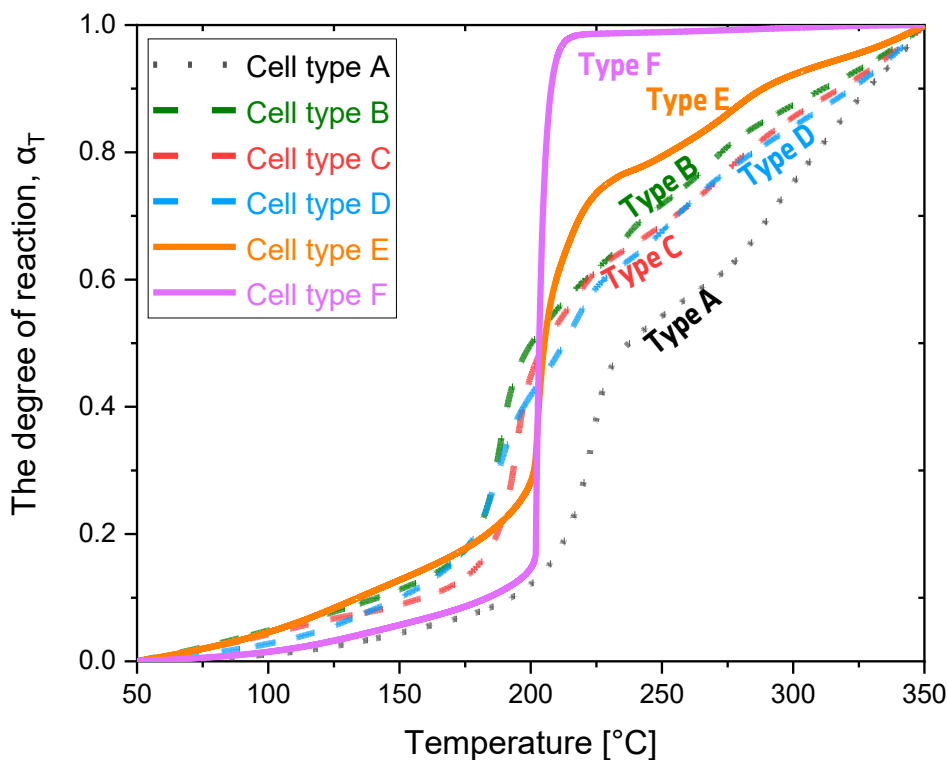


Figure 56. Average degree of reaction as a function of temperature, reproduced from literature [32].

As illustrated in Figure 56, the six prismatic automotive LIB cell types can be grouped into three categories based on the kinetic rate of their thermal decomposition reactions: **slow conversion** (cell type A), **moderate conversion** (cell types B, C, and D), and **fast conversion** (cell types E and F). This classification highlights the key reason why cell types E and F, despite containing thermally stable NCA cathodes (as indicated by their higher onset temperatures), display reduced stability at the full-cell level during abuse tests.

The decomposition of NCA in the presence of electrolyte proceeds significantly faster than that of NMC-based electrodes. Although the exothermic reaction in cell types E and F initiates at a comparatively higher temperature, the energy is released more rapidly. For instance, at 225 °C, approximately 99% of the total reaction in the cathode from cell type F and 74% in cell type E have been completed, whereas only 38% (cell type A), 62% (cell types B and C), and 59% (cell type D) of the reaction progress is observed in the corresponding NMC-based samples.

This faster reaction rate for NCA results in a rapid evolution of heat, which, under conditions with limited heat dissipation, can lead to localized temperature spikes. Such localized thermal buildup can increase the likelihood of triggering thermal runaway (TR) within the cell. This behavior is consistent with findings by Duh et al. [74], who evaluated thermal runaway risks of 18650 cells with different cathode chemistries using accelerating rate calorimetry (ARC). Their results showed that NCA cells exhibit higher maximum self-heating rates than NMC cells, despite slightly higher onset temperatures for thermal events. It is important to note that the testing methodologies — ARC, nail penetration, and DSC — differ in thermal boundary conditions. ARC operates under adiabatic conditions using a Heat-Wait-Seek protocol (see Figure 28), which contrasts with the localized thermal inputs in nail penetration and the uniform heating of DSC. Therefore, critical temperatures identified by these methods are not directly comparable. However, the thermal behavior and progression of TR across methods can be meaningfully compared because the underlying driver remains consistent: the exothermic decomposition of the positive electrode in the presence of electrolyte.

Supporting this, Ohneseit et al. [10] also reported through ARC measurements that although NCA-based cells have higher onset temperatures than NMC-based cells, they undergo thermal runaway more rapidly due to a faster rise in internal temperature — again underscoring the importance of reaction kinetics in thermal hazard assessment.

TGA Study

Thermogravimetric analysis (TGA) was employed to evaluate the thermal stability of the positive electrode by monitoring mass loss across three distinct temperature ranges, as described in Section 3.1.2. While cell types B and C — despite identical cathode chemistry — exhibited different behaviors in DSC due to the presence or absence of the additive LTFOP, the NCA-based cell types E and F showed comparable DSC results. Therefore, only the cathode sample from cell type F was selected as a representative for TGA analysis.

To closely replicate the cathode's in-cell environment, the scraped-off active material layer from each cell types with SOC 100 % was placed in a crucible equipped with a partially open lid featuring a central hole. This setup allowed for minimal exposure to ambient air while enabling gaseous byproducts to escape. All procedures — from cell disassembly and electrode harvesting to the TGA measurement — were conducted rapidly to minimize alterations to the material state due to air exposure or time delay. The TGA profile is presented in Figure 57, and the corresponding average mass loss within the three temperature intervals, along with the mass percentage of electrolyte, is summarized in Figure 58.

The electrolyte mass fraction displayed in Figure 58 was determined by subtracting the total mass of washed and dried cell components from the original mass of the complete LIB cell, thereby estimating the net electrolyte content.

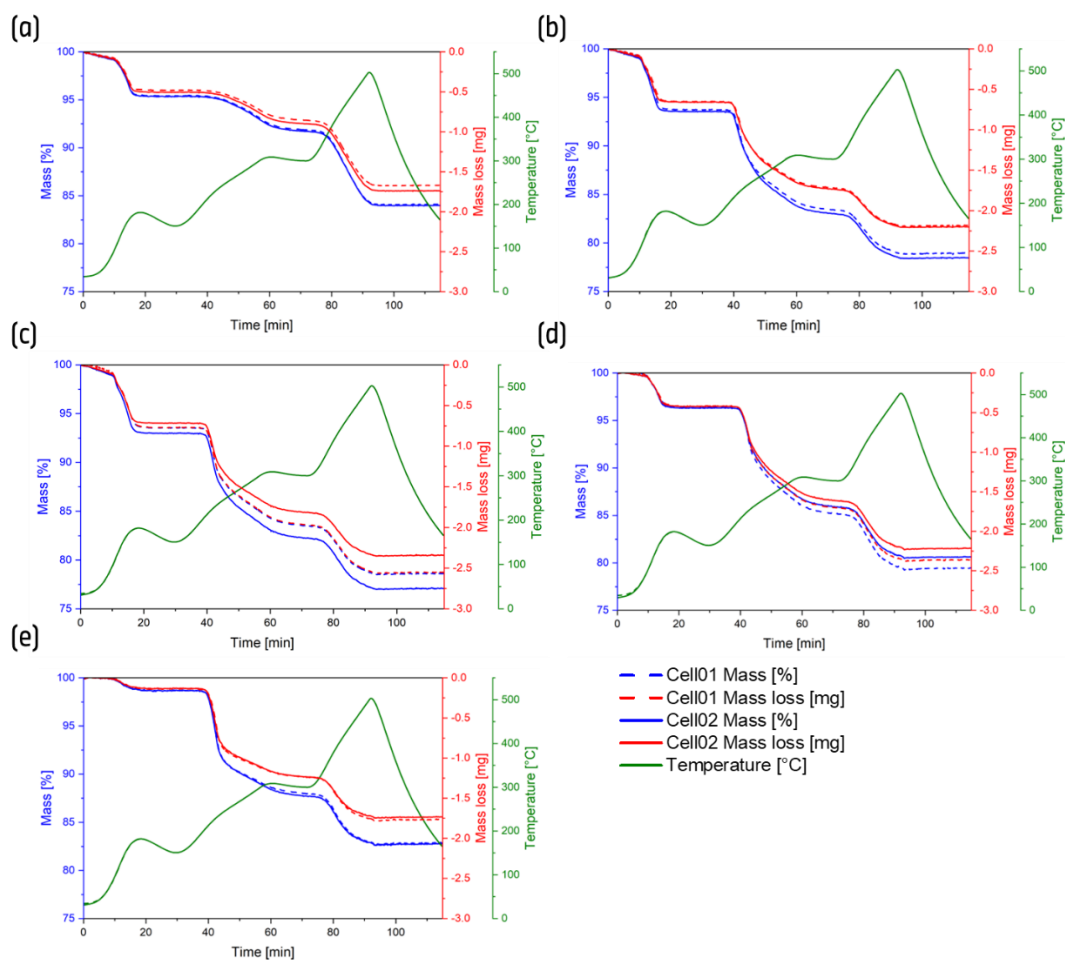


Figure 57. TGA results for harvested positive electrodes from 100% SOC LIB cells: (a) cell type A, (b) cell type B, (c) cell type C, (d) cell type D, and (e) cell type F. Each sample was analyzed in duplicate, shown as dashed and solid lines, reproduced from literature [32].

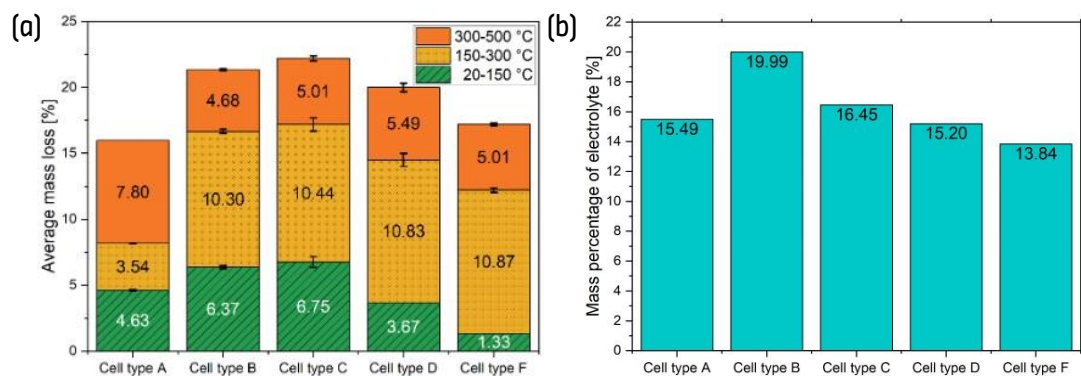


Figure 58. Summary of mass loss trends and electrolyte content: (a) average mass loss across three temperature intervals: 20–150 °C (green), 150–300 °C (yellow), and 300–500 °C (orange) and (b) mass percentage of electrolyte (excluding cell can weight), reproduced from literature [32].

The following observations and interpretations are drawn from Figure 57 and Figure 58.

- **20–150 °C (Heating rate: 10 K/min):**

In this temperature range, mass loss is primarily attributed to the evaporation of the electrolyte, and the extent of this loss is expected to correlate with the electrolyte content in the cell. As expected, the sample from cell type F, which has the lowest measured electrolyte content (13.84 %), exhibits the lowest mass loss (1.33 %). This trend continues for other cell types: cell type D (15.20 % electrolyte) loses 3.67%, and cell type A (15.49 %) loses 4.63 %.

However, a deviation is observed between cell types B and C. Although cell type B has the highest overall electrolyte fraction, its sample loses slightly less mass than cell type C. This anomaly is likely due to the presence of unabsorbed electrolyte that remained free in the cell casing upon opening, resulting in a lower actual electrolyte content in the sampled material from cell type B.

- **150–300 °C (Heating rate: 5 K/min):**

In contrast to the DSC experiments — where crucibles are sealed — the open-lid setup of TGA allows for complete evaporation of the electrolyte. Therefore, the mass loss observed in this range can be primarily attributed to oxygen release from the decomposition of the cathode active material, rather than oxidation reactions involving electrolyte [159,164,165]. From the inclination how fast or slow mass decreases in Figure 57, similar conclusions can be drawn as in the DSC study: the NCA sample from cell type F initiates decomposition at a higher temperature but undergoes a faster reaction once it begins. On the other hand, the NMC sample from cell type A, which has the lowest Ni and highest Li content, exhibits the slowest and most gradual decomposition, aligning with its more stable thermal behavior shown in Figure 53 (a) and Figure 56. In terms of mass loss: cell type F (NCA) shows the largest loss (10.87%) > cell types B, C, and D (NMCs) have comparable losses ranging from 10.30% to 10.83%. > cell type A (NMC) shows the lowest mass loss (3.54%), consistent with its slow reaction kinetics.

- **300–500 °C (Heating rate: 10 K/min):**

This range likely captures residual decomposition processes of the cathode material. Unlike the other samples, cell type A shows the highest mass loss above 300 °C, which is consistent with its previously observed kinetic limitations in thermal reactivity (see Figure 56). However, when considering the cumulative mass loss from 150 to 500 °C, cell type A still shows the lowest overall loss ($7.80 + 3.54 = 11.34\%$), reinforcing its characterization as the most thermally stable cathode. This behavior is also consistent with findings by Kasnatscheew et al. [159], who reported that delithiated NMCs with lower Ni content exhibit reduced mass loss between 180 and 370 °C.

Theoretically, oxygen release from cathode decomposition can reach a maximum of 16.5 %, based on the following assumptions: 1) the cathode active material constitutes 94 % of the cathode, and 2) 0.5 mol of oxygen can be released per 1 mol of cathode active material, as derived from equations (2.9) to (2.14) in Figure 4. The total oxygen release observed in two temperature ranges from 150 to 500 °C for cell types B (14.98 %), C (15.45 %), D (16.32 %) and F (15.88 %) closely approaches this theoretical maximum. In contrast, the cathode active material in cell type A is presumed not to have undergone complete degradation.

Furthermore, during the two isothermal phases within the above specified temperature ranges, a decrease in temperature is observed. This is likely due to the oven compensating for excess heat generated during the preceding heating phase, thereby regulating the temperature back to the setpoint. In the first isothermal phase, the temperature drop occurs more rapidly, which can be attributed to the higher preceding heating rate of 10 K/min, in contrast to the second phase. The final temperature at the end of the first isothermal phase stabilizes at approximately 150 °C, as preset.

7.2.3 The Correlation between Safety on Cell Level and Thermal Stability of the Positive Electrode

As emphasized in Section 2.2, a substantial body of thermal and thermodynamic research has pointed to the pivotal role of cathode materials in determining the safety profile of lithium-ion cells. Nevertheless, studies that directly correlate mechanical abuse test results — such as those obtained from needle penetration of automotive prismatic cells — with detailed thermal analysis of harvest cathodes from commercial cells remain limited. The objective of this section is to bridge those in order to provide a comprehensive overview of how the thermal stability of the cathode influences overall cell safety.

The comparative investigation in Section 7.2.1 evaluates the robustness of six automotive prismatic LIBs against internal short circuits and identifies the primary factors governing their safety performance. Multiple candidate parameters — including Ni and Li molar fractions, cell capacity, separator thickness, current collector thickness, and electrolyte mass fraction — were assessed against the number of penetrated layer sets (PLS), a quantitative proxy for ISC resilience derived from the needle penetration tests. Among these, Ni and Li molar fractions in the cathode exhibited the strongest correlation with PLS, highlighting cathode chemistry as the dominant determinant of safety.

In the subsequent Section 7.2.2, the thermal characteristics of the cathode materials were systematically analyzed using both conventional and newly proposed metrics — specifically, the onset temperature and the degree of reaction — as indicators of thermal stability. As shown in Figure 59, cells utilizing Ni-rich NMC or NCA cathodes, which are thermally less stable, undergo thermal runaway after fewer internal shorting events. These findings are in agreement with those of Barkholtz et al. [67], who correlated the thermal runaway behavior observed in ARC testing of commercial 18650-format cells with DSC- and TGA-derived thermal stability profiles of various cathode chemistries including LCO, LFP, and NCA (see Table 6).

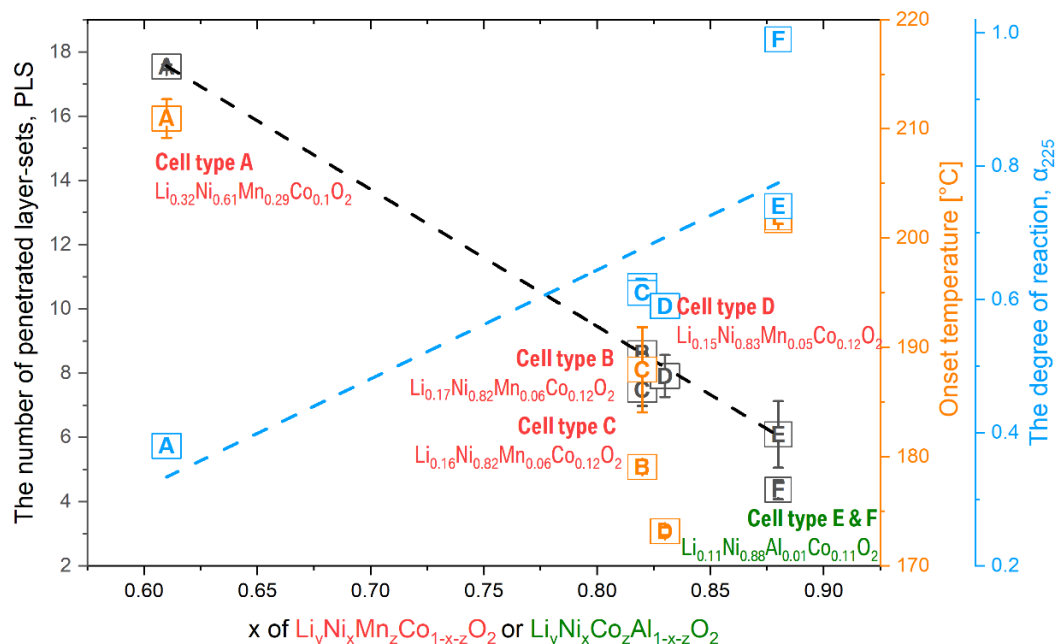


Figure 59. Correlation between cell-level safety and the thermal stability of the positive electrode, reproduced from literature [32].

While the observed relationship is robust, it represents a general trend rather than a strict rule. Thermal stability remains the primary factor but not the sole contributor to cell safety. This trend can be illustrated through three groupings:

- **High-Stability Group:** cell type A (NMC with Ni molar fraction of 0.61) exhibits the greatest resistance to ISC-induced thermal runaway, requiring a higher number of short circuits to trigger failure. The positive electrode retrieved from this cell exhibits the highest thermal stability, characterized by the highest decomposition onset temperature and the smallest degree of reaction.
- **Intermediate-Stability Group:** cell types B, C, and D (NMCs with Ni molar fractions between 0.82 and 0.83) require fewer PLS to reach thermal runaway than cell type A but more than NCA-based cells. The thermal analysis of their cathodes reveals a slightly lower onset temperature than cathode from cell type A and a medium degree of reaction.
- **Low-Stability Group:** cell types E and F (NCA with Ni molar fraction of 0.88) show the lowest PLS values, indicating higher susceptibility to ISC-triggered failure. Although onset temperatures of harvested NCAs are higher than those of the intermediate group, the reactions proceed far more rapidly, resulting in the highest degree of thermal reaction among the tested materials.

However, within the intermediate group, small variations in Ni and Li content do not fully explain the observed PLS differences, suggesting that other factors — such as cell assembly and electrolyte additives discussed in Chapter 5 and Section 7.2.2, respectively — may exert greater influence.

As presented in Figure 59, evaluating cathode thermal stability requires more than onset temperature alone. Reaction kinetics, or the rate at which decomposition occurs once triggered, is also critical. If only onset temperature were considered (e.g., as in Figure 54), NCA — despite its high Ni content — might misleadingly appear as the second most stable material. In reality, thermal decomposition of NCA cathodes from cell types E and F proceeds significantly faster than in any NMC-based cell once initiated, as evidenced by the data presented in Figure 56.

7.3 Conclusion

This study set out to answer a central question: what determines the safety of a lithium-ion battery cell? By conducting a systematic needle penetration analysis of six commercial automotive prismatic LIB cell types, we identified the critical penetration depth — more precisely, the number of penetrated layer-sets (PLS) — as a meaningful indicator of cell-level resilience against internal short circuits (ISC). Among a range of evaluated parameters, the strongest correlation was found between PLS and the Ni and Li molar fractions in the cathode active material.

To clarify this relationship, DSC and TGA analyses were performed on positive electrodes harvested at 100% SOC. The thermal stability of these electrodes was characterized using two criteria: onset temperature and the degree of reaction (α_T). The principal findings are summarized below:

1. While the anode, separator, and electrolyte were comparable across all cell types, the variation in cathode composition — particularly the Ni and Li molar fractions — proved to be the most influential factor affecting ISC tolerance.
2. A nearly linear decline in thermal stability was observed with increasing Ni content and decreasing Li content in the cathode active material. This stability is evaluated based on:
 - i. **Onset Temperature:** in the context of lithium-ion cell safety, the onset temperature signifies the threshold at which a significant amount of exothermic heat is released from the cathode. This is particularly important because the heat generation from the cathode dominates the transition to thermal runaway due to its rapid reaction kinetics. Cathodes with lower Ni and higher Li molar fractions exhibit higher onset temperatures and are thus considered more thermally stable. In this study, the cathode from cell type A ($\text{Li}_{0.32}\text{Ni}_{0.61}\text{Mn}_{0.29}\text{Co}_{0.1}\text{O}_2$) displayed the highest onset temperature of 211 °C and correspondingly the highest PLS of 17.54. In contrast, cell types B, C, and D, with higher Ni fractions (≈ 0.82 -0.83) and lower Li contents, exhibited lower onset temperatures ranging from 173 °C to 188 °C and reduced PLS values (7.49-8.62).

- ii. **Degree of Reaction (α_T):** this metric reflects the rate at which thermal decomposition progresses once triggered. A faster decomposition rate indicates more aggressive heat accumulation and, thus, higher susceptibility to thermal runaway. NCA-based cathodes from cell types E and F demonstrated the most rapid reactions, despite their relatively high onset temperatures, and showed the highest α_T values. These characteristics correlated with the lowest PLS values (4.37-6.09). In comparison, NMC-based cell types A – D showed broader PLS values between 7.49 and 17.54.

Based on these thermal metrics, the cathode materials can be ranked as follows:

- **Most Stable:** relatively low Ni-NMC; $\text{Li}_{0.32}\text{Ni}_{0.61}\text{Mn}_{0.29}\text{Co}_{0.1}\text{O}_2$ (cell type A)
 - **Moderately Stable:** relatively high Ni-NMC; $\text{Li}_{0.17}\text{Ni}_{0.82}\text{Mn}_{0.06}\text{Co}_{0.12}\text{O}_2$, $\text{Li}_{0.16}\text{Ni}_{0.82}\text{Mn}_{0.06}\text{Co}_{0.12}\text{O}_2$, $\text{Li}_{0.15}\text{Ni}_{0.83}\text{Mn}_{0.05}\text{Co}_{0.12}\text{O}_2$ (cell types B, C and D)
 - **Least Stable:** relatively high Ni-NCA; $\text{Li}_{0.11}\text{Ni}_{0.88}\text{Al}_{0.01}\text{Co}_{0.11}\text{O}_2$ (cell types E and F)
3. Enhanced thermal stability of cathode materials translates directly into improved cell-level safety. The sequence of thermal stability of positive electrode with electrolyte aligns closely with ISC tolerance at lithium-ion cell level, emphasizing the impact of cathode composition.
 4. However, thermal stability is not the sole determinant of battery safety. While Ni and Li ratios provide strong predictive capability, this applies primarily as a general trend. Minor variations in ISC performance were observed between cells with otherwise identical chemistries, such as B and C or E and F, indicating that additional variables — like cell assembly (see Chapter 5) and electrolyte additives — can modulate safety outcomes.
 5. At the materials level, even slight adjustments in Ni and Li concentrations can substantially affect the thermal behavior of the cathode in the presence of electrolyte. Additives offer further avenues for enhancing safety, as demonstrated by the improved performance of cell type C compared to cell type B, attributed to the inclusion of LTFOP despite identical baseline compositions.

While these findings establish thermal stability of the cathode-electrolyte system as a primary safety driver at the cell level, they also point to promising avenues for future investigation. Several factors that were beyond the scope of this study could be explored to refine the understanding of internal short circuit resilience:

- **Electrolyte Quantification in DSC/TGA:** current analyses were performed using unrinsed electrodes, preserving residual electrolyte to approximate in-cell conditions. However, excess electrolyte can skew measurements, particularly in mass loss regions and reaction enthalpies. For example, cell type B showed electrolyte surplus, distorting mass loss data (see Figure 58), and cell types E and F exhibited large variability in reaction enthalpy despite having the same cathode chemistry. More accurate evaluations could be achieved by applying a defined quantity of electrolyte to rinsed electrodes, thereby simulating the true in-cell mass fraction.
- **Cathode Microstructure and Composition:** ICP-OES provides only average chemical composition. Further investigation can be done into structural features such as multi-material blends or core-shell gradients, which may significantly influence both reaction kinetics and stability.
- **Design Variables beyond Cathode Chemistry:** although cathode thermal stability was shown to be the dominant safety determinant in this study, it is not the sole contributor, as discussed in Chapter 5 and 6. Other aspects — including additive selection, total electrolyte mass fraction, and electrode microstructure — can be evaluated in future studies to provide a more holistic understanding of cell safety.

In summary, precise electrolyte control, detailed analysis of cathode microstructures, and targeted additive studies would represent promising extensions of this research. Nonetheless, the results

presented in this chapter affirm that the optimization of cathode chemistry can significantly increase the resilience of lithium-ion cells under abuse conditions.

8 Summary and Outlook

As the global demand for battery electric vehicles (BEVs) continues to accelerate, lithium-ion batteries (LIBs) remain at the forefront of this transformation, providing the essential energy storage technology required for sustainable mobility. However, while energy capacities and driving ranges have steadily advanced, these improvements are intrinsically accompanied by heightened safety challenges. The inherent conflict between maximizing energy density and ensuring safety defines one of the most critical dilemmas for automotive LIB design. Higher stored energy increases the risk of catastrophic failures, primarily driven by thermal runaway (TR), which is initiated through a sequence of exothermic reactions typically triggered by internal short circuits (ISC). Once initiated, localized joule heating from ISC can degrade cell components, such as the separator, and stimulate further chemical reactions between cathode materials and electrolytes, leading to uncontrolled heat accumulation.

The primary aim of this work was to comprehensively investigate the mechanisms underlying LIB safety through a multi-tiered experimental approach that bridges materials-level thermodynamic properties with cell-level safety phenomena. This research sought to answer three critical questions:

- How thermally and thermodynamically stable are commercial high-nickel cathode active materials for BEV?
- What does affect ISC behavior at the cell level and how can this ISC systematically quantified?
- How does intrinsic cathode stability influence the resilience of LIB cells to thermal runaway?

The first stage focused on quantifying the thermodynamic stability of high-nickel layered oxide cathodes in Chapter 4 through high temperature drop solution calorimetry — MHTC and Alexsys-1000. Enthalpies of formation for commercial NMC622, NMC85, and NMC94 cathodes were systematically determined, revealing a clear compositional trend: increasing nickel content and decreasing manganese content led to progressively less exothermic formation enthalpies. Specifically, NMC622 exhibited an enthalpy of formation, $\Delta_f H^{\ominus, \text{elements}}$ of -647.21 ± 1.46 kJ/mol, NMC85 yielded -617.04 ± 1.53 kJ/mol, and NMC94 showed the least exothermic value of -608.42 ± 1.58 kJ/mol. These results quantitatively demonstrate that while higher nickel contents favor energy density, they compromise thermodynamic stability and presumably elevate vulnerability under abuse conditions.

In parallel, this study critically assessed the measurement capabilities of two distinct calorimetric instruments: the Setaram Alexsys-1000 and the Setaram MHTC. The Alexsys-1000, with its dual-cell symmetrical design and superior baseline stability, served as the reference method, delivering highly precise and reproducible results. For instance, the enthalpy of drop solution ($\Delta_{\text{ds}} H$) of NMC85 was measured by Alexsys-1000 from just 13 drops, yielding 57.38 ± 0.41 kJ/mol with minimal uncertainty. The MHTC, by contrast, demonstrated greater sensitivity to baseline fluctuations, asymmetry in heat flow paths, and higher uncertainty in enthalpy measurements. For the same NMC85, 48 drops were required with MHTC to obtain 55.67 ± 2.22 kJ/mol, with uncertainties roughly 3 to 6 times larger compared to Alexsys. This larger dispersion reflects structural limitations of the MHTC, such as the single calorimeter cell, smaller crucible volume, absence of bubbling tubes, and the vertical

asymmetry in heat flow detection. Despite these limitations, with meticulous calibration procedures — including sapphire calibration, baseline optimization, and sample preparation refinement — the MHTC was validated as a functional alternative for thermodynamic measurements, provided its operational constraints were rigorously managed.

Following the thermodynamic investigation, attention shifted to cell-level analysis of ISC phenomena. In Chapter 5, using the specially crafted nail where a thermocouple is embedded, the influence of internal assembly architecture was examined by comparing stacked and jelly-roll prismatic cell designs, recognizing that thermodynamic instability alone does not fully dictate safety outcomes. The internal assembly design of prismatic LIB cells was demonstrated to play a decisive role in dictating ISC propagation. Comparative nail penetration tests, performed on cells with stacked and jelly-roll architectures, revealed markedly different ISC behaviors. In stacked configurations, individual short circuits remained confined to isolated electrode stacks, allowing only limited portions of stored energy to be released at each penetration stage, thus producing discrete and self-limiting current spikes. This segmentation of energy release acted analogously to a series of miniature fuses, effectively fragmenting potential runaway events. Conversely, jelly-roll cells facilitated a more contiguous electrical pathway during ISC, tapping into larger portions of stored energy and producing sustained, escalating current profiles. The jelly-roll architecture, despite its manufacturing efficiency, thereby presents a heightened risk under abuse conditions, requiring additional mitigation strategies to maintain safety parity.

In Chapter 6, the investigation then advanced to evaluating an innovative safety feature: the floating can design addressing ISC risks between the cell can and the outermost anode. In conventional designs where the metal can is electrically tied to the positive terminal, any conductive bridge between the can and anode immediately triggers a low-resistance short circuit capable of initiating rapid thermal escalation. The floating can architecture, by introducing a high-resistance path exceeding 1 k Ω , can significantly mitigate this risk. Experimental validation through needle penetration tests confirmed that the floating can configuration substantially delayed ISC initiation, increasing the required penetration depth to induce TR, and reducing ISC current magnitudes even under severe abuse conditions. Complementary ARC experiments further demonstrated that floating cans maintained thermal behavior indistinguishable from conventional designs during quasi-adiabatic heating, confirming that this safety enhancement does not compromise the intrinsic thermal stability of the cell.

The final investigative stage in Chapter 7 bridged the material- and cell-level studies by integrating mechanical abuse tests with thermal characterization for a diverse set of commercial prismatic cells. Needle penetration experiments were designed to quantify cell safety margins using the metric of penetrated layer-sets (PLS). PLS allowed normalization across different cell designs, measuring the number of sequential ISC events required to trigger thermal runaway. The data revealed that cells with lower nickel cathodes, such as NMC with Ni molar fraction of 0.61, required substantially more PLS to reach failure, while NCA cathodes with Ni molar fraction of 0.88 reached runaway after significantly fewer ISC events. Intermediate stability was observed in NMC compositions containing Ni fractions between 0.82 and 0.83.

To corroborate the PLS findings with intrinsic material behavior, harvested cathodes were subjected to differential scanning calorimetry (DSC) and thermogravimetric analysis (TGA). The DSC quantified the onset temperatures and degree of reaction (α_T) for exothermic decomposition, while TGA revealed complementary mass loss profiles during thermal breakdown. High PLS cells exhibited elevated onset temperatures and slower reaction kinetics, reflected in lower α_T values, signaling superior thermal stability. The intermediate stability group, represented by NMCs with higher Ni content (around 0.82–0.83), showed moderate onset temperatures and α_T values, corresponding well with their intermediate PLS behavior. Conversely, cathodes extracted from NCA cells demonstrated higher onset temperatures but steep α_T progressions, aligning with their rapid ISC-induced failures observed during needle penetration tests. The integration of these results confirmed a strong

correlation between cathode thermal stability and practical cell safety performance under mechanical abuse.

Importantly, while nickel content clearly emerged as the primary predictor for ISC-induced safety margins, it was not the sole governing parameter as discussed in Chapter 5 and 6. Variations in ISC performance among cells with similar baseline chemistries emphasized the critical role of auxiliary design variables such as electrolyte formulation, separator materials, and chemical additives. Notably, cells employing electrolyte additives like LTFOP exhibited enhanced safety performance despite identical core chemistries, demonstrating that chemical engineering strategies can further mitigate thermal runaway risks. These outcomes underscore the necessity of a holistic design philosophy where cathode composition, electrolyte chemistry, cell architecture, and mechanical safety features are jointly optimized to achieve robust safety performance.

Throughout this dissertation, multiple novel experimental techniques were developed and validated. The introduction of ultra-slow nail penetration protocols enabled precise, layer-resolved mapping of ISC propagation. The use of embedded thermocouples provided real-time temperature data at the shorting interface, while external compensation circuits allowed accurate quantification of short-circuit current magnitudes during penetration events. Collectively, these innovations yielded unprecedented experimental resolution for diagnosing the evolution of ISC events and thermal escalation within LIB cells.

Despite these comprehensive findings, certain limitations persist. Laboratory-scale testing cannot fully replicate the complexity of multi-cell automotive battery packs, where thermal propagation, pack-level electrical balancing, and BTMS introduce additional variables. Furthermore, while a strong link between cathode composition and safety performance at cell level was established, further systematic studies exploring broader material variations or electrolyte innovations are necessary to refine predictive safety frameworks.

Future research should broaden compositional investigations to include emerging cathode families such as LFP or mixture of LFP and NMCs or emerging anode (Graphite with increasing weight ratio Si). Simultaneously, systematic studies of electrolyte additives must continue to optimize safety without compromising performance. As next-generation BEVs integrate fast-charging protocols, wider climate tolerance, and higher driving ranges, the importance of comprehensive safety assessments spanning extreme operational windows will only grow.

In conclusion, this dissertation delivers a comprehensive, multi-scale investigation into LIB safety, bridging material-level thermodynamics with cell-level ISC tolerance. It extends previous works by expanding the measurement of formation enthalpies to state-of-the-art high-nickel NMC compositions — NMC85 and NMC94. To deepen the understanding of cathode thermal stability, it introduces the degree of reaction as a critical descriptor alongside onset temperature, thereby clarifying why LIBs with NCA — despite high onset temperatures — can exhibit inferior safety performance compared to NMC-based systems. Beyond material-level analysis, this study dissects the ISC behavior under highly controlled nail/needle penetration protocols, and systematically evaluates the role of safety features such as floating can designs and internal electrode assemblies (stacks vs. jelly rolls). Ultimately, this research provides an integrated framework for comprehensively improving LIB safety, demonstrating that while cathode chemistry remains a primary determinant, safety features and assembly architectures play equally essential roles in advancing the safety of next-generation automotive lithium-ion batteries.

Appendix

Enlarged views of Figure 44 (b) and Figure 45 (a) are presented in Figure 60 and Figure 61.

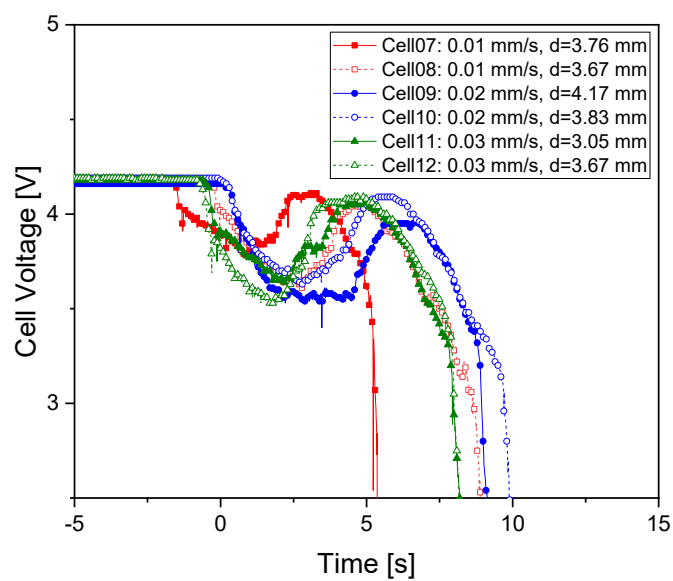


Figure 60. Enlarged detail view of Figure 44 (b).

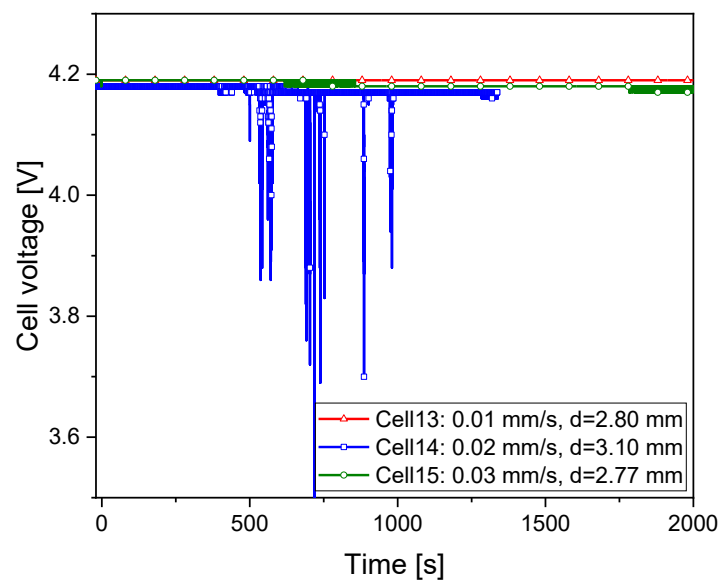


Figure 61. Enlarged detail view of Figure 45 (a).

Figure 62 illustrates the definition of the characteristic temperatures T_1 to T_5 , as obtained from accelerating rate calorimetry described in Section 6.2.3 (see Table 29). As an example, the graphs from Cell 4 with can on potential are presented.

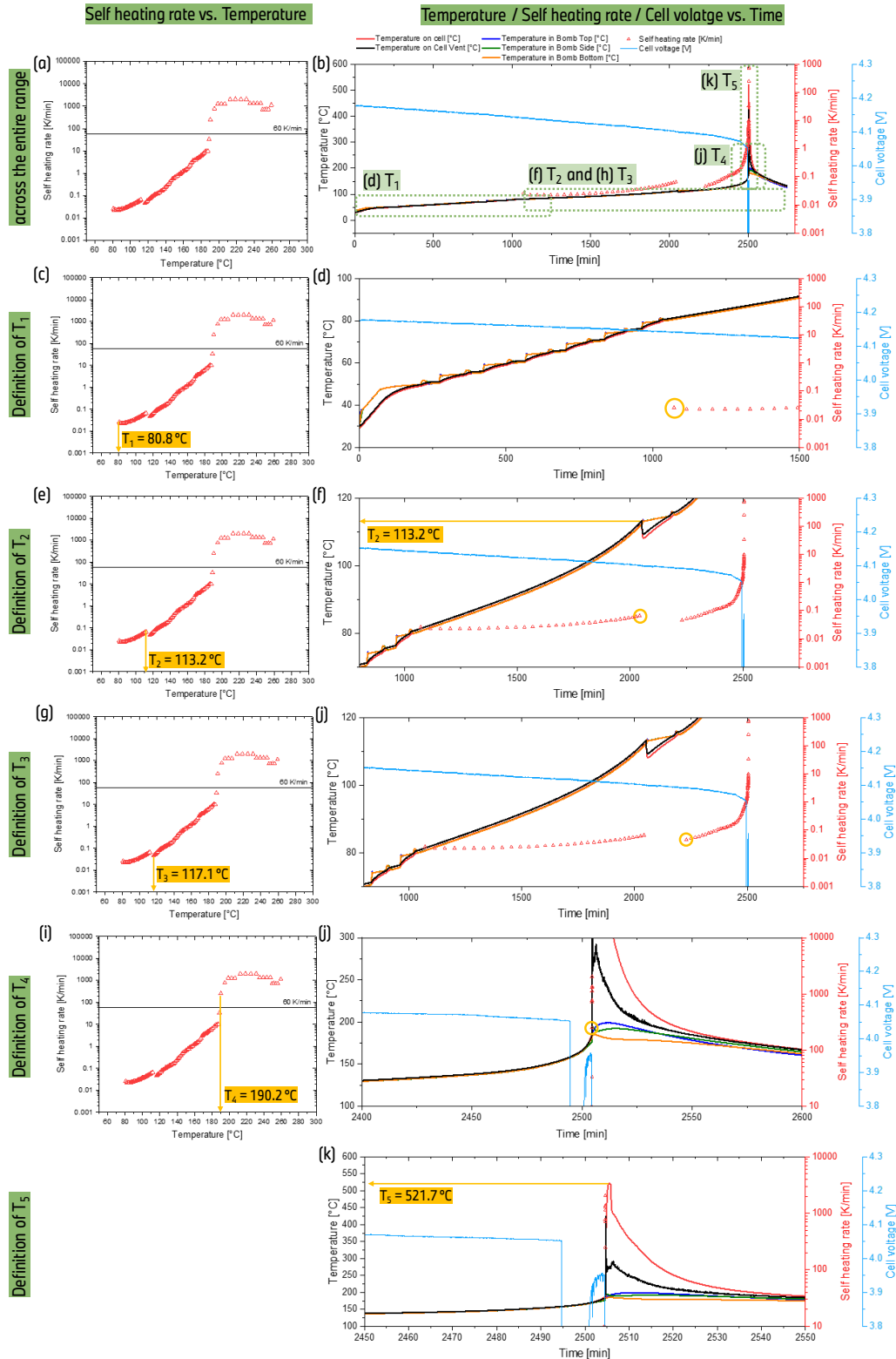


Figure 62. A detailed presentation of five characteristic temperatures (T_1 to T_5) using the HWS graphs of cell 4 with floating can as a representative example.

The temporary temperature dip in the measured signal in Figure 62 (f) – presumably resulting from a venting event – can be explained by Joule-Thomson effect, which describes the temperature change

of a real gas undergoing adiabatic expansion without performing external work. During such expansion, if no heat is exchanged with the surroundings as the adiabatic condition in ARC measurement, the internal energy of the gas changes, leading to a measurable temperature shift.

The temperature change (ΔT) associated with a pressure drop (ΔP) can be approximated using the following relation:

$$\Delta T = \mu_{JT} \cdot \Delta P$$

where μ_{JT} is the Joule-Thomson coefficient, dependent on the specific gas and its temperature. A positive μ_{JT} indicates a cooling effect, which is common for most gases.

To estimate the expected temperature drop, the following assumptions are made:

- Assumption 01: the vented gas consists primarily of CO_2 , generated from SEI breakdown, electrolyte decomposition, combustion of organic solvents and reaction with oxygen released from the cathode.
- Assumption 02: at the relevant temperature T_2 of 386 K (see Figure 62 (f)), the Joule-Thomson coefficient μ_{JT} of CO_2 lies 0.5-0.6 K/bar [166]. For estimation purposes, 0.5 K/bar is used.
- Assumption 03: based on design-dependent safety venting pressures (as discussed in Section 2.4.2), it is assumed that venting was triggered at 10 bar, releasing the gas into an ambient environment at 1 bar.

Under these conditions, the expected temperature drop is calculated as:

$$\Delta T = 0.5 \text{ K/bar} \cdot (10 - 1) \text{ bar} = 5.4 \text{ K}.$$

This estimated temperature decrease is comparable to the observed drop of 3.9 K in Figure 62 (f), supporting the hypothesis that the temporary cooling observed in Figure 62 results from gas release during venting.

Supplementary data corresponding to Figure 59 are shown in Table 33, including PLS, onset temperature, and degree of reaction in relation to the Ni molar fraction.

Table 33. PLS, onset temperature and the degree of reaction at 225 °C, α_{225} depending on Ni molar fraction.

Cell Type	A	B	C	D	E	F
Cathode chemistry	NMC				NCA	
Group	Most stable	Moderately stable			Least stable	
Composition	$\text{Li}_{0.32}\text{Ni}_{0.61}\text{Mn}_{0.29}\text{Co}_{0.1}\text{O}_2$	$\text{Li}_{0.17}\text{Ni}_{0.82}\text{Mn}_{0.06}\text{Co}_{0.12}\text{O}_2$	$\text{Li}_{0.16}\text{Ni}_{0.82}\text{Mn}_{0.06}\text{Co}_{0.12}\text{O}_2$	$\text{Li}_{0.15}\text{Ni}_{0.83}\text{Mn}_{0.05}\text{Co}_{0.12}\text{O}_2$	$\text{Li}_{0.11}\text{Ni}_{0.88}\text{Al}_{0.01}\text{Co}_{0.11}\text{O}_2$	
x of $\text{Li}_y\text{Ni}_x\text{Mn}_z\text{Co}_{1-x-z}\text{O}_2$ or $\text{Li}_y\text{Ni}_x\text{Co}_z\text{Al}_{1-x-z}\text{O}_2$	0.32	0.17	0.16	0.15	0.11	
The number of penetrated layer-sets, PLS	17.54	8.62	7.49	7.91	6.09	4.37
Onset temperature [°C]	210.95 ± 1.77	179.05 ± 0.64	187.95 ± 3.89	173.15 ± 0.35	201.65 ± 0.35	201.9 ± 0.00
The degree of reaction, α_{225}	0.38	0.62	0.61	0.59	0.74	0.99

References

- [1] X. Feng, M. Ouyang, X. Liu, L. Lu, Y. Xia, X. He, Thermal runaway mechanism of lithium ion battery for electric vehicles: a review, *Energy Storage Materials* 10 (2018) 246–267. <https://doi.org/10.1016/j.ensm.2017.05.013>.
- [2] W. Huang, X. Feng, X. Han, W. Zhang, F. Jiang, Questions and answers relating to lithium-ion battery safety issues, *Cell Reports Physical Science* 2 (2021) 100285. <https://doi.org/10.1016/j.xcrp.2020.100285>.
- [3] J. Zhang, L. Zhang, F. Sun, Z. Wang, An overview on thermal safety issues of lithium-ion batteries for electric vehicle application, *IEEE Access* 6 (2018) 23848–23863. <https://doi.org/10.1109/ACCESS.2018.2824838>.
- [4] R.C. Shurtz, A thermodynamic reassessment of lithium-ion battery cathode calorimetry, *J. Electrochem. Soc.* 167 (2020) 140544. <https://doi.org/10.1149/1945-7111/abc7b4>.
- [5] D. Lisbona, T. Snee, A review of hazards associated with primary lithium and lithium-ion batteries, *Process Safety and Environmental Protection* 89 (2011) 434–442. <https://doi.org/10.1016/j.psep.2011.06.022>.
- [6] R.C. Shurtz, J.C. Hewson, Review — materials science predictions of thermal runaway in layered metal-oxide cathodes: a review of thermodynamics, *J. Electrochem. Soc.* 167 (2020) 090543. <https://doi.org/10.1149/1945-7111/ab8fd9>.
- [7] M. Masoumi, Thermochemical and electrochemical investigations of $\text{Li}(\text{Ni}, \text{Mn}, \text{Co})\text{O}_2$ (NMC) as positive electrode material for lithium-ion batteries, Doctoral dissertation, Karlsruher Institut für Technologie (KIT) (2019).
- [8] M. Masoumi, M. Rohde, C. Ziebert, Y. Du, H.J. Seifert, Thermodynamic stabilities of layered lithium transition metal oxides $\text{LiNi}_x\text{Mn}_y\text{Co}_{1-x-y}\text{O}_2$ (NMC) studied by determining enthalpies of formation, in: *Sustainable Industrial Processing Summit and Exhibition*, Flogen, 2023: pp. 63–72.
- [9] M. Masoumi, D.M. Cupid, T.L. Reichmann, K. Chang, D. Music, J.M. Schneider, H.J. Seifert, Enthalpies of formation of layered $\text{LiNi}_x\text{Mn}_x\text{Co}_{1-2x}\text{O}_2$ ($0 \leq x \leq 0.5$) compounds as lithium ion battery cathode materials, *International Journal of Materials Research* 108 (2017) 869–878. <https://doi.org/10.3139/146.111553>.
- [10] S. Ohneseit, P. Finster, C. Floras, N. Lubenau, N. Uhlmann, H.J. Seifert, C. Ziebert, Thermal and mechanical safety assessment of type 21700 lithium-ion batteries with NMC, NCA and LFP cathodes—investigation of cell abuse by means of accelerating rate calorimetry (ARC), *Batteries* 9 (2023) 237. <https://doi.org/10.3390/batteries9050237>.
- [11] Y. Wu, S. Saxena, Y. Xing, Y. Wang, C. Li, W. Yung, M. Pecht, Analysis of manufacturing-induced defects and structural deformations in lithium-ion batteries using computed tomography, *Energies* 11 (2018) 925. <https://doi.org/10.3390/en11040925>.

- [12] Q. Wang, B. Jiang, B. Li, Y. Yan, A critical review of thermal management models and solutions of lithium-ion batteries for the development of pure electric vehicles, *Renewable and Sustainable Energy Reviews* 64 (2016) 106–128. <https://doi.org/10.1016/j.rser.2016.05.033>.
- [13] J. Li, E. Murphy, J. Winnick, P.A. Kohl, Studies on the cycle life of commercial lithium ion batteries during rapid charge–discharge cycling, *J. Power Sources* 102 (2001) 294–301. [https://doi.org/10.1016/S0378-7753\(01\)00821-7](https://doi.org/10.1016/S0378-7753(01)00821-7).
- [14] H. Adenusi, G.A. Chass, S. Passerini, K.V. Tian, G. Chen, Lithium batteries and the solid electrolyte interphase (SEI) — progress and outlook, *Advanced Energy Materials* 13 (2023) 2203307. <https://doi.org/10.1002/aenm.202203307>.
- [15] X. Wang, Y. Ding, Y. Deng, Z. Chen, Ni-rich/Co-poor layered cathode for automotive Li-ion batteries: promises and challenges, *Advanced Energy Materials* 10 (2020) 1903864. <https://doi.org/10.1002/aenm.201903864>.
- [16] B. Venditti, Visualized: what is the cost of electric vehicle batteries?, (2023). <https://elements.visualcapitalist.com/cost-of-electric-vehicle-batteries/> (accessed February 19, 2025).
- [17] T. Wulandari, D. Fawcett, S.B. Majumder, G.E.J. Poinern, Lithium-based batteries, history, current status, challenges, and future perspectives, *Battery Energy* 2 (2023) 20230030. <https://doi.org/10.1002/bte2.20230030>.
- [18] S.-T. Myung, F. Maglia, K.-J. Park, C.S. Yoon, P. Lamp, S.-J. Kim, Y.-K. Sun, Nickel-rich layered cathode materials for automotive lithium-ion batteries: achievements and perspectives, *ACS Energy Lett.* 2 (2017) 196–223. <https://doi.org/10.1021/acsenergylett.6b00594>.
- [19] H. Kim, A. Sahebzadeh, H.J. Seifert, C. Ziebert, J. Friedl, Needle penetration studies on automotive lithium-ion battery cells: influence of resistance between can and positive terminal on thermal runaway, *J. Power Sources* 592 (2024) 233902. <https://doi.org/10.1016/j.jpowsour.2023.233902>.
- [20] W. Li, E.M. Erickson, A. Manthiram, High-nickel layered oxide cathodes for lithium-based automotive batteries, *Nat. Energy* 5 (2020) 26–34. <https://doi.org/10.1038/s41560-019-0513-0>.
- [21] Y. Chen, S. Song, X. Zhang, Y. Liu, The challenges, solutions and development of high energy Ni-rich NCM/NCA LiB cathode materials, *J. Phys.: Conf. Ser.* 1347 (2019) 012012. <https://doi.org/10.1088/1742-6596/1347/1/012012>.
- [22] X. Zuo, K. Chang, J. Zhao, Z. Xie, H. Tang, B. Li, Z. Chang, Thermally-driven mesopore formation and oxygen release in delithiated NCA cathode particles, *J. Mater. Chem. A* 4 (2016) 51–58. <https://doi.org/10.1039/C5TA06869J>.
- [23] H. Rostami, J. Valio, P. Tynjälä, U. Lassi, P. Suominen, Life cycle of LiFePO₄ batteries: production, recycling, and market trends, *ChemPhysChem* 25 (2024) e202400459. <https://doi.org/10.1002/cphc.202400459>.
- [24] J. Duan, X. Tang, H. Dai, Y. Yang, W. Wu, X. Wei, Y. Huang, Building safe lithium-ion batteries for electric vehicles: a review, *EER*. 3 (2020) 1–42. <https://doi.org/10.1007/s41918-019-00060-4>.
- [25] M. Held, M. Tuchschnid, M. Zennegg, R. Figi, C. Schreiner, L.D. Mellert, U. Welte, M. Kompatscher, M. Hermann, L. Nachev, Thermal runaway and fire of electric vehicle lithium-ion battery and contamination of infrastructure facility, *Renewable and Sustainable Energy Reviews* 165 (2022) 112474. <https://doi.org/10.1016/j.rser.2022.112474>.
- [26] I.-T. Hsieh, Y. Wu, B. Li, Y. Qi, First-principles study of the structures and redox mechanisms of Ni-rich lithium nickel manganese cobalt oxides, *Solid State Ionics* 411 (2024) 116556. <https://doi.org/10.1016/j.ssi.2024.116556>.

- [27] A.C.M. Maciel, Nickel-rich NMC materials for lithium-ion batteries: surface reactivity and gas production, Doctoral Dissertation, Université de Picardie Jules Verne (2021). <https://theses.hal.science/tel-03617814v1>.
- [28] S. Hwang, S.M. Kim, S.-M. Bak, S.Y. Kim, B.-W. Cho, K.Y. Chung, J.Y. Lee, E.A. Stach, W. Chang, Using real-time electron microscopy to explore the effects of transition-metal composition on the local thermal stability in charged $\text{Li}_x\text{Ni}_y\text{Mn}_z\text{Co}_{1-y-z}\text{O}_2$ cathode materials, *Chem. Mater.* 27 (2015) 3927–3935. <https://doi.org/10.1021/acs.chemmater.5b00709>.
- [29] S. Hwang, S.M. Kim, S.-M. Bak, B.-W. Cho, K.Y. Chung, J.Y. Lee, W. Chang, E.A. Stach, Investigating local degradation and thermal stability of charged nickel-based cathode materials through real-time electron microscopy, *ACS Appl. Mater. Interfaces.* 6 (2014) 15140–15147. <https://doi.org/10.1021/am503278f>.
- [30] C. Tian, Y. Xu, W.H. Kan, D. Sokaras, D. Nordlund, H. Shen, K. Chen, Y. Liu, M. Doeff, Distinct surface and bulk thermal behaviors of $\text{LiNi}_{0.6}\text{Mn}_{0.2}\text{Co}_{0.2}\text{O}_2$ cathode materials as a function of state of charge, *ACS Appl. Mater. Interfaces.* 12 (2020) 11643–11656. <https://doi.org/10.1021/acsami.9b21288>.
- [31] H.-J. Noh, S. Youn, C.S. Yoon, Y.-K. Sun, Comparison of the structural and electrochemical properties of layered $\text{Li}[\text{Ni}_x\text{Co}_y\text{Mn}_z]\text{O}_2$ ($x = 1/3, 0.5, 0.6, 0.7, 0.8$ and 0.85) cathode material for lithium-ion batteries, *J. Power Sources* 233 (2013) 121–130. <https://doi.org/10.1016/j.jpowsour.2013.01.063>.
- [32] H. Kim, H.J. Seifert, C. Ziebert, P. Finster, J. Friedl, A comparative study of commercial automotive prismatic Li-ion cells using nail penetration test, differential scanning calorimetry and thermogravimetric analysis, *J. Power Sources* 623 (2024) 235416. <https://doi.org/10.1016/j.jpowsour.2024.235416>.
- [33] G. Guzmán, J. Vazquez-Arenas, G. Ramos-Sánchez, M. Bautista-Ramírez, I. González, Improved performance of LiFePO_4 cathode for Li-ion batteries through percolation studies, *Electrochimica Acta* 247 (2017) 451–459. <https://doi.org/10.1016/j.electacta.2017.06.172>.
- [34] Electric Vehicle Outlook 2024, BloombergNEF, 2024. https://d2iztrg3kgqpue.cloudfront.net/production/uploaded-files/BNEF_EVO_2024_Publish-6db4a8cd-e5ee-40a8-9f57-9881fc0b77af.pdf (accessed May 5, 2025).
- [35] Y. Huang, Y.-C. Lin, D.M. Jenkins, N.A. Chernova, Y. Chung, B. Radhakrishnan, I.-H. Chu, J. Fang, Q. Wang, F. Omenya, S.P. Ong, M.S. Whittingham, Thermal stability and reactivity of cathode materials for Li-ion batteries, *ACS Appl. Mater. Interfaces.* 8 (2016) 7013–7021. <https://doi.org/10.1021/acsami.5b12081>.
- [36] A. Kazemi, R. Mostaani, M.K. Ravari, M. Ghorbanzadeh, M. Yavarinasab, J. Enferadi, Z. Chen, N. Iqbal, Y. Xiang, W. Liu, A. Davoodi, Enhancing high rate performance of Lithium Titanium Oxide (LTO) anodes: a comprehensive review, *J. Power Sources* 630 (2025) 236051. <https://doi.org/10.1016/j.jpowsour.2024.236051>.
- [37] S. Chae, S. Choi, N. Kim, J. Sung, J. Cho, Integration of graphite and silicon anodes for the commercialization of high-energy lithium-ion batteries, *Angew. Chem. Int. Ed.* 59 (2020) 110–135. <https://doi.org/10.1002/anie.201902085>.
- [38] M. Winter, J.O. Besenhard, M.E. Spahr, P. Novák, Insertion electrode materials for rechargeable lithium batteries, *Adv. Mater.* 10 (1998) 725–763. [https://doi.org/10.1002/\(SICI\)1521-4095\(199807\)10:10<725::AID-ADMA725>3.0.CO;2-Z](https://doi.org/10.1002/(SICI)1521-4095(199807)10:10<725::AID-ADMA725>3.0.CO;2-Z).
- [39] J.O. Besenhard, H.P. Fritz, The electrochemistry of black carbons, *Angew. Chem. Int. Ed.* 22 (1983) 950–975. <https://doi.org/10.1002/anie.198309501>.
- [40] Y. Reynier, R. Yazami, B. Fultz, The entropy and enthalpy of lithium intercalation into graphite, *J. Power Sources* 119–121 (2003) 850–855. [https://doi.org/10.1016/S0378-7753\(03\)00285-4](https://doi.org/10.1016/S0378-7753(03)00285-4).

- [41] V.A. Sethuraman, L.J. Hardwick, V. Srinivasan, R. Kostecki, Surface structural disordering in graphite upon lithium intercalation/deintercalation, *J. Power Sources* 195 (2010) 3655–3660. <https://doi.org/10.1016/j.jpowsour.2009.12.034>.
- [42] M. Wachtler, O. Öttinger, R. Schweiss, *Industrial carbon and graphite materials, volume I: raw materials, production and applications*, 1st ed., Wiley-VCH, Weinheim, 2021. <https://doi.org/10.1002/9783527674046.ch7>.
- [43] J.-M. Tarascon, M. Armand, Issues and challenges facing rechargeable lithium batteries, *Nature* 414 (2001) 359–367.
- [44] F. Orsini, L. Dupont, B. Beaudoin, S. Grugeon, J.-M. Tarascon, Scanning and transmission electron microscopy contributions to the improvement of electrode materials and interfaces in the design of better batteries, *Int. J. Inorg. Mater.* 2 (2000) 701–715. [https://doi.org/10.1016/S1466-6049\(00\)00093-3](https://doi.org/10.1016/S1466-6049(00)00093-3).
- [45] R. Younesi, G.M. Veith, P. Johansson, K. Edström, T. Vegge, Lithium salts for advanced lithium batteries: Li–metal, Li–O₂, and Li–S, *EES* 8 (2015) 1905–1922. <https://doi.org/10.1039/C5EE01215E>.
- [46] S.S. Zhang, A review on electrolyte additives for lithium-ion batteries, *J. Power Sources* 162 (2006) 1379–1394. <https://doi.org/10.1016/j.jpowsour.2006.07.074>.
- [47] K. Xu, Nonaqueous liquid electrolytes for lithium-based rechargeable batteries, *Chem. Rev.* 35 (2004) 4304–4417. <https://doi.org/10.1002/chin.200450271>.
- [48] T. Dong, S. Zhang, Z. Ren, L. Huang, G. Xu, T. Liu, S. Wang, G. Cui, Electrolyte engineering toward high performance high nickel (Ni ≥ 80%) lithium-ion batteries, *Adv. Sci.* (2024). <https://doi.org/10.1002/advs.202305753>.
- [49] S.J. An, J. Li, C. Daniel, D. Mohanty, S. Nagpure, D.L. Wood, The state of understanding of the lithium-ion-battery graphite solid electrolyte interphase (SEI) and its relationship to formation cycling, *Carbon* 105 (2016) 52–76. <https://doi.org/10.1016/j.carbon.2016.04.008>.
- [50] Y. Lee, H. Lee, T. Lee, M.-H. Ryou, Y.M. Lee, Synergistic thermal stabilization of ceramic/copolyimide coated polypropylene separators for lithium-ion batteries, *J. Power Sources* 294 (2015) 537–544. <https://doi.org/10.1016/j.jpowsour.2015.06.106>.
- [51] X. Zhu, X. Jiang, X. Ai, H. Yang, Y. Cao, TiO₂ ceramic-grafted polyethylene separators for enhanced thermostability and electrochemical performance of lithium-ion batteries, *J. Membr. Sci.* 504 (2016) 97–103. <https://doi.org/10.1016/j.memsci.2015.12.059>.
- [52] K. Chen, Y. Li, H. Zhan, Advanced separators for lithium-ion batteries, *IOP Conf. Ser.: Earth Environ. Sci.* 1011 (2022) 012009. <https://doi.org/10.1088/1755-1315/1011/1/012009>.
- [53] P.G. Balakrishnan, R. Ramesh, T. Prem Kumar, Safety mechanisms in lithium-ion batteries, *J. Power Sources* 155 (2006) 401–414. <https://doi.org/10.1016/j.jpowsour.2005.12.002>.
- [54] J. Im, J. Ahn, J.Y. Kim, E.J. Park, S. Yoon, Y.-G. Lee, K.Y. Cho, High-voltage operation by mechanical interlocking adhesion of nickel-rich cathode and functional separator in lithium-ion batteries, *Chem. Eng. J.* 450 (2022) 138159. <https://doi.org/10.1016/j.cej.2022.138159>.
- [55] L. Kong, C. Li, J. Jiang, M.G. Pecht, Li-ion battery fire hazards and safety strategies, *Energies* 11 (2018) 2191. <https://doi.org/10.3390/en11092191>.
- [56] C. Shi, P. Zhang, L. Chen, P. Yang, J. Zhao, Effect of a thin ceramic-coating layer on thermal and electrochemical properties of polyethylene separator for lithium-ion batteries, *J. Power Sources* 270 (2014) 547–553. <https://doi.org/10.1016/j.jpowsour.2014.07.142>.

- [57] N. Lingappan, W. Lee, S. Passerini, M. Pecht, A comprehensive review of separator membranes in lithium-ion batteries, *Renew. Sustain. Energy Rev.* 187 (2023) 113726. <https://doi.org/10.1016/j.rser.2023.113726>.
- [58] S.P. Kühn, K. Edström, M. Winter, I. Cekic-Laskovic, Face to face at the cathode electrolyte interphase: from interface features to interphase formation and dynamics, *Adv. Mater. Interfaces* 9 (2022) 2102078. <https://doi.org/10.1002/admi.202102078>.
- [59] J.-A. Choi, S.H. Kim, D.-W. Kim, Enhancement of thermal stability and cycling performance in lithium-ion cells through the use of ceramic-coated separators, *J. Power Sources* 195 (2010) 6192–6196. <https://doi.org/10.1016/j.jpowsour.2009.11.020>.
- [60] A.J. Bard, L.R. Faulkner, *Electrochemical methods: fundamentals and applications*, 2nd ed., John Wiley and Sons (WIE), New York, 2000.
- [61] Y. Yu, J. Wang, P. Zhang, J. Zhao, A detailed thermal study of usual $\text{LiNi}_{0.5}\text{Co}_{0.2}\text{Mn}_{0.3}\text{O}_2$, LiMn_2O_4 and LiFePO_4 cathode materials for lithium ion batteries, *J. Energy Storage* 12 (2017) 37–44. <https://doi.org/10.1016/j.est.2017.03.016>.
- [62] R.A. Huggins, Do you really want an unsafe battery?, *J. Electrochem. Soc.* 160 (2013) A3001–A3005. <https://doi.org/10.1149/2.001305jes>.
- [63] Z. Zhang, D. Fouchard, J.R. Rea, Differential scanning calorimetry material studies: implications for the safety of lithium-ion cells, *J. Power Sources* 70 (1998) 16–20.
- [64] A. Veluchamy, C.-H. Doh, D.-H. Kim, J.-H. Lee, H.-M. Shin, B.-S. Jin, H.-S. Kim, S.-I. Moon, Thermal analysis of Li_xCoO_2 cathode material of lithium ion battery, *J. Power Sources* 189 (2009) 855–858. <https://doi.org/10.1016/j.jpowsour.2008.07.090>.
- [65] Y. Lee, S.-O. Kim, J. Mun, M.-S. Park, K.J. Kim, K.Y. Lee, W. Choi, Influence of salt, solvents, and additives on the thermal stability of delithiated cathodes in lithium-ion batteries, *J. Electroanal. Chem.* 807 (2017) 174–180. <https://doi.org/10.1016/j.jelechem.2017.11.046>.
- [66] A. Kvasha, C. Gutiérrez, U. Osa, I. De Meatza, J.A. Blazquez, H. Macicior, I. Urdampilleta, A comparative study of thermal runaway of commercial lithium ion cells, *Energy* 159 (2018) 547–557. <https://doi.org/10.1016/j.energy.2018.06.173>.
- [67] H.M. Barkholtz, Y. Preger, S. Ivanov, J. Langendorf, L. Torres-Castro, J. Lamb, B. Chalamala, S.R. Ferreira, Multi-scale thermal stability study of commercial lithium-ion batteries as a function of cathode chemistry and state-of-charge, *J. Power Sources* 435 (2019) 226777. <https://doi.org/10.1016/j.jpowsour.2019.226777>.
- [68] M. Wang, A. Navrotsky, S. Venkatraman, A. Manthiram, Enthalpy of formation of Li_xCoO_2 ($0.5 \leq x \leq 1.0$), *J. Electrochem. Soc.* 152 (2005) J82–J84.
- [69] Y. Idemoto, T. Matsui, Thermodynamic stability, crystal structure, and cathodic performance of $\text{Li}_x(\text{Mn}_{1/3}\text{Co}_{1/3}\text{Ni}_{1/3})\text{O}_2$ depend on the synthetic process and Li content, *Solid State Ionics* 179 (2008) 625–635. <https://doi.org/10.1016/j.ssi.2008.03.024>.
- [70] M. Wang, A. Navrotsky, Enthalpy of formation of LiNiO_2 , LiCoO_2 and their solid solution, $\text{LiNi}_{1-x}\text{Co}_x\text{O}_2$, *Solid State Ionics* 166 (2004) 167–173. <https://doi.org/10.1016/j.ssi.2003.11.004>.
- [71] G. Weil, Data Shows EVs are Less of a Fire Risk than Conventional Cars, (2024). <https://www.fairfaxcounty.gov/environment-energy-coordination/climate-matters/EV-less-fire-risk#:~:text=Kelly%20Blue%20Book%20reported%20on,gasoline%2Dpowered%20or%20hybrid%20vehicles.&text=Data%20from%20the%20National%20Transportation,fires%20for%20every%20100%2C000%20sold>. (accessed February 26, 2025).

- [72] P. Victor Chombo, Y. Laoonual, S. Wongwises, Lessons from the electric vehicle crashworthiness leading to battery fire, *Energies* 14 (2021) 4802. <https://doi.org/10.3390/en14164802>.
- [73] S. Kang, M. Kwon, J. Yoon Choi, S. Choi, Full-scale fire testing of battery electric vehicles, *Applied Energy* 332 (2023) 120497. <https://doi.org/10.1016/j.apenergy.2022.120497>.
- [74] Y.-S. Duh, Y. Sun, X. Lin, J. Zheng, M. Wang, Y. Wang, X. Lin, X. Jiang, Z. Zheng, S. Zheng, G. Yu, Characterization on thermal runaway of commercial 18650 lithium-ion batteries used in electric vehicles: a review, *J. Energy Storage* 41 (2021) 102888. <https://doi.org/10.1016/j.est.2021.102888>.
- [75] J. Young, A Mercedes-Benz fire jolts South Korea's E.V. transition, (2024). <https://www.nytimes.com/2024/08/27/world/asia/south-korea-electric-vehicle-fire.html> (accessed February 27, 2025).
- [76] V. Ruiz, A. Pfrang, A. Kriston, N. Omar, P. Van Den Bossche, L. Boon-Brett, A review of international abuse testing standards and regulations for lithium ion batteries in electric and hybrid electric vehicles, *Renew. Sustain. Energy Rev.* 81 (2018) 1427–1452. <https://doi.org/10.1016/j.rser.2017.05.195>.
- [77] Y. Liu, S. Xiong, J. Wang, X. Jiao, S. Li, C. Zhang, Z. Song, J. Song, Dendrite-free lithium metal anode enabled by separator engineering via uniform loading of lithiophilic nucleation sites, *Energy Storage Materials* 19 (2019) 24–30. <https://doi.org/10.1016/j.ensm.2018.10.015>.
- [78] K. Zou, X. Chen, Z. Ding, J. Gu, S. Lu, Jet behavior of prismatic lithium-ion batteries during thermal runaway, *Appl. Therm. Eng.* 179 (2020) 115745. <https://doi.org/10.1016/j.applthermaleng.2020.115745>.
- [79] S. Hoelle, H. Kim, S. Zimmermann, O. Hinrichsen, Lithium-ion battery thermal runaway: experimental analysis of particle deposition in battery module environment, *Batteries* 10 (2024) 173. <https://doi.org/10.3390/batteries10060173>.
- [80] A. Abaza, S. Ferrari, H.K. Wong, C. Lyness, A. Moore, J. Weaving, M. Blanco-Martin, R. Dashwood, R. Bhagat, Experimental study of internal and external short circuits of commercial automotive pouch lithium-ion cells, *J. Energy Storage* 16 (2018) 211–217. <https://doi.org/10.1016/j.est.2018.01.015>.
- [81] S.M. Rezvanizani, Z. Liu, Y. Chen, J. Lee, Review and recent advances in battery health monitoring and prognostics technologies for electric vehicle (EV) safety and mobility, *J. Power Sources* 256 (2014) 110–124. <https://doi.org/10.1016/j.jpowsour.2014.01.085>.
- [82] S. Ko, H. Otsuka, S. Kimura, Y. Takagi, S. Yamaguchi, T. Masuda, A. Yamada, Rapid safety screening realized by accelerating rate calorimetry with lab-scale small batteries, *Nat. Energy* (2025). <https://doi.org/10.1038/s41560-025-01751-7>.
- [83] R. Stringfellow, D. Ofer, S. Sriramulu, B. Barnett, Lithium-ion battery safety field-failure mechanisms, in: *ECS Meeting Abstracts*, Las Vegas, NV, 2010. <https://doi.org/10.1149/MA2010-02/5/322>.
- [84] G. Zhang, X. Wei, X. Tang, J. Zhu, S. Chen, H. Dai, Internal short circuit mechanisms, experimental approaches and detection methods of lithium-ion batteries for electric vehicles: a review, *Renew. Sustain. Energy Rev.* 141 (2021) 110790. <https://doi.org/10.1016/j.rser.2021.110790>.
- [85] M. Loveridge, G. Remy, N. Kourra, R. Genieser, A. Barai, M. Lain, Y. Guo, M. Amor-Segan, M. Williams, T. Amietszajew, M. Ellis, R. Bhagat, D. Greenwood, Looking deeper into the Galaxy (Note 7), *Batteries* 4 (2018) 3. <https://doi.org/10.3390/batteries4010003>.
- [86] C. Fear, D. Juarez-Robles, J.A. Jeevarajan, P.P. Mukherjee, Elucidating copper dissolution phenomenon in Li-ion cells under overdischarge extremes, *J. Electrochem. Soc.* 165 (2018) A1639–A1647. <https://doi.org/10.1149/2.0671809jes>.

- [87] B. Liu, Y. Jia, C. Yuan, L. Wang, X. Gao, S. Yin, J. Xu, Safety issues and mechanisms of lithium-ion battery cell upon mechanical abusive loading: A review, *Energy Storage Materials* 24 (2020) 85–112. <https://doi.org/10.1016/j.ensm.2019.06.036>.
- [88] J. Jaguemont, F. Bardé, A critical review of lithium-ion battery safety testing and standards, *Appl. Therm. Eng.* 231 (2023) 121014. <https://doi.org/10.1016/j.applthermaleng.2023.121014>.
- [89] P. Lyu, X. Liu, J. Qu, J. Zhao, Y. Huo, Z. Qu, Z. Rao, Recent advances of thermal safety of lithium ion battery for energy storage, *Energy Storage Materials* 31 (2020) 195–220. <https://doi.org/10.1016/j.ensm.2020.06.042>.
- [90] Galaxy Note7: What We Discovered, (2017). <https://news.samsung.com/global/infographic-galaxy-note7-what-we-discovered> (accessed February 21, 2025).
- [91] D. Ouyang, M. Chen, Q. Huang, J. Weng, Z. Wang, J. Wang, A review on the thermal hazards of the lithium-ion battery and the corresponding countermeasures, *Applied Sciences* 9 (2019) 2483. <https://doi.org/10.3390/app9122483>.
- [92] S. Mallick, D. Gayen, Thermal behaviour and thermal runaway propagation in lithium-ion battery systems – a critical review, *J. Energy Storage* 62 (2023) 106894. <https://doi.org/10.1016/j.est.2023.106894>.
- [93] H. Yan, K.C. Marr, O.A. Ezekoye, Thermal runaway behavior of nickel–manganese–cobalt 18650 lithium-ion cells induced by internal and external heating failures, *J. Energy Storage* 45 (2022) 103640. <https://doi.org/10.1016/j.est.2021.103640>.
- [94] M. Zhang, J. Du, L. Liu, A. Stefanopoulou, J. Siegel, L. Lu, X. He, X. Xie, M. Ouyang, Internal short circuit trigger method for lithium-ion battery based on shape memory alloy, *J. Electrochem. Soc.* 164 (2017) A3038–A3044. <https://doi.org/10.1149/2.0731713jes>.
- [95] D.P. Finegan, E. Darcy, M. Keyser, B. Tjaden, T.M.M. Heenan, R. Jervis, J.J. Bailey, R. Malik, N.T. Vo, O.V. Magdysyuk, R. Atwood, M. Drakopoulos, M. DiMichiel, A. Rack, G. Hinds, D.J.L. Brett, P.R. Shearing, Characterising thermal runaway within lithium-ion cells by inducing and monitoring internal short circuits, *Energy Environ. Sci.* 10 (2017) 1377–1388. <https://doi.org/10.1039/C7EE00385D>.
- [96] S. Santhanagopalan, P. Ramadass, J. (Zhengming) Zhang, Analysis of internal short-circuit in a lithium ion cell, *J. Power Sources* 194 (2009) 550–557. <https://doi.org/10.1016/j.jpowsour.2009.05.002>.
- [97] Y. Sun, Y. Yuan, L. Lu, X. Han, X. Kong, H. Wang, M. Ouyang, P. Gao, H. Zheng, K. Wang, A comprehensive research on internal short circuits caused by copper particle contaminants on cathode in lithium-ion batteries, *eTransportation* 13 (2022) 100183. <https://doi.org/10.1016/j.etrans.2022.100183>.
- [98] D. Mohanty, E. Hockaday, J. Li, D.K. Hensley, C. Daniel, D.L. Wood, Effect of electrode manufacturing defects on electrochemical performance of lithium-ion batteries: cognizance of the battery failure sources, *J. Power Sources* 312 (2016) 70–79. <https://doi.org/10.1016/j.jpowsour.2016.02.007>.
- [99] W. Li, H. Wang, Y. Zhang, M. Ouyang, Flammability characteristics of the battery vent gas: a case of NCA and LFP lithium-ion batteries during external heating abuse, *J. Energy Storage* 24 (2019) 100775. <https://doi.org/10.1016/j.est.2019.100775>.
- [100] D. Andre, S.-J. Kim, P. Lamp, S.F. Lux, F. Maglia, O. Paschos, B. Stiaszny, Future generations of cathode materials: an automotive industry perspective, *J. Mater. Chem. A* 3 (2015) 6709–6732. <https://doi.org/10.1039/C5TA00361J>.
- [101] C. Ziebert, Online pressure and gas analysis of lithium-ion cells during abuse tests, (2023). <https://doi.org/10.56367/OAG-040-10412> (accessed May 1, 2025).

- [102] B. Lei, W. Zhao, C. Ziebert, N. Uhlmann, M. Rohde, H. Seifert, Experimental analysis of thermal runaway in 18650 cylindrical Li-ion cells using an accelerating rate calorimeter, *Batteries* 3 (2017) 14. <https://doi.org/10.3390/batteries3020014>.
- [103] R. Srinivasan, B.G. Carkhuff, M.H. Butler, A.C. Baisden, Instantaneous measurement of the internal temperature in lithium-ion rechargeable cells, *Electrochimica Acta* 56 (2011) 6198–6204. <https://doi.org/10.1016/j.electacta.2011.03.136>.
- [104] G. Pistoia, *Lithium-ion batteries advances and applications*, 1st ed., Elsevier, Oxford, 2014. <https://doi.org/10.1016/B978-0-444-59513-3.00017-0>.
- [105] A. Augeard, T. Singo, P. Desprez, F. Perisse, S. Menecier, M. Abbaoui, Arc analysis to the CID of Li-ion battery cells in high-current applications, in: *IEEE 60th Holm Conference on Electrical Contacts*, IEEE, New Orleans, 2014. <https://doi.org/10.1109/HOLM.2014.7031038>.
- [106] Elektroauto-Batterie und Antriebstechnologie, (2025). <https://www.bmw.de/de/elektroauto/batterie-technologie.html#kosten> (accessed February 23, 2025).
- [107] L. Lander, C. Tagnon, V. Nguyen-Tien, E. Kendrick, R.J.R. Elliott, A.P. Abbott, J.S. Edge, G.J. Offer, Breaking it down: A techno-economic assessment of the impact of battery pack design on disassembly costs, *Applied Energy* 331 (2023) 120437. <https://doi.org/10.1016/j.apenergy.2022.120437>.
- [108] M.F.R. Zwicker, M. Moghadam, W. Zhang, C.V. Nielsen, Automotive battery pack manufacturing – a review of battery to tab joining, *J. Adv. Join. Process.* 1 (2020) 100017. <https://doi.org/10.1016/j.jajp.2020.100017>.
- [109] G. Karimi, X. Li, Thermal management of lithium-ion batteries for electric vehicles: thermal management of Li-ion battery packs, *Int. J. Energy Res.* 37 (2013) 13–24. <https://doi.org/10.1002/er.1956>.
- [110] G.W.H. Höhne, W.F. Hemminger, H.-J. Flammersheim, *Differential scanning calorimetry*, Springer, Berlin, Heidelberg, 2003. <https://doi.org/10.1007/978-3-662-06710-9>.
- [111] N.M. Nurazzi, N. Abdullah, M.N.F. Norrrahim, S.H. Kamarudin, S. Ahmad, S.S. Shazleen, M. Rayung, M.R.M. Asyraf, R.A. Ilyas, M. Kuzmin, *Polylactic acid-based nanocellulose and cellulose composites*, 1st ed., CRC Press, Boca Raton, 2022. <https://doi.org/10.1201/9781003160458-7>.
- [112] T. Tyagi, J. Ahlawat, Differential scanning calorimetry (DSC), *Vigyan Varta* 5 (2024) 265–267.
- [113] N.F.A. Zainal, J.M. Saiter, S.I.A. Halim, R. Lucas, C.H. Chan, Thermal analysis: basic concept of differential scanning calorimetry and thermogravimetry for beginners, *Chem. Teach. Int.* 3 (2021) 59–75. <https://doi.org/10.1515/cti-2020-0010>.
- [114] E. Ghanbari, S.J. Picken, J.H. Van Esch, Analysis of differential scanning calorimetry (DSC): determining the transition temperatures, and enthalpy and heat capacity changes in multicomponent systems by analytical model fitting, *J. Therm. Anal. Calorim.* 148 (2023) 12393–12409. <https://doi.org/10.1007/s10973-023-12356-1>.
- [115] P. Gabbott, *Principles and applications of thermal analysis*, 1st ed., Blackwell, Singapore, 2008. <https://doi.org/10.1002/9780470697702.ch1>.
- [116] N. Saadatkhah, A. Carillo Garcia, S. Ackermann, P. Leclerc, M. Latifi, S. Samih, G.S. Patience, J. Chaouki, Experimental methods in chemical engineering: thermogravimetric analysis—TGA, *Can. J. Chem. Eng.* 98 (2020) 34–43. <https://doi.org/10.1002/cjce.23673>.
- [117] E. Calvet, H. Prat, *Recent progress in microcalorimetry*, Elsevier, Pergamon, 1963. <https://doi.org/10.1016/C2013-0-10017-7>.

- [118] A. Navrotsky, Progress and new directions in calorimetry: a 2014 perspective, *J. Am. Ceram. Soc.* 97 (2014) 3349–3359. <https://doi.org/10.1111/jace.13278>.
- [119] A. Navrotsky, Progress and new directions in high temperature calorimetry revisited, *Physics and Chemistry of Minerals* 24 (1997) 222–241. <https://doi.org/10.1007/s002690050035>.
- [120] M. Scharrer, L. Bonatti, T. Geraci, S.V. Ushakov, J. Majzlan, M. Bustamante, H. Kojitani, X. Guo, H. Xu, L. Zhang, K. Lilova, S. Hayun, T. Subramani, A. Navrotsky, The joys and jitters of high-temperature calorimetry, *J. Am. Ceram. Soc.* (2025) e20381. <https://doi.org/10.1111/jace.20381>.
- [121] M. Lepple, Kupfer- und Eisenoxide als Konversions-Elektrodenmaterialien für Lithium-Ionen-Batterien: Thermodynamische und Elektrochemische Untersuchungen, Doctoral dissertation, Karlsruher Institut für Technologie (KIT) (2015). DOI: 10.5445/KSP/1000051891.
- [122] SETARAM the CALVET line, (2025). <https://setaramsolutions.com/app/uploads/sites/2/2023/03/EN-CALVET.pdf> (accessed May 5, 2025).
- [123] G.A. Uriano, National bureau of standards certificate standard reference material 720 synthetic sapphire (α -Al₂O₃), Office of Standard Reference Materials, Washington, D.C., 1982.
- [124] A. Karmakar, H. Zhou, B.S. Vishnugopi, J.A. Jeevarajan, P.P. Mukherjee, State-of-charge implications of thermal runaway in Li-ion cells and modules, *J. Electrochem. Soc.* 171 (2024) 010529. <https://doi.org/10.1149/1945-7111/ad1ecc>.
- [125] B. Mao, P. Huang, H. Chen, Q. Wang, J. Sun, Self-heating reaction and thermal runaway criticality of the lithium ion battery, *International Journal of Heat and Mass Transfer* 149 (2020) 119178. <https://doi.org/10.1016/j.ijheatmasstransfer.2019.119178>.
- [126] T. Gao, J. Bai, D. Ouyang, Z. Wang, W. Bai, N. Mao, Y. Zhu, Effect of aging temperature on thermal stability of lithium-ion batteries: part A – High-temperature aging, *Renewable Energy* 203 (2023) 592–600. <https://doi.org/10.1016/j.renene.2022.12.092>.
- [127] M. Reichert, J. Haetge, D. Berghus, C. Wendt, V. Meier, U. Rodehorst, S. Passerini, F. Schappacher, M. Winter, Lithium-ion cell nail penetration safety experiments under adiabatic conditions, *ECST* 61 (2014) 87–103. <https://doi.org/10.1149/06127.0087ecst>.
- [128] J. Ye, H. Chen, Q. Wang, P. Huang, J. Sun, S. Lo, Thermal behavior and failure mechanism of lithium ion cells during overcharge under adiabatic conditions, *Applied Energy* 182 (2016) 464–474. <https://doi.org/10.1016/j.apenergy.2016.08.124>.
- [129] W. Zhao, G. Luo, C.-Y. Wang, Modeling nail penetration process in large-format Li-ion cells, *J. Electrochem. Soc.* 162 (2015) A207–A217. <https://doi.org/10.1149/2.1071501jes>.
- [130] L. Zhang, Y. Liu, X. Huang, Dynamic thermal runaway evolution of Li-ion battery during nail penetration, *International Journal of Heat and Mass Transfer* 233 (2024) 126020. <https://doi.org/10.1016/j.ijheatmasstransfer.2024.126020>.
- [131] Z. An, W. Li, X. Du, L. Jia, Q. Li, D. Zhang, Experimental study on behaviors of lithium-ion cells experiencing internal short circuit and thermal runaway under nail penetration abuse condition, *Applied Thermal Engineering* 247 (2024) 123058. <https://doi.org/10.1016/j.applthermaleng.2024.123058>.
- [132] D.P. Finegan, B. Tjaden, T. M. M. Heenan, R. Jervis, M.D. Michiel, A. Rack, G. Hinds, D.J.L. Brett, P.R. Shearing, Tracking Internal Temperature and Structural Dynamics during Nail Penetration of Lithium-Ion Cells, *J. Electrochem. Soc.* 164 (2017) A3285–A3291. <https://doi.org/10.1149/2.1501713jes>.

- [133] B. Mao, H. Chen, Z. Cui, T. Wu, Q. Wang, Failure mechanism of the lithium ion battery during nail penetration, *International Journal of Heat and Mass Transfer* 122 (2018) 1103–1115. <https://doi.org/10.1016/j.ijheatmasstransfer.2018.02.036>.
- [134] J. Wang, W. Mei, Z. Cui, W. Shen, Q. Duan, Y. Jin, J. Nie, Y. Tian, Q. Wang, J. Sun, Experimental and numerical study on penetration-induced internal short-circuit of lithium-ion cell, *Applied Thermal Engineering* 171 (2020) 115082. <https://doi.org/10.1016/j.applthermaleng.2020.115082>.
- [135] J. Diekmann, S. Doose, S. Weber, S. Münch, W. Haselrieder, A. Kwade, Development of a new procedure for nail penetration of lithium-ion cells to obtain meaningful and reproducible results, *J. Electrochem. Soc.* 167 (2020) 090504. <https://doi.org/10.1149/1945-7111/ab78ff>.
- [136] S. Huang, X. Du, M. Richter, J. Ford, G.M. Cavaliheiro, Z. Du, R.T. White, G. Zhang, Understanding Li-ion cell internal short circuit and thermal runaway through small, slow and in situ sensing nail penetration, *J. Electrochem. Soc.* 167 (2020) 090526. <https://doi.org/10.1149/1945-7111/ab8878>.
- [137] S. Liu, S. Huang, Q. Zhou, K. Snyder, M.K. Long, G. Zhang, In situ measurement of dynamic internal short circuit resistance during nail penetration of lithium-ion cells and its implications on cell robustness and abuse tolerance, *J. Electrochem. Soc.* 170 (2023) 060515. <https://doi.org/10.1149/1945-7111/acd814>.
- [138] Aluminium-Halbzeug EN AW-6012 (AlMgSiPb - 3.0615), (2025). <https://batz-burgel.com/metallhandel/lieferant-aluminium/en-aw-6012/> (accessed March 26, 2025).
- [139] Thermal conductivity of stainless steel explained & chart, (2025). <https://steelprogroup.com/stainless-steel/properties/thermal-conductivity/> (accessed March 26, 2025).
- [140] Günther+Schramm Technisches Datenblatt von AlMgSiPb, (2025). https://www.gs-stahl.de/images/AlMgSiPb__AlMgSiPb.pdf (accessed May 29, 2025).
- [141] V.S. Yungman, V.P. Glushko, V.A. Medvedev, L.V. Gurvich, *Thermal constants of substances*, 1st ed., Wiley, United States, 1999.
- [142] J.M. McHale, A. Navrotsky, G.R. Kowach, V.E. Balbarin, F.J. DiSalvo, Energetics of ternary nitrides: Li–Ca–Zn–N and Ca–Ta–N systems, *Chem. Mater.* 9 (1997) 1538–1546. <https://doi.org/10.1021/cm970244r>.
- [143] R.A. Robie, B.S. Hemingway, *Thermodynamic properties of minerals and related substances at 298.15 K and 1 Bar (105 Pascals) pressure and at higher temperatures*, United states government printing office, Washington, 1995. <https://doi.org/10.3133/b2131>.
- [144] M. Wang, A. Navrotsky, Thermochemistry of $\text{Li}_{1-x}\text{Mn}_{2-x}\text{O}_4$ ($0 \leq x \leq 1/3$) spinel, *J. Solid State Chem.* 178 (2005) 1182–1189. <https://doi.org/10.1016/j.jssc.2004.12.007>.
- [145] N. Birkner, A. Navrotsky, Thermodynamics of manganese oxides: effects of particle size and hydration on oxidation-reduction equilibria among hausmannite, bixbyite, and pyrolusite, *American Mineralogist* 97 (2012) 1291–1298. <https://doi.org/10.2138/am.2012.3982>.
- [146] N.A. Mayer, D.M. Cupid, R. Adam, A. Reif, D. Rafaja, H.J. Seifert, Standard enthalpy of reaction for the reduction of Co_3O_4 to CoO , *Thermochimica Acta* 652 (2017) 109–118. <https://doi.org/10.1016/j.tca.2017.03.011>.
- [147] L. Wang, A. Navrotsky, R. Stevens, B.F. Woodfield, J. Boerio-Goates, Thermodynamics of CoO – MgO solid solutions, *J. Chem. Thermodyn.* 35 (2003) 1151–1159. [https://doi.org/10.1016/S0021-9614\(03\)00083-1](https://doi.org/10.1016/S0021-9614(03)00083-1).

- [148] H. Banerjee, C.P. Grey, A.J. Morris, Stability and redox mechanisms of Ni-rich NMC cathodes: insights from first-principles many-body calculations, *Chem. Mater.* 36 (2024) 6575–6587. <https://doi.org/10.1021/acs.chemmater.4c00928>.
- [149] T. Kim, The origin of the aggressive degradation of Ni-rich transition metal oxide cathodes for high-energy density lithium-ion batteries, *J. Solid State Chem.* 310 (2022) 123040. <https://doi.org/10.1016/j.jssc.2022.123040>.
- [150] S.W. Holman, R.R. Lawrence, L. Barr, Melting-points of aluminium, silver, gold, copper, and platinum, *Lond. Edinb. Dubl. Phil. Mag.* 42 (1896) 37–51. <https://doi.org/10.1080/14786449608620888>.
- [151] D. Oehler, J. Bender, P. Seegert, T. Wetzel, Investigation of the effective thermal conductivity of cell stacks of Li-ion batteries, *Energy Technology* 9 (2021) 2000722. <https://doi.org/10.1002/ente.202000722>.
- [152] Y. Zeng, D. Chalise, S.D. Lubner, S. Kaur, R.S. Prasher, A review of thermal physics and management inside lithium-ion batteries for high energy density and fast charging, *Energy Storage Materials* 41 (2021) 264–288. <https://doi.org/10.1016/j.ensm.2021.06.008>.
- [153] H. Maleki, S.A. Hallaj, J.R. Selman, R.B. Dinwiddie, H. Wang, Thermal properties of lithium-ion battery and components, *J. Electrochem. Soc.* 146 (1999) 947–954. <https://doi.org/10.1149/1.1391704>.
- [154] D. Werner, A. Loges, D.J. Becker, T. Wetzel, Thermal conductivity of Li-ion batteries and their electrode configurations – a novel combination of modelling and experimental approach, *J. Power Sources* 364 (2017) 72–83. <https://doi.org/10.1016/j.jpowsour.2017.07.105>.
- [155] M. Fleckenstein, S. Fischer, O. Bohlen, B. Bäker, Thermal impedance spectroscopy - a method for the thermal characterization of high power battery cells, *J. Power Sources* 223 (2013) 259–267. <https://doi.org/10.1016/j.jpowsour.2012.07.144>.
- [156] T.R. Jow, C.C. Liang, Lithium-aluminum electrodes at ambient temperatures, *J. Electrochem. Soc.* 129 (1982) 1429–1434. <https://doi.org/10.1149/1.2124178>.
- [157] J. Lamb, C.J. Orendorff, E.P. Roth, J. Langendorf, Studies on the thermal breakdown of common Li-ion battery electrolyte components, *J. Electrochem. Soc.* 162 (2015) A2131–A2135. <https://doi.org/10.1149/2.0651510jes>.
- [158] R.C. Shurtz, J.D. Engerer, J.C. Hewson, Predicting high-temperature decomposition of lithiated graphite: part I. review of phenomena and a comprehensive model, *J. Electrochem. Soc.* 165 (2018) A3878–A3890. <https://doi.org/10.1149/2.0541816jes>.
- [159] J. Kasnatscheew, S. Röser, M. Börner, M. Winter, Do increased Ni contents in $\text{LiNi}_x\text{Mn}_y\text{Co}_z\text{O}_2$ (NMC) electrodes decrease structural and thermal stability of Li ion batteries? A thorough look by consideration of the Li^+ extraction ratio, *ACS Appl. Energy Mater.* 2 (2019) 7733–7737. <https://doi.org/10.1021/acsaem.9b01440>.
- [160] Y. Qin, Z. Chen, J. Liu, K. Amine, Lithium tetrafluoro oxalato phosphate as electrolyte additive for lithium-ion cells, *Electrochem. Solid-State Lett.* 13 (2010) A11. <https://doi.org/10.1149/1.3261738>.
- [161] J. Wang, D. Zhao, Y. Cong, N. Zhang, P. Wang, X. Fu, X. Cui, Analyzing the mechanism of functional groups in phosphate additives on the interface of $\text{LiNi}_{0.8}\text{Co}_{0.15}\text{Al}_{0.05}\text{O}_2$ cathode materials, *ACS Appl. Mater. Interfaces* 13 (2021) 16939–16951. <https://doi.org/10.1021/acsaami.0c21535>.
- [162] S.-M. Bak, E. Hu, Y. Zhou, X. Yu, S.D. Senanayake, S.-J. Cho, K.-B. Kim, K.Y. Chung, X.-Q. Yang, K.-W. Nam, Structural changes and thermal stability of charged $\text{LiNi}_x\text{Mn}_y\text{Co}_z\text{O}_2$ cathode materials studied by combined in situ time-resolved XRD and mass spectroscopy, *ACS Appl. Mater. Interfaces* 6 (2014) 22594–22601. <https://doi.org/10.1021/am506712c>.

- [163] G. Mulder, N. Omar, S. Pauwels, M. Meeus, F. Leemans, B. Verbrugge, W. De Nijs, P. Van Den Bossche, D. Six, J. Van Mierlo, Comparison of commercial battery cells in relation to material properties, *Electrochimica Acta* 87 (2013) 473–488. <https://doi.org/10.1016/j.electacta.2012.09.042>.
- [164] D.J. Xiong, L.D. Ellis, J. Li, H. Li, T. Hynes, J.P. Allen, J. Xia, D.S. Hall, I.G. Hill, J.R. Dahn, Measuring oxygen release from delithiated $\text{LiNi}_x\text{Mn}_y\text{Co}_{1-x-y}\text{O}_2$ and its effects on the performance of high voltage Li-ion cells, *J. Electrochem. Soc.* 164 (2017) A3025–A3037. <https://doi.org/10.1149/2.0291713jes>.
- [165] J. Lamb, L. Torres-Castro, J.C. Hewson, R.C. Shurtz, Y. Preger, Investigating the role of energy density in thermal runaway of lithium-ion batteries with accelerating rate calorimetry, *J. Electrochem. Soc.* 168 (2021) 060516. <https://doi.org/10.1149/1945-7111/ac0699>.
- [166] J. Wang, Z. Wang, B. Sun, Improved equation of CO_2 Joule–Thomson coefficient, *J. CO2 Util.* 19 (2017) 296–307. <https://doi.org/10.1016/j.jcou.2017.04.007>.